

Faculty of Engineering and Information Technology

**Topological Shape Optimization of Microstructures of  
Materials using Level Set Methods**

A thesis submitted for the degree of

**Doctor of Philosophy**

**Yu WANG**

(2015)

**Title of the thesis:**

Topological shape optimization of microstructures of materials using level set methods

**Ph.D. student:**

Yu Wang

E-mail: [Yu.Wang-11@student.uts.edu.au](mailto:Yu.Wang-11@student.uts.edu.au)

**Supervisor:**

Prof Nong Zhang

E-mail: [Nong.Zhang@uts.edu.au](mailto:Nong.Zhang@uts.edu.au)

**Co-Supervisor:**

Dr Zhen Luo

E-mail: [Zhen.Luo@uts.edu.au](mailto:Zhen.Luo@uts.edu.au)

**Address:**

School of Electrical, Mechanical and Mechatronic Systems

The University of Technology, Sydney, NSW 2007, Australia

# Certificate of Original Authorship

I certify that the work in this thesis has not previously been submitted for a degree nor has it been submitted as part of requirements for a degree except as fully acknowledged within the text.

I also certify that the thesis has been written by me. Any help that I have received in my research work and the preparation of the thesis itself has been acknowledged. In addition, I certify that all information sources and literature used are indicated in the thesis.

Signature of Student:

A handwritten signature in black ink, appearing to read "Wang Yu".

**YU WANG**

Date:

# Acknowledgments

My thesis could not have come to fruition without the assistance of many contributors.

Hereby, I would express my deep gratitude to my principal Professor Nong Zhang. He supported me with great direction, advices and any other helps in my research. His knowledge, hard-working and research attitude fostered my development in various aspects.

I am profoundly grateful to my co-supervisor Dr Zhen Luo. Without his kindness of helping me to verify the simulation, the completion of this thesis would be impossible. He provided me with great guidance during my whole candidature period. He is the most brilliant and helpful co-supervisor to me. I would also express my gratitude to Dr Jinchen Ji, Dr Paul Walker and Dr Yiqiang Wang, who often offered their time in discussing research issues during my PhD research program.

I would like to thank my colleagues, Xingxing Zhou, Jinglai Wu, Lifu Wang, Sangzhi Zhu, Tianxiao Zhang, Guangzhogn Xu, Jiageng Ruan, Robert Heal, Li Sun, Bo Zhu, Mingming Zhao, for their supports.

I also wish to gratefully acknowledge the consistent financial support of the following agents: China Scholarship Council (CSC) and University of Technology, Sydney (UTS).

Most especially to my family, words alone cannot express what I own them for their encouragement and whose patient love enabled me to complete this thesis.

# Publications and Conference Contributions

The following publications are part of the thesis

## Peer reviewed international scientific journal publications

- [1] **Y. Wang**, Z. Luo, N. Zhang, Topological optimization of structures using a multilevel nodal density-based approximant, *CMES: Computer Modeling in Engineering & Sciences*. Vol. 84, Issue.3, pp. 229-252, 2012.
- [2] **Y. Wang**, Z. Luo, J. Wu, N. Zhang, Topology optimization for micro compliant mechanisms using the element-free Galerkin method, *Advances in Engineering Software*. Vol. 85, pp. 61-72, 2015.
- [3] **Y. Wang**, Z. Luo, N. Zhang, QF. Qing, Topological shape optimization of multifunctional tissue engineering scaffolds with level set method. *Structural and Multidisciplinary Optimization*. (Major revision, Manuscript ID SMO-14-039)
- [4] **Y. Wang**, Z. Luo, N. Zhang, Topological design for mechanical metamaterials using a multiphase level set method, *Structural and Multidisciplinary Optimization*. (Major revision, Manuscript ID SMO-15-0079)
- [5] **Y. Wang**, Z. Luo, N. Zhang, Design of micro-structured metamaterials using a multiphase level set method, *Engineering Optimization* (Major revision, Manuscript ID GENO-2014-0193)
- [6] Z. Luo, N. Zhang, **Y. Wang**, A physically meaningful level set method for topology optimization of structures, *CMES: Computer Modeling in Engineering & Sciences*. Vol. 83, Issue.1, pp. 73-96, 2012
- [7] Z. Luo, N. Zhang, **Y. Wang**, W. Gao, Topology optimization of structures using meshless density variable approximants, *International Journal for Numerical Methods in Engineering*, Vol. 93, Issue.4, pp. 443-464, 2013

*Peer reviewed international scientific conference publications*

- [1] **Yu Wang**, Zhen Luo. Shape and topology optimization using a nodal density-based level set method, *The 14th Asia Pacific Vibration Conference APVC 14*, 5-8 December 2011, The Hong Kong Polytechnic University.
- [2] **Y. Wang**, Z. Luo. A radial point-based meshfree Galerkin method for topology optimization, *The 4th International Conference on Computational Methods ICCM 2012*, 25-27 November, Gold Coast, Australia.
- [3] N. Zhang, **Y. Wang**, Z. Luo. Structural topology optimization using meshfree methods, *The 23rd International Congress of Theoretical and Applied Mechanics ICTAM 2012*, 19-24 August, 2012, Beijing, China.
- [4] Z. Luo, **Y. Wang**, N. Zhang, Topology optimization of lightweight structures using a meshless shepard function approximant, *The 7th Australasian Congress on Applied Mechanics ACAM 7*, 9-12 December, 2012, Adelaide, Australia.
- [5] **Y. Wang**, Z. Luo, N. Zhang, Topology optimization of compliant mechanisms using element-free methods, *The 2013 World Congress on Global Optimization WCGO 2013*, 7-12 July, 2013, The Yellow Mountains, China. *Advances in Global Optimization* Springer Proceedings in Mathematics & Statistics, 95, 2015, pp 217-226
- [6] **Y. Wang**, Z. Luo, N. Zhang, Design optimization of structures using a nodal density-based SIMP method, *The 13th Asia-Pacific Congress for Computational Mechanics, APCOM 2013*, 11-14 December, 2013, Singapore.
- [7] **Y. Wang**, Z. Luo, N. Zhang, The topological design of metamaterials using a level set method, *The 11th World Congress on Computational Mechanics WCCM XI 2014*, 21-25 July, 2014, Barcelona.

# Abstract

Topology optimization has been regarded as a most promising approach in the conceptual stage of structural design. It has experienced rapid development over the past two decades and has been applied to a wide range of engineering problems. This thesis will focus on the level-set based topology optimization method, which was originally developed by Osher and Sethian in 1988 and have been successfully incorporated into the structural optimization. With the implicit representation scheme, the level set methods can be easily applied to handle the complex shape and topology changes of the structural design.

This work is divided into three parts. The first part is the necessary background for understanding the main focuses of the thesis. It includes the first four chapters: Chapter 1 provides the background the topology optimization, and overview of the current topology optimization methods, as well as application in the material design fields. Chapter 2 gives a description of the numerical homogenization method. Chapter 3 introduces the theory of the conventional level-set methods, and Chapter 4 provides details of for a parameterized level set method with numerical examples.

The second part of this thesis is about the design of mechanical/elastic metamaterials, which is contented in Chapter 5. In this part, we integrate the parameterized level set method with the numerical homogenization method for the design problems of metamaterials. Meanwhile, a multiphase level-set based scheme for designing metamaterials is proposed. In the parameterized level set method, a set of compactly supported radial basis functions (CSRBF) is employed to interpolate each implicit level set function, which transfer the most

difficult topology optimization problem into an easiest “size” optimization problem in the area of structural optimization. This method will be free of the Courant–Friedrichs–Lewy (CFL) condition and the re-initialization scheme. The propagation of the level set function can be driven by other well-developed optimization that involves gradient information. Moreover, this method can freely create new holes inside the material regions of the two-dimensional (2D) design domain. The optimal designs for mechanical metamaterials with extreme and prescribed properties are presented in this chapter as well (e.g. negative thermal expansion and negative Poisson’s ratios).

In the third part of this thesis, Chapter 6, we applied the parametric level set method and the numerical homogenization method for designing three-dimensional (3D) scaffolds for the tissue engineering. Numerical examples are used to demonstrate the effectiveness of the optimization method in designing the scaffold with a range of multifunctional properties. The efficiency, convergence and accuracy of the present methods are also highlighted.

Finally conclusions are given in Chapter 7.

*Keywords:* Topological shape optimization; Let set method; Homogenization method; Microstructures, Mechanical metamaterial; Tissue engineering scaffold.

# Contents

<b>Certificate of Original Authorship .....</b>	<b>i</b>
<b>Acknowledgments .....</b>	<b>ii</b>
<b>Publications and Conference Contributions.....</b>	<b>iii</b>
<b>Abstract.....</b>	<b>v</b>
<b>List of Tables .....</b>	<b>xi</b>
<b>List of Figures .....</b>	<b>xii</b>
<b>Nomenclature.....</b>	<b>xvi</b>
<b>1    Introduction.....</b>	<b>1</b>
1.1 Background .....	1
1.2 Literature Review .....	2
1.2.1 Topology Optimization Methods.....	3
1.2.2 Topological Design of Metamaterials.....	10
1.2.3 Topological Design of Scaffold Architectures .....	12
1.3 Contribution and Organization of the Thesis .....	14
<b>2    Homogenization Method .....</b>	<b>16</b>
2.1 Homogenization Theory.....	16
2.2 Homogenization Method for Elasticity Problem.....	19
2.3 Numerical Homogenization Method and Examples.....	23
2.3.1 Calculate Effective Elasticity Tensor for 2D Composite.....	24
2.3.2 Calculate Effective Elasticity Tensor for 3D Composite.....	26
<b>3    Level Set Method for Topology Optimization.....</b>	<b>29</b>
3.1 Representation of the Boundary via LSM .....	29
3.2 Hamilton-Jacobi Equations and Numerical Solution .....	30

3.2.1 Hamilton-Jacobi Equations.....	30
3.2.2 Discrete Solution to Hamilton-Jacobi Equations.....	32
3.3 Quantities Approximation in Level Set Function.....	34
3.3.1 Quantities Approximation.....	34
3.3.2 Numerical Example for Propagation of LSF .....	37
3.3.3 Numerical Example for Mean Curvature Flow (1).....	40
3.3.4 Numerical Example for Mean Curvature Flow (2).....	42
3.4 Numerical Issues of Level Set Method .....	44
3.4.1 Re-Initialization of Level Set Surface .....	44
3.4.2 Numerical Example for Re-Initialization .....	46
3.4.3 Velocity Extension.....	48
3.4.4 Numerical Example for Velocity Extension.....	49
<b>4 A Parameterized Level Set Method for Structural Shape and Topology Optimization .....</b>	<b>53</b>
4.1 Parameterization of Shape and Topology Optimization .....	53
4.1.1 Compactly Supported Radial Basis Functions .....	54
4.1.2 Parameterization of the Level Set Function.....	61
4.2 Shape Derivative of the Optimization Problem .....	63
4.3 Optimization Method .....	66
4.3.1 Optimality Criteria Method .....	66
4.3.2 The Method of Moving Asymptotes.....	70
4.4 Numerical Examples .....	74
4.4.1 Mitchell-Type Structure.....	74
4.4.2 Cantilever Beam A.....	79
4.4.3 Cantilever Beam B.....	87
<b>5 Design of Mechanical Metamaterials.....</b>	<b>93</b>
5.1 Multi-Phase Level Set Method.....	93

5.2 Multi-Phase Material Representation Model .....	96
5.3 Design of Multi-Phase Composites .....	98
5.3.1 Multi-Phase Material Representation Model .....	98
5.3.2 Calculation of Effective Material Properties .....	99
5.3.3 Numerical Implementation .....	101
5.3.4 Thermoelastic Metamaterials .....	104
5.3.5 Multifunctional Metamaterials .....	109
5.4 Numerical Examples .....	111
5.4.1 Metamaterials with Extreme Thermal Expansion .....	111
5.4.2 Metamaterials with ZTE .....	118
5.4.3 Metamaterials with NTE .....	120
5.4.4 Multifunctional Metamaterial .....	122
5.4.5 Summary .....	136
<b>6 Design of Tissue Engineering Scaffold Architecture .....</b>	<b>137</b>
6.1 Homogenization of Elasticity and Permeability .....	137
6.2 Multi-Objective Optimization Problem .....	140
6.2.1 Level Set Material Description Model .....	140
6.2.2 Formulation of the Optimization Problem by PLSM .....	141
6.3 Numerical Implementation of the Multi-Objective Topology Optimization Problem .....	143
6.4 Numerical Examples .....	144
6.4.1 Design Results with Different Mesh Level .....	145
6.4.2 Convergent Histories .....	147
6.4.3 Optimal Designs with Different Porosities .....	151
6.4.4 Summary .....	160
<b>7 Conclusions and Future Work .....</b>	<b>160</b>
7.1 Conclusions .....	160

7.2 Future Work .....	161
<b>References .....</b>	<b>163</b>

# List of Tables

Table 5-1 Thermoelastic parameters of optimal microstructures .....	116
Table 5-2 Thermoelastic parameters for optimal microstructures .....	118
Table 5-3 Thermoelastic parameters for optimal microstructures .....	120
Table 5-4 Initial parameters and initial design for Case (1).....	123
Table 5-5 Initial parameters and corresponding solutions for Case (1).....	124
Table 5-6 Initial parameters and optimal results for Case (2).....	127
Table 5-7 Initial parameters and corresponding optimal solutions for Case (3).....	131
Table 5-8 Initial parameters and corresponding optimal solutions for Case (4).....	134
Table 6-1 Optimization parameters and properties of designed microstructures .....	146
Table 6-2 Optimal designs of scaffold architecture under the porosity 40%.....	153
Table 6-3 Optimal designs of scaffold architecture under the porosity 50%.....	154
Table 6-4 Optimal designs of scaffold architecture under the porosity 70%.....	155
Table 6-5 Initial parameters and corresponding optimal solutions.....	156

# List of Figures

Figure 2.1 Characteristic dimension of inhomogeneity and scale enlargement.....	18
Figure 2.2 Elasticity problem for composite with periodic microstructures.....	20
Figure 2.3 Periodicity conditions of the unit cell.....	23
Figure 2.4 (a) Geometry of the unit cell; (b) finite element mesh of the unit cell .....	25
Figure 2.5 The deformation of unit cell under different load cases .....	26
Figure 2.6 (a) Geometry of the unit cell; (b) Finite element mesh of the unit cell .....	27
Figure 3.1 boundary representation using 3D level set surface .....	30
Figure 3.2 Numerically approximated Heaviside function .....	35
Figure 3.3 Numerically approximated Dirac function .....	36
Figure 3.4 Initial level set function .....	38
Figure 3.5 The propagation of LSF in normal speed at iteration 15, 30, 45, and 70. ....	39
Figure 3.6 The evolution of mean curvature flow.....	42
Figure 3.7 The evolution of mean curvature flow 2.....	44
Figure 3.8 The process of re-initializing the level set function as a signed distance function	48
Figure 3.9 Initial zero level set and correspondent 3d surface of the level set function .....	50
Figure 3.10 The process of velocity extension .....	52
Figure 4.1 Supported domain of knot $i$ with radius $d_{mi}$ .....	55
Figure 4.2 (a): Shapes of Wendland-C2; (b), (c):its derivatives in the $X$ and $Y$ directions... ..	57
Figure 4.3 (a): Shapes of Wendland-C4; (b), (c):its derivatives in the $X$ and $Y$ directions.. ..	59
Figure 4.4 (a): Shapes of Wendland-C6; (b), (c):its derivatives in the $X$ and $Y$ directions.. ..	60

---

Figure 4.5 Design domain of the Mitchell-type structure .....	75
Figure 4.6 The evolution process of Mitchell-type structure .....	77
Figure 4.7 The evolution process of material distribution for Mitchell-type structure .....	78
Figure 4.8 The convergent histories of objective and volume constraint .....	79
Figure 4.9 Design domain of the cantilever beam .....	80
Figure 4.10 The evolution process of cantilever beam .....	82
Figure 4.11 The evolution process of material distribution for cantilever beam .....	83
Figure 4.12 The convergent histories of objective and volume constraint .....	84
Figure 4.13 (a) Optimal configuration and (b) level set surface with mesh 80×48 .....	85
Figure 4.14 The convergent histories with mesh 80×48 .....	85
Figure 4.15 (a) Optimal configuration and (b) level set surface with mesh 140×84 .....	86
Figure 4.16 The convergent histories with mesh 140×84 .....	86
Figure 4.17 Design domain of cantilever beam .....	87
Figure 4.18 The evolution process of cantilever beam .....	89
Figure 4.19 The evolution process of material distribution for cantilever beam .....	90
Figure 4.20 The convergent histories of objective and volume constraint .....	91
Figure 4.21 Optimized topologies comparison with different optimization techniques .....	92
Figure 5.1 Distribution of multi-phase material in the design domain .....	97
Figure 5.2 Schematic of multi-phase periodic structures with microstructures .....	99
Figure 5.3 (a) Orthotropy with two symmetry axes; (b) Orthotropy with four symmetry axes (square symmetry) .....	103
Figure 5.4 Flowchart of the numerical implementation with MPLSM .....	103
Figure 5.5 Plots of design variables and their level set surfaces ( $\Phi^1$ and $\Phi^2$ ) .....	114

---

Figure 5.6 Contour plots (first row) and level set surfaces (second row) for solid material phases .....	115
Figure 5.7 Convergence of the objective function .....	115
Figure 5.8 Convergence of the volume constraints .....	116
Figure 5.9 Optimal microstructures with extreme effective thermal properties .....	117
Figure 5.10 Optimal microstructures for zero effective thermal expansion .....	119
Figure 5.11 Optimal microstructures for negative effective thermal expansion .....	121
Figure 5.12 Convergent histories of the objective function .....	128
Figure 5.13 (a) Contour of solid 1; (b) Contour of solid 2; (c) Contours of solids .....	128
Figure 5.14 (a) LS surface of solid 1; (b) LS surface of solid 2; (c) Material distribution of two solids .....	129
Figure 5.15 Convergent histories of the objective function .....	131
Figure 5.16 (a) LS contour of solid 1; (b) LS contour of solid 2; .....	132
Figure 5.17 (a) LS surface of solid 1; (b) LS surface of solid 2; .....	132
Figure 5.18 Convergent histories of the objective function .....	134
Figure 5.19 (a) LS contour of solid 1; (b) LS contour of solid 2; (c) LS contours of two solids .....	135
Figure 5.20 (a) LS surface of solid 1; (b) LS surface of solid 2; (c) Material distribution of two solids .....	135
Figure 6.1 Optimization results for porosity 50% under different mesh level .....	146
Figure 6.2 The optimization process of microstructured metamaterial .....	149
Figure 6.3 Repetitive unit cell of the optimal configuration .....	150
Figure 6.4 Convergent histories of the objective function .....	150

Figure 6.5 Compare the achieved properties of optimal design with the upper Hashin-Shtrikman bound ..... 159

Figure 6.6 Compare the achieved properties of optimal design with the computational results from Challis (2012) ..... 159

# Nomenclature

## Global abbreviations used in this thesis

CAMD	=	Continuous approximation of material distribution
CFL	=	Courant–Friedrichs–Lewy
CS-RBF	=	Compactly supported radial basis function
EFG	=	Element-free Galerkin
ESO	=	Evolutionary structural optimization
FEM	=	Finite element method
GCMMA	=	globally convergent method of moving asymptotes
H-J PDE	=	Hamilton–Jacobi partial differential equation
KKT	=	Karush-Kuhn-Tucker
LSFs	=	Level set functions
LSM	=	Level set-based method
MLPG	=	Meshless local Petrov-Galerkin
MLS	=	Moving least squares
MMA	=	Method of moving asymptotes
MPLSM	=	Multi-phase level set method
NPR	=	Negative Poisson’s ratios
NTE	=	Negative thermal expansion

OC	=	Optimality criteria
PDI	=	Pointwise density interpolation
PLSM	=	Parametric level set method
PIM	=	Point interpolation method
PUM	=	Partition of unity method
PDE	=	Partial differential equation
RBFs	=	Radius basis functions
RPIM	=	Radial point interpolation method
RKPM	=	Reproducing kernel particle method
SIMP	=	Solid isotropic material with penalization
SPH	=	Smooth particle hydrodynamic method
ZTE	=	Zero thermal expansion
2D	=	Two dimensional
3D	=	Three dimensional

# 1 Introduction

## 1.1 Background

It is known that the natural resources available to human beings are very limited, which means we should use these resources more efficiently. In the field of engineering computations, design optimization plays a very important role in finding the best possible solution to an engineering problem. How to achieve an optimum for an engineering problem has been under investigation for decades. The process of engineering design is divided into four main stages, including 1) recognizing the need of engineering problem, 2) formulating functional specifications and requirements, 3) establishing mathematical formulation, and 4) optimizing the conceptual design to satisfy the design and manufacturability requirements. Among the four stages of the design process, the conceptual design is critical for exploring the overall connectivity and layout of a structure. The earlier conceptual design is traditionally conceived as a kind of structural art that demands the designer with great ingenuity and experience. Nowadays, intense technological competition requires reduction of design costs and time of the products while maintaining high quality and functionality. In recent decades, the development of computer technology has provided the opportunity to develop methods of rational design and optimization. This has already occurred to structural optimization.

The structural optimization is actually a research field dealing with structural elements or structural systems and is employed in several engineering fields. Its main task is to find the best possible geometry and topology of structural layout that meets all requirements to be

---

imposed by functionality and manufacturing conditions. In the past two decades, there has been a number of works in the area of structural optimization. Structural optimization has become a multidisciplinary field with applications in diversified fields, such as automotive, aeronautical, mechanical, civil, nuclear, naval and off-shore engineering. As a result of rapidly growing applications of structural optimization for achieving lightweight but high performance structural designs, the importance of the research in structural optimization methods is realized by more and more scientists and engineers, and methods are allowed for a wide range of applications. The structural optimization can be classified into two scales: macroscopic and micro designs (Bendsøe and Sigmund 2003). The structural optimization at the level of macroscopic focuses on macroscopic geometry such as thicknesses or boundaries, while the microscopic is to study the relationship between the microstructures and their macroscopic behavior of a composite material/structure.

## **1.2 Literature Review**

Structural optimization can often be classified into size, shape and topology optimization. Among these different optimizations, topology optimization has been recognized as the most promising but the most challenging approach in the conceptual stage of design, which has experienced considerable development over the past two decades with a wide range of engineering applications (Bendsøe and Sigmund 2003). It is essentially a numerical process to iteratively re-distribute a given amount of material inside the design domain subject to loads and boundary conditions, until a prescribed objective function is optimized under specified design constraints. By now, several different topology optimization methods have been developed, including the homogenization method (Bendsøe and Kikuchi 1988; Guedes

---

and Kikuchi 1990), the Solid Isotropic Material with Penalization (SIMP) method (Zhou and Rozvany 1991; Mlejnek 1992; Bendsøe and Sigmund 1999), the evolutionary structural optimization (ESO) method (Xie and Steven 1993; Huang et al. 2006), and the level set-based method (LSM) (Sethian and Wiegmann 2000; Wang et al. 2003; Allaire et al. 2004; Luo et al. 2013), as well as some alternative methods for topology optimization, e.g. the nodal-density interpolation based methods (Guest et al. 2004; Matsui and Terada 2004; Kang and Wang 2011; Luo et al. 2013).

### **1.2.1 Topology Optimization Methods**

Topology optimization of continuum structures essentially belongs to a set of integer programming problems with a large number of discrete design variables (0, 1). More efficient gradient-based optimization algorithms cannot be directly applied to solve such optimization problems in large scale due to the discrete nature of the problem. To this end, the homogenization and SIMP methods have been widely employed to relax the original discrete topology optimization problem, to allow the design variables taking intermediate densities from 0 and 1. In doing so, the original optimization problem is changed to a relaxed optimization problem with range-bounded continuous design variables.

Homogenization method was proposed by Bendsøe and Kikuchi (1988). Prior to this, Cheng and Olhoff (1981) reported important characteristics about the optimal design of solid elastic plates. They pointed out that a global optimal solution generally does not exist within the class of smooth functions, or within the class of smooth functions with a finite number of discontinuities. This result led to a series of works on optimal design problems using a microstructure. Kohn and Strang (1986) introduced a ‘relaxation’ concept to deal with an

ill-posed variational problem that can be formulated for optimal design. The ‘relaxation’ concept implies that the introduction of microstructure and use of the homogenization method allow an optimal solution. Rozvany et al. (1987) investigated the implication of this relaxation concept with the design of perforated elastic plates. Bendsøe and Kikuchi (1988) developed a methodology for topology optimization using the homogenization method. This new optimization approach created a paradigm shift in the structural optimization field. Suzuki and Kikuchi (1991) established an optimization problem, in which the objective is to minimize the mean compliance. This approach was also extended to dynamic problems. Díaz and Kikuchi (1992) proposed an eigenvalue optimization method in which the objective function is to maximize a single eigenvalue. Ma et al. (1995) constructed a multi-eigenvalue optimization method with the convex approach in the optimization process. They also extended this approach to a frequency response optimization problem. Frecker et al. (1997) applied this approach to the design of compliant mechanisms.

The SIMP, as an extension of the homogenization method, has experienced great popularity in topology optimization of solid mechanics problem, owing to its conceptual simplicity and implementation easiness. In SIMP-based topology optimization methods, a ‘power-law’ criterion Bendsøe and Sigmund (1999) is usually applied to penalize the intermediate densities of elements, to ensure the solution of the relaxed 0-1 design close to the original binary (0,1) design as much as possible. In addition, numerical schemes such as filtering schemes (Bourdin 2001; Sigmund 2001; Luo et al. 2005) may be required to eliminate numerical instabilities, e.g. the checkerboards and mesh-dependence (Díaz and Sigmund 1995), in order to make a physically meaningful solution. It can be found that most of the

---

current SIMP approaches are based on element-wise design variables (Bendsøe and Sigmund 2003). By this way, both the topological geometry of material distribution and the physical fields would be evaluated via elemental density variables that are piecewise constant. In topology optimization of continuum structures, the element-wise variables may be one of the reasons for the occurrence of numerical instabilities, including checkerboards, local minima, and mesh-dependency (Diaz and Sigmund 1995; Sigmund 2001). To avoid these issues, the perimeter control and mesh-independent filtering methods should be included in the topology optimization (Sigmund and Petersson 1998).

Later, there have been several alternative approaches based on point-wise design variables have been proposed, such as (Guest et al. 2004; Matsui and Terada 2004; Rahmatalla and Swan 2004; Paulino and Le 2009; Kang and Wang 2011). According to these approaches, the density variables at the nodes of the finite elements can be considered as the design variables, and element material properties are then obtained in terms of nodal densities via interpolation schemes. For instance, Rahmatalla and Swan (2004) proposed several options to implement the point-wise interpolation for material density fields, although “layering” or “islanding” type numerical instabilities occurred in the design. Matsui and Terada (2004) studied a so-called CAMD (continuous approximation of material distribution) method based on the homogenization method, in which element material densities were interpolated via the nodal density values (design variables). Guest et al.(2004) introduced nodal design variables and projection schemes into topology optimization to achieve minimum length-scale control and checkerboard-free characteristics. Nodal material densities are regarded as the design variables to calculate the element material densities and element stiffness

---

matrices. Paulino and Le (2009) proposed a kind of hybrid low-order finite elements, in which the nodes for design variable vector are inconsistent with the nodes for displacement vector. Kang and Wang (2011) proposed a nodal-density topology optimization method using the Shepard interpolation and higher-order finite elements to eliminate the numerical instabilities, e.g. the checkerboards.

Meanwhile, many researchers are concentrating on searching alternative numerical methods for topology optimization, without having to keep the connectivity of structured elements, which develop the concepts of meshless methods only in terms of a set of arbitrarily scattered field nodes. As an alternative method to topology optimization of structures, the meshless method is relatively simple, but able to provide sufficient numerical accuracy and stability for certain classes of problems. There are at least 10 different meshless methods with a number of publications in a broad range of areas (Belytschko et al. 1994; Belytschko et al. 1995; Atluri and Zhu 1998; Atluri et al. 2004; Liu and Gu 2005). The typical methods include the smooth particle hydrodynamic method (SPH) (Gingold and Monaghan 1977), the reproducing kernel particle method (RKPM) (Liu et al. 1995), the hp-clouds (HP) method (Duarte and Oden 1996), and the partition of unity method (PUM) (Babuska and Melenk 1995), the element-free Galerkin (EFG) method (Belytschko et al. 1995), the meshless local Petrov-Galerkin (MLPG) method (Zhu and Atluri 1998), the point interpolation method (PIM) (Liu and Gu 2001). Each meshless method has its particular characteristics to suit a specific class of problems. One of the common techniques is the Galerkin method with global/local weak-forms, which has received much popularity in the area of mechanics problems including topology optimization of structures. However, one of

the major shortcomings of the meshless Galerkin methods is the lack of Kronecker delta function property. The radial point interpolation method (RPIM) (Liu and Gu 2001) is a meshless method developed using Galerkin weak-forms, with Radial Basis Function (RBF)-based shape functions constructed by a set of nodes arbitrarily distributed in the supported domain. This method is meshless in terms of the interpolation rather than fitting of design variables. In the numerical process, the background cells are required only for the integration of the weak form over the design domain. The major advantage of RPIM is that the shape functions possess the Kronecker delta property, which allows direct enforcement of the essential boundary conditions. In RPIM, the RBF shape function with an augment of polynomials can not only overcome the singularity of the PIM polynomials but improve the accuracy of the results and the interpolation stability.

The level set method (LSM) (Osher and Sethian 1988; Sethian 1999) is originally developed for tracking, modelling, and simulating the evolution of moving fronts with shape and topology changes by merging and breaking boundaries. It essentially leads to an Eulerian system of partial differential equation, which is capable of performing topological changes and capturing geometric evolutions at the interface and the boundaries. Osher and Santosa (2001) studied the shape and topology optimization of an inhomogeneous drum by incorporating the shape derivative (Sokołowski and Zolesio 1992) into the level set method. The evolving interface is then tracked by solving a Hamilton–Jacobi equation and the descent of the objective is ensured by a steepest descent method. Wang et al. (2003) presented a way by implicitly embedding the structural boundary into a scalar function of higher dimension as zero level set, and a first-order Hamilton–Jacobi partial differential

---

equation (PDE) is then established to update the scalar level-set function until an optimal design is achieved. Wang and Wang (2004) extended the previous method by establishing a ‘color’ level set model to perform multi-phase design optimization. The level set method makes topological changes possible along with shape variations during the optimization process by tracking the motion of structural boundaries. The highlight of their works should be the connection of the shape derivative with the level set method. But several numerical requirements of solving the Hamilton–Jacobi PDE need to be carefully handled in order to make the initial value problem meaningful (Wang and Wang 2004). Allaire et al. (2004) studied the level set shape and topology optimizations by combining the shape sensitivity analysis with the front propagation technologies, including an extension to different designs.

It is well known that the conventional level-set shape and topology optimization is a family of methods by fully taking into account the advantages of free implicit representation (Wang et al. 2003; Wang and Wang 2004; van Dijk et al. 2012). But the time step constrained by the Courant–Friedrichs–Lewy (CFL) condition must be sufficiently small to ensure numerical stability when the finite difference scheme is used (Osher 2002). The free design boundary also cannot be uniquely determined during the optimization because it is very difficult to prevent the level set function deviating away from the signed distance function (Sethian 1999). Thus, inaccurate design boundaries with too flat or too steep surfaces might be developed. It is suggested to periodically reinitialize the level set function as a signed distance function by solving another set of Hamilton–Jacobi (H–J) PDEs to maintain the numerical accuracy (Peng et al. 1999). The re-initialization in some cases may prevent nucleation of new holes in the 2D design domain, but it is only true for 2D

---

structures since new holes can be automatically nucleated for 3D cases (Allaire et al. 2004). Another important issue in LSM is the extension of the normal velocity field. The normal velocity field originally derived from shape sensitivity analysis is merely defined at the design boundary, but the velocities within a neighborhood of the design boundary should be provided for solving the H–J equation on a fixed Eulerian mesh. Therefore, the normal velocities must be extended to the neighborhood of the design boundary (Osher 2002) or to the whole domain (Allaire et al. 2004). The natural way is to preserve the normal velocity to be constant along the curve normal (Sethian 1999). Due to these reasons, it has been shown (Allaire et al. 2004; Wang and Wang 2004; Allaire and Jouve 2005) that the convergence of conventional level set methods to reach the optimal design is slow, and the design is easy to run into a local minimum (Haber 2004; Wang et al. 2007). To find a local optimal solution that is less sensitive to the initial guess, many methods have been used to modify the original H–J PDE, but it is reported that the modifications will lead to an inaccurate solution (Burger et al. 2004). A number of schemes have been attempted to automatically create holes (Sokołowski and Zolesio 1992; Burger et al. 2004; Wang and Wei ; Wang and Wang 2006). Hence, the numerical issues of conventional level set methods would limit their further application to structural optimization problems.

More recently, several alternative LSMs in parametric or equivalent forms, e.g. (Belytschko et al. 2003; Haber 2004; Luo and Tong 2008; Luo et al. 2009; Luo et al. 2012) have been developed for topological shape optimization, mainly with a view to avoiding the numerical issues in the standard LSMs mentioned above. In particular, Luo (2007) proposed a parametric level set method (PLSM) for topological shape optimization of continuum

---

---

structures, which has shown its ability as a powerful structural optimization method. It can remain the favourable features of the LSMs while avoid the unfavourable issues of their classic forms, to enable the direct application of many well-established gradient-based optimization algorithms (Belytschko et al. 2003; Haber 2004; Luo et al. 2007; Luo et al. 2012) to the level set methods.

### **1.2.2 Topological Design of Metamaterials**

In the pursuit of materials with superior performance, there has been an increased interest in designing new materials exhibiting exotic properties throughout the history of human beings (Lakes 1987; Lakes 1993; Lakes 1996; Evans and Alderson 2000). In particular, metamaterials, a magic world of man-made composites connected with unconventional properties and ubiquitous applications, have been experiencing great popularity in the field of structural optimization (Sigmund 1994; Sigmund and Torquato 1996; Sigmund 2000; Guest and Prévost 2006; Guest and Prévost 2007). Metamaterials gain their fascinating properties from specifically designed and periodically arranged micro- or nano-structures rather than from their composition. In other words, the geometry and layout of the internal structure plays an important role in determining the unusual properties of such artificial composites. A revolutionary start of metamaterials was made by Veselago (1968) who developed electromagnetic metamaterials exhibiting negative permittivity and negative permeability. Recently, the concept of electromagnetic metamaterials (Smith et al. 2004; Huang et al. 2012; Otomori et al. 2013) has been applied to develop mechanical or elastic metamaterials, with different parameters to denote unusual elastic properties of materials. So far, several different types of mechanical metamaterials have been developed for various

applications, such as acoustic or phononic metamaterials with negative bulk modulus and mass density (Lakes 1987; Milton 1992; Evans and Alderson 2000; Piat et al. 2011; Wang et al. 2014), metamaterials with negative Poisson's ratios (NPR, also named auxetics) (Chen and Chan 2007; Wang et al. 2014), metamaterials with negative compressibility (Nicolaou and Motter 2012) and pentamode metamaterials (Kadic et al. 2013).

In engineering, the expansion and contraction of materials and structures must be considered, when changes in dimension as a result of temperature. Since most materials in service will experience a range of operating temperatures, the thermal expansion caused by temperature changes is of interest from both a technological and fundamental standpoint (Sigmund and Torquato 1996). The thermal expansion is an important metric used to measure the degree of temperature in changing the dimension of materials. A negative thermal expansion (NTE) or zero thermal expansion (ZTE) material has the counterintuitive property that contracts when increasing temperature within a certain range of temperatures. It is proved that three-phase materials can gain extraordinary properties beyond those of the individual phase. The materials with extreme thermoelastic property are usually achieved by combining three material phases by using conventional materials, such as metals or plastics, into a new periodically structured composite.

Poisson's ratio (Evans and Alderson 2000) is usually defined as the ratio of transverse contraction strain to longitudinal extension strain under uniaxial tension, which is fundamental for measuring the performance of elastic materials (Lekhnitskii 1963). The classic theory of elasticity allows the Poisson's ratio to be negative, but the definition of Poisson's ratio contains a minus sign so that most conventional materials have positive

---

ratios. In contrast to conventional materials with positive Poisson's ratios, materials with negative Poisson's ratios exhibit counter-intuitive properties, namely expanding laterally when stretched and contracting laterally when compressed. Since the work of (Lakes 1987), the metamaterials with NPR (auxetics) have attracted much attention, due to the potential for a range of applications. So far several intuition and heuristic methods have been developed to design the elastic metamaterials (Yang et al. 2004). However, novel elastic metamaterials with multifunction, e.g. NPR and NTE, NPR and ZTE have been seldom studied.

### **1.2.3 Topological Design of Scaffold Architectures**

In the early 1990s, the tissue engineering was mainly developed to overcome the limitations of tissue graft and alloplastic repair (Lanza et al. 2011). The fundamental essence of tissue engineering is adapting a porous degradable material called scaffold to transplant bio-factors like stem-cell and gene-therapy approaches , which is used to stimulate tissue repair (Hollister 2005). The design of the porous biomaterial, such as scaffold architecture, plays an important role in the tissue regeneration. A fundamental tissue engineering design hypothesis is that the scaffold should provide a biomimetic mechanical environment for initial function and sufficient porosity for cell migration and cell/gene delivery (Hollister et al. 2002). To fulfill the multifunctional requirements, in the design of scaffold architecture, there are several functional characteristics to be considered, including porosity, mechanical modulus and permeability/diffusivity (Kang et al. 2010). For example, bone tissue engineering scaffolds should be designed to have high diffusivity, permeability or porosity for better cell migration and biologics transport, to meet the multi-criteria requirements.

---

Furthermore, the multifunctional characteristics would often vary with the specific tissue. For instance, to maintain the health of bone tissues, taking the trabecular bone as an example, the elastic modulus has a wide range from 10 to 1500 MPa (Goulet et al. 1994). While the aggregate modulus for the articular cartilage is relatively much smaller and also spans a smaller range from 0.5 to 3.0 MPa (Boschetti et al. 2004), compared to that of the trabecular bone. Thus, the design of scaffolds is actually to explore suitable internal architecture to satisfy their multiple properties.

The multifunctional tissue scaffolds are attracting increasingly attention in the field of bio engineering, and a number of different design methods (Hollister et al. 2002) have been developed to generate scaffolds over the past. More recently, with the rapid development of computational design engineering, topology optimization technique has shown its potential as a powerful design tool for micro-structured scaffolds. Topology optimization has been applied to design scaffolds to achieve the optimized topological layout of the microstructure. For instance, Lin et al. (2004) applied homogenization-based topology optimization method to design 3D internal scaffold architecture to simultaneously meet desired elastic properties and mass transport porosity. Guest and Prévost (2006) extended the projection method (Guest et al. 2004) to achieve topology optimization design of 3D scaffolds to maximize bulk modulus and isotropic permeability. de Kruijf et al.(2007) employed topology optimization to achieve the optimized scaffold structures with maximized bulk modulus and thermal conductivity in two-dimensional (2D) structures based on Pareto optimality. Challis et al. (2008) applied the level set method to design isotropic microstructures that have maximized bulk modulus and isotropic conductivity. de Kruijf et al.(2010) employed the

homogenization-based topology optimization method to generate 3D internal scaffold architecture, which can match desired elastic properties and porosity simultaneously.

### **1.3 Contribution and Organization of the Thesis**

The contributions of our research work are briefly summarized as follows:

Firstly, we incorporate the numerical homogenization method into a parameterized level set method (PLSM) to develop a topological shape optimization approach for the design of periodic composites of microstructures, which will be more efficient and effective. The numerical homogenization method is used to determine the effective properties, while the PLSM is applied to achieve the optimized shape and topology of the microstructure.

Secondly, we will develop a multi-material topological shape optimization method for designing mechanical metamaterials, based on a multi-phase level set method (MPLSM). In this approach, the homogenization method is used to calculate the effective material properties of the microstructure, while MPLSM is established to achieve topological shape evolutions of the microstructure in the multi-phase design domain. The proposed method is as a matter of fact a general computational design methodology, which is applicable to create any artificially structured composites under periodicity.

In the last part, we extend the PLSM to design the 3D microstructure of scaffold architecture to meet the multifunctional characteristics. The scaffold is treated as a periodic composite material, and thus the design domain is only a unit cell. The effective properties of scaffold will be computed by the numerical homogenization method by discretising the design domain into a finite number of elements. The optimization procedure is then conduct

by the PLSM to optimize the shape and topology of the unit cell to achieve the prescribed properties such as porosity, effective stiffness, and effective permeability.

## 2 Homogenization Method

Since the homogenization method will be employed to compute effective properties of composite with periodic microstructures, in Chapters 5 and 6, the basic theories of the homogenization method are introduced in this chapter. Meanwhile, two numerical examples will be presented to illustrate the performance of the homogenization method for evaluating effective constitutive parameters of micro-structured materials.

### 2.1 Homogenization Theory

Composite materials are kind of man-made material with different dissimilar constituents, and the properties of a composite are different from its individual constituents. A porous body can be considered as a simple case of a composite, comprising solids and voids, which is usually used in topology optimization. In this thesis, composites consisting of periodic microstructures (namely, micro-structured composites) are considered. It is assumed that in comparison with the dimensions of the macroscopic structure the size of the periodic microstructure should be very small. In this manner, the effective constitutive parameters of composites can be computed by using a numerical homogenization method (Sigmund 1994).

Since 1970s, the mathematical theory of the homogenization has been developed, which is used as an alternative approach to evaluate the effective properties of the homogenized material (Cioranescu and Paulin 1979). From a mathematical point of view, the theory of homogenization is a limit theory that uses the asymptotic expansion and the assumption of

---

periodicity to substitute the differential equations with rapidly oscillating coefficients into the differential equations, whose coefficients are constant or slowly varying, aiming to achieve the solutions close to the initial equations (Hassani and Hinton 1998). Hence, this method can be used to predict the overall properties of composites.

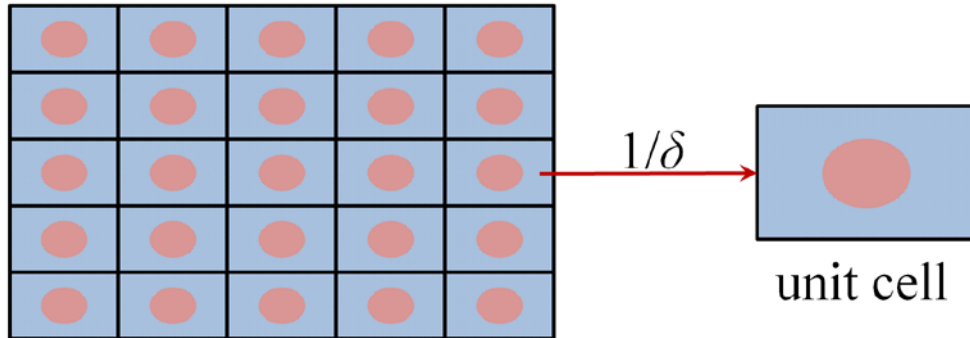
A heterogeneous medium can be considered having a regular periodicity when the functions denote some physical quantity of the medium, which have the following property:

$$F(\mathbf{x} + \mathbf{N}\mathbf{Y}) = F(\mathbf{x}) \quad (2.1)$$

where  $\mathbf{x} = (x_1, x_2, x_3)$  is the position vector of the point;  $\mathbf{N}$  is a  $3 \times 3$  diagonal matrix with 3 arbitrary integer numbers; and  $\mathbf{Y} = [Y_1, Y_2, Y_3]^T$  is a constant vector to determine the period of the structure;  $F$  is a scalar or vectorial or tensorial function of the position vector  $\mathbf{x}$ .

In the theory of homogenization, compared with the dimensions of the overall domain the period  $\mathbf{Y}$  is assumed to be very small. Thus, there are two different scales of dependencies for all quantities: one is the macroscopic or global level variable that denotes slow variations, and the other is the microscopic or local level variable that describes rapid oscillations. As shown by Figure 2.1, the ratio of the real length of a unit vector in the microscopic coordinate to the real length of a unit vector in the macroscopic coordinate is a small parameter  $\delta$ ,  $\mathbf{y}$  is a local (microscopic) coordinate system. So we have  $\delta\mathbf{y} = \mathbf{x}$  or  $\mathbf{y} = \mathbf{x}/\delta$ . If  $\Phi(\mathbf{x})$  is a physical quantity of a strongly heterogeneous medium, the small parameter  $\delta$  provides an indication of the proportion between the dimensions of the unit cells of a composite and the overall domain, regarded as the characteristic inhomogeneity dimension.

The quantity  $1/\delta$  can work as a magnification factor that enlarges the dimensions of a unit cell to be comparable with the dimensions of the material.



**Figure 2.1 Characteristic dimension of inhomogeneity and scale enlargement**

If we assign a macroscopic coordinate system  $\mathbf{x} = (x_1, x_2, x_3)$  in  $\mathbb{R}^3$  space to define the domain of the composite material problem  $\Omega$ , then assuming periodicity, the domain can be regarded as a collection of parallel piped cells of identical dimensions  $\delta Y_1, \delta Y_2, \delta Y_3$ , where  $Y_1, Y_2, Y_3$ , are the sides of the unit cell in a local (microscopic) coordinate system  $\mathbf{y} = (y_1, y_2, y_3) = \mathbf{x}/\delta$ . For a fixed  $\mathbf{x}$  in the macroscopic level, any dependency on  $\mathbf{y}$  can be considered  $Y$ -periodic. Moreover, it is assumed that the form and composition of the unit cell is unchanged, and the function  $\Phi(\mathbf{x})$  varies in a smooth way with the macroscopic variable  $\mathbf{x}$ . This means that for different points the structure of the composite may vary, but if one looks through a microscope at a point at  $\mathbf{x}$ , a periodic pattern can be found. In the double-scale technique, functions determining the behavior of the composite can be treated by asymptotically expanding the solution in powers of the small parameter  $\varepsilon$ , named as the double-scale asymptotic expansion (Hassani and Hinton 1998), which is expanded as:

$$\Phi^\delta(\mathbf{x}) = \Phi^0(\mathbf{x}, \mathbf{y}) + \delta\Phi^1(\mathbf{x}, \mathbf{y}) + \delta^2\Phi^2(\mathbf{x}, \mathbf{y}) + \dots \quad (2.2)$$

where  $\delta \rightarrow 0$  and functions  $\Phi^0(\mathbf{x}, \mathbf{y})$ ,  $\Phi^1(\mathbf{x}, \mathbf{y})$ , ... are smooth with respect to  $\mathbf{x}$  and  $Y$ -periodic in  $\mathbf{y}$ , which means that they will take equal values on the opposite sides of the unit cell. The case can refer to the following facts: (1) the derivative of a periodic function is also periodic with the same period; (2) the integral of the derivative for a function over the period is zero. (These facts can easily be verified by the definition of derivative and periodicity); (3) If  $\Phi = \Phi(\mathbf{x}, \mathbf{y})$  and  $\mathbf{y}$  depends on  $\mathbf{x}$ , then:

$$\frac{d\Phi}{d\mathbf{x}} = \frac{\partial\Phi}{\partial\mathbf{x}} + \frac{\partial\Phi}{\partial\mathbf{y}} \frac{\partial\mathbf{y}}{\partial\mathbf{x}} \quad (2.3)$$

Since  $\mathbf{y} = \mathbf{x}/\delta$ , it has

$$\frac{d\Phi}{d\mathbf{x}} = \frac{\partial\Phi}{\partial\mathbf{x}} + \frac{1}{\delta} \frac{\partial\Phi}{\partial\mathbf{y}} \quad (2.4)$$

## 2.2 Homogenization Method for Elasticity Problem

To illustrate the application of homogenization theory in general elasticity problem, here we will consider the elasticity problem for composite with periodic microstructures. Body forces  $\mathbf{f}$  and tractions  $\mathbf{t}$  are applied. As shown in Figure 2.2, problem domain  $\Omega$  is assumed to be an open subset of  $\mathbf{R}^3$  with a smooth boundary on  $\Gamma$  involving  $\Gamma_d$  (where displacements are prescribed) and  $\Gamma_t$  (the traction boundary). The unit cell of the cellular body  $Y$  is defined as  $Y = [0, Y_1] \times [0, Y_2] \times [0, Y_3]$ . Here, the coordinate system  $\mathbf{x} = (x_1, x_2, x_3)$  is used to define the global domain of the composite material and  $\mathbf{y} = (y_1, y_2, y_3)$  is the local (microscopic) coordinate system, with the relationship  $\mathbf{y} = \mathbf{x}/\delta$ .

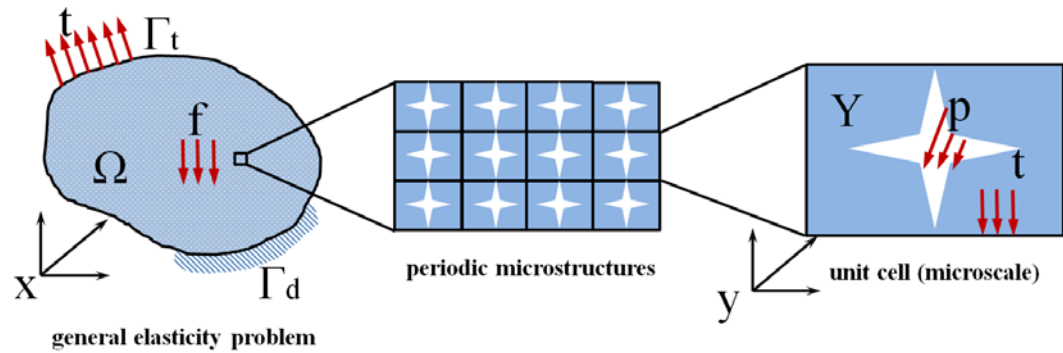


Figure 2.2 Elasticity problem for composite with periodic microstructures

The stress-strain and strain-displacement relations are expressed as:

$$\sigma_{ij}^\delta = C_{ijkl}^\delta \epsilon_{kl}^\delta \quad (2.5)$$

$$\epsilon_{kl}^\delta = \frac{1}{2} \left( \frac{\partial u_k^\delta}{\partial x_l} + \frac{\partial u_l^\delta}{\partial x_k} \right) \quad (2.6)$$

The equilibrium equation can be stated as: find  $\mathbf{u}^\delta \in \mathbf{V}^\delta$ , such that

$$\int_{\Omega_\delta} C_{ijkl} \frac{\partial u_k^\delta}{\partial x_l} \frac{\partial v_i}{\partial x_j} d\Omega = \int_{\Omega_\delta} f_i^\delta v_i d\Omega + \int_{\Gamma_t} t_i v_i d\Gamma + \int_{S^\delta} p_i^\delta v_i dS \quad \forall \mathbf{v} \in \mathbf{V}^\delta \quad (2.7)$$

where  $\mathbf{v}$  is the virtual displacement field, and  $\mathbf{V}^\delta$  is the kinematically admissible displacement space.

Assuming that the elastic constants of the solid satisfy the symmetry relations as

$$C_{ijkl} = C_{jikl} = C_{ijlk} = C_{klji}, \quad \exists \alpha > 0: C_{ijkl}^\delta \epsilon_{kl}^\delta = \alpha \epsilon_{ij}^\delta \epsilon_{ij}^\delta, \quad \forall \epsilon_{ij}^\delta = \epsilon_{ij}. \quad (2.8)$$

Using the double-scale asymptotic expansion, the displacement field  $u$  and stress field  $\sigma$  can be expanded as

$$u^\delta(x) = u^0(x, y) + \delta u^1(x, y) + \delta^2 u^2(x, y) + \dots \quad (2.9)$$

$$\mathbf{\sigma}^\delta(x) = \sigma^0(x, y) + \delta \sigma^1(x, y) + \delta^2 \sigma^2(x, y) + \dots \quad (2.10)$$

Then, Eq. (2.7) can be expressed as

$$\begin{aligned} & \int_{\Omega_\delta} C_{ijkl} \left\{ \frac{1}{\delta^2} \frac{\partial u_k^0}{\partial y_l} \frac{\partial \nu_i}{\partial y_j} + \frac{1}{\delta} \left[ \left( \frac{\partial u_k^0}{\partial x_l} + \frac{\partial u_k^1}{\partial y_l} \right) \frac{\partial \nu_i}{\partial y_j} + \frac{\partial u_k^0}{\partial y_l} \frac{\partial \nu_i}{\partial x_j} \right] + \right. \\ & \left. \left[ \left( \frac{\partial u_k^0}{\partial x_l} + \frac{\partial u_k^1}{\partial y_l} \right) \frac{\partial \nu_i}{\partial x_j} + \left( \frac{\partial u_k^1}{\partial x_l} + \frac{\partial u_k^2}{\partial y_l} \right) \frac{\partial \nu_i}{\partial y_j} \right] + \delta(\dots) \right\} d\Omega \\ & = \int_{\Omega_\delta} f_i^\delta \nu_i d\Omega + \int_{\Gamma_t} t_i \nu_i d\Gamma + \int_{S^\delta} p_i^\delta \nu_i dS \quad \forall \mathbf{v} \in \mathbf{V}_{\Omega \times Y} \end{aligned} \quad (2.11)$$

$\mathbf{V}_\Omega = \mathbf{v}(x)$  is defined in  $\Omega|_{\mathbf{v}}$  and  $\mathbf{v}|_{\Gamma_d} = 0$ ;  $\mathbf{V}_Y = \mathbf{v}(y)$  is defined in  $Y|_{\mathbf{v}(y)}$ , which are smooth enough and  $\mathbf{Y}$ -periodic.

There is a fact that with  $\delta \rightarrow 0$  a  $Y$ -periodic function  $\Psi(y)$  has

$$\int_{\Omega_\delta} \Psi\left(\frac{\mathbf{x}}{\delta}\right) d\Omega = \frac{1}{|Y|} \int_{\Omega} \int_Y \Psi(\mathbf{y}) dY d\Omega \quad (2.12)$$

For the macroscopic mechanical behavior, following the fact above and equating the terms with the same power of  $\delta = 0$  and  $\delta = 1$ , in Eq. (2.12), it can obtain

$$\begin{aligned} & \int_{\Omega} \left[ \frac{1}{|Y|} \int_Y \left( C_{ijkl} - C_{ijpq} \frac{\partial \chi_p^{kl}}{\partial y_q} \right) dY \right] \frac{\partial u_k^0}{\partial x_l} \frac{\partial \nu_i}{\partial x_j} d\Omega \\ & = \int_{\Omega} \left[ \frac{1}{|Y|} \int_Y \left( C_{ijkl} \frac{\partial \psi_k}{\partial y_l} \right) dY \right] \frac{\partial \nu_i}{\partial x_j} d\Omega + \int_{\Omega} \left[ \frac{1}{|Y|} \int_Y f_i dY \right] \frac{\partial \nu_i}{\partial x_j} d\Omega + \int_{\Gamma_t} t_i \nu_i d\Gamma \quad \forall \mathbf{v} \in \mathbf{V}_\Omega \end{aligned} \quad (2.13)$$

By denoting,

$$\begin{aligned}
 C_{ijkl}^H(\mathbf{x}) &= \frac{1}{|Y|} \int_Y \left( C_{ijkl} - C_{ijpq} \frac{\partial \chi_p^{kl}}{\partial y_q} \right) dY, \\
 \tau_{ij}(\mathbf{x}) &= \int_Y C_{ijkl} \frac{\partial \psi_k}{\partial y_l} dY, \\
 b_i(\mathbf{x}) &= \frac{1}{|Y|} \int_Y f_i dY
 \end{aligned} \tag{2.14}$$

Eq. (2.13) can be written as

$$\int_{\Omega} C_{ijkl}^H \frac{\partial u_k^0(\mathbf{x})}{\partial x_l} \frac{\partial \nu_i(\mathbf{x})}{\partial x_j} d\Omega = \int_{\Omega} \tau_{ij}(\mathbf{x}) \frac{\partial \nu_i(\mathbf{x})}{\partial x_j} d\Omega + \int_{\Omega} b_i(\mathbf{x}) \nu_i(\mathbf{x}) d\Omega + \int_{\Gamma_t} t_i(\mathbf{x}) d\Gamma \quad \forall \mathbf{v} \in \mathbf{V}_{\Omega} \tag{2.15}$$

This equation is similar to the equation of virtual displacement, Eq. (2.7) and represents the macroscopic equilibrium.  $C_{ijkl}^H$  represents the homogenized elastic constants and can also be written in a symmetrical form as:

$$C_{ijkl}^H(\mathbf{x}) = \frac{1}{|Y|} \int_Y \left( \varepsilon_{pq}^{0(ij)} - \varepsilon_{pq}^{*(ij)} \right) C_{pqrs} \left( \varepsilon_{rs}^{0(kl)} - \varepsilon_{rs}^{*(kl)} \right) dY \tag{2.16}$$

$\varepsilon^0$  is the prescribed macroscopic strain field (unit strain in the horizontal direction; unit strain in the vertical direction; unit shear strain);  $\varepsilon_{rs}^{*(kl)}$  is the locally varying strain fields which can be defined by

$$\varepsilon_{rs}^{*(kl)} = \varepsilon_{rs}^* \left( \chi^{kl} \right) = \frac{1}{2} \left( \frac{\partial \chi_r^{kl}}{\partial y_s} + \frac{\partial \chi_s^{kl}}{\partial y_r} \right) \tag{2.17}$$

where  $\chi^{kl}$  is the solution of the following cell problem

$$\int_Y \left( \varepsilon_{pq}^0 - \varepsilon_{pq}^* (\chi^{ij}) \right) C_{pqrs} \varepsilon_{rs}^* (\nu^{kl}) dY = 0 \quad \forall \mathbf{v} \in \mathbf{V}_Y \tag{2.18}$$

Based on the homogenization method, if the whole domain of the material comprises by a periodic cell structure, as well as uniform applied tractions on the boundaries of the holes of the cells, the macroscopic performance of the composite is able to be predicted by only solving the elasticity behavior in microscopic level.

## 2.3 Numerical Homogenization Method and Examples

In this section, the calculation of the effective homogenized elastic material properties is introduced to illustrate how to evaluate the homogenized material properties via numerical homogenization method. On the element level, the effective homogenized elastic material properties can be written as the sums of the followings:

$$C_{ijkl}^H(\mathbf{x}) = \frac{1}{|Y|} \sum_{e=1}^Y \int_{Y^e} (\varepsilon_{pq}^{0(ij)} - \varepsilon_{pq}^{*(ij)}) C_{pqrs}^e(\mathbf{x}) (\varepsilon_{rs}^{0(kl)} - \varepsilon_{rs}^{*(kl)}) dY^e \quad (2.15)$$

where  $C_{ijkl}^H$  is the effective elasticity tensor,  $\varepsilon^0$  is the unit test strain field,  $|Y|$  is the volume of the cell,  $Y^e$  is the area of element  $e$ ,  $\varepsilon^*$  are locally vary strain fields.

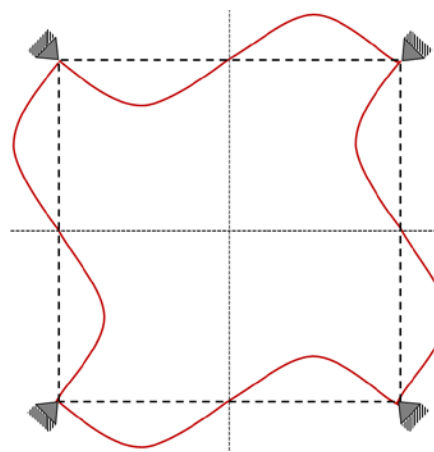


Figure 2.3 Periodicity conditions of the unit cell

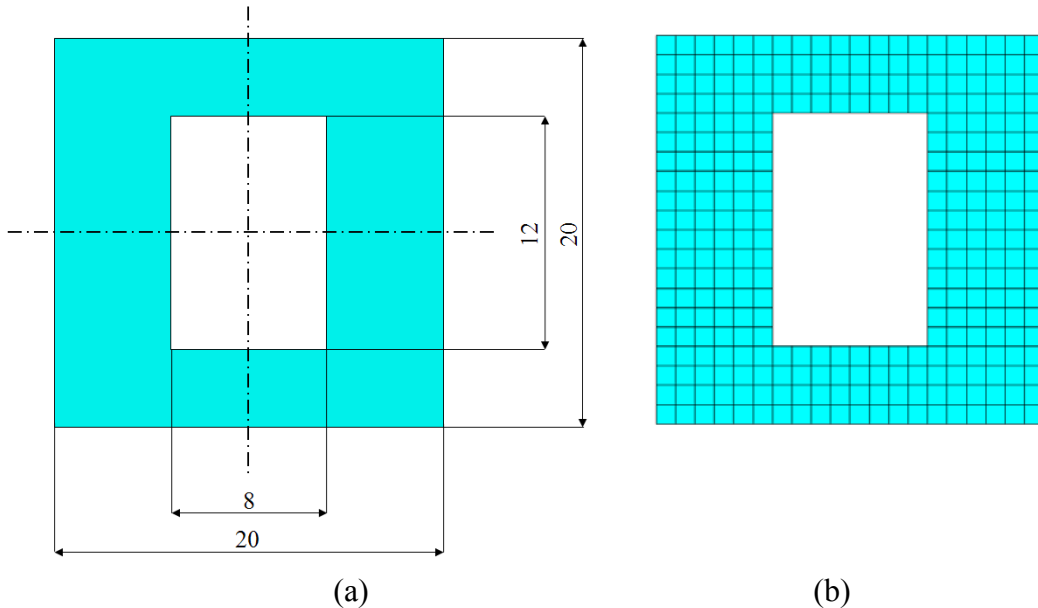
To calculate the effective properties of composites, the appropriate boundary conditions must be considered for the displacement characteristic function  $\chi$ . For a 2D plane-strain case, the boundary conditions must be specified, when only one fourth or half of the unit cell is considered. It is also important to consider symmetry of material elasticity to each unit cell (e.g. orthotropy or isotropy). In this case, to adopt the numerical approach in more general cases including materials with isotropic, orthotropic and anisotropic symmetry, the periodic boundary conditions of the design domain is specified. This can be achieved by using the elimination scheme (Andreassen and Andreasen 2014), which takes equal displacement values on opposite sides of the unit cell as shown in Figure 2.3.

### 2.3.1 Calculate Effective Elasticity Tensor for 2D Composite

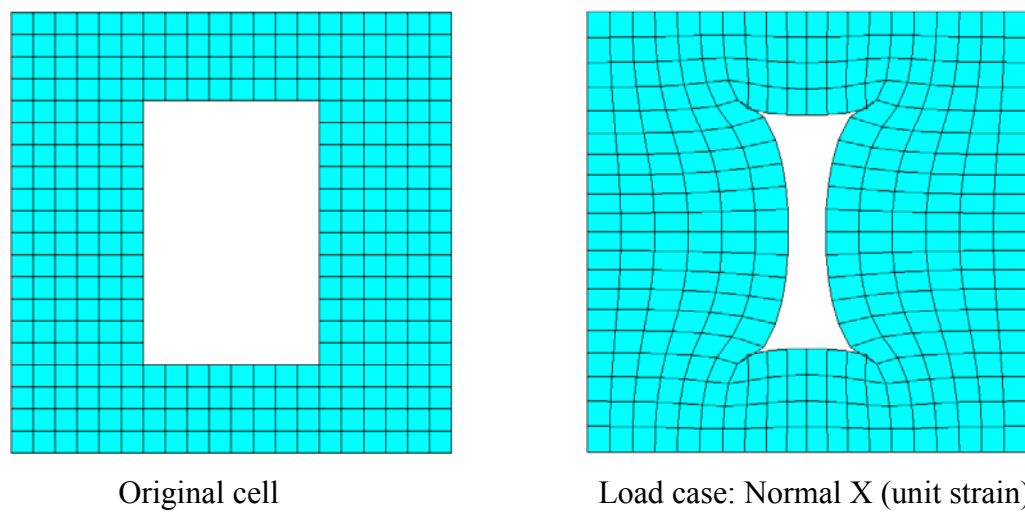
In this section, the calculation of the effective elasticity tensor via numerical homogenization method is presented by a two dimensional (2D) composite example. The composite is composed by two phases: solid and void. The unit cell is periodically arranged, and the geometry of the unit cell is shown in the Figure 2.4(a). It is assumed the solid phase with homogeneous material properties: Young's modulus  $E = 25$ , Poisson's Ratio  $\nu = 0.25$ , which means its elasticity tensor is

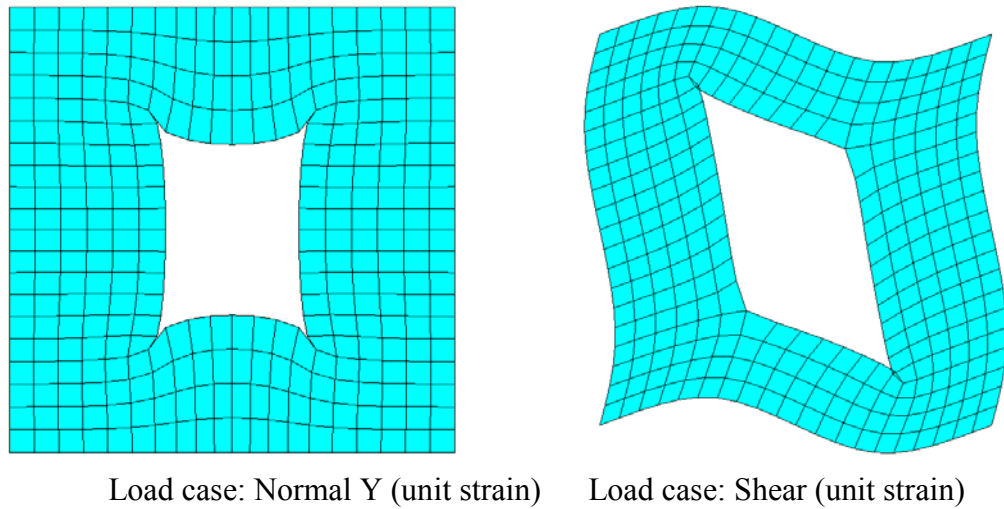
$$C_{base} = \begin{bmatrix} 30 & 10 & 0 \\ 10 & 30 & 0 \\ 0 & 0 & 10 \end{bmatrix}$$

The FEM is employed to discretize the unit cell and obtain the displacement field. In this work, the design domain is discretized by 304 eight-node linear displacement finite elements, as shown in Figure 2.4(b).



**Figure 2.4 (a) Geometry of the unit cell; (b) finite element mesh of the unit cell**





**Figure 2.5 The deformation of unit cell under different load cases**

For the 2D problem, there are three load cases to be solved by using the finite element method independently to get the displacement field, as illustrated in Figure 2.5. All load cases must be solved by enforcing periodic boundary conditions in the unit cell for the triggered initial strains. By calculating using the numerical homogenization method, the numerical results of the effective elasticity tensor  $C^H$  is

$$C^H = \begin{bmatrix} 12.8862 & 3.1770 & 0 \\ 3.1770 & 17.4581 & 0 \\ 0 & 0 & 2.6820 \end{bmatrix}$$

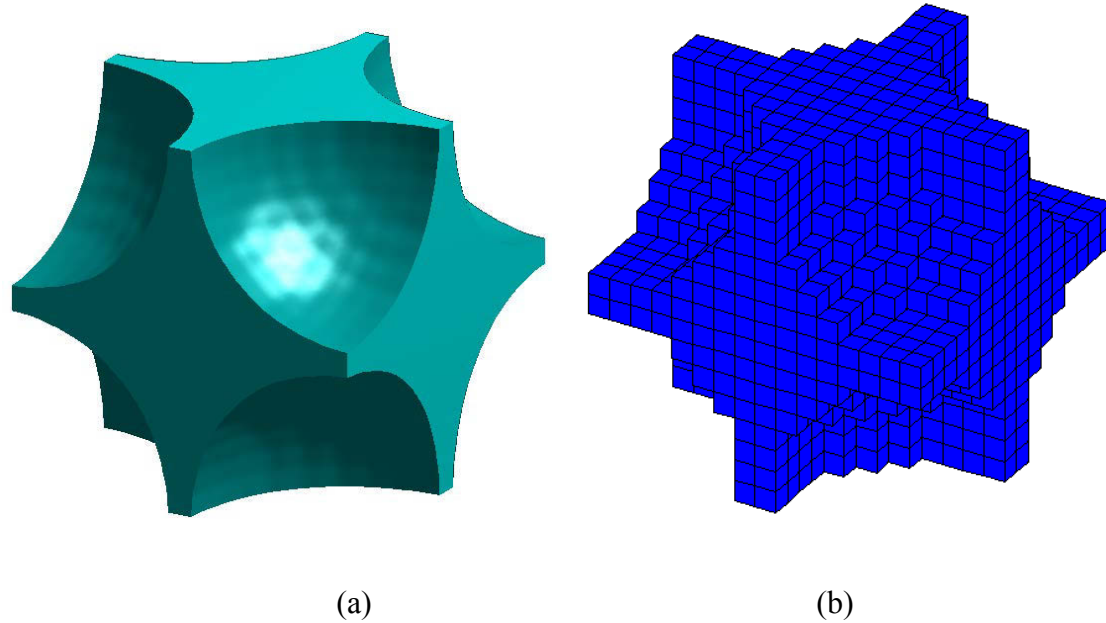
From the resulting value of the effective elasticity tensor, it can be noticed that the composite is elastic orthotropic material, which has symmetry relative to both axes.

### 2.3.2 Calculate Effective Elasticity Tensor for 3D Composite

In this numerical example, the effective elasticity tensor of a three dimensional (3D) composite will be calculated by numerical method. The composite is composed by two

phases: solid and void, and solid phase can be treated as a cube with the dimension  $15 \times 15 \times 15$ . There are 8 sphere holes located at the corners with the radius equal to 7. The geometry of the unit cell is shown in the Figure 2.6(a), which is an orthotropic unit cell periodically arranged within the composite. It is assumed the solid phase with homogeneous material properties: Young's modulus  $E = 1$ , Poisson's Ratio  $\nu = 0.33$ , which means its elasticity tensor is

$$C_{base} = \begin{bmatrix} 1.4816 & 0.7298 & 0.7298 & 0 & 0 & 0 \\ 0.7298 & 1.4816 & 0.7298 & 0 & 0 & 0 \\ 0.7298 & 0.7298 & 1.4816 & 0 & 0 & 0 \\ 0 & 0 & 0 & 0.3759 & 0 & 0 \\ 0 & 0 & 0 & 0 & 0.3759 & 0 \\ 0 & 0 & 0 & 0 & 0 & 0.3759 \end{bmatrix}$$



**Figure 2.6 (a) Geometry of the unit cell; (b) Finite element mesh of the unit cell**

The finite element method (FEM) is employed to discretize the unit cell and obtain the displacement field. In this work, the design domain is discretized by 3375 eight-node brick elements, as shown in Figure 2.6(b). The numerical results of the effective elasticity tensor  $C^H$  is

$$C^H = \begin{bmatrix} 0.5675 & 0.1942 & 0.1942 & 0 & 0 & 0 \\ 0.1942 & 0.5675 & 0.1942 & 0 & 0 & 0 \\ 0.1942 & 0.1942 & 0.5675 & 0 & 0 & 0 \\ 0 & 0 & 0 & 0.1361 & 0 & 0 \\ 0 & 0 & 0 & 0 & 0.1361 & 0 \\ 0 & 0 & 0 & 0 & 0 & 0.1361 \end{bmatrix}$$

From the resulting value of the effective elasticity tensor, it can be noticed that composite is material with orthotropic elasticity in 3D, which has symmetry relative to three axes.

# 3 Level Set Method for Topology Optimization

Level Set Method (LSM) is an efficient computational approach to track the propagation of dynamic interface, which represent the interfaces between material phases implicitly by zero level set of a Level Set Function (LSF) in a fixed Eulerian grid (Sethian and Wiegmann 2000; Wang et al. 2003; Allaire et al. 2004). The value of the LSF defines the geometry of the structure and allows a crisp description of the boundaries. Depending on the representation of the interfaces in the mechanical model numerically, it can improve the accuracy with which the mechanical response is captured in the vicinity of the boundaries. In contrast to explicit boundary descriptions of classic shape optimization, the level-set based topology optimization methods enable the topological changes of the structure during boundary shape variations.

## 3.1 Representation of the Boundary via LSM

In level-set based topology optimization methods, one of the key concepts is to implicitly represent the structural boundary as the zero level set of a higher-dimensional LSF. For example, if  $\Phi(\mathbf{x})$  is an LSF over a reference domain  $D$ , Figure 3.1 shows a 2D boundary of the structure that is represented by the 3D level set surface, where the level set function is used to uniformly denote the different material phases inside the reference domain as follows:

$$\begin{cases} \Phi(\mathbf{x}) > 0 & \forall \mathbf{x} \in \Omega \setminus \partial\Omega \\ \Phi(\mathbf{x}) = 0 & \forall \mathbf{x} \in \partial\Omega \\ \Phi(\mathbf{x}) < 0 & \forall \mathbf{x} \in D \setminus (\Omega \cup \partial\Omega) \end{cases} \begin{array}{l} \text{(Solid region)} \\ \text{(Boundary)} \\ \text{(Void)} \end{array} \quad (3.1)$$

where  $\Phi$  is the level-set function,  $D$  is the Eulerian reference domain (design domain in this work),  $\partial\Omega$  is the boundary of the solid domain and  $\Omega$  is the solid domain.

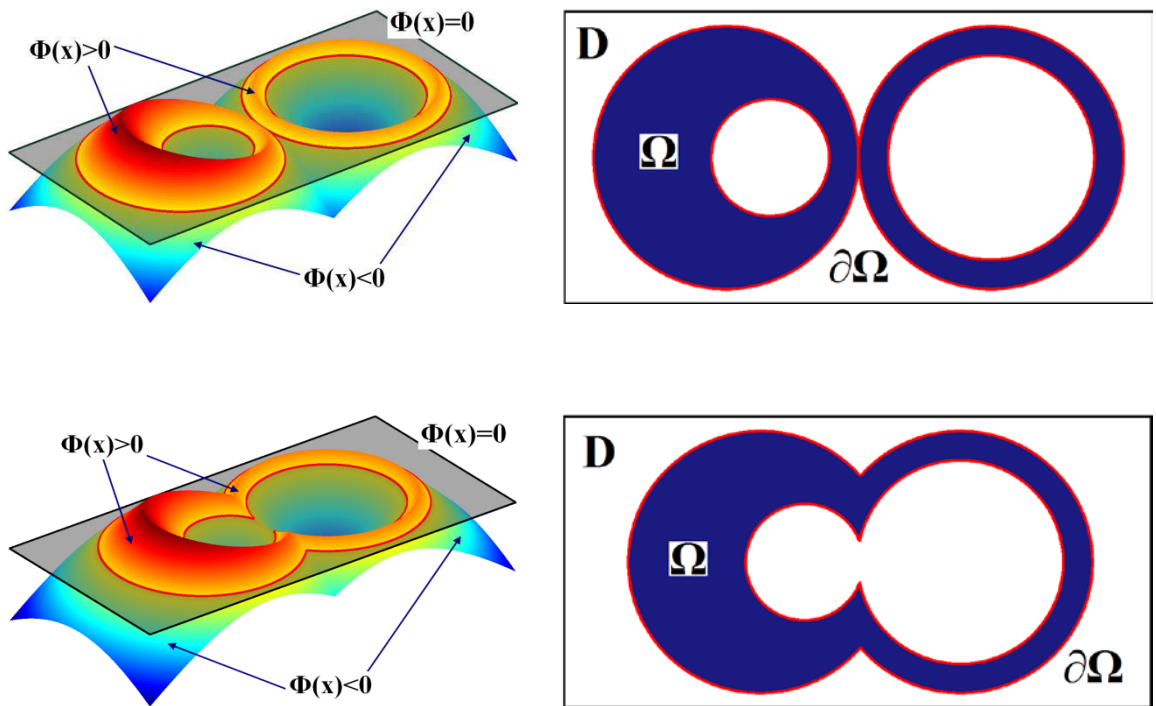


Figure 3.1 boundary representation using 3D level set surface

## 3.2 Hamilton-Jacobi Equations and Numerical Solution

### 3.2.1 Hamilton-Jacobi Equations

As presented in the section 3.1, the boundary is represented as the zero level set of a LSF. The level set surface would move up and down on a fixed Euler grid during the optimization

process, which lead to the changes in the shape or topology of the boundary. In the conventional LSM, the LSF is evolved by Hamilton-Jacobi equation which can be numerically solved by the finite difference method (Sethian 1999; Osher 2002). During the whole process, the level set where the design boundary located will constantly keep zero.

$$\Phi(\mathbf{x}) \equiv 0 \quad \forall \mathbf{x} \in \partial\Omega \quad (3.2)$$

To enable the dynamic motion, the pseudo-time  $t$  is introduced into the LSF  $\Phi(\mathbf{x})$ . Then the evolution of the LSF  $\Phi(\mathbf{x}, t)$  is linked to the propagation of the boundary located at  $\Phi(\mathbf{x}) = 0$ . The implicit dynamic function  $\Phi(\mathbf{x}, t)$  is used to both represent the boundary and evolve the boundary. The dynamic motion leads to the following first-order Hamilton-Jacobi partial differential equation (H-J PDE) by differentiating  $\Phi(\mathbf{x}, t)$  on both sides with respect to  $t$ . We can get the follow equation with the chain rule

$$\frac{\partial \Phi(\mathbf{x}, t)}{\partial t} + \mathbf{v} \cdot \nabla \Phi(\mathbf{x}, t) = 0 \quad (3.3)$$

where  $\mathbf{v}$  is the velocity vector field, stated as

$$\mathbf{v} = \frac{d\mathbf{x}}{dt} \quad (3.4)$$

The velocity field  $\mathbf{v}$  actually includes two components: normal velocity field and tangent velocity field. However, only the normal velocity component  $\mathbf{v}_n$  contributes to the shape evolution of the design boundary (Sethian 1999; Osher 2002).

$$\mathbf{n} = -\frac{\nabla \Phi}{|\nabla \Phi|} \quad (3.5)$$

$$\mathbf{v}_n = \mathbf{v} \cdot \mathbf{n} = \left( \frac{d\mathbf{x}}{dt} \right) \cdot \left( -\frac{\nabla \Phi}{|\nabla \Phi|} \right) \quad (3.6)$$

Hence, moving boundary along the normal direction  $\mathbf{n}$  is equivalent to transporting level set function  $\Phi(\mathbf{x}, t)$  by solving the H-J PDE with finite difference schemes (Wang et al. 2003; Allaire et al. 2004) on a fixed Euler rectilinear grid.

$$\frac{\partial \Phi(\mathbf{x}, t)}{\partial t} - \mathbf{v}_n |\nabla \Phi(\mathbf{x}, t)| = 0 \quad (3.7)$$

$\mathbf{v}_n$  known only on the interface is assumed to speed in the outward normal direction and is generally determined by the shape derivative analysis. However, in order to obtain approximate solutions of the H-J PDE,  $\mathbf{v}_n$  is naturally required to be extended at least to a narrow band of the boundary or the entire computational domain  $\Omega$ .

### 3.2.2 Discrete Solution to Hamilton-Jacobi Equations

To apply numerical methods to evolve  $\Phi$  in time,  $\Phi$  and  $\mathbf{v}$  are defined at every grid on a Cartesian grid.  $\Phi^{(n)} = \Phi$  (Kadic et al. 2013) indicates the values of  $\Phi$  at points in time  $t^{(n)}$ . Updating  $\Phi$  in time consisting of finding new values of  $\Phi$  after time increment  $\Delta t$ , The new value of  $\Phi$  is denoted by  $\Phi^{(n+1)} = \Phi(t^{(n+1)})$ , where  $t^{(n+1)} = t^{(n)} + \Delta t$ . Then, using a simple “forward Euler method”, it can obtain the time discretization of Eq. (3.3) as

$$\frac{\Phi^{(n+1)} - \Phi^{(n)}}{\Delta t} + \mathbf{v}^{(n)} \cdot \nabla \Phi^{(n)} = 0 \quad (3.8)$$

Here, we consider the nonlinear Hamilton-Jacobi equation in 2D space:

$$\frac{\Phi_{ij}^{(n+1)} - \Phi_{ij}^{(n)}}{\Delta t} + H(\Phi_x, \Phi_y) = 0 \quad (3.9)$$

where  $H(\Phi_x, \Phi_y)$  is Hamilton Function,  $\Phi_x, \Phi_y$  are the partial differential of  $\Phi$  with respect to  $x, y$ .

The discrete solution to the Hamilton-Jacobi equation is acquired by using a “upwind difference scheme” (Osher 2002). The upwind scheme adaptively calculates forward or backward difference at a point according to the direction of the velocity field at that point. Generally, the underlying idea of the upwind scheme is that information is always spreading from the known area to the unknown area, and what the upwind scheme does is to speculate about the information in the unknown area by using that in the known area.

On the Cartesian grid,  $\Delta x, \Delta y$  are grid spaces in horizontal and vertical directions  $x, y$ , then the coordinates of the any point in the grid can be denoted as  $(x_i, y_j)$ .  $D_{\pm}^x$  and  $D_{\pm}^y$  are forward (+) and backward (-) finite difference operators defined as follows

$$D_{\pm}^x \Phi_{ij}^{(n)} = \pm \frac{(\Phi_{i\pm 1,j}^{(n)} - \Phi_{ij}^{(n)})}{\Delta x}, \quad D_{\pm}^y \Phi_{ij}^{(n)} = \pm \frac{(\Phi_{i,j\pm 1}^{(n)} - \Phi_{ij}^{(n)})}{\Delta y} \quad (3.10)$$

The first-order upwind scheme for 2D cases is stated as

$$\Phi_{ij}^{(n+1)} = \Phi_{ij}^{(n)} - \Delta t (\max((\mathbf{v}_n)_{ij}, 0) \nabla^+ + \min((\mathbf{v}_n)_{ij}, 0) \nabla^-) \quad (3.11)$$

where

$$\nabla^+ = \left[ \max(D_{-}^x \Phi_{ij}^{(n)}, 0)^2 + \min(D_{+}^x \Phi_{ij}^{(n)}, 0)^2 + \max(D_{-}^y \Phi_{ij}^{(n)}, 0)^2 + \min(D_{+}^y \Phi_{ij}^{(n)}, 0)^2 \right]^{1/2} \quad (3.12)$$

$$\nabla^- = \left[ \max(D_+^x \Phi_{ij}^{(n)}, 0)^2 + \min(D_-^x \Phi_{ij}^{(n)}, 0)^2 + \max(D_+^y \Phi_{ij}^{(n)}, 0)^2 + \min(D_-^y \Phi_{ij}^{(n)}, 0)^2 \right]^{1/2} \quad (3.13)$$

It is noted that the above scheme can be extended to higher orders (Sethian 1999; Osher 2002). For the discrete level set methods, on the one hand, the mesh should be fine enough to remove the numerical truncation errors caused by the polynomial snaking phenomena (Wang and Wang 2006) once low-order shape functions are used. In practice, a finer mesh can enable the nodal values and the shape functions to illustrate structural topology with enough smoothness on a fixed Eulerian grid. A fine mesh is also favorable for ameliorating discontinuity of the partial derivatives of the level set function to avoid numerical denegation. On the other hand, the time step must be limited to ensure the stability of the above first-order upwind scheme. By the Courant-Friedrichs-Lowy (CFL) condition the smallest element size is restricted to satisfy (Sethian 1999; Osher 2002):

$$\Delta t \leq \frac{\min(\Delta x, \Delta y)}{\max |(v_n)_{ij}|} \quad (3.14)$$

### 3.3 Quantities Approximation in Level Set Function

#### 3.3.1 Quantities Approximation

In the optimization process, it is often necessary to approximate some quantities, such as: the normal vector, curvature, perimeter, and area. All these geometric quantities can be expressed as functions in terms of the implicit LSF  $\Phi(x)$  in the level set model. For example

(1) The area of the elastic material  $|\Omega|$  can be computed as

$$|\Omega| = \int_D H(\Phi) d\Omega \quad (3.15)$$

where  $H$  is the smoothed Heaviside function that is approximated as:

$$H(x) = \begin{cases} \theta & x < -\Delta \\ \frac{3(1-\theta)}{4} \left( \frac{x}{\Delta} - \frac{x^3}{3\Delta^3} \right) + \frac{1+\theta}{2} & -\Delta \leq x < \Delta \\ 1 & x \geq \Delta \end{cases} \quad (3.16)$$

where  $\theta$  is a small positive number to ensure nonsingular of the stiffness matrix, and  $\Delta$  is the width of numerical approximation for the Heaviside function as shown in the Figure 3.2.

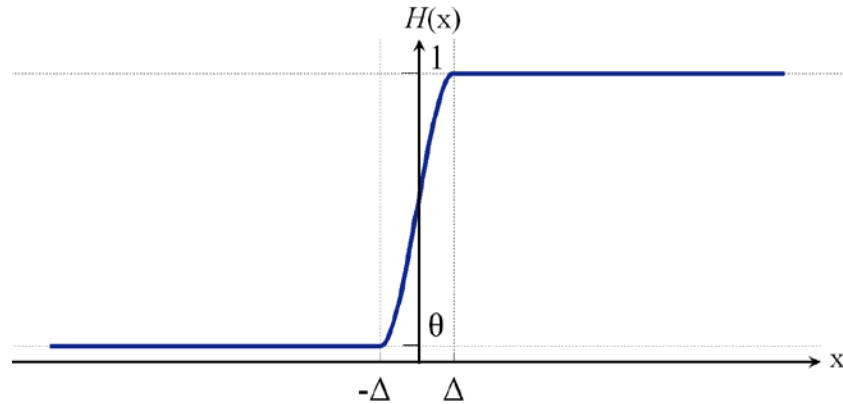


Figure 3.2 Numerically approximated Heaviside function

(2) The perimeter of the boundary  $|\partial\Omega|$  can be calculated as:

$$|\partial\Omega| = \int_D \delta(\Phi) |\nabla\Phi| d\Omega \quad (3.17)$$

where  $\delta$  is the Dirac function that is numerically approximated, as shown in the Figure 3.3.

$$\delta(x) = \begin{cases} \frac{3(1-\theta)}{4\Delta} \left( 1 - \frac{x^2}{\Delta^2} \right) & |x| \leq \Delta \\ 0 & |x| > \Delta \end{cases} \quad (3.18)$$

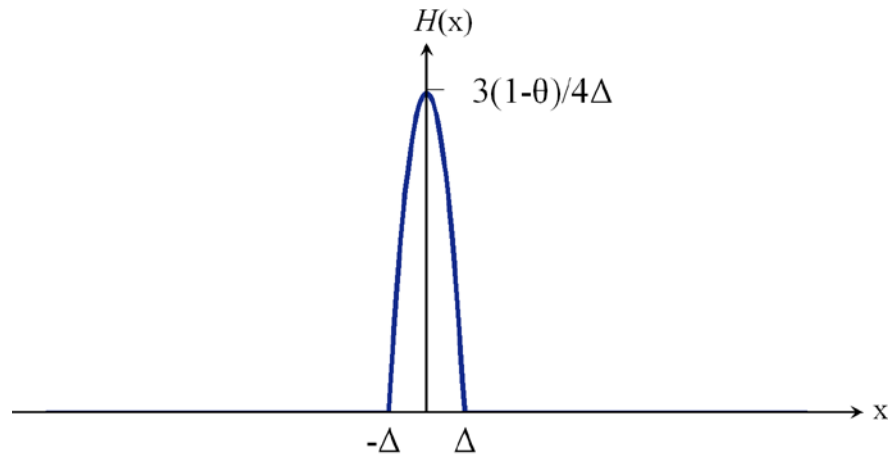


Figure 3.3 Numerically approximated Dirac function

(3) The normal vector  $\mathbf{n}$  to indicate the direction of increasing  $\Phi$ , is approximated as

$$\mathbf{n} = -\frac{\nabla \Phi}{|\nabla \Phi|} \quad (3.19)$$

(4) The mean curvature  $\kappa$  is defined as the divergence of the normal vector  $\mathbf{n}$ , expressed as:

$$\kappa = \nabla \frac{-\nabla \Phi}{|\nabla \Phi|} \quad (3.20)$$

When  $\Phi$  is a 2D function,  $\kappa$  is the mean curvature of the curve, stated as

$$\kappa = \frac{-\frac{\partial^2 \Phi}{\partial x^2} \left( \frac{\partial \Phi}{\partial y} \right)^2 + 2 \frac{\partial \Phi}{\partial x} \frac{\partial^2 \Phi}{\partial x \partial y} \frac{\partial \Phi}{\partial y} - \frac{\partial^2 \Phi}{\partial y^2} \left( \frac{\partial \Phi}{\partial x} \right)^2}{\left[ \left( \frac{\partial \Phi}{\partial x} \right)^2 + \left( \frac{\partial \Phi}{\partial y} \right)^2 \right]^{\frac{3}{2}}} \quad (3.21)$$

When  $\Phi$  is a 3D function,  $\kappa$  is the mean curvature of the surface, stated as:

$$\kappa = \frac{-B \frac{\partial^2 \Phi}{\partial x^2} - C \frac{\partial^2 \Phi}{\partial y^2} - A \frac{\partial^2 \Phi}{\partial z^2} + 2 \frac{\partial \Phi}{\partial x} \frac{\partial^2 \Phi}{\partial x \partial y} \frac{\partial \Phi}{\partial y} + 2 \frac{\partial \Phi}{\partial y} \frac{\partial^2 \Phi}{\partial y \partial z} \frac{\partial \Phi}{\partial z} + 2 \frac{\partial \Phi}{\partial z} \frac{\partial^2 \Phi}{\partial z \partial x} \frac{\partial \Phi}{\partial x}}{\left[ \frac{A + B + C}{2} \right]^{\frac{3}{2}}},$$

where

$$A = \left( \frac{\partial \Phi}{\partial y} \right)^2 + \left( \frac{\partial \Phi}{\partial z} \right)^2, B = \left( \frac{\partial \Phi}{\partial x} \right)^2 + \left( \frac{\partial \Phi}{\partial z} \right)^2, C = \left( \frac{\partial \Phi}{\partial x} \right)^2 + \left( \frac{\partial \Phi}{\partial y} \right)^2$$

(3.22)

Once the normal component of the velocity of which a point on the surface moves is given by the mean curvature of the surface, the surfaces evolves under mean curvature flow (Ecker 2004). Substituting the mean curvature  $\kappa$  into the Eq. (3.7), it will obtain the mean curvature flow function

$$\frac{\partial \Phi}{\partial t} = \kappa |\nabla \Phi| = \nabla \left( \frac{\nabla \Phi}{|\nabla \Phi|} \right) |\nabla \Phi|$$

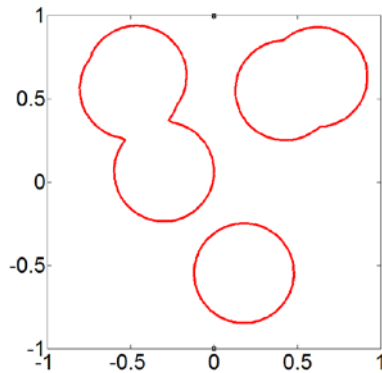
(3.23)

It is known that the surface moving in its normal direction with the mean curvature velocity is also interpreted in the literature as the anisotropic diffusing (Huisken 1990), which diffuses along tangent plane only, so that, it is able to eliminate the deviation of the surface. The character is beneficial to the topology optimization process to achieve a design boundary with enough smoothness. There are several numerical examples employed to demonstrate the performance of the mean curvature flow in section 3.3.3 and 3.3.4.

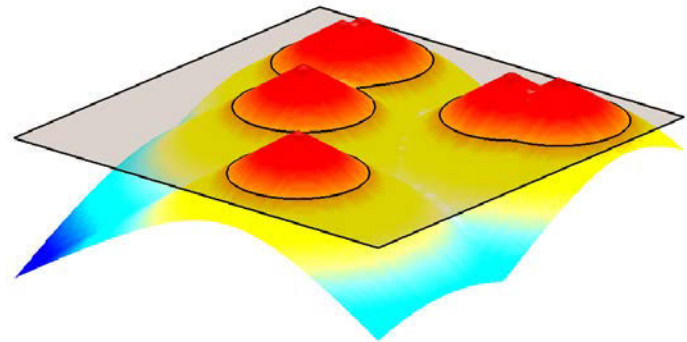
### 3.3.2 Numerical Example for Propagation of LSF

In this section, there is a numerical example to show the LSF propagating in the normal speed. In a 2D space  $D = \{(x, y) \in \mathbb{R}^2: -1 < x < 1, -1 < y < 1\}$ , the space is discretized by  $200 \times 200$

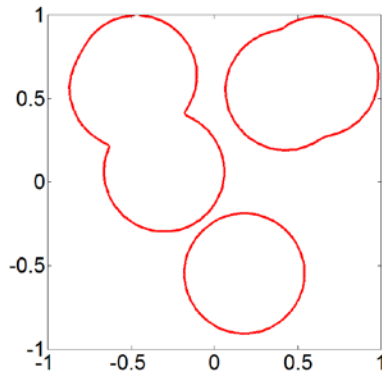
grid. Given the normal speed is  $v_n=1$ , and time step is set as  $\Delta t=0.2\Delta h$  ( $\Delta h$  is the grid spacing). The H-J PDE is discretized by the first-order Godunov's scheme (Godunov 1983). The zero level set of the initial LSFs are circles randomly located in the space as shown in the Figure 3.4. The propagation of 2D boundary (zero level set of LSFs) and corresponding level set surface at different iterations are shown in Figure 3.4.



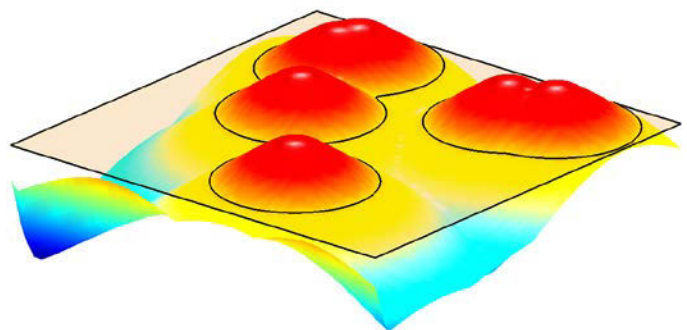
(a)



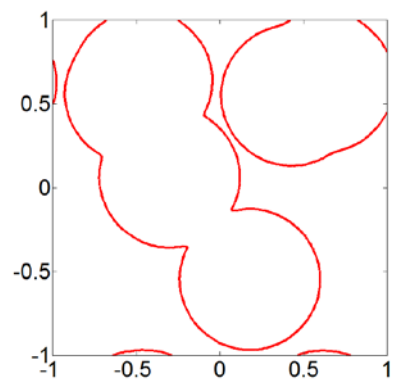
(b)

**Figure 3.4 Initial level set function**


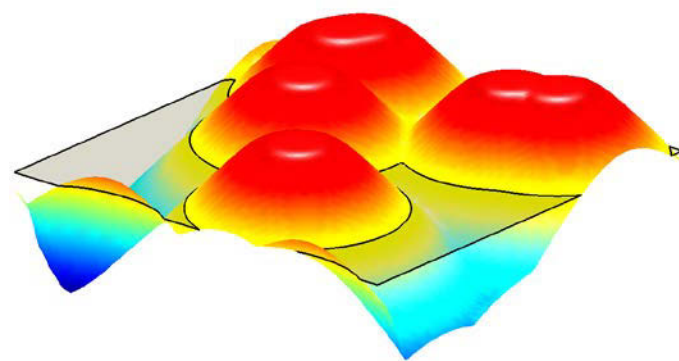
(a1)



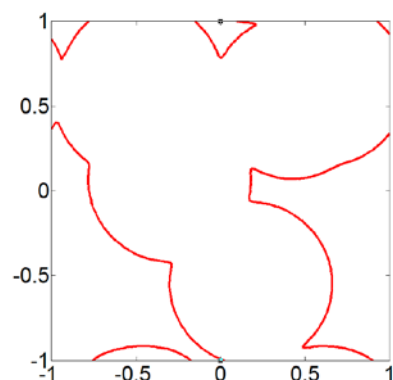
(b1)



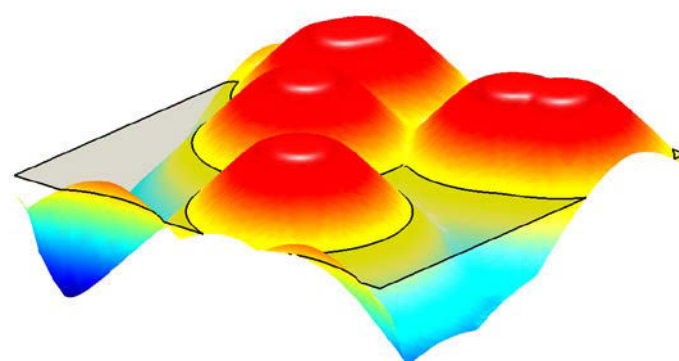
(a2)



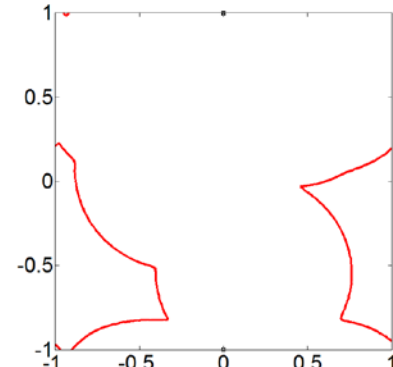
(b2)



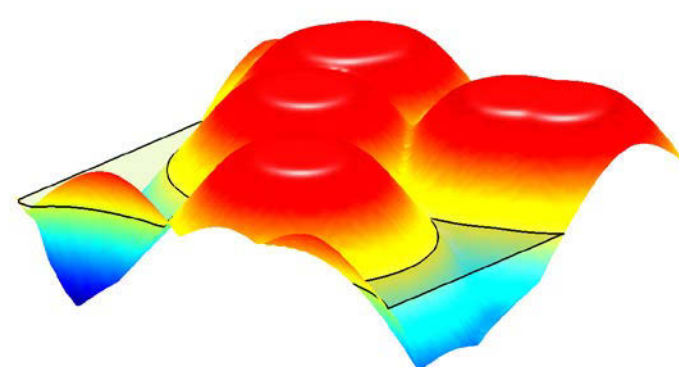
(a3)



(b3)



(a4)

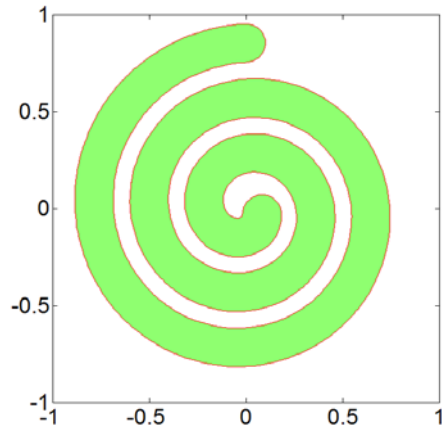


(b4)

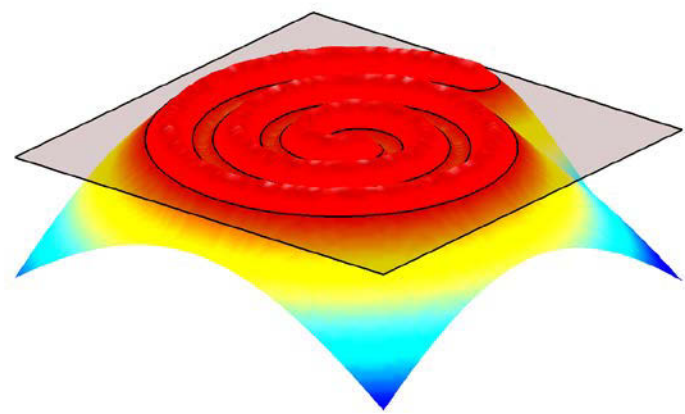
**Figure 3.5 The propagation of LSF in normal speed at iteration 15, 30, 45, and 70.**

### 3.3.3 Numerical Example for Mean Curvature Flow (1)

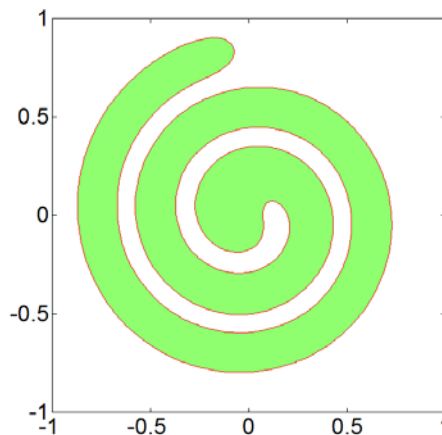
In this numerical example, the original boundary is a spiral in 2D space with  $D = \{(x, y) \in \mathbb{R}^2 : -1 < x < 1, -1 < y < 1\}$ . The space is discretized by  $80 \times 80$  grid, and time step is set as  $\Delta t = 0.2\Delta h^2$  ( $\Delta h$  is the grid spacing). Same as the previous numerical example, the H-J PDE is discretized by first order Godunov's scheme (Godunov 1983). The propagation of 2D boundaries and corresponding 3D surfaces during the evolution are shown in Figure 3.6.



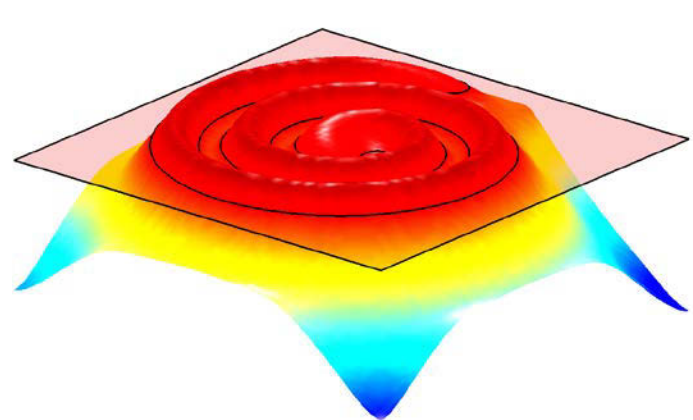
(a)



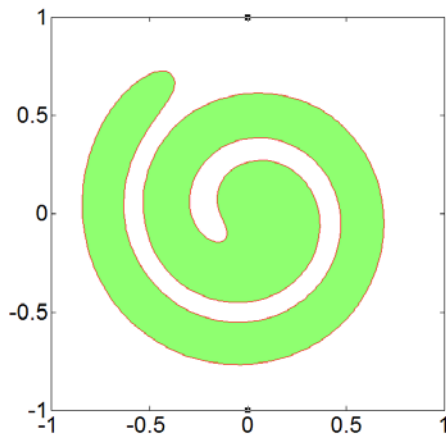
(b)



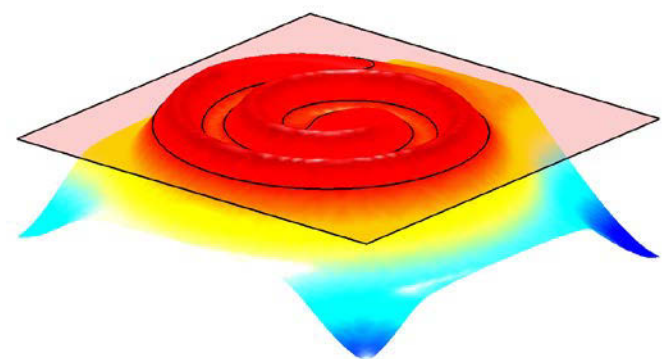
(a1)



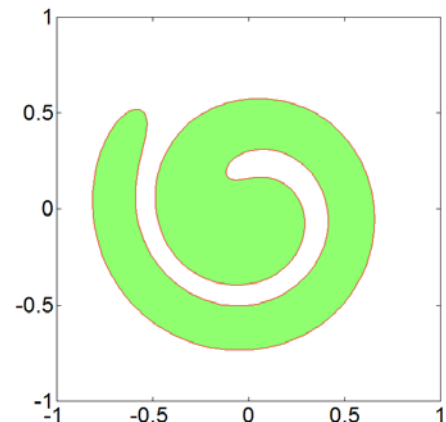
(b1)



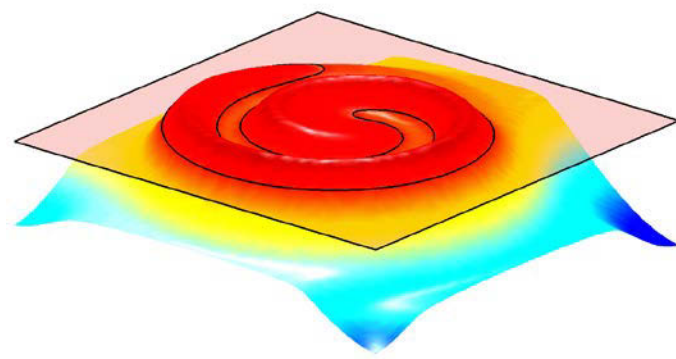
(a2)



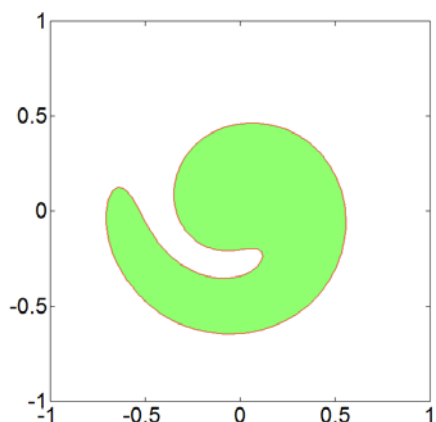
(b2)



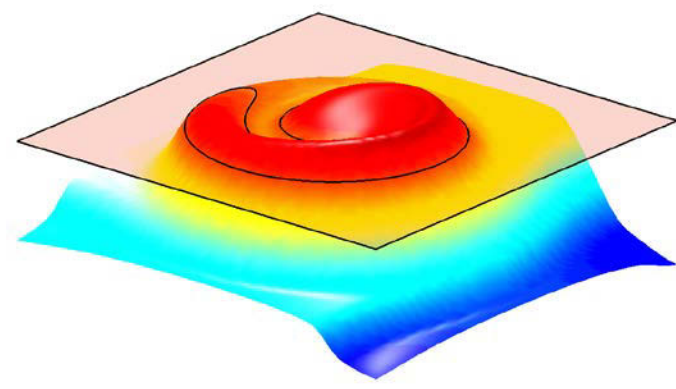
(a3)



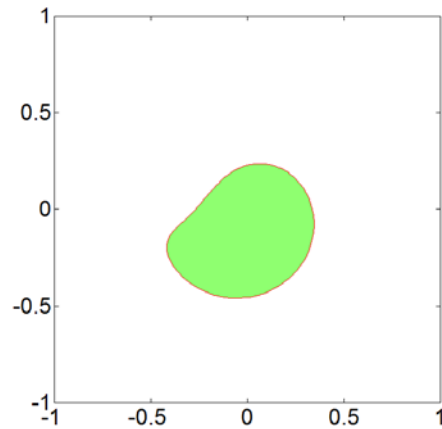
(b3)



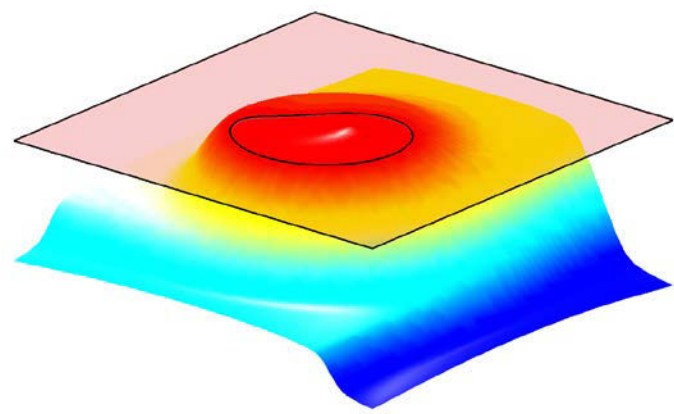
(a4)



(b4)



(a5)



(b5)

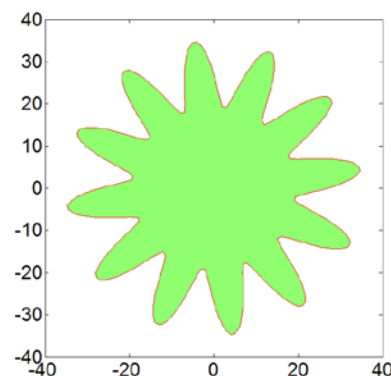
**Figure 3.6 The evolution of mean curvature flow**

(a) initial 2d boundary and (b) corresponding 3d surface;

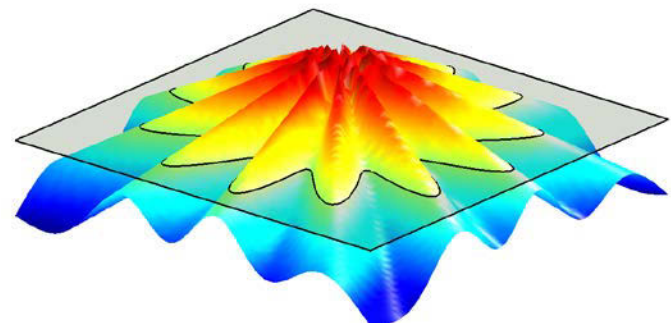
(a1-5) and (b1-5) are the boundaries and surfaces at iteration 100, 300, 500, 1000, 1800.

### 3.3.4 Numerical Example for Mean Curvature Flow (2)

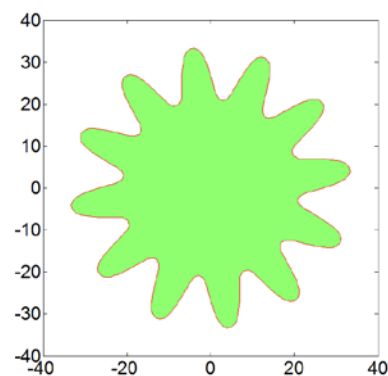
In this numerical example, a lacelike 2d boundary constructed in 2D space  $D = \{ (x, y) \in \mathbb{R}^2 : -40 < x < 40, -40 < y < 40 \}$ . The space is discretized by  $80 \times 80$  grid, and time step is set as  $\Delta t = 0.2 \Delta h^2$  ( $\Delta h$  is the grid spacing). The H-J PDE is still discretized by first order Godunov's scheme (Godunov 1983) as well. The propagation of 2D boundaries and corresponding 3D surfaces during the evolution are shown in Figure 3.7.



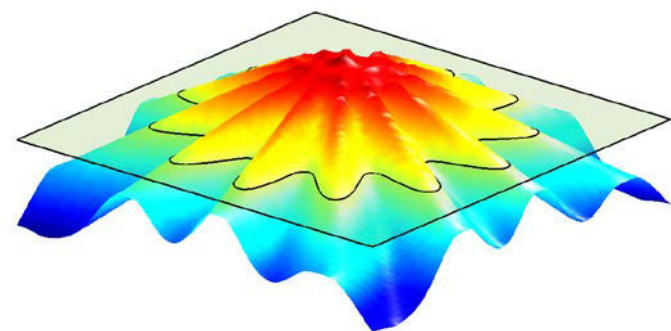
(a)



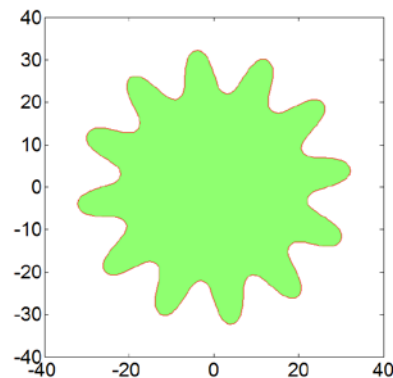
(b)



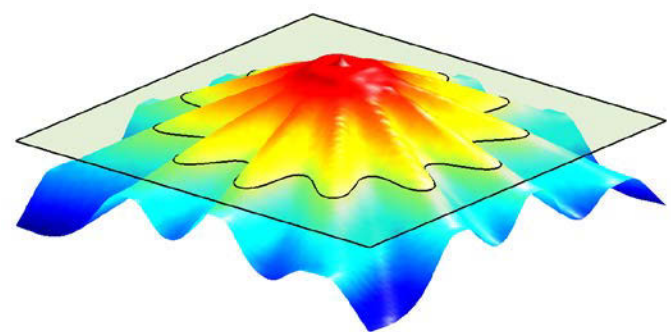
(a1)



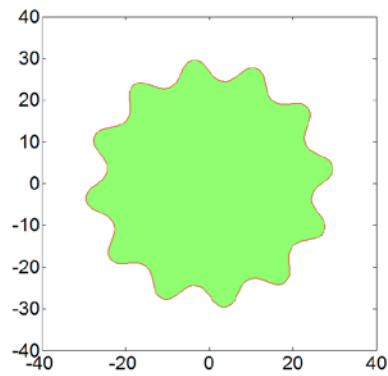
(b1)



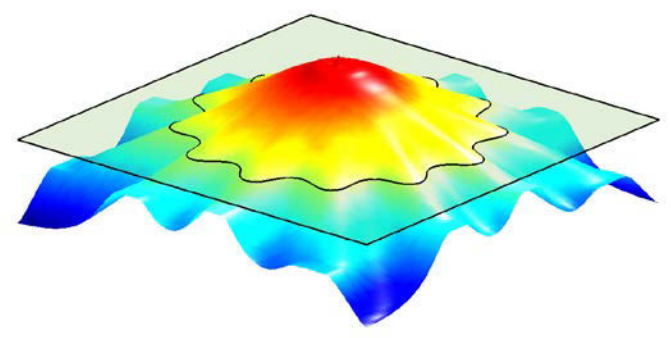
(a2)



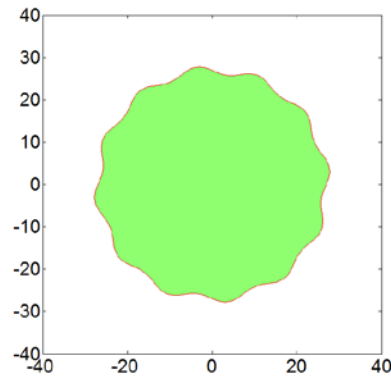
(b2)



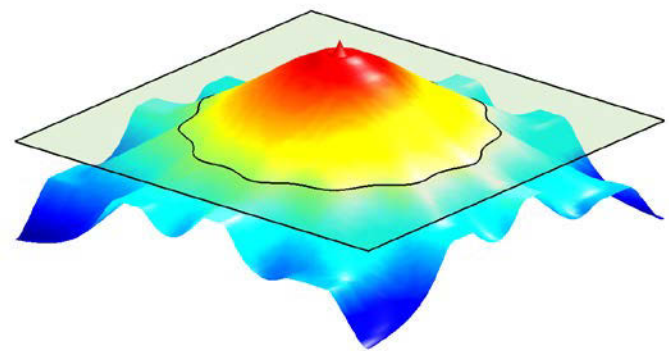
(a3)



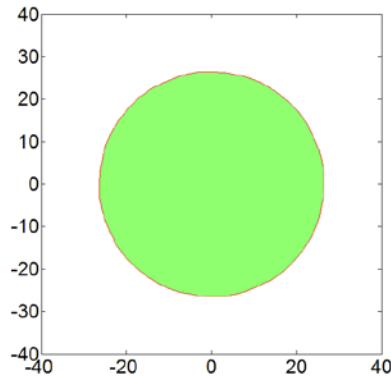
(b3)



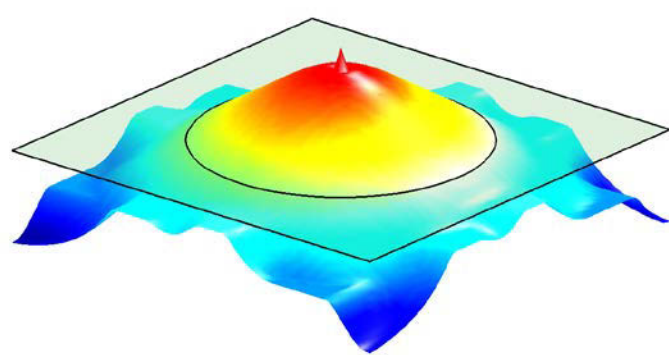
a4)



(b4)



(a5)



(b5)

**Figure 3.7 The evolution of mean curvature flow 2**  
 (a) initial 2d boundary and (b) corresponding 3d surface;  
 (a1-5) and (b1-5) are the boundaries and surfaces at iteration 10, 20, 50, 80, 150.

## 3.4 Numerical Issues of Level Set Method

### 3.4.1 Re-Initialization of Level Set Surface

The implicit level set function can be any type once it is a smooth function satisfying Eq. (3.1). However, to get highly accurate numerical results, it is usually regularized as a signed distance function which is a subset of implicit functions and defined as follows (Osher and Sethian 1988):

$$\Phi(x) = \begin{cases} \min(|x - x_I|) & \forall x \in D \setminus \Omega \\ 0 & \forall x \in \partial\Omega \\ -\min(|x - x_I|) & \forall x \in \Omega \setminus \partial\Omega \end{cases} \quad (3.24)$$

where  $x_I$  is the positions to sample the LSF.

An important feature of the signed distance function is

$$|\nabla \Phi(x)| = 1, \quad \forall x \in D \quad (3.25)$$

During the optimization process, the level set surface may become too steep or too flat, which deviates away from the signed distance function, leading to instability. Thus, it is necessary to apply the re-initialization iteratively for regularizing the level set surface as a signed distance function. One method to conduct the re-initialization is using the PDE based method (Peng et al. 1999), which needs to solve another PDE:

$$\frac{\partial \Phi}{\partial t} = \text{sign}(\Phi_0)(1 - |\nabla \Phi|) \quad (3.26)$$

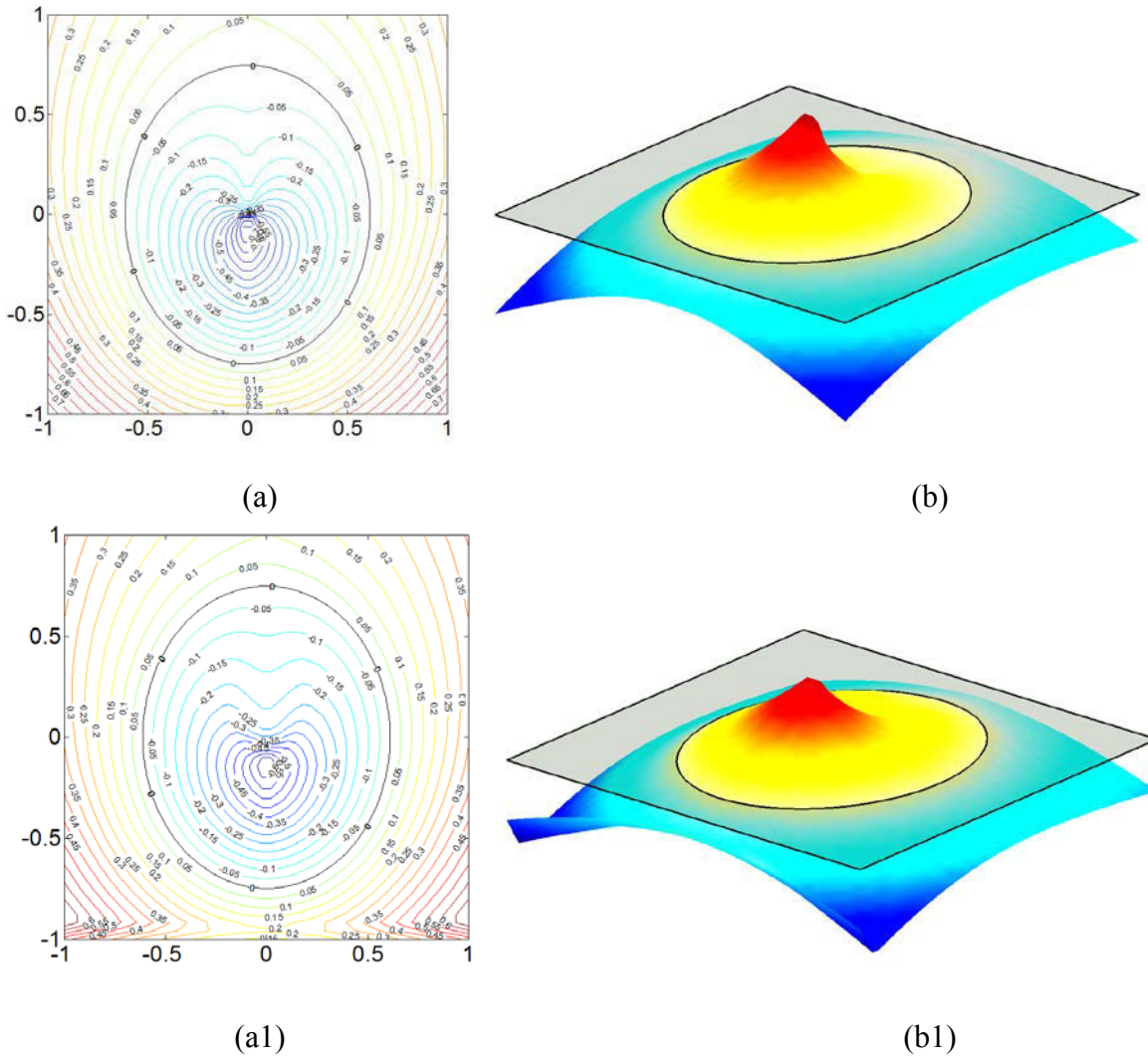
where  $\Phi_0$  is the LSF that to be corrected, and  $\text{sign}$  is the sign function as:

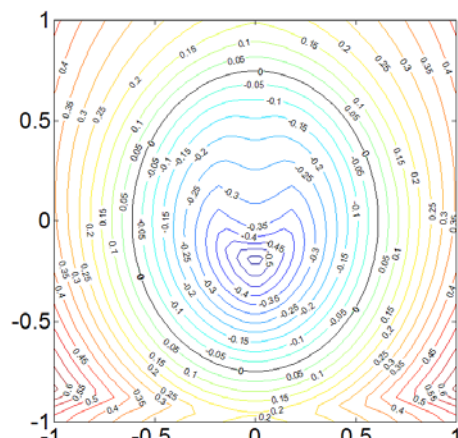
$$\text{sign}(\Phi) = \begin{cases} 1 & \Phi > 0 \\ 0 & \Phi = 0 \\ -1 & \Phi < 0 \end{cases} \quad (3.27)$$

Only the deviated LSF would be regulated by this manner. In a similar way, the upwind finite difference scheme can be used to get the steady-state solution of Eq. (3.23) and make  $|\Phi| = 1$  indirectly.

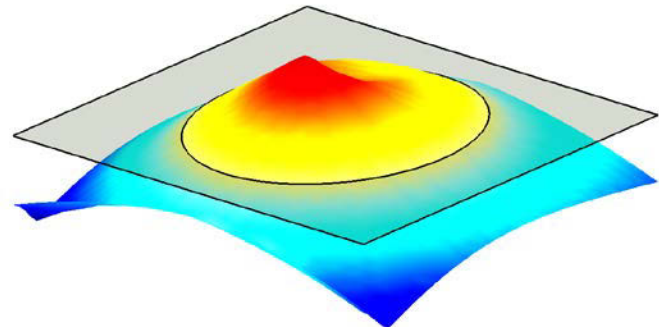
### 3.4.2 Numerical Example for Re-Initialization

The original boundary is a spiral in 2D space  $D = \{(x, y) \in \mathbb{R}^2: -1 < x < 1, -1 < y < 1\}$ . The space is discretized by  $50 \times 50$  grid, and time step is set as  $\Delta t = 0.2\Delta h$  ( $\Delta h$  is the grid spacing). The H-J PDE is discretized by first order Godunov's scheme and the propagation of 2D boundaries and corresponding 3D surfaces are shown in Figure 3.8. During the re-initialization process, it is not hard to notice that the level set surface is regularized as a signed distance function without any change of the interface of zero level set.

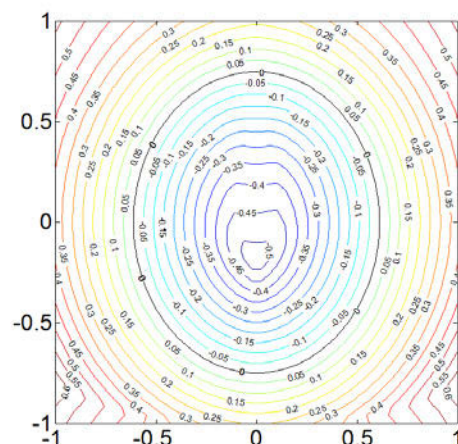




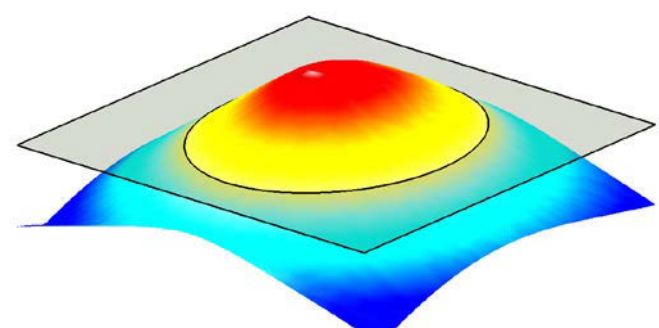
(a2)



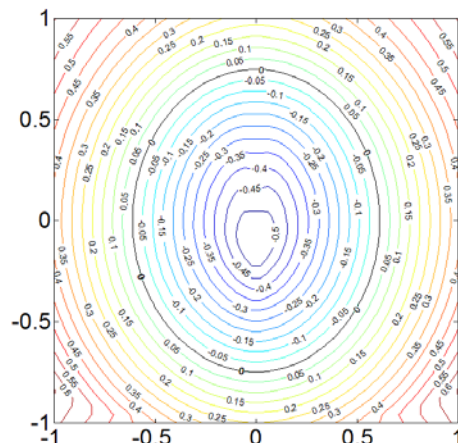
(b2)



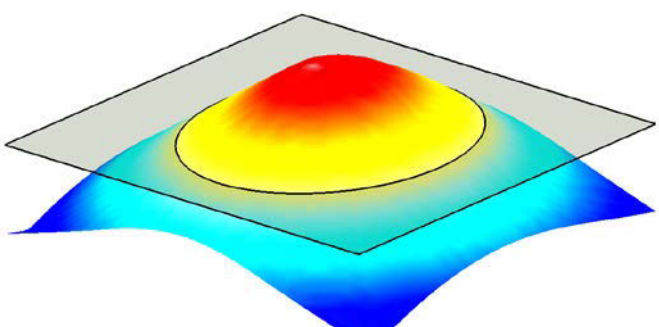
(a3)



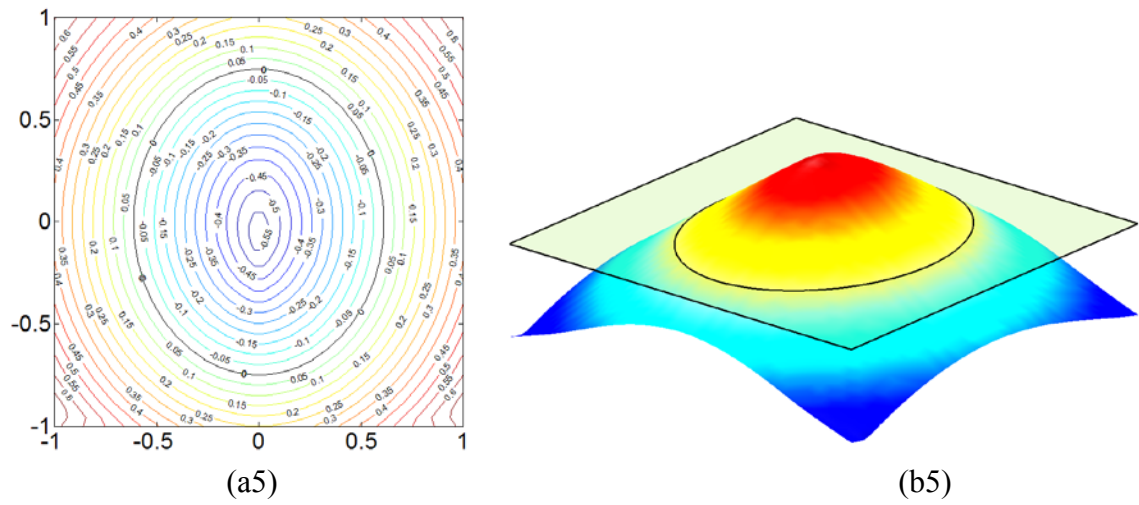
(b3)



(a4)



(b4)



**Figure 3.8 The process of re-initializing the level set function as a signed distance function**

(a) and (b) are the initial contours and correspondent 3d surface of the level set function;  
 (a1-5) and (b1-5) are the contours and surfaces at iteration 10, 25, 50, 60, 73.

### 3.4.3 Velocity Extension

By using the LSM, another numerical issue during the optimization process is about the velocity fields. The update of level set surface is the co-effect of various velocity fields. These velocity fields are caused by different factors, for instant, the description of objective functions (mean compliance or mechanical advantage), volume constraint or the quadratic energy functional. The domains of above mentioned velocity fields are not the same. Some velocity fields exist throughout the design domain and others are defined only on the boundary. When dealing with numerical implementations, it is necessary to extend the interfacial velocity to the whole domain or at least to a narrow band along the boundary, named velocity extension.

The ways to extend the interfacial velocity are not unique, and the most often used two methods include the PDE-based method [33, 78] (Peng et al. 1999) and the Fast Marching Method (Sethian 1999). Here, the PDE-based method is described as

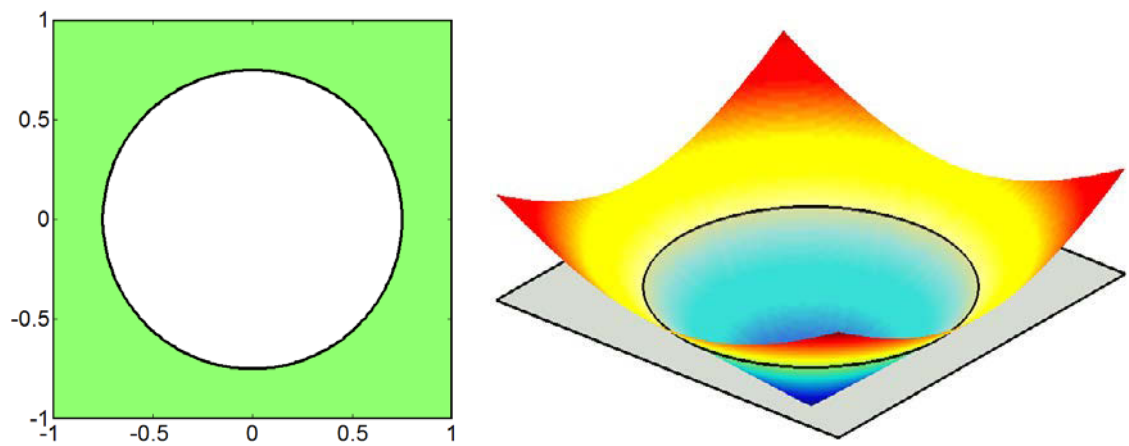
$$\mathbf{v}_t + \text{sign}(\Phi) \frac{\nabla \Phi}{|\nabla \Phi|} \cdot \mathbf{v} = 0 \quad (3.28)$$

where  $\mathbf{v}$  is the velocity field,  $\Phi(x)$  is the signed distance function, and function  $\text{sign}(\Phi)$  is defined as Eq. (3.24). After solving Eq. (3.25) for its steady state, the velocity field is extended along the normal directions of the boundary.

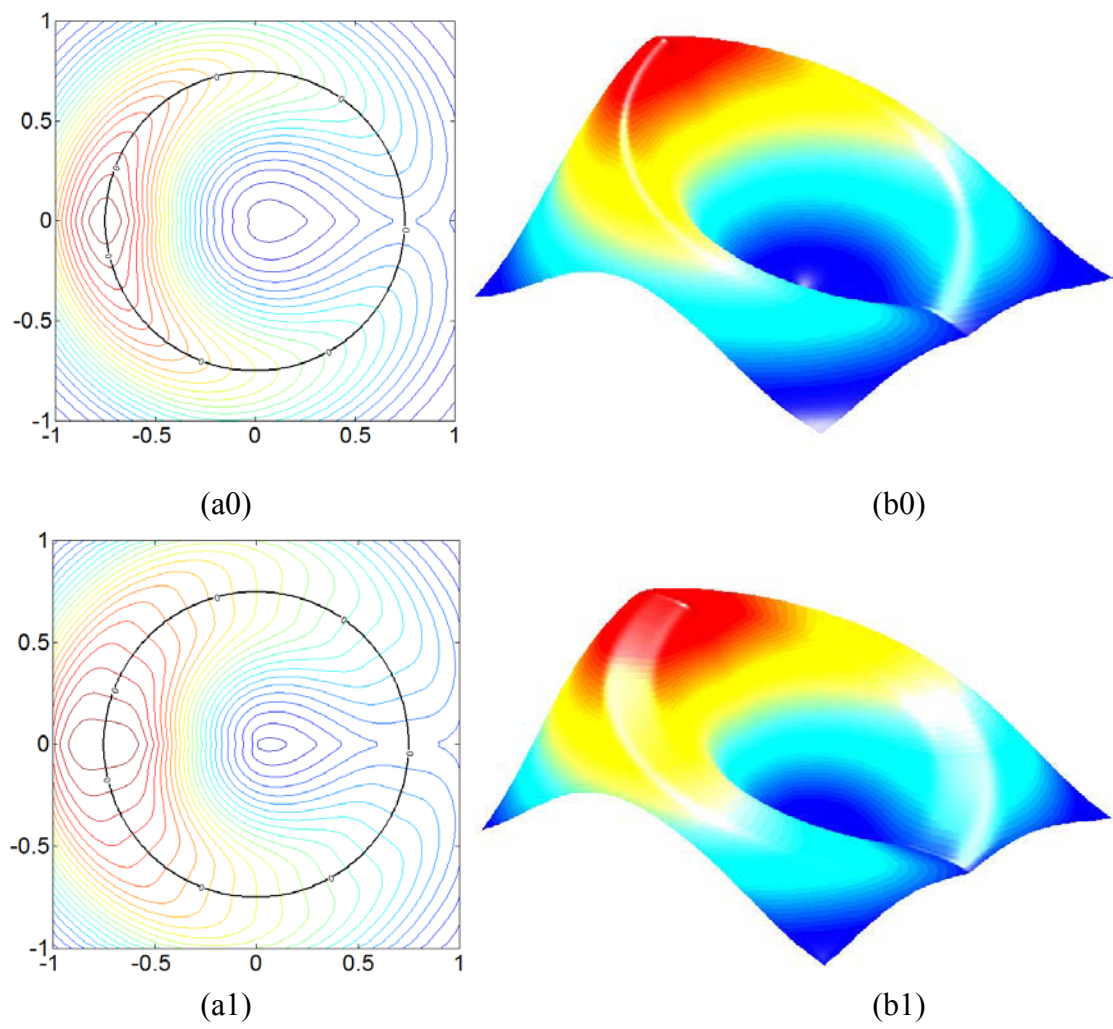
### 3.4.4 Numerical Example for Velocity Extension

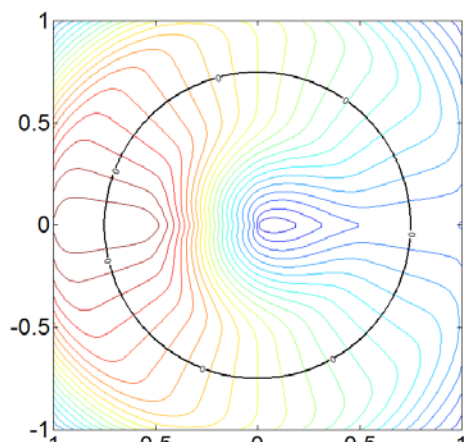
The original boundary is a spiral in 2D space  $D = \{(x, y) \in \mathbb{R}^2: -1 < x < 1, -1 < y < 1\}$ . The space is discretized by  $100 \times 100$  grid, and time step is set as  $\Delta t = 0.2\Delta h$  ( $\Delta h$  is the grid spacing). The H-J PDE is discretized by first order Godunov's scheme. The velocity field of the level set surface is extended to the entire domain along the normal direction while the zero level set of surface is kept constantly. The original level set function is shown in Figure 3.9, and the contours of the velocity field and the corresponding 3D surfaces over the evolution process are shown in Figure 3.10.

It can be found that the interfacial velocity is extended to the whole domain gradually during the process of velocity extension. However, the zero level set of the LSF surface remains the same along the whole process.

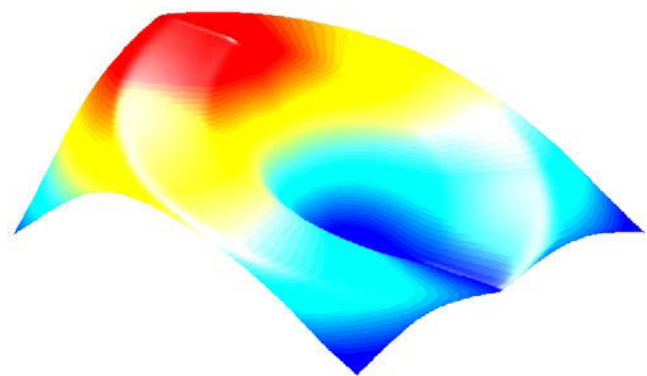


**Figure 3.9 Initial zero level set and correspondent 3d surface of the level set function**

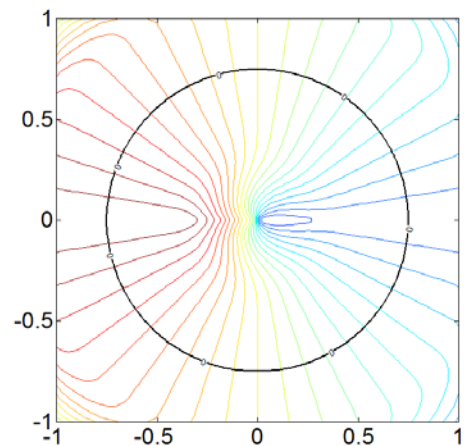




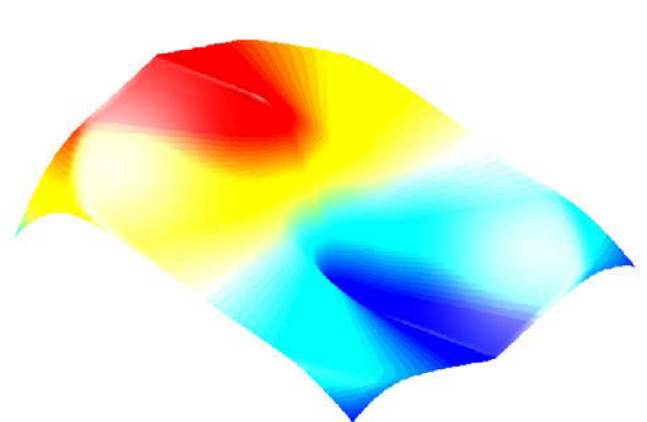
(a2)



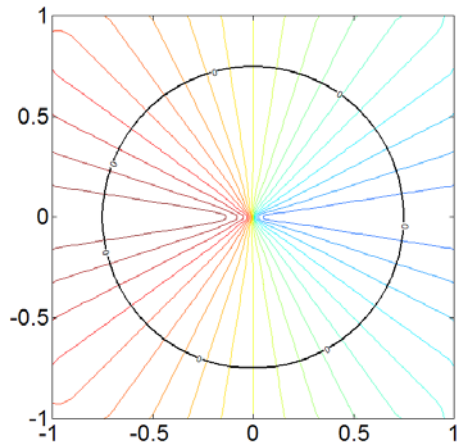
(b2)



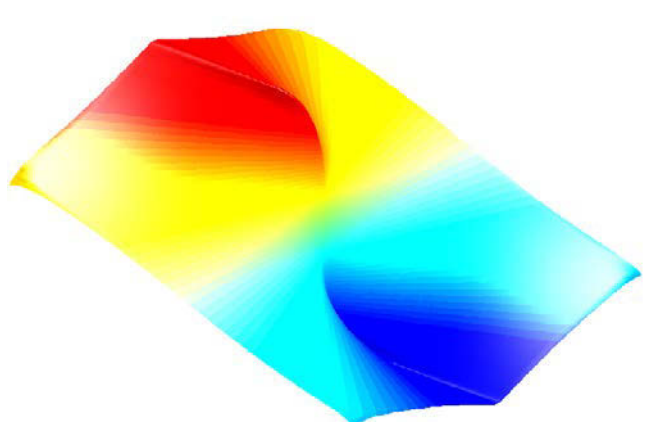
(a3)



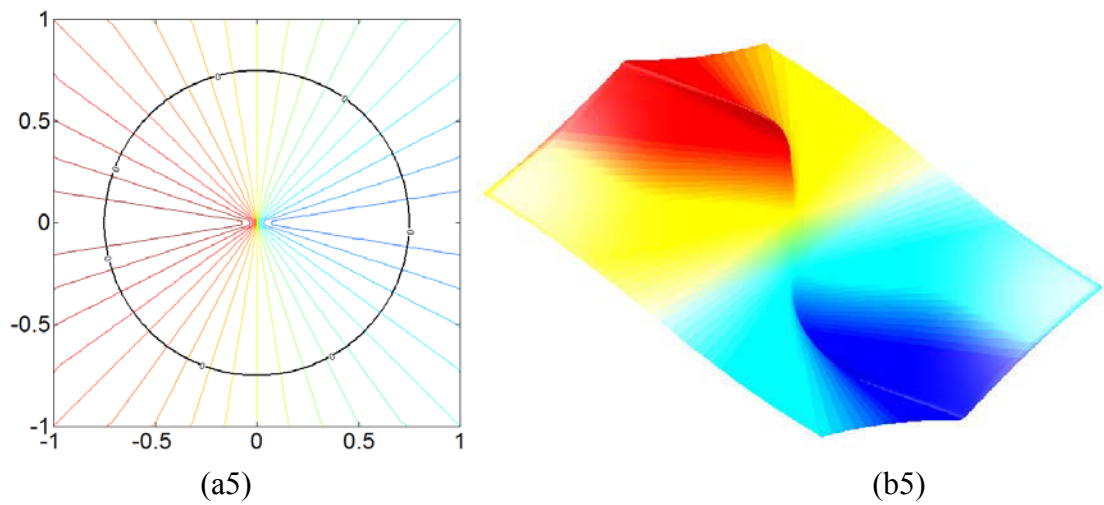
(b3)



(a4)



(b4)



**Figure 3.10 The process of velocity extension**

(a0) and (b0) are the initial contour and 3d surface for the velocity field of the LSF;  
(a1-5) and (b1-5) are the contours and surfaces at iteration 10, 20, 40, 60, 98.

# 4 A Parameterized Level Set Method for Structural Shape and Topology Optimization

Parametric Level Set Method (PLSM) is developed as an alternative to perform structural shape and topology optimization. In this method, the compactly supported radial basis function (CS-RBF) is employed to interpolate the level set function with a desirable smoothness. Then, the time-space coupled initial value problem, defined as the H-J PDE, is converted to a parametric problem. The shape functions are spatial only while the expansion coefficients (design variables) are temporal. An efficient convex programming is applied to solve the parametric optimization, leading to higher computational efficiency.

## 4.1 Parameterization of Shape and Topology Optimization

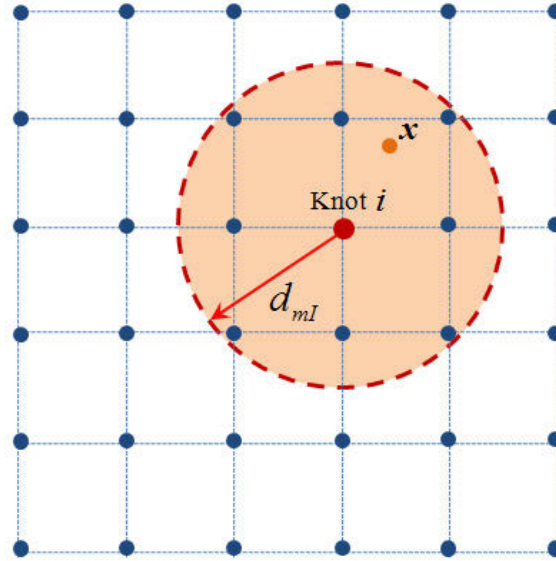
Radius basis functions (RBFs) are radially symmetric functions centered at a particular point or knot (Buhmann 2003), such as globally supported RBFs or compactly supported RBFs (CS-RBFs), which have been popularly used in approximating multivariate scattered data in recent years (Schaback and Wendland 1999; Wang and Wang 2006). The globally supported RBFs have been used to interpolate the level set function for structural topology optimization (Wang et al. 2007). However, the free shape parameter has a great influence on the accuracy of the interpolation, and the fully dense matrix will seriously impact the

computational efficiency when approximating systems with a large amount of candidate points. Thus, a well-established scheme to determine its optimal value is still absent. Later, the CS-RBFs is used as an alternative way of overcome these shortcomings (Luo et al. 2009). CS-RBFs has been popular in multivariate interpolations due to its strictly positive-definite property and matrix sparseness (Wendland 1995). The positive definiteness and continuity can be incarnated by finding a non-negative and non-vanishing Fourier transform in terms of the theorem of Bochner (Schaback and Wendland 1999). It is noted that the support of the CS-RBFs is a limited subdomain around a sample knot which is used to measure the contribution of a given node. The particular attractiveness of CS-RBFs is that the interpolant can naturally inherit the continuity of the RBFs, which would enable us to select appropriate shape functions with favorable continuity.

#### **4.1.1 Compactly Supported Radial Basis Functions**

A variety of CS-RBFs are available (Buhmann 2003) in approximating complicated functions, and the basis function is schematically illustrated in Figure 4.1. Any of CS-RBFs can be applied to interpolate the scalar function with desired smoothness and completeness once CS-RBFs knots are properly arranged in the design domain. In PLSM, a popularly studied family of CS-RBFs with various continuity order  $C^{2k}$  ( $k = 1, 2, 3$ ) (Wendland 1995; Wendland 2006), such as CS-RBFs with  $C^2$ ,  $C^4$  and  $C^6$  continuity, are usually adopted to interpolate the LSF. It is obvious that the  $C^6$  function has the highest differentiability relevant to the steepest caps of shape and derivatives. Hence, it might be more sensitive to the variation of the radius for support domain. A too small support radius cannot enable CS-RBFs to effectively span the inner-constraint gaps, and a too large radius would remarkably

increase the computation time. In general, larger support domains should be applied to low-order CS-RBFs and smaller ones to high-order CS-RBFs. The experiential criterion of choosing an appropriate support radius is to make a trade-off in both ensuring the non-singularity of the interpolation and guaranteeing a modest numerical effort.



**Figure 4.1 Supported domain of knot  $i$  with radius  $d_{mi}$**

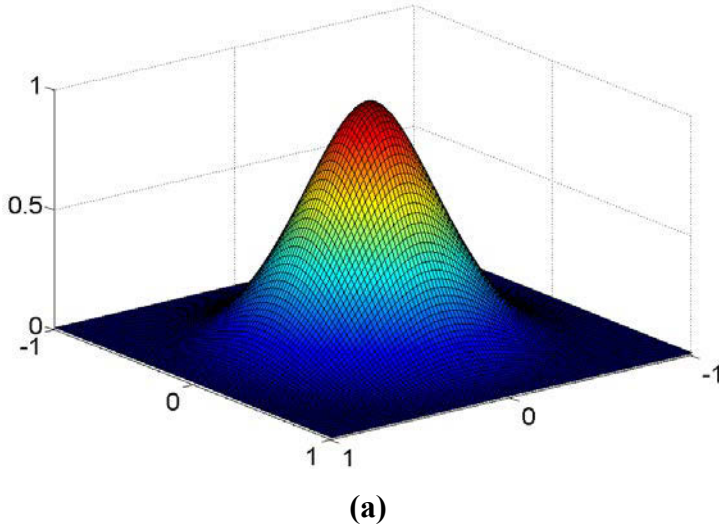
For the CS-RBFs of Wendland  $C^2$  continuity (Wendland-C2), the CS-RBF is given as

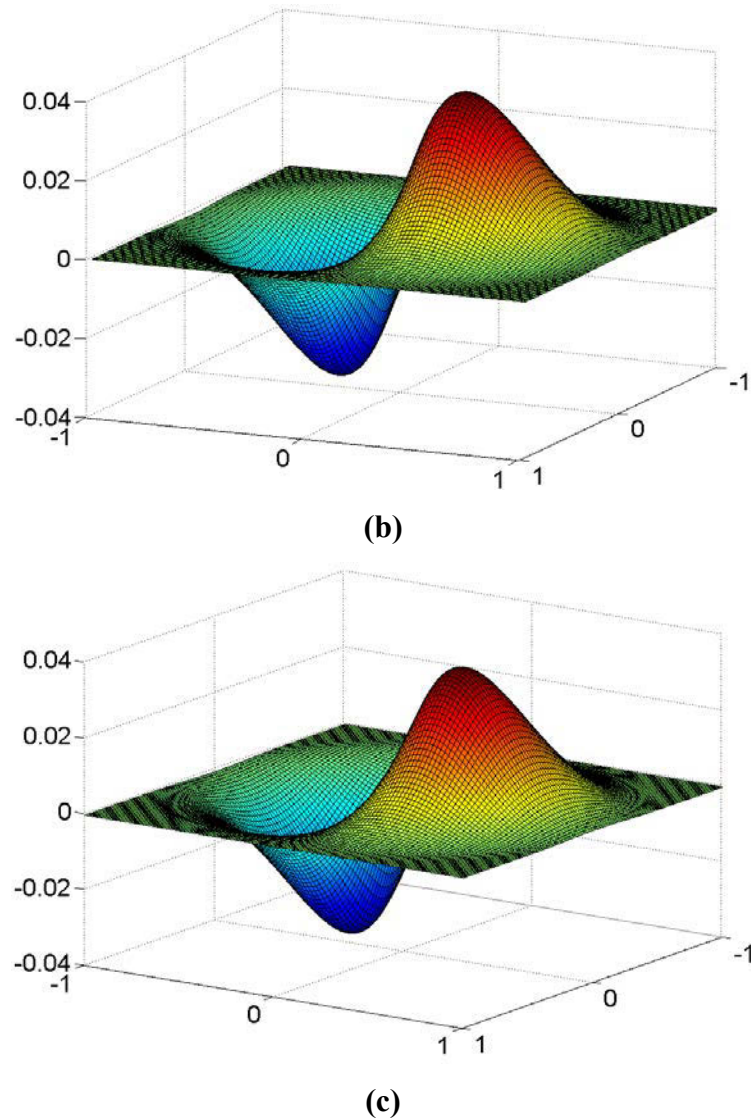
$$\varphi_i(r) = \max \{0, (1-r)^4 (4r+1)\} \quad (i = 1, 2, \dots, N) \quad (4.1)$$

The gradient of this CS-RBF is

$$\begin{aligned}
\frac{\partial \varphi}{\partial \mathbf{x}^d} &= \frac{\partial \varphi}{\partial r} \frac{\partial r}{\partial \mathbf{x}^d} \\
&= -4 \max \{0, (1-r)\}^3 (4r+1) \frac{\partial r}{\partial \mathbf{x}^d} + 4 \max \{0, (1-r)\}^3 (1-r) \frac{\partial r}{\partial \mathbf{x}^d} \quad (4.2) \\
&= \max \{0, (1-r)\}^3 (-20r) \frac{\partial r}{\partial \mathbf{x}^d} \quad (d = 1, 2, \dots, \text{Dimension})
\end{aligned}$$

where  $r$  is the radius of support domain and is usually defined in a 2D Euclidean space by  $r = \|\mathbf{x} - \mathbf{x}_i\|/d_{ml}$ , with  $d_{ml}$  is the radius of support at knot  $i$ . The size of the support domain of the basis function at the knot is determined by parameter  $d_{ml}$ . The popular CS-RBFs, Wendland-C2, and its derivatives are shown in Figure 4.2.





**Figure 4.2 (a): Shapes of Wendland-C2; (b), (c):its derivatives in the  $X$  and  $Y$  directions**

The CS-RBF with  $C^4$  continuity (Wendland-C4) are given, respectively, as

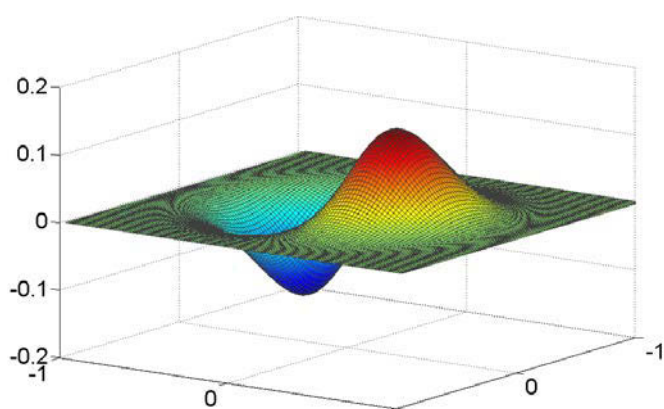
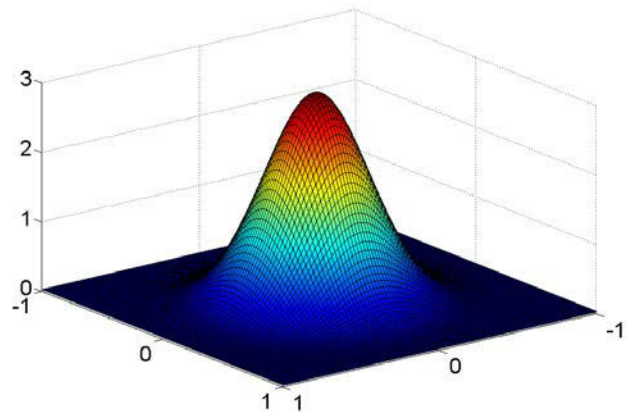
$$\varphi_i(r) = \max \{0, (1-r)\}^6 (35r^2 + 18r + 3) \quad (i = 1, 2, \dots, N) \quad (4.3)$$

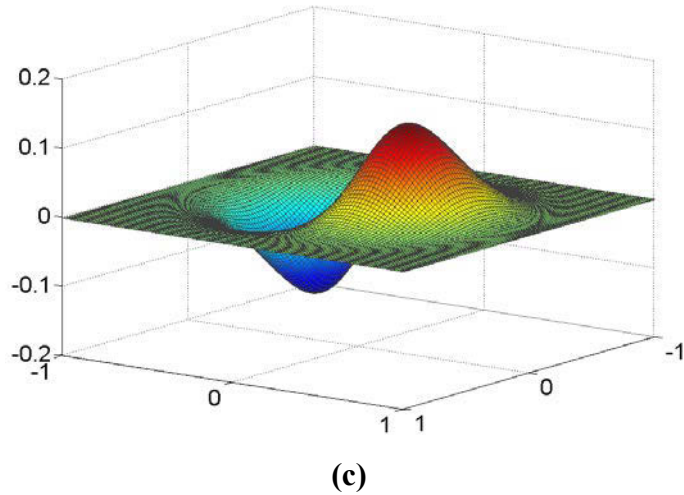
Its derivative are calculated as

$$\frac{\partial \varphi}{\partial \mathbf{x}^d} = \frac{\partial \varphi}{\partial r} \frac{\partial r}{\partial \mathbf{x}^d} = \max \{0, (1-r)\}^5 (-280r^2 - 56r) \frac{\partial r}{\partial \mathbf{x}^d} \quad (4.4)$$

$$(d = 1, 2, \dots, \text{Dimension})$$

The shape of Wendland-C4 and its derivatives are shown in Figure 4.3.





**Figure 4.3 (a): Shapes of Wendland-C4; (b), (c):its derivatives in the X and Y directions**

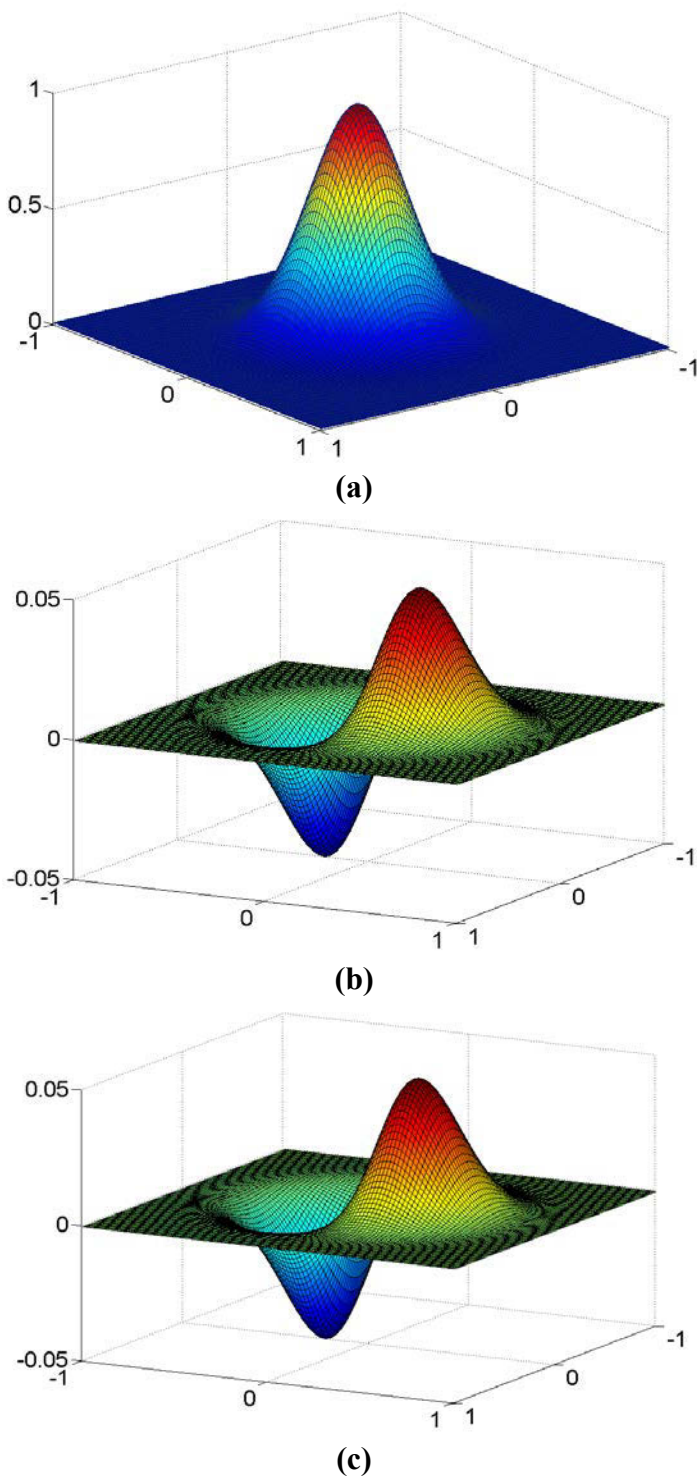
The CS-RBF with C6 continuity and its derivative are given, respectively, as

$$\varphi_i(r) = \max \{0, (1-r)\}^8 (32r^4 + 25r^2 + 8r + 1) \quad (i = 1, 2, \dots, N) \quad (4.5)$$

$$\frac{\partial \varphi}{\partial \mathbf{x}^d} = \frac{\partial \varphi}{\partial r} \frac{\partial r}{\partial \mathbf{x}^d} = \max \{0, (1-r)\}^7 (-352r^3 - 154r^2 - 22r) \frac{\partial r}{\partial \mathbf{x}^d} \quad (4.6)$$

$(d = 1, 2, \dots, \text{Dimension})$

The shape of CS-RBF Wendland-C6 and its derivatives are shown in Figure 4.4



**Figure 4.4 (a): Shapes of Wendland-C6; (b), (c):its derivatives in the X and Y directions**

It has been proved that the CS-RBFs can approximate functions with desirable completeness once the CS-RBFs are properly arranged in the domain. In practice the Wendland-C2 functions are smooth enough to ensure a favourable approximation and robust with respect to the change of the support radius (Luo and Tong 2008) in structural optimization. Other CS-RBFs with higher differentiability have been investigated by (Wendland 1995), which may be more sensitive to the changes of the support radius.

Meanwhile, an appropriate radius of support domain is required to ensure the non-singularity of the function interpolation and guarantee the computational efficiency simultaneously. Thus, an experiential criterion in selecting a suitable radius of support is often needed. In the thesis, the CS-RBFs designed by Wendland (Wendland 2006) with desired smoothness is employed to interpolate the higher-dimensional level set function. The CS-RBFs with  $C^2$  continuity is chosen in the PLSM.

#### **4.1.2 Parameterization of the Level Set Function**

Using the CS-RBFs, the level set function can be described by centrally positioning the CS-RBFs at their pre-specified knots over the whole design domain, as

$$\Phi(\mathbf{x}) = \boldsymbol{\varphi}(\mathbf{x})^T \mathbf{c} \quad (4.7)$$

with a vector of the shape functions

$$\boldsymbol{\varphi}(\mathbf{x}) = [\varphi_1(\mathbf{x}), \varphi_2(\mathbf{x}), \dots, \varphi_N(\mathbf{x})]^T \in \mathbb{R}^N \quad (4.8)$$

and the expansion coefficient vector

$$\mathbf{c} = [c_1, c_2, \dots, c_N]^T \in \mathbb{R}^N \quad (4.9)$$

The initial values for the generalized expansion coefficients are decided by  $\mathbf{c} = \mathbf{B}^{-1}\mathbf{h}$ , where the interpolation values  $\mathbf{h} = (h_1, h_2, h_3, \dots, h_N) \in \mathbb{R}^N$  at knot locations are given in advance.

The collection matrix  $\mathbf{B}$  is theoretically invertible due to the strict positive definiteness of the CS-RBFs (Buhmann 2003; Wang, Lim et al. 2007).

The LSF is uniquely determined in terms of the given interpolating data of the LSF located at the knots, owing to the property of strict positive definiteness of the CS-RBFs. The interpolation by CS-RBFs results in a separation scheme of the space and time. The shape functions are only spatial function and the generalized expansion coefficients are only time dependent. Thus, the decoupling of the time and space terms of the H-J PDE is

$$\boldsymbol{\varphi}(\mathbf{x})^T \frac{\partial \mathbf{c}(t)}{\partial t} - \mathbf{v}_n |\nabla \boldsymbol{\varphi}(\mathbf{x})^T \mathbf{c}(t)| = 0 \quad (4.10)$$

The normal velocity  $\mathbf{v}_n$  is related to the time derivative of the expansion coefficients as

$$\mathbf{v}_n = \frac{\boldsymbol{\varphi}(\mathbf{x})^T}{|\nabla \boldsymbol{\varphi}(\mathbf{x})^T \mathbf{c}(t)|} \frac{\partial \mathbf{c}(t)}{\partial t} \quad (4.11)$$

It is noted that all the terms involved in  $\mathbf{v}_n$  are evaluated at the knots over the whole design domain, thus, the normal velocity  $\mathbf{v}_n$  is actually extended to the entire design domain. In this way, the H-J PDE has been parameterized into a system of algebraic equations with a set of unknown expansion coefficients  $\mathbf{c}(t)$ , which is regarded as the design variables in the topology optimization problem. Hence, the propagation of the LSFs is just a problem of finding  $\mathbf{c}(t)$  using an appropriate optimization algorithm.

## 4.2 Shape Derivative of the Optimization Problem

This section will focus on the shape evolution of implicit surface representation by a parametric method. Due to the well-established theory of the stiffness design problem, it has been widely used in shape and topology optimizations as the workbench example. Here, the linear elastic structure is applied for the advantage of simplicity but without losing generality. The mathematical model based on the LSM is established as:

$$\begin{cases} \text{Minimize}_{(u, \Phi)} J(u, \Phi) = \int_D f(u) H(\Phi) d\Omega \\ \text{Subject to} \quad \begin{cases} G(u, \Phi) = \int_D H(\Phi) d\Omega - V^* \leq 0 \\ a(u, \Phi) = l(v, \Phi) \leq 0 \quad \forall v \in \mathbf{U} \end{cases} \end{cases} \quad (4.12)$$

where  $G$  is the constraint to limit material usage,  $V^*$  is the prescribed volume,  $\mathbf{U}$  is the kinematically admissible set of displacements,  $v$  is the virtual displacement field belonging to  $\mathbf{U}$ , and  $\Gamma_D$  is the admissible Dirichlet boundary

The state equation for the elastic continuum structures is given in the weak form of  $a(u, v, \Phi) = l(v, \Phi)$ . The bilinear energy form  $a(u, v, \Phi)$  is described as

$$a(u, v, \Phi) = \int_D C_{ijkl} \varepsilon_{ij}(u) \varepsilon_{kl}(v) H(\Phi) d\Omega \quad (4.13)$$

The linear load form  $l(v, \Phi)$  is specified as

$$l(v, \Phi) = \int_D p v H(\Phi) d\Omega + \int_{\Gamma} \tau v d\Gamma \partial \quad (4.14)$$

$\partial D$  is further decomposed as

$$\partial D = \partial D_D \cup \partial D_N, \quad \partial D_N = \partial D_{N1} \cup \partial D_{N2} \quad (4.15)$$

where  $\partial D_D$  is the Dirichlet boundary (zero displacement) and  $\partial D_N$  is the Neumann boundary.  $\partial D_N$  is divided into two parts,  $\partial D_{N1}$  and  $\partial D_{N2}$ , which indicate the non-homogenous (force traction) and homogeneous (traction-free) boundaries, respectively.

In the level set based parametric shape and topology optimization, to minimize a specified objective functional over a set of admissible domains, it is necessary to establish the relationship between cost functional and design variables by using a sensitivity analysis method. Here, the shape derivative analysis of Sokolowski and Zolesio (2009) is applied.

For the self-adjoint problem like the mean compliance problem of linear elasticity, the Lagrangian function  $L(u, \lambda, \Lambda, \Phi)$  for the optimization problem can be defined according to the linearity of the admissible displacement field  $\mathbf{U}$  and the constraints as

$$L(u, \Phi) = J(u, \Phi) + l(u, \Phi) - a(u, v, \Phi) + \Lambda \left[ \int_{\Omega} H(\Phi) d\Omega - V^* \right] \quad (4.16)$$

Based on a use of the concept of material derivatives, we find the shape derivative of the Lagrangian (Wang, Wang et al. 2003; Wang and Wang 2004; Allaire and Jouve 2005; Wang and Wei 2005) as

$$\frac{dL(u, \Phi)}{dt} = \int_{\Omega} \beta(u, \Phi) |\nabla \Phi| \mathbf{v}_n \delta(\Phi) d\Omega = \int_{\Gamma} \beta(u, \Phi) \mathbf{v}_n d\Gamma \quad (4.17)$$

where

$$\beta(u, v, \Phi) = f(u, u) - C_{ijkl} \varepsilon_{ij}(u) \varepsilon_{kl}(v) + [pv + \nabla(\tau v) \cdot \mathbf{n} + \kappa(\tau v)] + \Lambda \quad (4.18)$$

and  $\kappa = \operatorname{div} \mathbf{n} = \nabla \cdot \mathbf{n} = \nabla \cdot (-\nabla \Phi / |\nabla \Phi|)$  is the mean curvature in two dimensions. Now, recalling the  $\mathbf{v}_n$  defined in Eq. (4.7) and substituting it into Eq. (4.17), the shape derivative of the Lagrangian is further written as

$$\frac{dL(u, \Phi)}{dt} = \sum_{i=1}^N \int_{\Gamma} \beta(u, v, \Phi) \frac{\varphi_i}{|\nabla \Phi(\mathbf{x})^T \mathbf{c}(t)|} \frac{\partial \mathbf{c}(t)}{\partial t} d\Gamma \quad (4.19)$$

where  $i = 1, 2, \dots, N$  indicates the number of CS-RBF knots. This equation is expanded as

$$\frac{dL(u, \Phi)}{dt} = \sum_{i=1}^N p^T \dot{\mathbf{c}}(t) + \sum_{i=1}^N q^T \dot{\mathbf{c}}(t), \quad \dot{\mathbf{c}}(t) = \frac{\partial \mathbf{c}(t)}{\partial t} \quad (4.20)$$

where  $c_i$  are the design variables that are actually the expansion coefficients of the CS-RBF interpolant, and  $p^T$  and  $q^T$  are defined as

$$p^T = \int_{\Gamma} \beta(u, v, \Phi) \frac{\varphi_i}{|\nabla \Phi(\mathbf{x})^T \mathbf{c}(t)|} d\Gamma \quad (4.21)$$

$$q^T = \Lambda \int_{\Gamma} \frac{\varphi_i}{|\nabla \Phi(\mathbf{x})^T \mathbf{c}(t)|} d\Gamma \quad (4.22)$$

On the other hand, the shape derivative of Lagrangian  $L$  can be given using the chain rule

$$\frac{dL(u, \Phi)}{dt} = \left( \sum_{i=1}^N \frac{\partial J(u, \Phi)}{\partial c_i} + \Lambda \sum_{i=1}^N \frac{\partial G(u, \Phi)}{\partial c_i} \right) \dot{c}_i(t) \quad (4.23)$$

By comparing the corresponding terms in Eq. (4.19) and Eq. (4.23), the design sensitivities for the objective function and the constraint can be obtained as

$$\frac{J(u, \Phi)}{\partial c_i} = \int_{\Gamma} \beta(u, v, \Phi) \frac{\varphi_i}{|\nabla \varphi(\mathbf{x})^T \mathbf{c}(t)|} d\Gamma \quad (4.24)$$

$$\frac{\partial G(u, \Phi)}{\partial c_i} = \int_{\Gamma} \frac{\varphi_i}{|\nabla \varphi(\mathbf{x})^T \mathbf{c}(t)|} d\Gamma \quad (4.25)$$

Therefore, the general shape and topology optimization problem has been transformed into a general size optimization problem, which enables the direct application of more elaborate gradient-based optimization algorithms in this field, such as OC and MMA (Svanberg 1987).

## 4.3 Optimization Method

In PLSM, the H-J PDE has been transferred into a system of algebraic equations in the numerical iterative process, and the original topological optimization is transformed into an easiest size optimization, in which the only unknowns are the expansion coefficients  $\mathbf{c}(t)$  that are actually defined as the design variables. Hence, the propagation of the boundary and the evolvement of the level set function, as well as the changes of the shape and topology of the structure are just a problem of updating  $\mathbf{c}(t)$  using optimization algorithm.

### 4.3.1 Optimality Criteria Method

For shape and topology optimization problems, efficient schemes such as the optimality criteria method have been widely employed (Rozvany, Ong et al. 1987; Zhou and Rozvany 1991; Rozvany and Kirsch 1995). It is known that the OC method is more efficient for optimization problems with a large number of design variables while only a few constraints (Rozvany, Ong et al. 1987), which is the typical case in the continuous shape and topology optimization with a global material usage constraint. By adopting the OC method, the

expansion coefficients of the CS-RBFs interpolation are directly posed as design variables and are iteratively updated.

With the level set method, the optimization problem of the stiffness designs is defined as

$$\begin{cases} \text{Minimize}_{\mathbf{c} = (c_1, c_2, \dots, c_N)^T} J(u, \Phi) = \frac{1}{2} \int_D C_{ijkl} \varepsilon_{ij}(u) \varepsilon_{kl}(u) H(\Phi) d\Omega \\ \text{Subject to} \begin{cases} G(u, \Phi) = \int_D H(\Phi) d\Omega - V^* \leq 0 \\ a(u, \Phi) = l(v, \Phi) \leq 0 \quad \forall v \in \mathbf{U} \\ c_{i,\min} \leq c_i \leq c_{i,\max} \end{cases} \end{cases} \quad (4.26)$$

where  $i = 1, 2, \dots, N$  and  $N$  is the number of design variables (expansion coefficients). In the equation above, lower and upper bounds  $c_{i,\min}$  and  $c_{i,\max}$  on the design variables  $\mathbf{c}$  are considered as additional constraints, as required in the OC method.

Introducing Lagrange multipliers  $\lambda_1$  and  $\lambda_2$ , the Lagrangian  $L$  is re-constructed as

$$\bar{L}(u, \Phi) = J(u, \Phi) + \Lambda V(\Phi) + \lambda_1 (c_{i,\min} - c_i) + \lambda_2 (c_i - c_{i,\max}) \quad (4.27)$$

The Kuhn–Tucker conditions can be obtained according to the stationary conditions of  $\bar{L}$

$$\frac{\partial J(u, \Phi)}{\partial c_j} + \Lambda \frac{\partial V(\Phi)}{\partial c_i} + \lambda_1 + \lambda_2 = \begin{cases} = 0 & \text{if } c_{i,\min} \leq c_i \leq c_{i,\max} \\ \geq 0 & \text{if } c_i < c_{i,\min} \\ \leq 0 & \text{if } c_i > c_{i,\max} \end{cases} \quad (4.28)$$

$$\begin{aligned} \int_{\Omega} V d\Omega - V^* &\leq 0 \\ \Lambda \left( \int_{\Omega} V d\Omega - V^* \right) &= 0, \quad \Lambda \geq 0 \end{aligned} \quad (4.29)$$

$$\begin{aligned} c_{i,\min} - c_i &\leq 0 \\ \lambda_1 (c_{i,\min} - c_i) &= 0, \quad \lambda_1 \geq 0 \end{aligned} \tag{4.30}$$

$$\begin{aligned} c_i - c_{i,\max} &\leq 0 \\ \lambda_2 (c_i - c_{i,\max}) &= 0, \quad \lambda_2 \geq 0 \end{aligned} \tag{4.31}$$

Regarding the bound constraints of expansion coefficients, if  $c_{i,\min} \leq c_i \leq c_{i,\max}$ , the design variable is active ( $\lambda_1 = \lambda_2 = 0$ ) and it can be changed during the optimization process. Otherwise,  $c_i < c_{i,\min}$  means only the lower bound is active and the design variable is then passive ( $\lambda_1 \geq 0, \lambda_2 = 0$ ), and  $c_i > c_{i,\max}$  indicates only the upper bound is active and the design variable is also passive ( $\lambda_2 \geq 0, \lambda_1 = 0$ ). The passive design variables cannot be changed and can only be determined by the values of bounds. Practically, it is always possible to find a pair of regularized bounds  $c_{j,\min}$  and  $c_{j,\max}$  such that all the design variables can satisfy bound constraints. The bounds are usually decided by finding the minimum and maximum values of the most recently obtained solution, because the difference of two adjacent solutions should be very close once an appropriate move limit is imposed.

The Kuhn–Tucker conditions give rise to a large number of non-linear algebraic equations, and it is not an easy task to find their solutions directly. Instead, some more efficient updating schemes based on the Kuhn–Tucker conditions (Rozvany and Kirsch 1995) have been developed as alternative to renew the design variables .

Assuming that the design variables are active, the stationary condition is again given as

$$\frac{\partial \bar{L}(u, \Phi)}{\partial c_i} = \frac{\partial J(u, \Phi)}{\partial c_i} + \Lambda \frac{\partial V(\Phi)}{\partial c_i} = 0 \quad (4.32)$$

Two successive solutions will be very close ( $c_i^{(k+1)} / c_i^{(k)} \approx 1$ ) when the design is approaching the optimal point. Thus, an updating format may be designed as

$$c_i^{(k+1)} = \left( \frac{\partial J(u, \Phi)}{\partial c_i^{(k)}} \right) \left/ \left( \Lambda^{(k)} \frac{\partial V(\Phi)}{\partial c_i^{(k)}} \right) \right. c_i^{(k)} \quad (4.33)$$

where  $k$  denotes the iteration number.

It is defined that

$$D_i^{(k)} = \left( \frac{\partial J(u, \Phi)}{\partial c_i^{(k)}} \right) \left/ \left( \max \left( \mu, \Lambda^{(k)} \frac{\partial V(\Phi)}{\partial c_i^{(k)}} \right) \right) \right. \quad (4.34)$$

where  $\mu$  is a very small positive constant used to remove the zero terms. Then, the iteration pattern for the design variables can be described as

$$c_i^{(k+1)} = D_i^{(k)} c_i^{(k)} \quad (4.35)$$

The design sensitivities are, respectively, established as

$$\frac{\partial J(u, \Phi)}{\partial c_i^{(k)}} = \sum_{i=1}^N \int_{\Gamma} \beta(u, v, \Phi) \frac{\phi_i}{|\nabla \Phi(\mathbf{x})^T \mathbf{c}(t)|} d\Gamma \quad (4.36)$$

$$\frac{\partial V(\Phi)}{\partial c_i^{(k)}} = \sum_{i=1}^N \int_{\Gamma} \frac{\phi_i}{|\nabla \Phi(\mathbf{x})^T \mathbf{c}(t)|} d\Gamma \quad (4.37)$$

The following scheme is one option for imposing lateral constraints for the design variables

$$\left(2 \times \min \left\{c_1^{(k)}, c_2^{(k)}, \dots, c_N^{(k)}\right\} \rightarrow c_{\min }^{(k)}\right) \leq c^{(k+1)} \leq 2 \times \max \left\{c_1^{(k)}, c_2^{(k)}, \dots, c_N^{(k)}\right\} \quad (4.38)$$

Artificial parameters, the damping factor  $\zeta (0 < \zeta < 1)$  and the move limit  $m = 0.01$  ( $0 < m < 1$ ), are further introduced to stabilize the optimization process (Bendsøe and Kikuchi 1988; Bendsøe and Sigmund 2003). The lateral constraints,  $\tilde{c}_i^{(k+1)} = \tilde{D}_i^{(k)} \tilde{c}_i^{(k)} \leq \tilde{c}_{\min }$  and  $\tilde{c}_i^{(k+1)} = \tilde{D}_i^{(k)} \tilde{c}_i^{(k)} \geq \tilde{c}_{\max }$ , are also considered, where  $\tilde{c}$  is the regularized design variable vector ranging from 0 to 1, and  $\tilde{c}_{\min }$  and  $\tilde{c}_{\max }$  are the regularized lateral limits.

To numerically facilitate the update, they are selected as  $\tilde{c}_{\min } = 0.0001$  and  $\tilde{c}_{\max } = 1$ . Then, the final updating scheme is given as

$$\tilde{c}_i^{(k+1)} = \begin{cases} \max \{(1-m) \tilde{c}_i^{(k)}, \tilde{c}_{\min }\} & \text { if }(\tilde{D}_i^{(k)})^{\zeta} \tilde{c}_i^{(k)} \leq \max \{(1-m) \tilde{c}_i^{(k)}, \tilde{c}_{\min }\} \\ \min \{(1-m) \tilde{c}_i^{(k)}, \tilde{c}_{\max }\} & \text { if }(\tilde{D}_i^{(k)})^{\zeta} \tilde{c}_i^{(k)} \geq \min \{(1-m) \tilde{c}_i^{(k)}, \tilde{c}_{\max }\} \\ (\tilde{D}_i^{(k)})^{\zeta} \tilde{c}_i^{(k)} & \text { otherwise } \end{cases} \quad (4.39)$$

### 4.3.2 The Method of Moving Asymptotes

The OC method has been successfully applied to solve problems with a large amount of design variables and single constraint, which usually includes the establishment of a heuristic updating scheme to renew the design variables. However, it is difficult to deal with multiple constrained optimization problems. Till now, several of the mathematical programming methods have been applied as more powerful and more theoretically well-established schemes to solve advanced optimization problems multiple constraints. Svanberg (Svanberg 1987) generalized the CONLIN approach (Fleury 1989) as the method

of moving asymptotes (MMA) by introducing two sets of lower and upper asymptotes to dynamically adjust the convexity of the approximations.

MMA as a kind of sequential convex programming has been regarded as one of the well-established algorithms for topology optimization problems (Luo, Chen et al. 2005). Specifically, using the concept of the conservative convex separable approximations, the original optimization problem can be transformed into a set of linearized, convex and separable sub-problems based on the first or second derivatives at the current and previous points. In particular, any of the sub-problems has a strictly convex objective function, which indicates a globally convergent optimum. At each step, the dual or the interior-point method can be used to renew design variables.

A new version of the globally convergent MMA (GCMMA) (Svanberg 2002) has also been developed as a more robust scheme in contrast to the previous versions. However, even if the newest version of GCMMA, it does not necessarily guarantee a globally convergent solution because the original problem itself is not convex in despite of all sub-problems are strictly convex.

When GCMMA is used to solve the parameterization problem, an algorithm for selecting the move limit size is incorporated to stabilize the optimization. As aforementioned, the move limit size here is different from the time-step size imposed by the CFL condition. Therefore, the present method is expected to have a faster convergence, especially, for a finer mesh. In the conventional LSM, the methods for finding the Lagrange multiplier of the volume constraint appeared to be less effective. A fixed Lagrange multiplier was introduced

---

to make the mass conservative despite the fact that the constraint cannot be well satisfied during the entire optimization process. An alternative way for deciding the Lagrange multiplier is under the assumption that the volume can remain unchanged during the front propagation, but actually the LSMs cannot make the volume conservative due to the drift of the volume during the optimization process. Wang (2007) applied the bisection algorithm to push the volume back, but it is difficult to handle multiple constraints. However, the GCMMA is very effective to handle multiple constraints no matter they are globally or locally imposed.

According to GCMMA method, the original optimization formulation should be further adjusted by introducing some artificial parameters for the sake of ensuring a feasible initial design point, which is re-expressed as

$$\begin{cases}
\begin{aligned}
& \text{Minimize} && J(\boldsymbol{\alpha}) + \left\{ a_0 z + \sum_{j=1}^m (b_j y_j + \frac{1}{2} d_j y_j^2) \right\} \\
& \text{Subject to} && \begin{cases} G_j(\boldsymbol{\alpha}) - a_j z - y_j \leq \bar{G}_j, \quad j = 1, 2, \dots, m \\ z \geq 0, y_j \geq 0, \quad j = 1, 2, \dots, m \\ c_{i,\min} \leq c_i \leq c_{i,\max}, \quad i = 1, 2, \dots, N \\ \text{Equilibrium equation} \end{cases}
\end{aligned}
\end{cases} \quad (4.40)$$

where  $J$  is the objective function given in Eq. (4.26), and  $G_j (j = 1, 2, \dots, m)$  are constraints.

$c_{i,\min}$  and  $c_{i,\max}$  are the lateral constraints of the design variables (also the expansion coefficients)  $c_i$ .  $a_0 > 0$ ,  $a_i \geq 0$ ,  $b_i > 0$ ,  $d_i > 0$  and  $b_i + d_i > 0$  are the artificial parameters.

$y = (y_1, y_2, \dots, y_m)^T \in \mathbb{R}^m$  and  $z \in \mathbb{R}$ , where  $m$  is the number of constraints and  $N$  is the number of design variables.

Then, the MMA sub-optimization problem is defined in the Eq. (4.41) in accordance with the MMA approximating expansions (Svanberg 1987; Svanberg 1998; Svanberg 2002). The Karush-Kuhn-Tucker (KKT) optimality criteria for the sub-problem are both necessary and sufficient, as the sub-problem is a convex optimization problem and the Slater's constraint qualification can be applied. Then, the sub-problem is solved by employing the “primal-dual interior-point” method (Svanberg 1998).

$$\left\{
\begin{array}{ll}
\text{Minimize} & \mathbf{g}_0^{(\kappa, \nu)}(\mathbf{c}) + \left\{ a_0 z + \sum_{j=1}^m (b_j y_j + \frac{1}{2} d_j y_j^2) \right\} \\
\text{Subject to} & \begin{cases} \mathbf{g}_j^{(\kappa, \nu)}(\mathbf{c}) - a_j z - y_j \leq 0, \quad j = 1, 2, \dots, m \\ z \geq 0, y_j \geq 0, \quad j = 1, 2, \dots, m \\ \max \{c_{i,\min}, \theta_i^{(\kappa)}\} \leq c_i^{(\kappa)} \leq \max \{c_{i,\max}, \eta_i^{(\kappa)}\}, \quad i = 1, 2, \dots, N \\ \text{Equilibrium equation} \end{cases}
\end{array}
\right. \quad (4.41)$$

The double index  $(\kappa, \nu)$  denotes the  $\nu$ th inner iteration within the  $\kappa$ th outer iteration. Before starting a new outer iteration, the inner iteration should be first performed according to the algorithm of Svanberg (Svanberg 2002). The MMA approximating functions is given as

$$\mathbf{g}_j^{(\kappa, \nu)}(\mathbf{c}) = \sum_{i=1}^N \left( \frac{p_{ij}^{(\kappa, \nu)}}{U_i^{(\kappa)} - c_i^{(\kappa, \nu)}} + \frac{q_{ij}^{(\kappa, \nu)}}{c_i^{(\kappa)} - L_i^{(\kappa, \nu)}} \right) + r_j^{(\kappa, \nu)} \quad (4.42)$$

where

$$p_{ij}^{(\kappa, \nu)} = (U_i^{(\kappa)} - c_i^{(\kappa)})^2 \left( \max \left\{ 0, \frac{\partial g_j(c^{(\kappa)})}{\partial c_i} \right\} + \rho_i^{(\kappa, \nu)} (c_{i,\max} - c_{i,\min}) \right) h \quad (4.43)$$

$$q_{ij}^{(\kappa, \nu)} = (c_i^{(\kappa)} - L_i^{(\kappa)})^2 \left( \max \left\{ 0, \frac{\partial g_j(c^{(\kappa)})}{\partial c_i} \right\} + \rho_i^{(\kappa, \nu)} (c_{i,\max} - c_{i,\min}) \right) \quad (4.44)$$

$$r_j^{(\kappa,\nu)} = g_j(c^{(\kappa)}) - \sum_{i=1}^N \left( \frac{p_{ij}^{(\kappa,\nu)}}{U_i^{(\kappa)} - c_i^{(\kappa)}} + \frac{q_{ij}^{(\kappa,\nu)}}{c_i^{(\kappa)} - L_i^{(\kappa)}} \right) \quad (4.45)$$

To conduct the MMA, the detailed selection for the parameter  $\rho$  to ensure the convexity, and the asymptotes  $L_i^{(\kappa)}$  and  $U_i^{(\kappa)}$  used to adjust the convexity can be determined according to the scheme suggested by Svanberg (Svanberg 2002).

## 4.4 Numerical Examples

In order to have an equitable assessment of the performance of the PLSM, the well-established minimum compliance problem is chosen (Bendsøe and Sigmund 2003), and optimal processes and results from three benchmark numerical examples are presented in this section.

### 4.4.1 Mitchell-Type Structure

Figure 4.5 is the design domain of the Mitchell-type structure with an aspect ratio of 2:1 corresponding to length over height and three concentrated force vertically applied at the bottom, with the force value  $F_1=20\text{KN}$  and  $F_2=10\text{KN}$ . The objective function is to minimize the structural strain energy under the volume fraction is constraint to 40%. The design domain is discretized with  $100 \times 50$  quadrilateral elements. The given material is steel with a Young's modulus  $E = 210\text{GPa}$  and Poisson's ratio  $\nu = 0.3$ .

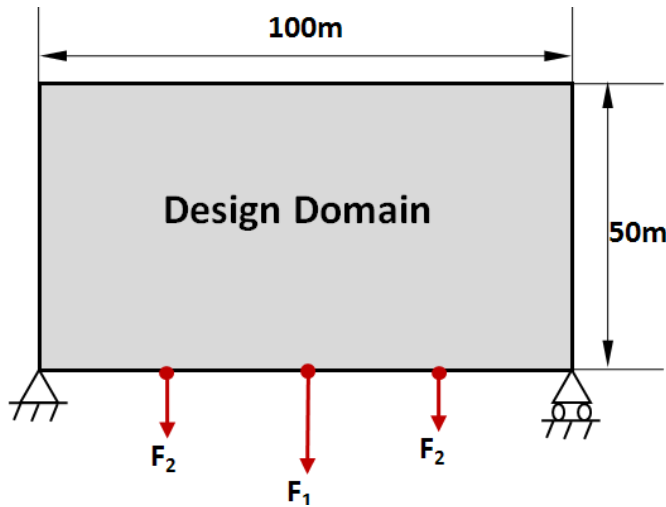
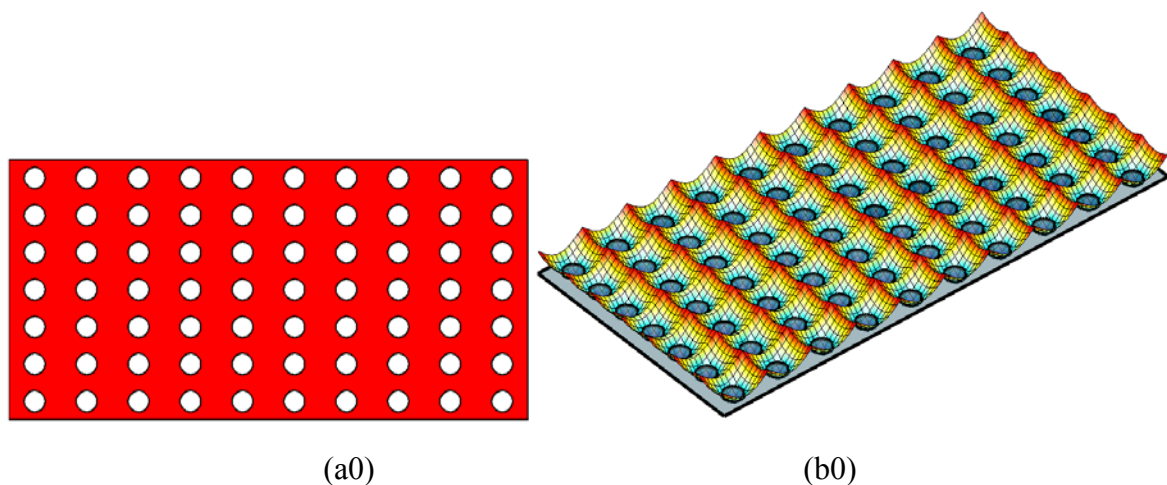
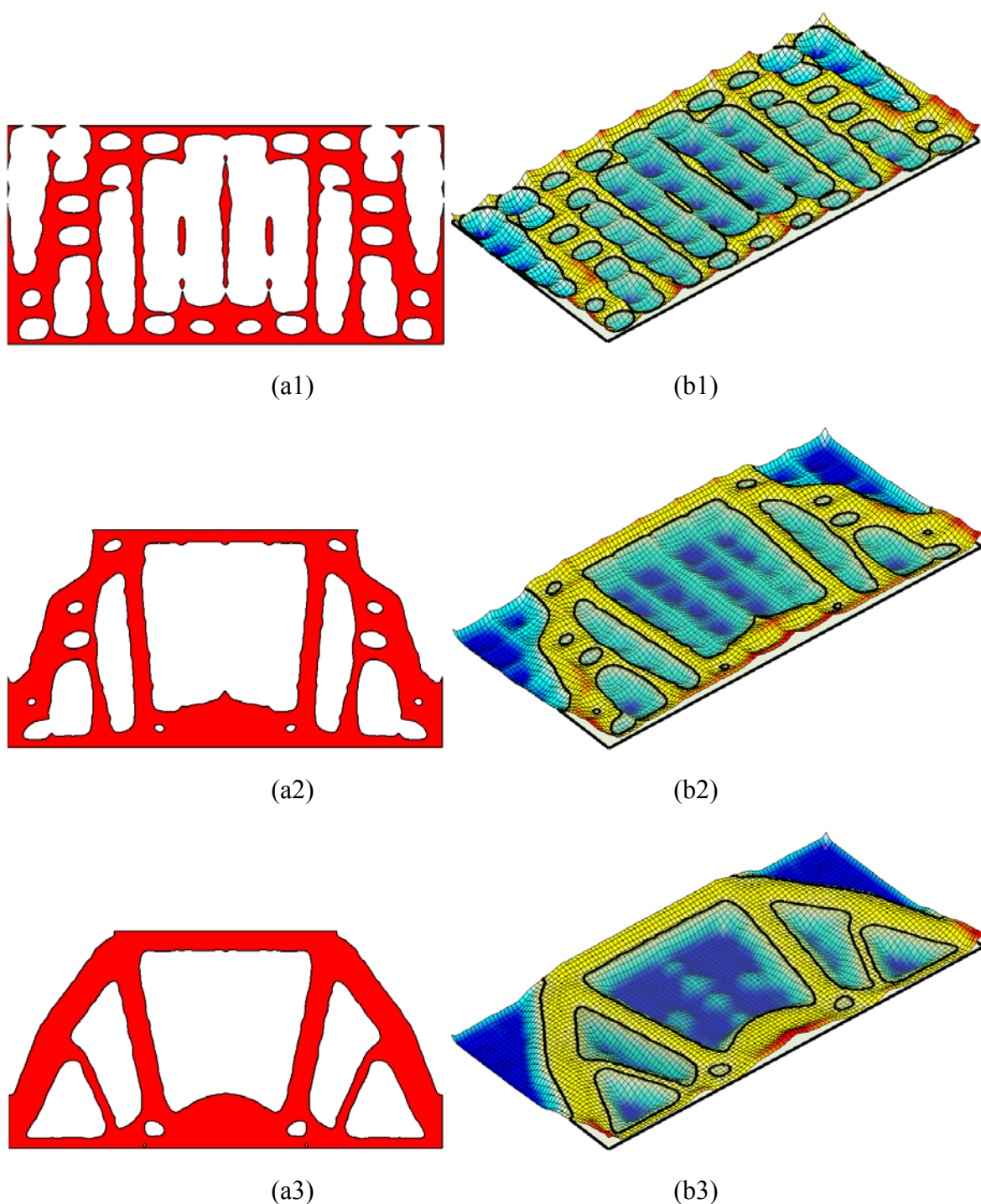
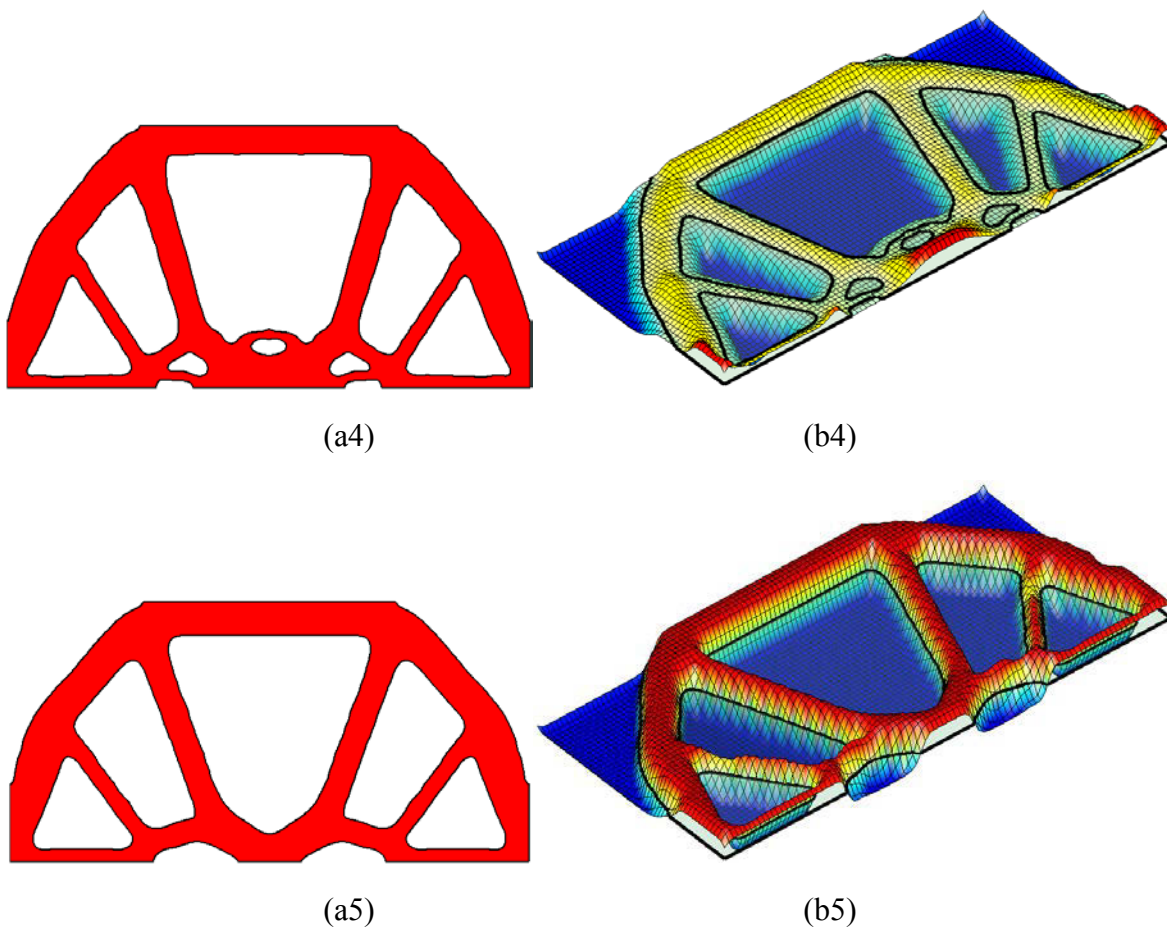


Figure 4.5 Design domain of the Mitchell-type structure

The initial design boundary and corresponding level set surface are given in Figure 4.65 (a) and (b). The contours denoting the history of the design boundary changes and the corresponding level set surfaces during the evolution are given in Figure 4.6 (a1-4) and (b1-4), and the optimal configuration and related level set surface are separately shown in Figure 4.6 (a5) and (b5). The evolution of material distributions are shown in Figure 4.7.

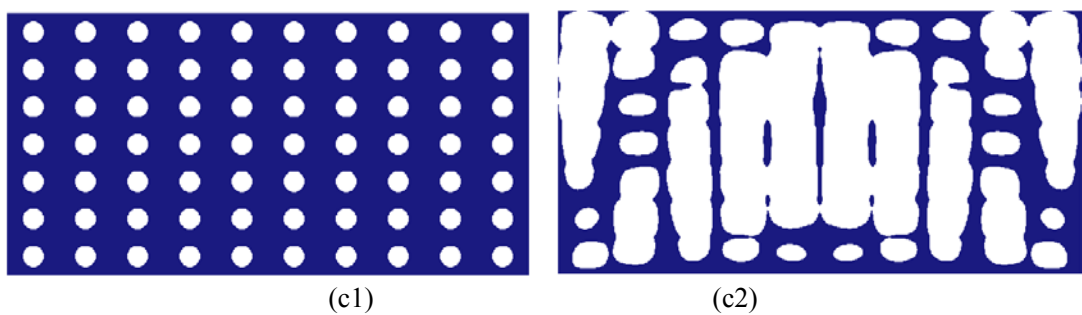


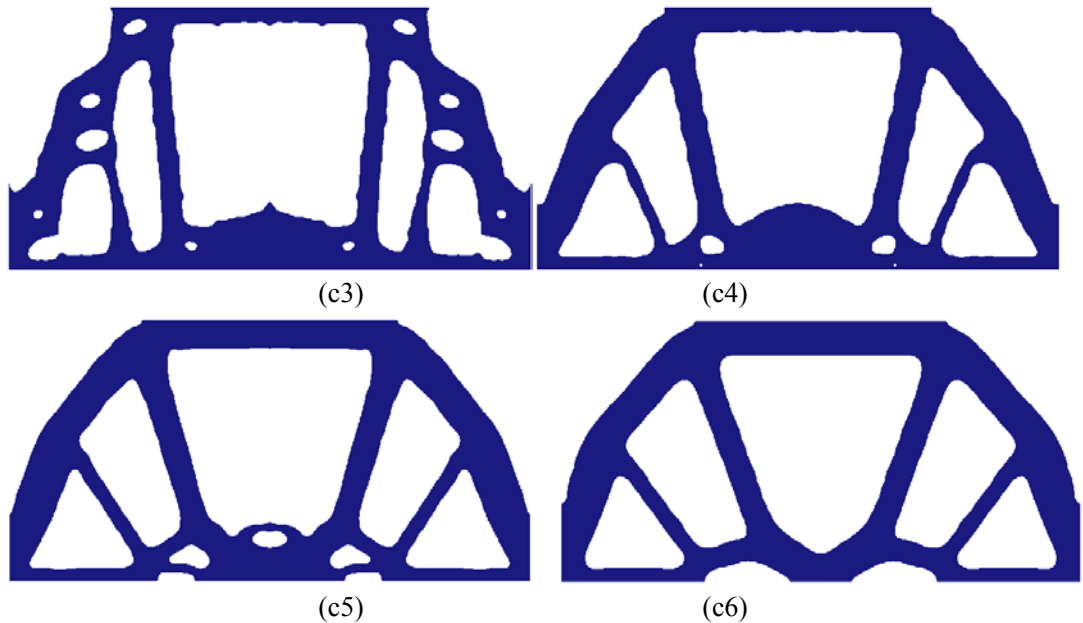




**Figure 4.6 The evolution process of the Mitchell-type structure**

(a1) initial boundary (zero level set) and (b1) correspondent level set surface;  
 (a2-4) and (b2-4) are the boundaries and level set surfaces at iteration 3, 5, 10, and 20;  
 (a5) and (b5) are the optimal configuration and related level set surface.





**Figure 4.7 The evolution process of material distribution for the Mitchell-type structure**

It is easy to find that the optimal structure is characterized by a smooth boundary, which demonstrates that the proposed method is also able to handle the shape and topology optimization simultaneously, which is regarded as the characteristic of an implicit representation using level set methods (Wang, Wang et al. 2003; Allaire, Jouve et al. 2004).

The convergent histories of the objective value (structural strain energy) and the volume constraint over the iterations are shown in Figure 4.8. The iterative design procedure is converged after 109 iterations. The structural strain energy rapidly decreases from over 400 N.m to below 100 N.m after 20 iterations. The evolvement of the structural topology is completed within the first 20 iterations, and the structural strain energy is reduced to 93.52 N.m. The volume constraints are conservative retained at 40%.

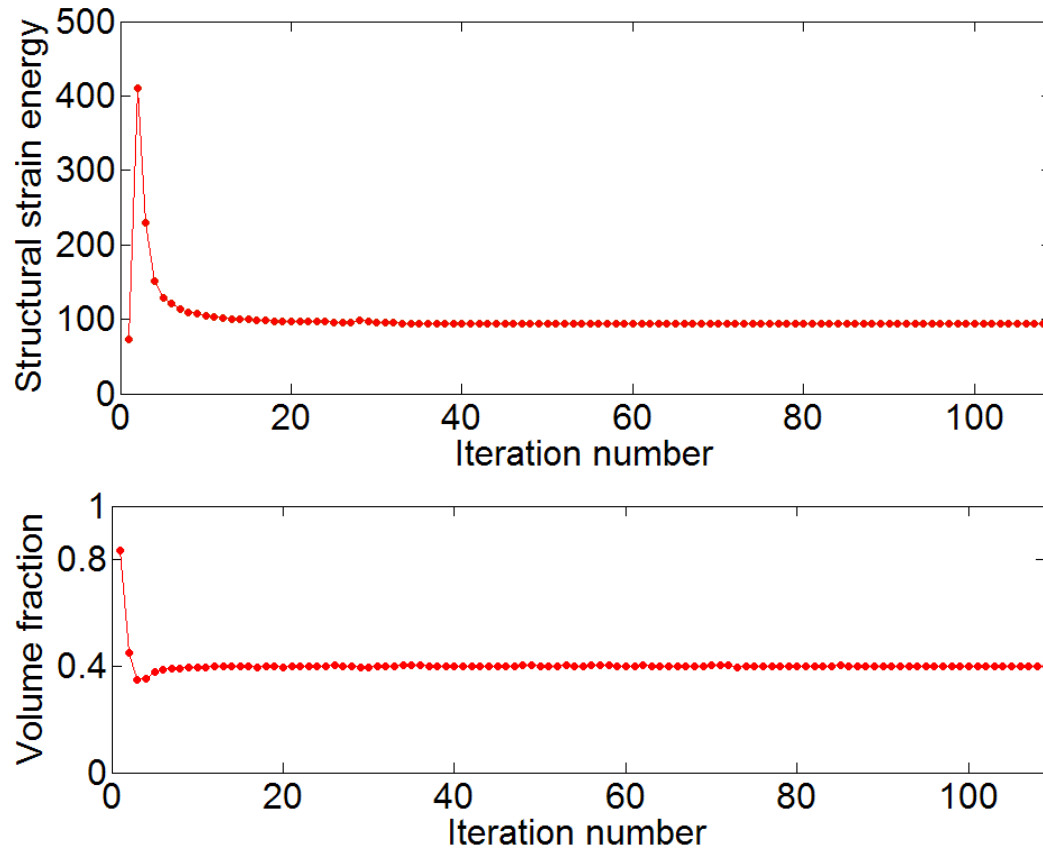
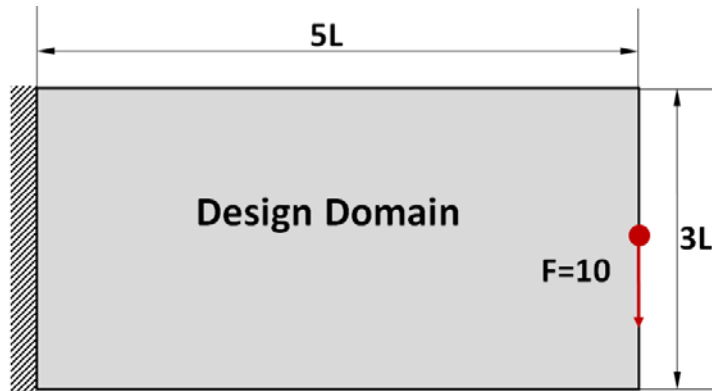


Figure 4.8 The convergent histories of objective and volume constraint

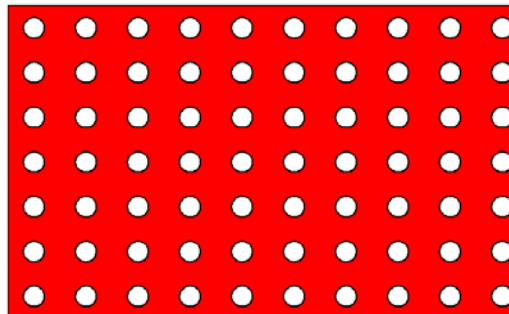
#### 4.4.2 Cantilever Beam A

The second example is a short cantilever beam, as shown in Figure 4.9. The design domain of the cantilever beam has an aspect ratio of 5:3 and is discretized with  $100 \times 60$  quadrilateral elements. The left side of the domain is fixed as the Dirichlet boundary while the right side is treated as a non-homogenous Neumann boundary with a concentrated force  $F=10$  vertically applied at the center point. The given artificial material is assumed with a Young's modulus  $E = 1$  and Poisson's ratio  $\nu = 0.3$ . The assumed volume fraction is 30%.

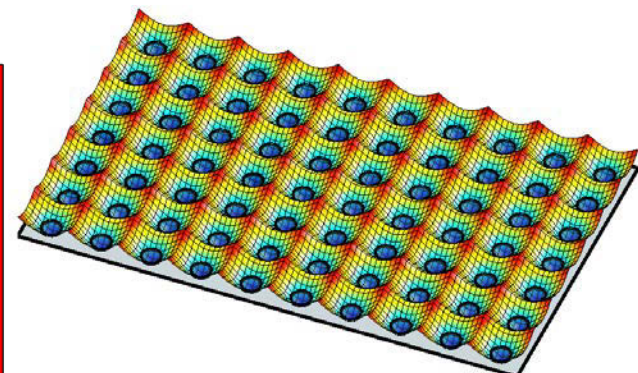


**Figure 4.9 Design domain of the cantilever beam**

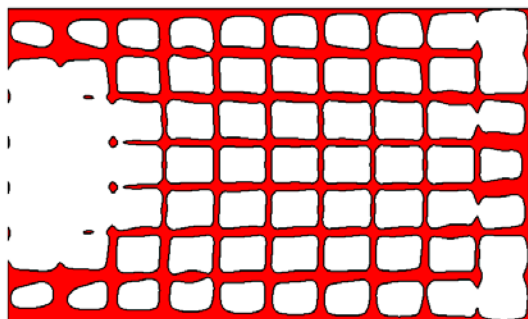
The initial design boundary and corresponding level set surface are given in Figure 4.10 (a) and (b). The contours denoting the history of the design boundary changes and the corresponding level set surfaces during the evolution are given in Figure 4.10 (a1-4) and (b1-4), and the optimal configuration and related level set surface are separately shown in Figure 4.10 (a5) and (b5). The evolution of material distributions are shown in Figure 4.11.



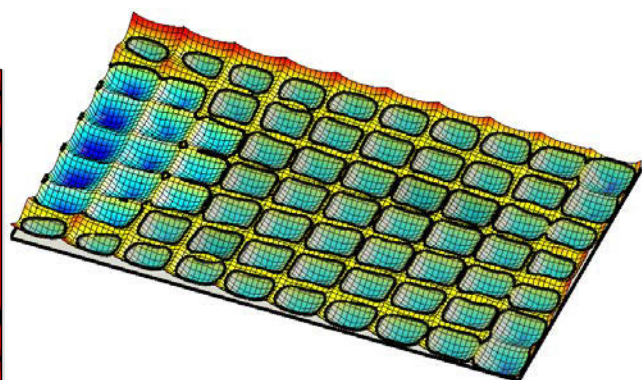
(a0)



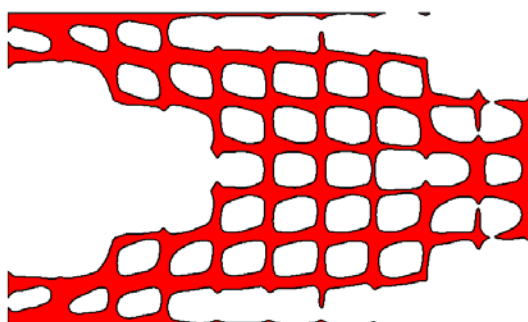
(b0)



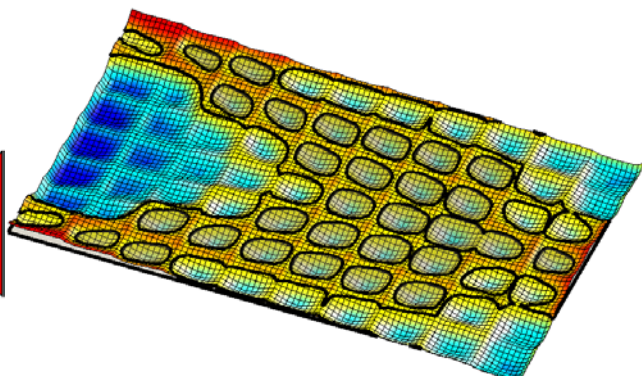
(a1)



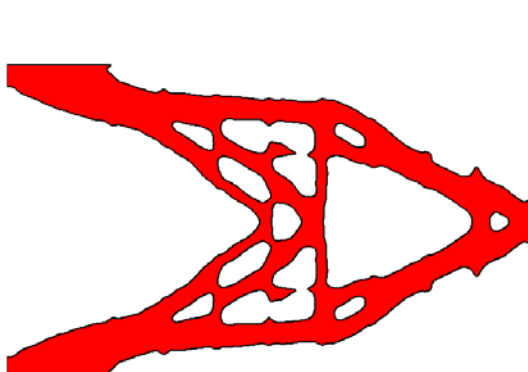
(b1)



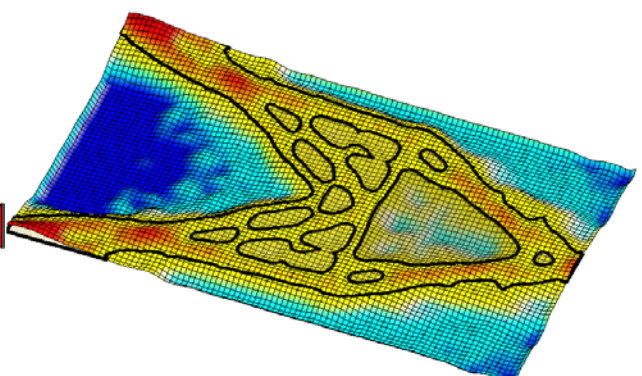
(a2)



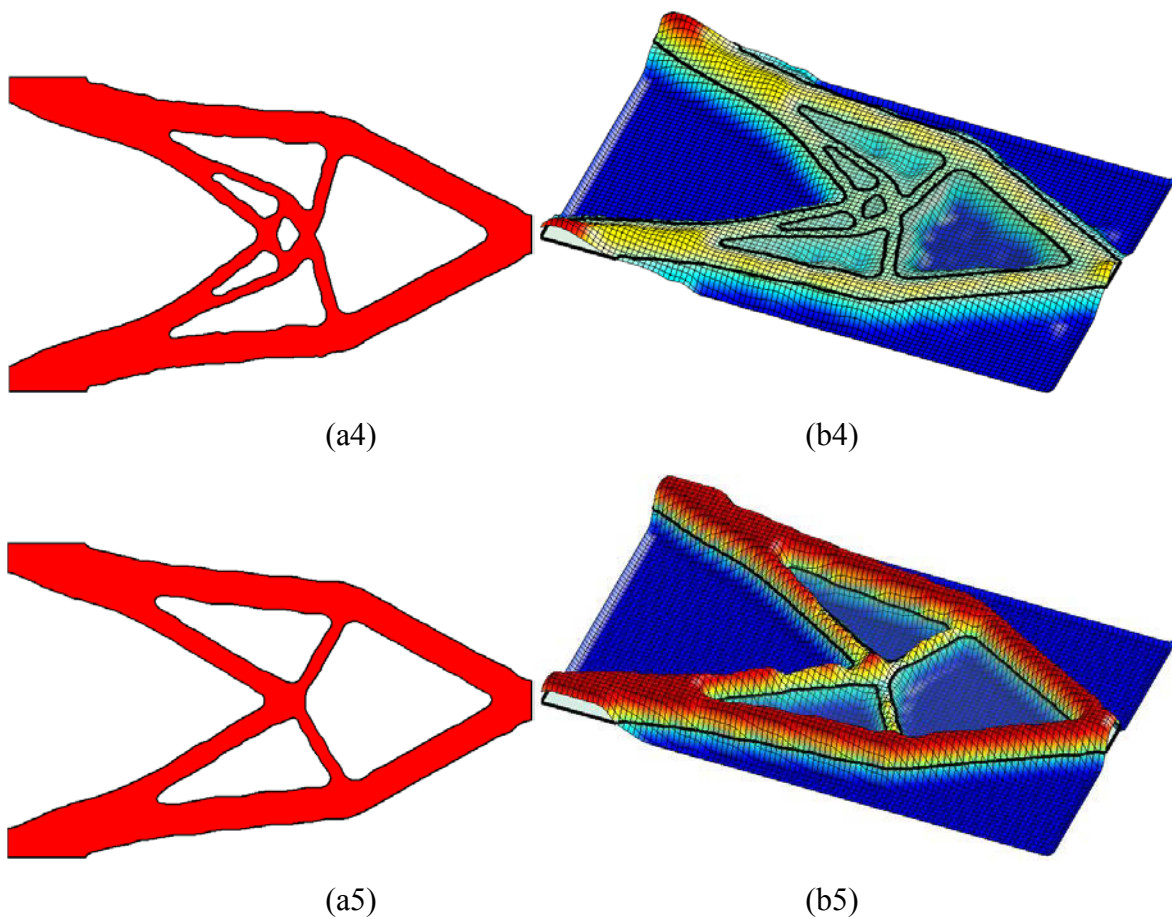
(b2)



(a3)

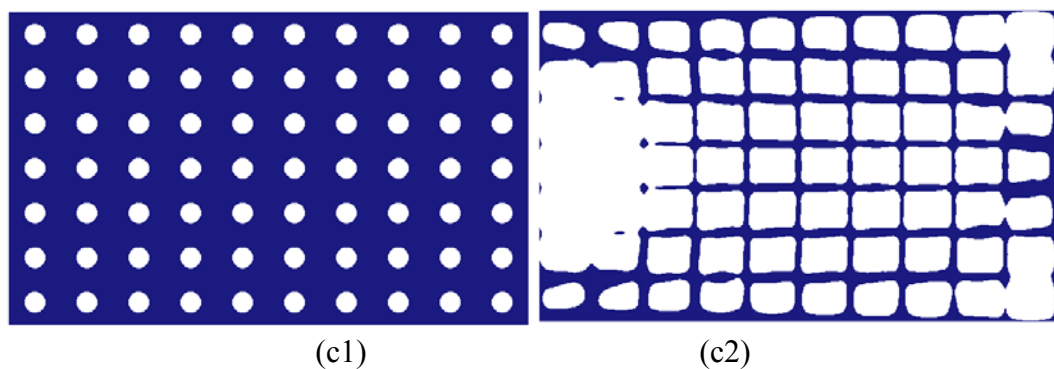


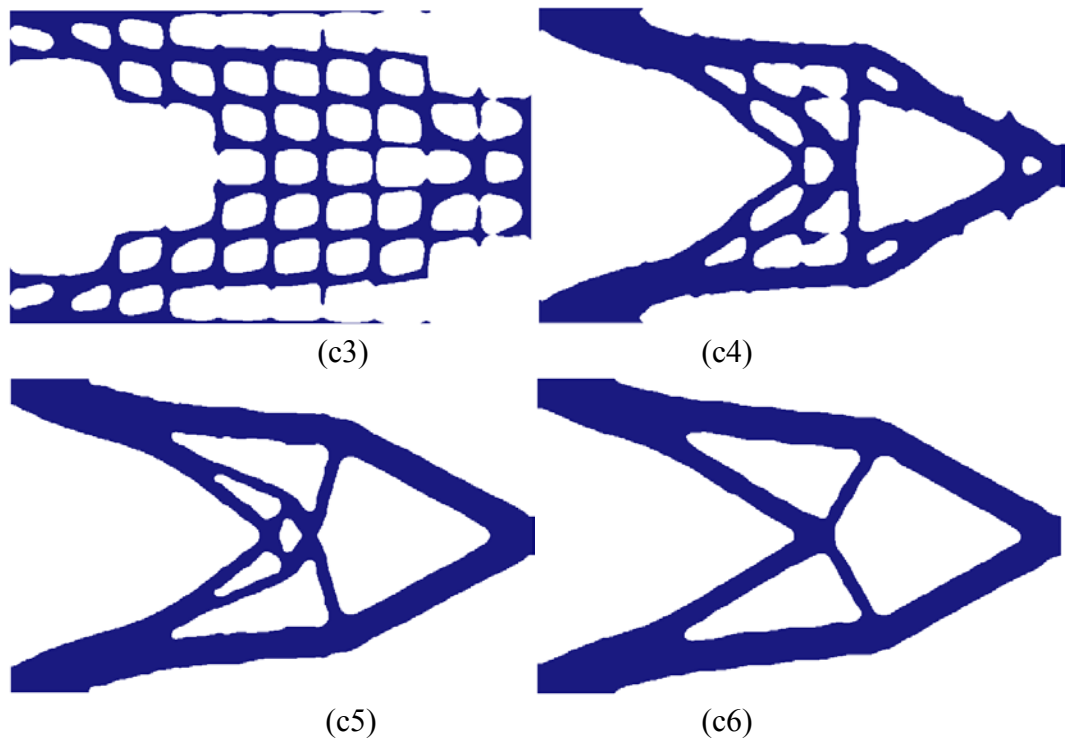
(b3)



**Figure 4.10 The evolution process of cantilever beam**

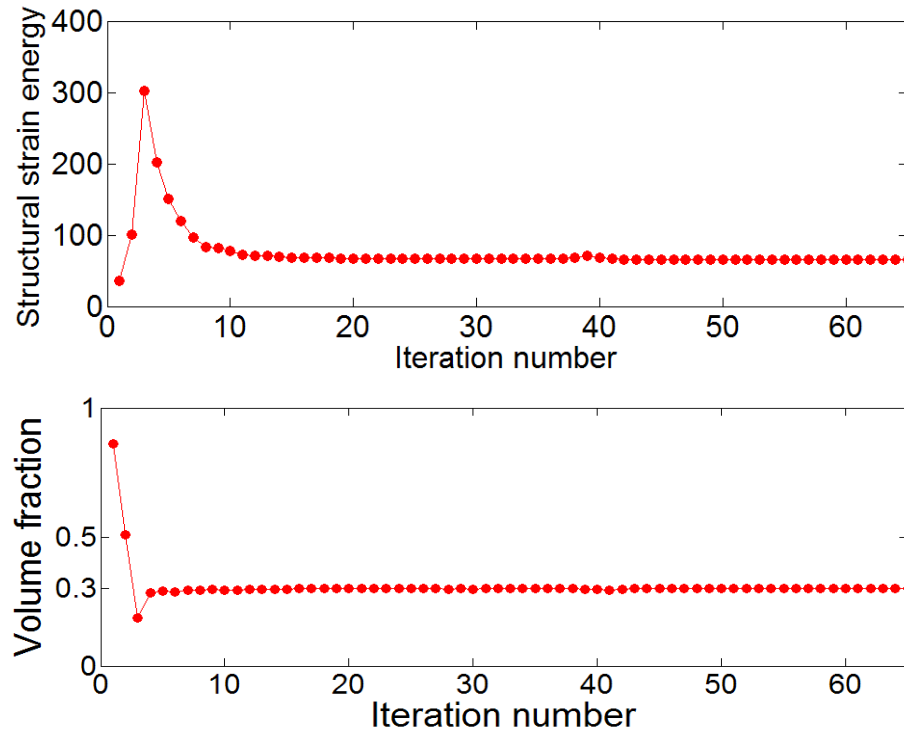
(a1) initial boundary(zero level set) and (b1) correspondent level set surface;  
(a2-4) and (b2-4) are the boundaries and level set surfaces at iteration 3, 5, 10, and 20;  
(a5) and (b5) are the optimal configuration and related level set surface.





**Figure 4.11 The evolution process of material distribution for cantilever beam**

The convergent histories of the structural strain energy and the volume constraint over the iterations are shown in Figure 4.12. The iterative design procedure is repeated until the change in each design variable from step to step is lower than  $10^{-4}$ . It can be seen that the objective value increases from 0 to 3 iterations due to the violation of the volume constraint at the beginning stage. After that, the structural strain energy rapidly decreases from over 300 to lower than 70 after 65 iterations. The evolvement of the structural topology is completed within the initial 15 iterations, and the structural strain energy is reduced to 65.47. The volume constraints are conservative.



**Figure 4.12 The convergent histories of objective and volume constraint**

Figure 4.13 to 4.16 display the optimized topologies by discretizing the design domain with different mesh levels:  $80 \times 58$  and  $140 \times 84$ , respectively. From the comparison, despite the refinement of mesh level, the topology designs are almost the same, which means the proposed interpolation method is a mesh independency solution. The iteration numbers increase with the higher mesh level. As a unique feature of an implicit representation using LSMs, the resulting designs under different refinement of mesh level are characterized by smooth boundaries and distinct interfaces.

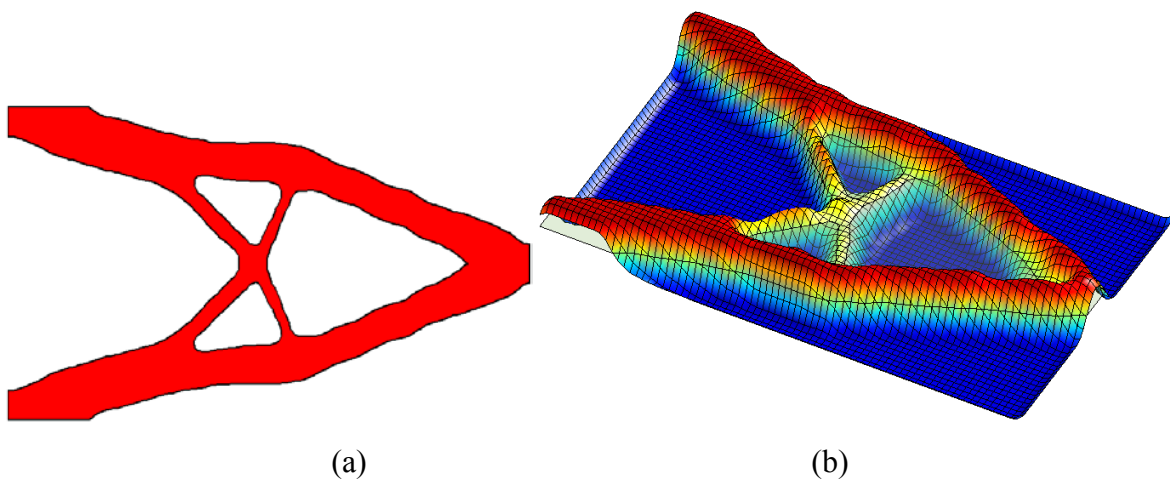


Figure 4.13 (a) Optimal configuration and (b) level set surface with mesh  $80 \times 48$

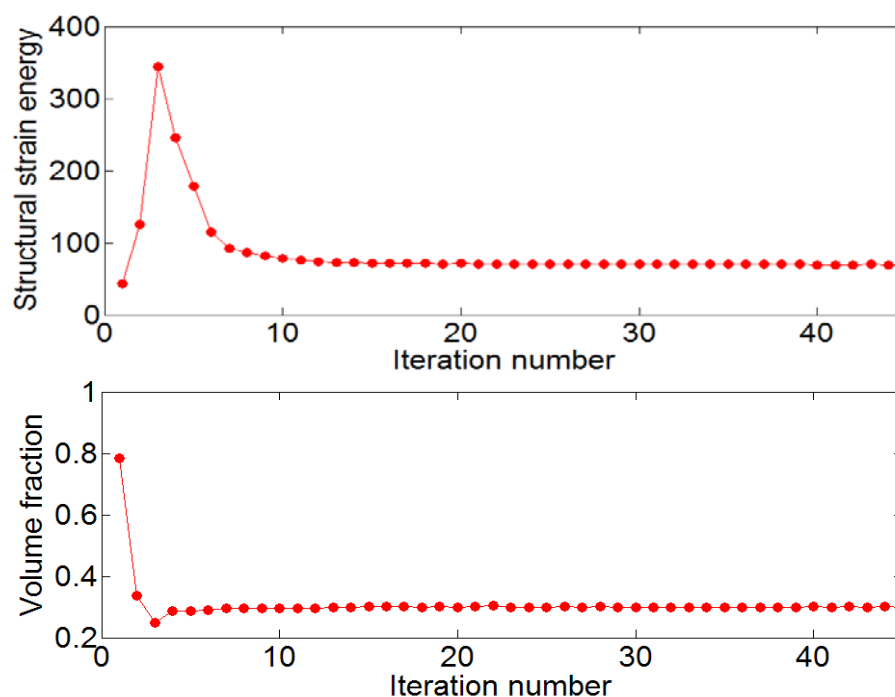
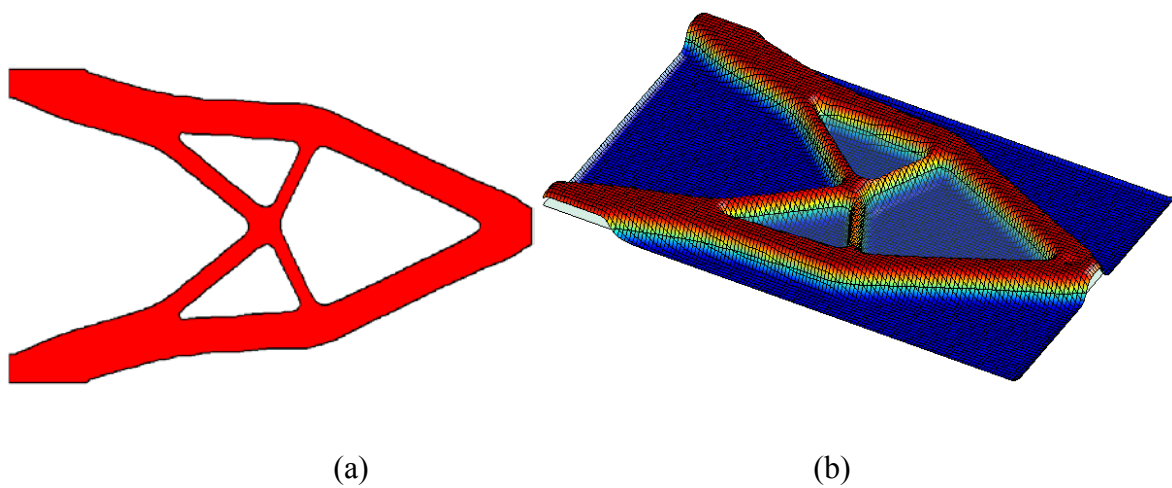
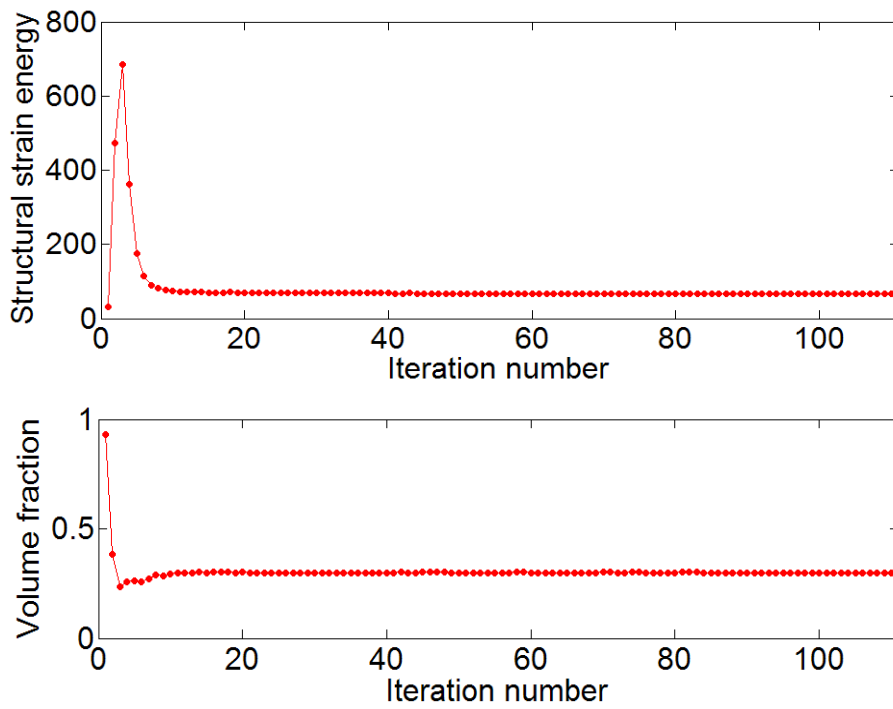


Figure 4.14 The convergent histories with mesh  $80 \times 48$



**Figure 4.15 (a) Optimal configuration and (b) level set surface with mesh  $140 \times 84$**



**Figure 4.16 The convergent histories with mesh  $140 \times 84$**

### 4.4.3 Cantilever Beam B

Another cantilever beam problem is investigated as the third numerical example. The beam has an aspect ratio of 2:1 corresponding to length over height as shown in Figure 4.17. The left side of the domain is fixed as the Dirichlet boundary while a vertically force  $F=1\text{KN}$  is applied to at the bottom-right corner of the structure. The design domain is discretized with  $100\times 50$  quadrilateral elements. The given material is steel with a Young's modulus  $E = 210\text{GPa}$  and Poisson's ratio  $\nu = 0.3$ . The assumed volume fraction is 50%.

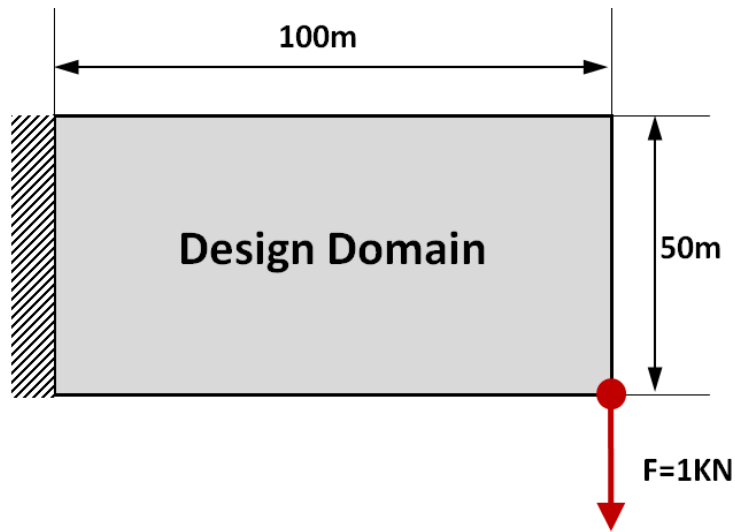
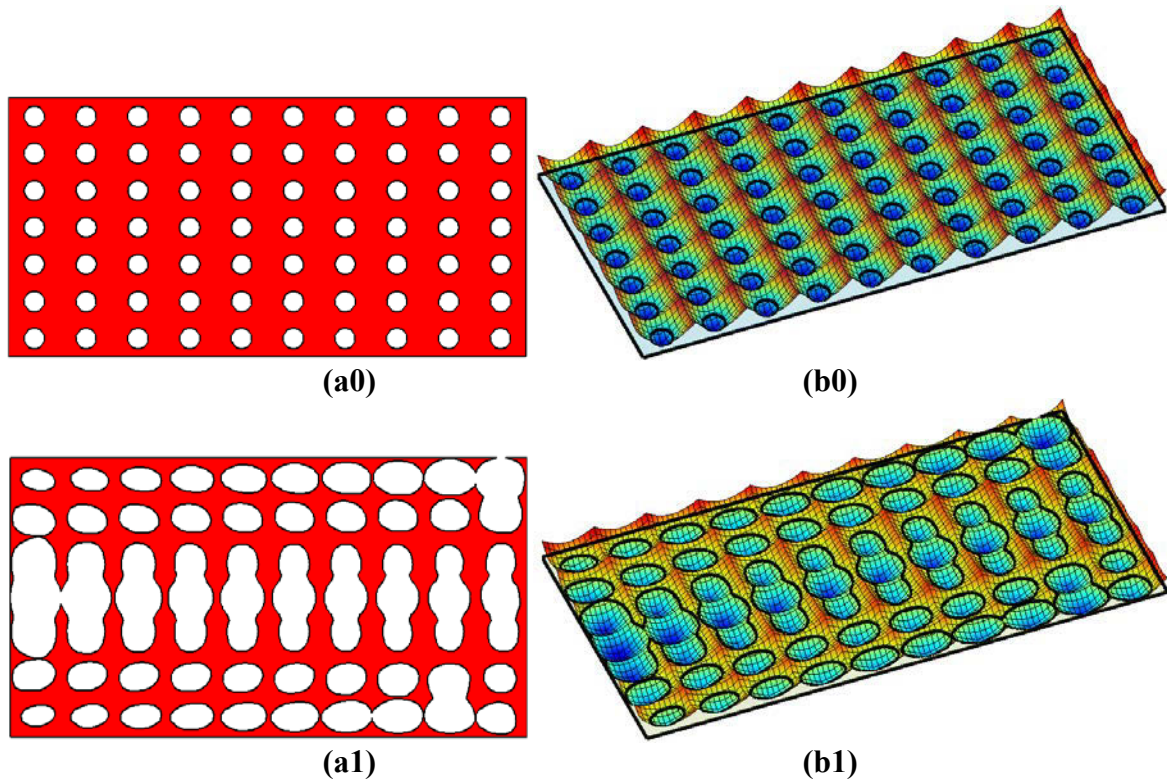


Figure 4.17 Design domain of cantilever beam

The initial design boundary and corresponding level set surface are given in Figure 4.18 (a) and (b). The contours denoting the history of the design boundary changes and the corresponding level set surfaces during the evolution are given in Figure 4.18 (a1-4) and (b1-4), and the optimal configuration and related level set surface are separately shown in Figure 4.18 (a5) and (b5). The evolution of material distributions is shown in Figure 4.19.

The numerical examples presented above are the typical structural design problems to find a structure with minimum strain energy for a given volume fraction: 50%. It should be noted that the volume fraction is normally set based on the design requirement. For the material distribution methods, once very low volume fraction is demanded, very fine discretization meshes are required, as the structures break up if coarse meshes are used. However, for boundary based method, for comparatively small volume fractions, the method can still predict the lay-out of truss like structures that give a good prediction of the optimal connectivities and the optimal location of nodal points.



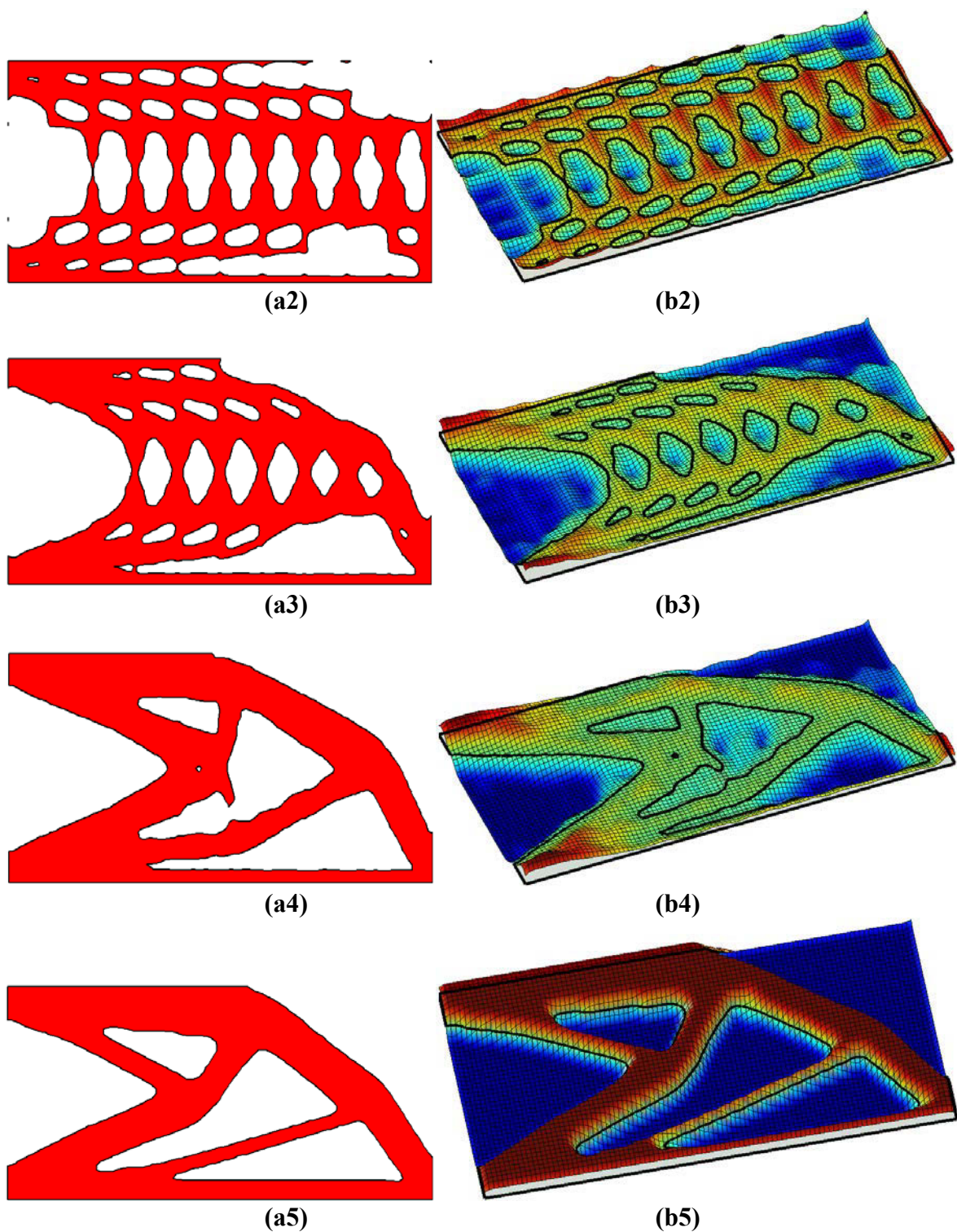


Figure 4.18 The evolution process of cantilever beam

(a1) initial boundary (zero level set) and (b1) correspondent level set surface;  
 (a2-4) and (b2-4) are the boundaries and level set surfaces at iteration 3, 5, 10, and 20;  
 (a5) and (b5) are the optimal configuration and related level set surface.

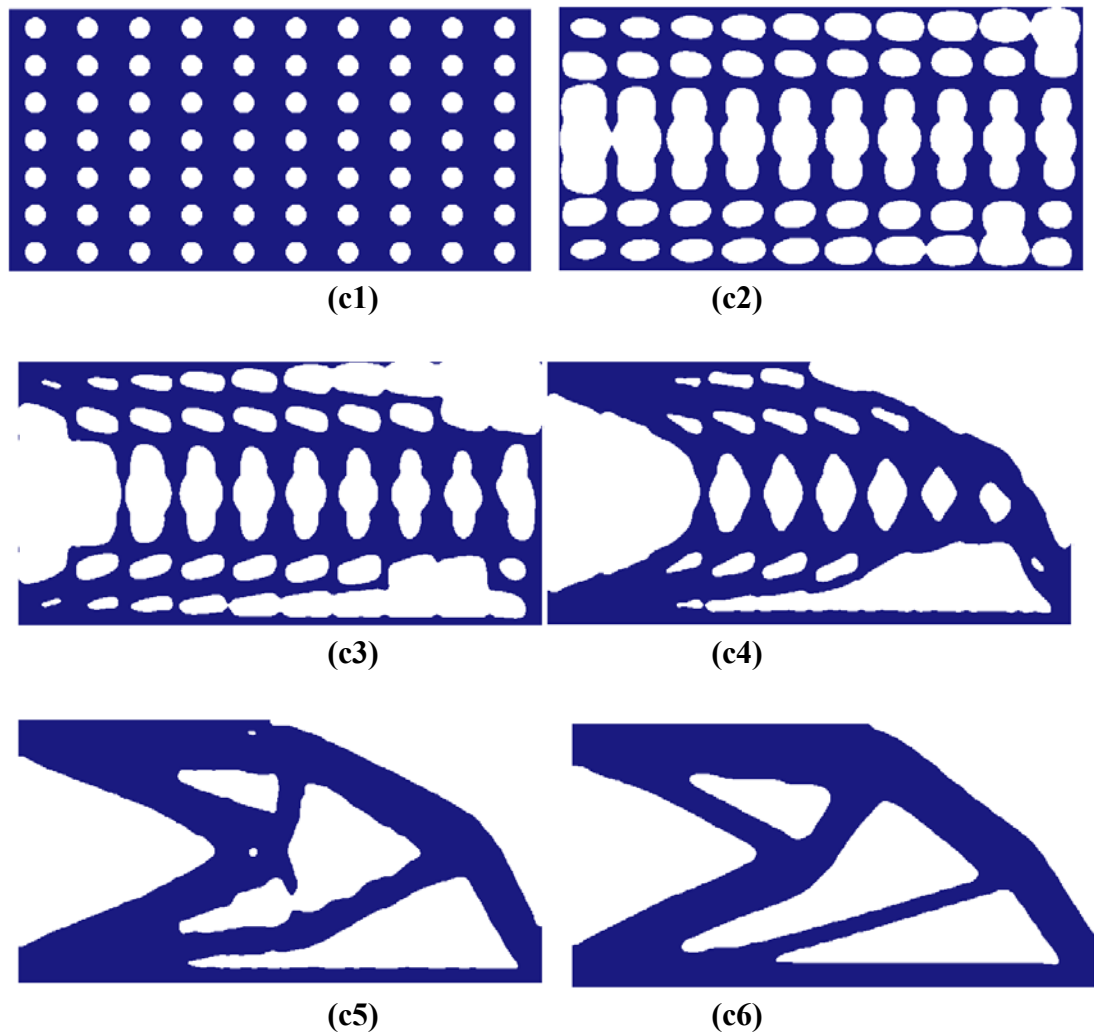
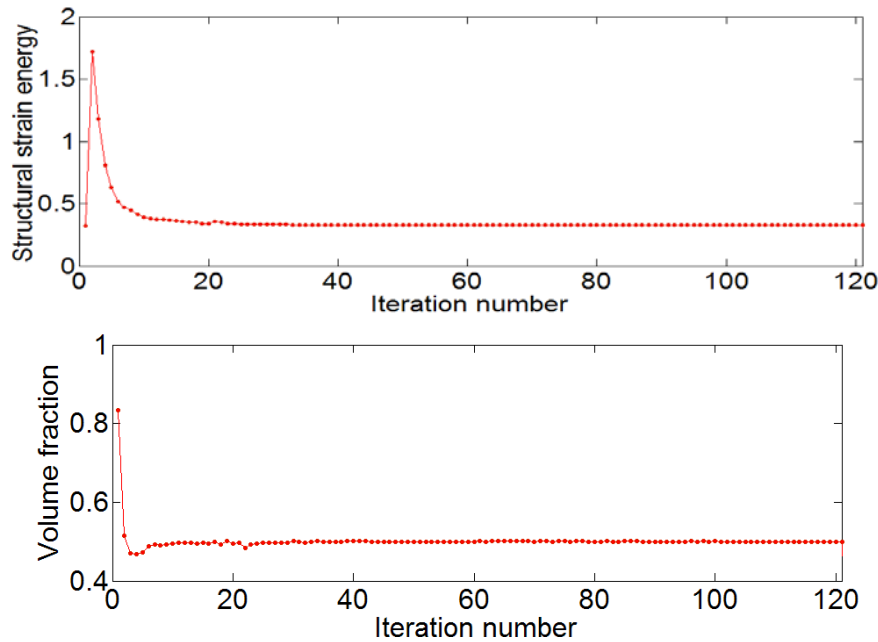


Figure 4.19 The evolution process of material distribution for cantilever beam

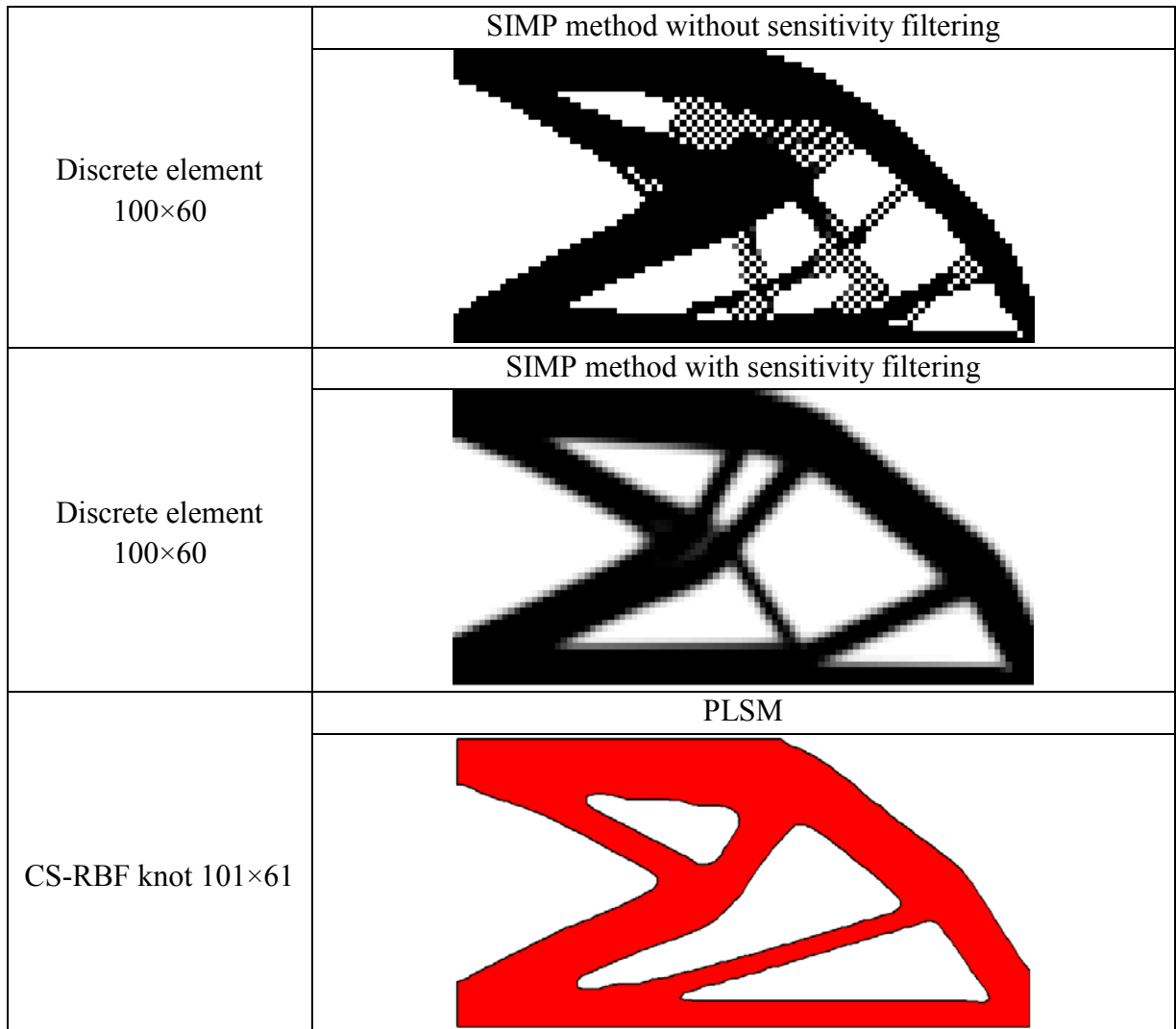


**Figure 4.20 The convergent histories of objective and volume constraint**

The convergent histories of the objective value (structural strain energy) and the volume constraint over the iterations are shown in Figure 4.20. The iterative design procedure is converged after 122 iterations. The structural strain energy rapidly decreases from over 1.5 N.m to below 0.4 N.m after 20 iterations. The evolvement of the structural topology is completed within the initial 20 iterations, and the structural strain energy is reduced to 0.3286 N.m. The volume constraints are conservative retained at 50%.

Figure 4.21 displays the optimized topology plots using the PLSM and conventional SIMP method with and without sensitivity filtering (Sigmund 2001), respectively. It can be seen that the results obtained via the SIMP method without sensitivity filtering suffer from the checkerboard patterns and “islanding” phenomenon, while these numerical instabilities are eliminated with the sensitivity filtering by using the traditional SIMP method. As for the

PLSM, this solution is able to provide the design boundary with enhanced smoothness and eliminate checkerboard patterns and “islanding” phenomenon without any filtering.



**Figure 4.21 Optimized topologies comparison with different optimization techniques**

# 5 Design of Mechanical Metamaterials

Metamaterials are artificially engineered composites consisting of arrays of micro- and nanostructured under periodicity, designed to have unusual properties that are not easily found in nature. In this thesis, a topological shape optimization method for design of metamaterials will be proposed using a new multiphase level set method (MPLSM). The homogenization method is applied to evaluate the effective macroscopic properties of a periodic composite material, while the MPLSM will be utilized to implement shape and topology evolutions of the microstructure. Firstly, a multi-phase level set representation model is established to describe the boundaries of the multi-phase microstructure using a combination of all level set functions, without overlaps and empties. Secondly, a set of CS-RBFs is employed to interpolate each implicit level set function, which will transfer the original H-J PDE into a system of algebraic equations, as well as the most difficult topology optimization into an easiest “size” optimization. The only unknowns of the size optimization are the expansion coefficients of the interpolant, which are defined as the design variables to be updated using a more efficient optimization algorithm. Finally, several typical numerical examples are used to demonstrate the effectiveness of the proposed method for designing metamaterials with expected effective properties.

## 5.1 Multi-Phase Level Set Method

In LSMs, the design boundary is embedded implicitly as the zero level set of a higher-dimensional level set function (e.g. 2D boundary to 3D surface) (Osher and Sethian 1988; Sethian 1999). A LSF  $\Phi(\mathbf{x})$  with Lipschits continuity is defined over a reference domain  $D$ .

---

For a multiphase design problem,  $M$  LSFs are used to describe  $M+1$  material phases including one void phase and  $M$  solid phases.

$$\begin{cases} \Phi^m(\mathbf{x}) > 0 & \forall \mathbf{x} \in \Omega^m \setminus \Gamma^m \\ \Phi^m(\mathbf{x}) = 0 & \forall \mathbf{x} \in \Gamma^m \\ \Phi^m(\mathbf{x}) < 0 & \forall \mathbf{x} \in D \setminus (\Omega^m \cup \Gamma^m) \end{cases} \quad (m = 1, 2, \dots, M) \quad (5.1)$$

Where the reference domain  $D$  includes all admissible shapes of;  $\Omega^m$  denotes the domain with positive value of the  $m$ th level set function,  $\Gamma^m$  is the boundary of the  $m$ th level set function.

In PLSM, the CS-RBFs are introduced to interpolate the higher-dimensional level set function. The level set function can be described by the interpolation of the CS-RBFs at their pre-specified knots over the whole design domain, as

$$\Phi^m(\mathbf{x}, t) = \boldsymbol{\varphi}(\mathbf{x})^T \boldsymbol{c}^m(t) = \sum_{i=1}^N \varphi_i(\mathbf{x})^T c_i^m(t) \quad (5.2)$$

with a vector of the shape functions (CS-RBFs)

$$\boldsymbol{\varphi}(\mathbf{x}) = [\varphi_1(\mathbf{x}), \varphi_2(\mathbf{x}), \dots, \varphi_N(\mathbf{x})]^T \in \mathbb{R}^N \quad (5.3)$$

and the expansion coefficient vector

$$\boldsymbol{c}^m(t) = [c_1^m(t), c_2^m(t), \dots, c_N^m(t)]^T \in \mathbb{R}^N \quad (5.4)$$

where  $N$  is the total number of the knots in the design domain.

The interpolating of CS-RBFs leads to a separation scheme of the space and time. The shape functions are only spatial function and the generalized expansion coefficients are only time dependent. Thus, the decoupling of the time and space terms of the H-J PDE is

$$\varphi(\mathbf{x})^T \dot{\mathbf{c}}^m(t) - \mathbf{v}_n^m \left| \nabla \varphi(\mathbf{x})^T \mathbf{c}^m(t) \right| = 0 \quad \text{where } \dot{\mathbf{c}}^m(t) = \frac{d\mathbf{c}^m(t)}{dt} \quad (5.5)$$

The normal velocity  $\mathbf{v}_n^m$  is related to the time derivative of the expansion coefficients as

$$\mathbf{v}_n^m = \frac{\varphi(\mathbf{x})^T \dot{\mathbf{c}}^m(t)}{\left| \nabla \varphi(\mathbf{x})^T \mathbf{c}^m(t) \right|}, \text{ where } \mathbf{v}_n^m = \frac{\varphi(\mathbf{x})^T \dot{\mathbf{c}}^m(t)}{\left| \nabla \varphi(\mathbf{x})^T \mathbf{c}^m(t) \right|} \quad (5.6)$$

It is noted that all the terms involved in  $\mathbf{v}_n^m$  are evaluated at the knots over the whole design domain, thus, the normal velocity  $\mathbf{v}_n^m$  is actually extended to the entire design domain. In this way, the H-J PDE has been parameterized into a system of algebraic equations with a set of unknown expansion coefficients  $\mathbf{c}^m(t)$  (the design variables). Hence, the propagation of the LSFs is just a problem of finding  $\mathbf{c}^m(t)$  using optimization algorithms.

To solve the multi-phase design problem using the parametric level set method, we will propose a level set representation model for the multiphase design domain of microstructure based on the concept in (Sigmund and Torquato 1997; Gibiansky and Sigmund 2000), in which each individual phase will be represented through a simple artificial mixture assumption of all level set functions.

## 5.2 Multi-Phase Material Representation Model

Based on the previous work (Bendsøe and Sigmund 1999), the multimaterial level set model of structures will be extended to the design of materials. In the multi-phase level set representation model, each material phase is represented by a combination of different level set functions. For instance, with respect to the composite material with one, two or three solid material phases, the elastic stiffness  $\mathbf{C}(\mathbf{x})$  at any point  $\mathbf{x}$  can be calculated by

$$\begin{aligned}
 \mathbf{C}^{(1)}(\mathbf{x}, \Phi) &= H(\Phi^1) \mathbf{C}^1, \\
 \mathbf{C}^{(2)}(\mathbf{x}, \Phi) &= H(\Phi^1)(1 - H(\Phi^2)) \mathbf{C}^1 + H(\Phi^1)H(\Phi^2) \mathbf{C}^2, \\
 \mathbf{C}^{(3)}(\mathbf{x}, \Phi) &= H(\Phi^1)(1 - H(\Phi^2)) \mathbf{C}^1 + H(\Phi^1)H(\Phi^2)(1 - H(\Phi^3)) \mathbf{C}^2 + H(\Phi^1)H(\Phi^2)H(\Phi^3) \mathbf{C}^3, \\
 &\dots
 \end{aligned} \tag{5.7}$$

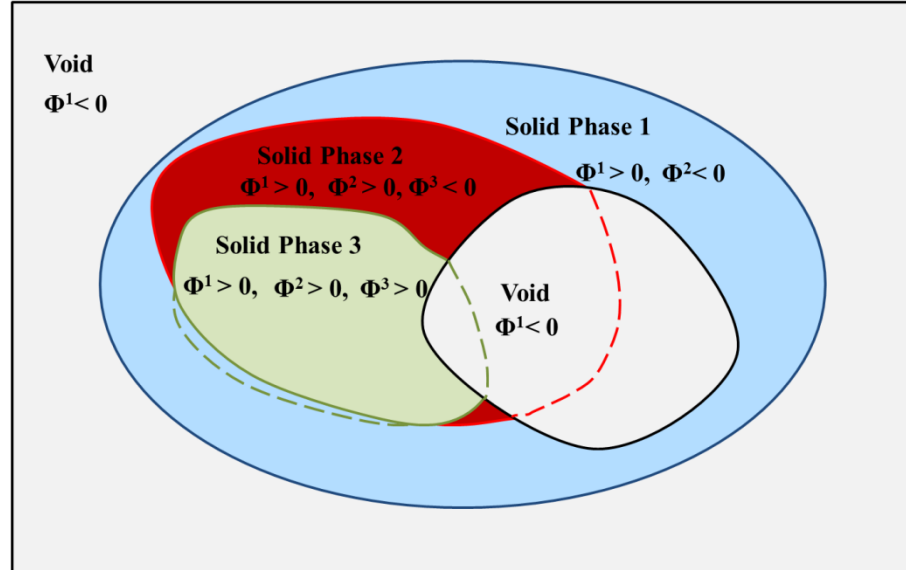
where  $H(\Phi^l)$  is the Heaviside function corresponding to the  $m^{\text{th}}$  level set function. For a case with  $M$  solid phase materials, the elastic stiffness  $\mathbf{C}(\mathbf{x})$  can be obtained in a similar way by following the above model.

Since the thermal expansion  $\boldsymbol{\alpha}(\mathbf{x})$  is only related to the mixture of materials, it will have the form as

$$\begin{aligned}
 \boldsymbol{\alpha}^{(1)}(\mathbf{x}, \Phi) &= \boldsymbol{\alpha}^1, \\
 \boldsymbol{\alpha}^{(2)}(\mathbf{x}, \Phi) &= (1 - H(\Phi^2)) \boldsymbol{\alpha}^1 + H(\Phi^2) \boldsymbol{\alpha}^2, \\
 \boldsymbol{\alpha}^{(3)}(\mathbf{x}, \Phi) &= (1 - H(\Phi^2)) \boldsymbol{\alpha}^1 + H(\Phi^2)(1 - H(\Phi^3)) \boldsymbol{\alpha}^2 + H(\Phi^2)H(\Phi^3) \boldsymbol{\alpha}^3, \\
 &\dots
 \end{aligned} \tag{5.8}$$

As illustrated by the multi-phase level set representation model above, a number of  $M+1$  material phases (including the void phase) can be represented by using  $M$  level set functions.

Based on this multi-phase material representation model, the distribution of multiple materials can be described in the design domain. As given in Figure 5.1, the level set function  $\Phi^1$  is firstly used to distinguish the solid (blue, red and green regions  $\Phi^1 > 0$ ) and the void phase (grey  $\Phi^1 < 0$ ),  $\Phi^2$  is then applied to determine the first material phase (blue region  $\Phi^1 > 0$  and  $\Phi^2 < 0$ ) from the material phases, and  $\Phi^3$  is finally used to identify the second material phase (red region  $\Phi^1 > 0$ ,  $\Phi^2 > 0$  and  $\Phi^3 < 0$ ) and the third material phase (green region  $\Phi^1 > 0$ ,  $\Phi^2 > 0$  and  $\Phi^3 > 0$ ). This multi-phase material representation model has an explicit mathematical expression, which is able to provide a unique and distinct description for each material phase. It guarantees that any point inside the design domain indicates one and only one material phase, without overlaps and empties of different material phases.



**Figure 5.1 Distribution of multi-phase material in the design domain**

## 5.3 Design of Multi-Phase Composites

### 5.3.1 Multi-Phase Material Representation Model

For designing the multi-phase thermoelastic composites, the material are composed by three phases, including two solid phases and one void phases. Via the multi-phase material representation model given in the previous section, the elasticity tensor  $C$  and thermal strain coefficient tensor  $\alpha$  at point  $\mathbf{x}$  for three phase design problem can be written as a combination of the two level set functions  $\Phi^1$  and  $\Phi^2$  as:

$$C_{ijkl}(\mathbf{x}, \Phi) = H(\Phi^1)(1 - H(\Phi^2))C_{ijkl}^1 + H(\Phi^1)H(\Phi^2)C_{ijkl}^2 \quad (5.9)$$

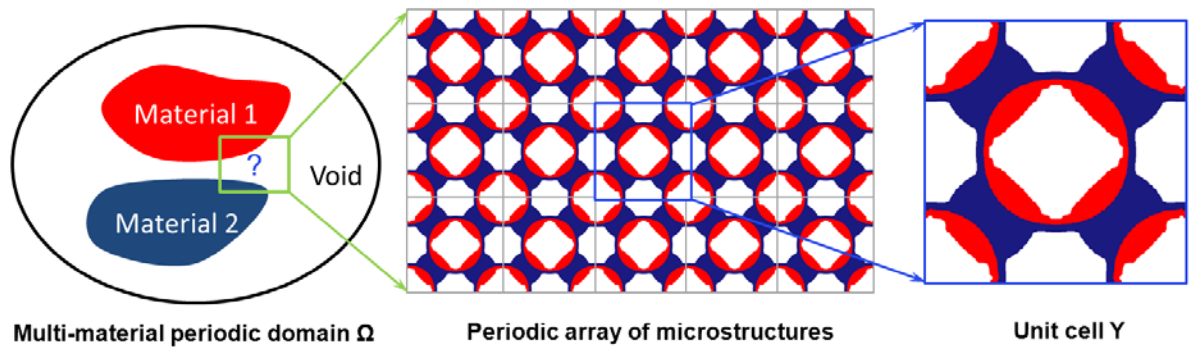
$$\alpha_{ij}(\mathbf{x}, \Phi) = (1 - H(\Phi^2))\alpha_{ij}^1 + H(\Phi^2)\alpha_{ij}^2 \quad (5.10)$$

where  $i, j, k, l = 1, 2, \dots, d$  ( $d$  is the dimension of space). The two solid material phases have different elastic moduli and thermal expansion coefficients, which are described by  $C_{ijkl}^1$  and  $C_{ijkl}^2$ ,  $\alpha_{ij}^1$  and  $\alpha_{ij}^2$ , respectively.

With the discretization of finite elements,  $H(\Phi^1)$  can be used to indicate whether an element is solid or void, namely  $H(\Phi^1)=0$  being a void element while  $H(\Phi^1)=1$  being a solid element. Based on the definition of  $H(\Phi^1)=1$ ,  $H(\Phi^2)$  is further used to distinguish if the solid element is occupied by the solid material 1 or by the solid material 2. Thus, the combination of  $H(\Phi^1)=1$  and  $H(\Phi^1)=0$  represents an element with the solid material 1, and the combination of  $H(\Phi^1)=1$  and  $H(\Phi^2)=1$  is the solid material 2. In this way, each material phase in the design domain can be uniquely represented by the above model.

### 5.3.2 Calculation of Effective Material Properties

Homogenization theory is based on the asymptotic expansion of the governing equation, enabling a separation of the macro- and microscopic length scales, so as to extract homogeneous effective material properties from heterogeneous media. To evaluate the effective properties of the composite using the homogenization method (Guedes and Kikuchi 1990), we assume that (1) the metamaterials consist of an assembly of microstructures (unit cell), as shown in Figure 5.2; (2) the size of the microstructure is much smaller than the buck composite to allow scale-decomposition; and (3) the effective homogenized property of the composite can be predicted by a single unit cell.



**Figure 5. 2 Schematic of multi-phase periodic structures with microstructures**

In this study, the topological shape optimization will be performed within the unit cell  $Y$  that is regarded as the design domain. The period  $Y$  is assumed to be very small in comparison with the dimension of the overall domain  $\Omega$  of the medium. According to the theory of homogenization, the effective homogenized properties of the composite material can be computed as follows

$$C_{ijkl}^H = \frac{1}{|Y|} \int_Y C_{pqrs} (\varepsilon_{pq}^{0(ij)} - \varepsilon_{pq}^{*(ij)}) (\varepsilon_{rs}^{0(kl)} - \varepsilon_{rs}^{*(kl)}) dY \quad (5.11)$$

$$\beta_{kl}^H = \frac{1}{|Y|} \int_Y C_{pqrs} (\alpha_{pq} - \varepsilon_{pq}^\alpha) (\varepsilon_{rs}^{0(kl)} - \varepsilon_{rs}^{*(kl)}) dY \quad (5.12)$$

$$\alpha_{ij}^H = (C_{ijkl}^H)^{-1} \beta_{kl}^H \quad (5.13)$$

where  $C_{ijkl}^H$  is the effective elasticity tensor,  $\beta_{kl}^H$  is the effective thermal stress coefficient tensor, and  $\alpha_{ij}^H$  is the effective thermal strain coefficient tensor;  $|Y|$  is the volume (area) of the cell;  $C_{pqrs}$  is the locally varying elasticity tensor;  $\varepsilon^0$  is the prescribed strain fields (unit strain in the horizontal direction; unit strain in vertical direction; unit shear strain for 2D cases).

In the above equations:

(1) The locally varying strain fields  $\varepsilon_{rs}^{*(kl)}$  are defined by

$$\varepsilon_{rs}^{*(kl)} = \varepsilon_{rs}^* (\chi^{kl}) = \frac{1}{2} \left( \frac{\partial \chi_r^{kl}}{\partial y_s} + \frac{\partial \chi_s^{kl}}{\partial y_r} \right) \quad (5.14)$$

in which the displacement fields  $\chi^{kl}$  can be obtained by solving the following equation

$$\int_Y C_{pqrs} \varepsilon_{pq}(v) \varepsilon_{rs}^* (\chi^{kl}) dY = \int_Y C_{pqrs} \varepsilon_{pq}(v) \varepsilon_{rs}^{0(kl)} dY, \quad \forall v \in \bar{U}(Y) \quad (5.15)$$

where  $v$  is the virtual displacement field.

- (2) The locally varying thermal strain tensor  $\alpha_{pq}$  corresponds to a unit strain caused by a unit thermal load, and the strain fields  $\varepsilon_{pq}^\alpha$  based on the displacement fields are defined by

$$\varepsilon_{pq}^\alpha = \frac{1}{2} \left( \frac{\partial \Lambda_p}{\partial y_q} + \frac{\partial \Lambda_q}{\partial y_p} \right) \quad (5.16)$$

Where  $\Lambda$  are the displacement fields in the unit cell, which can be obtained by solving the following equations for a unit thermal load, as follows:

$$\int_Y C_{ijpq} \varepsilon_{ij}(\tau) \varepsilon_{pq}^\alpha(\Lambda) dY = \int_Y C_{ijpq} \varepsilon_{ij}(\tau) \alpha_{pq} dY, \quad \forall \tau \in \bar{U}(Y) \quad (5.17)$$

Where  $\tau$  is a virtual temperature field,  $\bar{U}$  is the kinematically admissible displacement space with  $Y$ -period.

### 5.3.3 Numerical Implementation

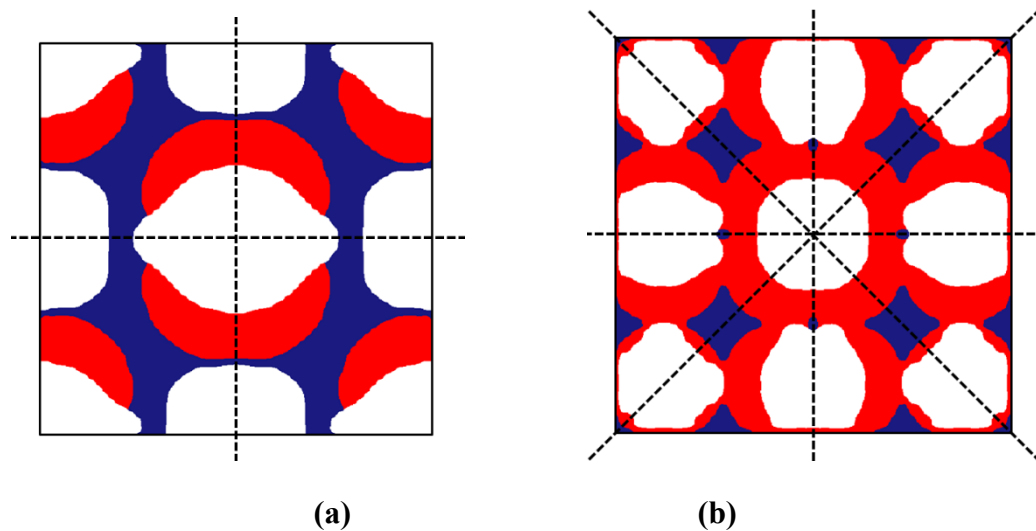
The design problem is formulated by selecting an appropriate objective function under a lower bound on the stiffness. For thermoelastic composite consisting of periodic microstructures, it is important to consider symmetry to each unit cell, which include either geometry (e.g. square symmetry) or material elasticity (e.g. orthotropy or isotropy) symmetry. The periodic boundary conditions of the design domain can be achieved by using the elimination scheme (Andreassen and Andreasen 2014), ensuring the orthotropy of the materials. Furthermore, this paper will consider the speciallyorthotropic (e.g. design domain with 2 symmetry axes in Figure 5.3(a)) and balanced orthotropic (e.g. design domain with 4 symmetry axes in Figure 5.3(b)) materials, which can be obtained by directly specifying the geometrical symmetries. It is noted that the square symmetry of the unit cell is equal to the

balanced material orthotropy of linear elastic structures (Paulino et al. 2009). More details about geometry symmetry and material property symmetry for orthotropy and isotropy refer to (Sigmund and Torquato 1996; Paulino et al. 2009). In the following examples, the design domain is discretized by a number of  $60 \times 60 = 3600$  four-node bilinear finite elements. It should be noted that, for the cell problem shown in this chapter, the thermoelastic properties are considered as the design objectives, thus, it is unnecessary to introduce any loading/boundary conditions on in the periodic cell.

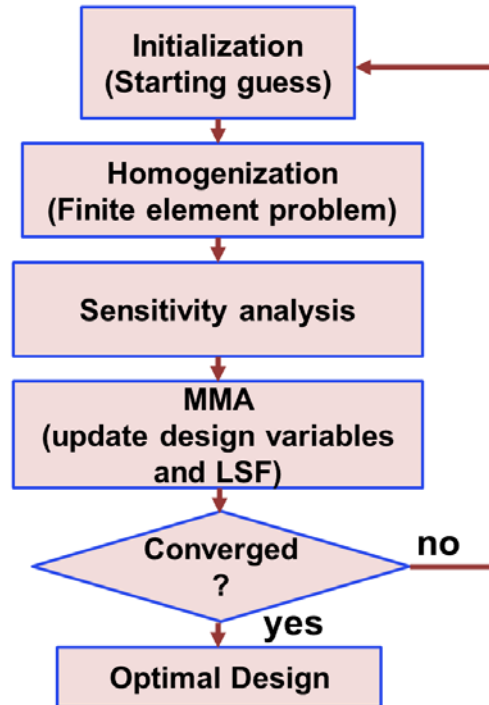
Since the FEM is difficult to accurately evaluate the strain for those elements crossed by the level set boundary (Makhija and Maute 2013), additional numerical schemes are often required. In this study, the “ersatz” material model (Allaire et al. 2004) has been widely used to compute the strain of the elements cut by the boundary. In the numerical homogenization, the equilibrium equations are solved using the finite element method to calculate the effective material properties.

The flowchart of the numerical implementation is shown in Figure 5.4. As the flowchart shows, in MPLSM, there is no re-initialization is required, the propagation of the level set surface is driven by dynamically updating the design variables using MMA (Svanberg 1987), which is unconditionally stable and without the limitation of CFL condition. Moreover, the proposed level set method can freely create new holes inside the material regions of the multi-phase design domain, as a result of the natural extension of the velocity field and the removal of the periodically applied global re-initializations. The convergence criteria is the objective function values of two conservative iterations is lower than 0.001, or the maximum number of iterations is less than 100 which is based on the numerical experience.

---



**Figure 5.3 (a) Orthotropy with two symmetry axes; (b) Orthotropy with four symmetry axes (square symmetry)**



**Figure 5.4 Flowchart of the numerical implementation with MPLSM**

### **5.3.4 Thermoelastic Metamaterials**

The metamaterials have attracted increasing attention as they have unusual or exotic properties which can hardly be found in the natural materials. It is now known that these unusual properties are mainly dependent on the particular features in the material's micro- or nano-structure deform when subjected to a mechanical load. The expansion and contraction of materials and structures must be considered in engineering applications, when changes in dimension as a result of temperature. The thermal expansion is an important metric used to measure the degree of temperature in changing the dimension of materials. It is noticed that micro-structured composite with three material phases (two solid phases and void phase) will be able to achieve the extreme properties beyond those of the individual phase. Hence, the MPLSM can be properly applied to design the microstructures for metamaterials with extreme themoelastic properties.

#### *5.3.4.1 Formulation of the Optimization Problem*

The aim of this work is to optimize the topology and shape of the microstructure under specified effective thermal strain tensors  $\alpha_{ij}^H$  or thermal stress tensors  $\beta_{kl}^H$  and with a given amount of multiple material phases (three-phase in total) within the design domain. It should also be possible to constraint elastic symmetries such as orthotropy, square symmetry or isotropy of the resulting materials. An optimization problem including these features can be written as

$$\left\{
 \begin{array}{l}
 \text{Find : } c_i^1, c_i^2 \ (i=1,2,\dots,N) \\
 \text{Minimize : } f(\alpha_{ij}^H(c_i^1, c_i^2), \beta_{ij}^H(c_i^1, c_i^2)) \\
 \quad \quad \quad (i,j=1,2,\dots,d, \ d \text{ is the dimension of space}) \\
 \text{Subject to : } V_{\min}^1 \leq V^1 \leq V_{\max}^1, \\
 \quad \quad \quad V_{\min}^2 \leq V^2 \leq V_{\max}^2, \\
 \quad \quad \quad g_{m(\min)} \leq g_m(C_{ijkl}^H) \ (m=1,\dots,M) \\
 \quad \quad \quad c_{\min}^1 \leq c_i^1 \leq c_{\max}^1, \\
 \quad \quad \quad c_{\min}^2 \leq c_i^2 \leq c_{\max}^2,
 \end{array}
 \right. \quad (5.18)$$

The objective function  $f$  can be any combination of the thermal strain and stress coefficients  $\alpha_{ij}^H$  and  $\beta_{ij}^H$ . The numerical examples will show how to achieve zero, negative, extreme thermal expansion coefficient, and extreme thermal stress coefficient, respectively, by optimizing the shape and topology of the microstructure. For simplicity, the following derivation will focus on the topological optimization problem to design zero thermal expansions, as an example to showcase the implementation of the design sensitivity analysis.

In this case the optimization is to minimize the objective function:  $f = (\alpha_{11}^H)^2 + (\alpha_{22}^H)^2$ .

The volume of the design domain is  $|Y|$ , the volume fractions of the two solid phases can be calculated as

$$V^1 = \frac{1}{|Y|} \int_Y H(\Phi^1) (1 - H(\Phi^2)) dY, \quad (5.19)$$

$$V^2 = \frac{1}{|Y|} \int_Y H(\Phi^1) H(\Phi^2) dY \quad (5.20)$$

In Eq.(5.18),  $V_{\min}^1$ ,  $V_{\max}^1$ ,  $V_{\min}^2$  and  $V_{\max}^2$  are lower and upper bounds to limit the volume fractions of solid phase 1 and solid phase 2, respectively. Sometimes, the volume fraction of each individual phase can be fixed by setting the lower bound to be the upper bound. In order to design the composite material with extreme thermal properties, we will introduce a lower bound to constrain the components of the effective elasticity matrix or on the bulk modulus of the material, which can be written as  $g_{m(\min)} \leq g_m(C_{ijkl}^H)$ .

### 5.3.4.2 Sensitivity Analysis

Due to the parameterization of the level set function, many more efficient gradient-based optimization algorithm, e.g. the Method of Moving Asymptotes (MMA) (Svanberg 1987), can be applied to solve the optimization problem. The implementation of the MMA requires the first-order derivatives of the objective function and constraints with respect to the design variables that are actually the coefficients of the interpolant.

Based on the sensitivity analysis given in Eq. (4.17), the derivative of  $C_{ijkl}^H$  with respect to time  $t$  is obtained as

$$\frac{dC_{ijkl}^H}{dt} = \frac{1}{|Y|} \int_Y \left( \varepsilon_{pq}^{0(ij)} - \varepsilon_{pq}^* (\chi^{ij}) \right) \frac{\partial C_{pqrs}}{\partial \Phi^m} \left( \varepsilon_{rs}^{0(kl)} - \varepsilon_{rs}^* (\chi^{kl}) \right) \mathbf{v}_n^m |\nabla \Phi^m| dY \quad (5.21)$$

$$\begin{aligned} \text{when } m = 1: \quad & \frac{\partial C_{pqrs}}{\partial \Phi^1} = \delta(\Phi^1) (1 - H(\Phi^2)) C_{ijkl}^1 + \delta(\Phi^1) H(\Phi^2) C_{ijkl}^2 \\ m = 2: \quad & \frac{\partial C_{pqrs}}{\partial \Phi^2} = -H(\Phi^1) \delta(\Phi^2) C_{ijkl}^1 + H(\Phi^1) \delta(\Phi^2) C_{ijkl}^2 \end{aligned} \quad (5.22)$$

In PLSM, the normal velocity  $\mathbf{v}_n^m$  is expressed as

$$\mathbf{v}_n^m = \frac{\varphi_i(\mathbf{x})}{|\nabla \varphi_i(\mathbf{x}) c_i^m(t)|} \frac{dc_i^m(t)}{dt} \quad (5.23)$$

Substitute  $\mathbf{v}_n$  in Eq. (5.22), we can obtain the following equation

$$\frac{dC_{ijkl}^H}{dt} = \frac{1}{|Y|} \int_Y \left( \varepsilon_{pq}^{0(ij)} - \varepsilon_{pq}^* (\chi^{ij}) \right) \frac{\partial C_{pqrs}}{\partial \Phi^m} \left( \varepsilon_{rs}^{0(kl)} - \varepsilon_{rs}^* (\chi^{kl}) \right) \varphi_i(\mathbf{x}) dY \frac{dc_i^m(t)}{dt} \quad (5.24)$$

$$(i = 1, 2, \dots, N)$$

where  $N$  is the total number of the CS-RBF knots. By using the chain rule, at the same time, we can equivalently have

Then, if considering  $c$  as the only unknown parameters, the Eq. (5.24) can also be expressed by using chain rule as

$$\frac{dC_{ijkl}^H}{dt} = \frac{\partial C_{ijkl}^H}{\partial c_i^m(t)} \frac{dc_i^m(t)}{dt} \quad (5.25)$$

Comparing the corresponding terms in Eq. (5.24) and Eq. (5.25), the derivative of  $C_{ijkl}^H$  with respect to the design variables  $c_i^m$  of any solid material phase  $m$  can be easily obtained:

$$\frac{\partial C_{ijkl}^H}{\partial c_i^m} = \frac{1}{|Y|} \int_Y \left( \varepsilon_{pq}^{0(ij)} - \varepsilon_{pq}^* (\chi^{ij}) \right) \frac{\partial C_{pqrs}}{\partial \Phi^m} \left( \varepsilon_{rs}^{0(kl)} - \varepsilon_{rs}^* (\chi^{kl}) \right) \varphi_i(\mathbf{x}) dY \quad (5.26)$$

$$(i = 1, 2, \dots, N)$$

Similarly, the design sensitivities of the thermal stress  $\beta_{kl}^H$  with respect to  $c^m$  are given by

$$\frac{\partial \beta_{kl}^H}{\partial c_i^1} = \frac{1}{|Y|} \int_Y \left( \alpha_{pq} - \varepsilon_{pq}^\alpha (\Lambda) \right) \left( \delta(\Phi^1) (1 - H(\Phi^2)) C_{ijkl}^1 + \delta(\Phi^1) H(\Phi^2) C_{ijkl}^2 \right) \left( \varepsilon_{rs}^{0(kl)} - \varepsilon_{rs}^* (\chi^{kl}) \right) \varphi_i(\mathbf{x}) dY$$

$$(i = 1, 2, \dots, N) \quad (5.27)$$

$$\begin{aligned}
 \frac{\partial \beta_{kl}^H}{\partial c_i^2} = & \frac{1}{|Y|} \int_Y \left( \alpha_{pq} - \varepsilon_{pq}^{\alpha}(\Lambda) \right) \left( -H(\Phi^1) \delta(\Phi^2) C_{ijkl}^1 + H(\Phi^1) \delta(\Phi^2) C_{ijkl}^2 \right) \left( \varepsilon_{rs}^{0(kl)} - \varepsilon_{rs}^*(\chi^{kl}) \right) \varphi_i(\mathbf{x}) dY \\
 & + \frac{1}{|Y|} \int_Y C_{ijkl} \left( -\delta(\Phi^2) \alpha_{ij}^1 + \delta(\Phi^2) \alpha_{kl}^2 \right) \left( \varepsilon_{rs}^{0(kl)} - \varepsilon_{rs}^*(\chi^{kl}) \right) \varphi_i(\mathbf{x}) dY \\
 (i = 1, 2, \dots, N)
 \end{aligned} \tag{5.28}$$

The sensitivities of  $\alpha_{ij}^H$  with respect to the design variables can be found by differentiating Eq. (5.13) as

$$\frac{\partial \alpha_{ij}^H}{\partial c_i^m} = \frac{d(C_{ijkl}^H)^{-1}}{dc_i^m} \beta_{kl}^H + (C_{ijkl}^H)^{-1} \frac{\partial \beta_{kl}^H}{\partial c_i^m} \quad (i = 1, 2, \dots, N) \tag{5.29}$$

The derivative of the objective function is expressed by

$$\frac{\partial f}{\partial c_i^m} = 2\alpha_{11}^H \frac{\partial \alpha_{11}^H}{\partial c_i^m} + 2\alpha_{22}^H \frac{\partial \alpha_{22}^H}{\partial c_i^m} \quad (i = 1, 2, \dots, N) \tag{5.30}$$

The derivatives for the volume constraints about the design variables are given by

$$\frac{\partial V^1}{\partial c_i^1} = \frac{1}{|Y|} \int_Y \delta(\Phi^1) (1 - H(\Phi^2)) \varphi_i(\mathbf{x}) dY \quad (i = 1, 2, \dots, N) \tag{5.31}$$

$$\frac{\partial V^2}{\partial c_i^1} = \frac{1}{|Y|} \int_Y \delta(\Phi^1) H(\Phi^2) \varphi_i(\mathbf{x}) dY \quad (i = 1, 2, \dots, N) \tag{5.32}$$

$$\frac{\partial V^1}{\partial c_i^2} = \frac{1}{|Y|} \int_Y -H(\Phi^1) \delta(\Phi^2) \varphi_i(\mathbf{x}) dY \quad (i = 1, 2, \dots, N) \tag{5.33}$$

$$\frac{\partial V^2}{\partial c_i^2} = \frac{1}{|Y|} \int_Y H(\Phi^1) \delta(\Phi^2) \varphi_i(\mathbf{x}) dY \quad (i = 1, 2, \dots, N) \tag{5.34}$$

### 5.3.5 Multifunctional Metamaterials

The Poisson's ratio of a solid is defined as the ratio of transverse contraction strain to longitudinal stretching strain under uniaxial tension, used to measure the performance of elastic materials(Evans and Alderson 2000). The metamaterials with negative Poisson's ratio (NPR, also called Auxetics) has attracted much attention, due to the potential for a range of applications. However, since most materials in service will experience a range of operating temperatures, the thermal expansion due to temperature changes would effect on the performance of auxeticity, particularly when experiencing dramatic temperature fluctuation or operating at the extreme hot or cold environment. Out of this concern, it is necessary to design the NPR metamaterials with zero or low thermal expansion coefficient. It may be also interesting to exploit the metamaterials with two negative indexes (NPR and NTE), as this phenomena may rarely be found. It may also be used as a blueprint for the design of new multifunctional material, including NPR and NTE.

#### 5.3.5.1 Formulation of the Optimization Problem

The aim of this work is to optimize the topology and shape of the microstructure to achieve the target effective thermal strain tensors  $\alpha_{ij}^{Obj}$  and elasticity tensor  $C_{ijkl}^{Obj}$  under a given amount of multiple material phases (three-phase in total) within the design domain. It should also be possible to constraint elastic symmetries such as orthotropy, square symmetry or isotropy of the resulting materials. An optimization problem including these features can be written as

$$\left\{
 \begin{array}{l}
 \text{Find: } c_i^1, c_i^2 \ (i=1,2,\dots,N) \\
 \text{Minimize: } f = \frac{1}{2} \sum_{i,j=1}^d \omega_{ij} (\alpha_{ij}^H - \alpha_{ij}^{Obj})^2 + \frac{1}{2} \sum_{i,j,k,l=1}^d \eta_{ijkl} (C_{ijkl}^H - C_{ijkl}^{Obj})^2 \\
 \text{Subject to: } a(\mathbf{u}, \mathbf{v}, \varphi) = l(\mathbf{v}, \varphi), \ \forall \mathbf{v} \in U_{ad} \\
 \quad V_{\min}^1 \leq V^1 \leq V_{\max}^1 \\
 \quad V_{\min}^2 \leq V^2 \leq V_{\max}^2 \\
 \quad c_{\min}^1 \leq c_i^1 \leq c_{\max}^1 \\
 \quad c_{\min}^2 \leq c_i^2 \leq c_{\max}^2
 \end{array}
 \right. \quad (5.35)$$

where  $\omega_{ij}$  and  $\eta_{ijkl}$  are the weighting factors associated with the corresponding component thermal strain tensors and elasticity tensor;  $\mathbf{u}$  is the displacement field;  $\mathbf{v}$  is the virtual displacement and  $U_{ad}$  is the set of kinematically admissible displacements;  $V_{\min}^1$ ,  $V_{\max}^1$ ,  $V_{\min}^2$  and  $V_{\max}^2$  are lower and upper bounds to limit the volume fractions of solid phase 1 and solid phase 2, respectively;  $c_{\min}^1$ ,  $c_{\max}^1$ ,  $c_{\min}^2$  and  $c_{\max}^2$  are the lower and upper bounds of the two sets of design variables.

### 5.3.5.2 Sensitivity Analysis

For the implementation of the MMA requires the first-order derivatives of the objective function and constraints with respect to the design variables. The derivative of the objective function is expressed by

$$\frac{\partial f}{\partial \mathbf{c}^m} = \sum_{i,j=1}^d \omega_{ij} (\alpha_{ij}^H - \alpha_{ij}^{Obj}) \frac{\partial \alpha_{ij}^H}{\partial \mathbf{c}^m} + \sum_{i,j,k,l=1}^d 2\eta_{ijkl} (C_{ijkl}^H - C_{ijkl}^{Obj}) \frac{\partial C_{ijkl}^H}{\partial \mathbf{c}^I} \quad (m=1,2) \quad (5.36)$$

where  $\frac{\partial C_{ijkl}^H}{\partial c^m}$  and  $\frac{\partial \alpha_{ij}^H}{\partial c^m}$  have been given in section 5.3.4.1. The derivatives for the volume constraints about the design variables are same those presented in section 5.3.4.1.

## 5.4 Numerical Examples

For numerical simplicity but without losing any generality, the numerical cases in this thesis will focus on three-phase topology optimization problems of linear elastic structures. For the three-phase composites, the artificial material properties are given as follows: Young's moduli  $E^1 = E^2 = 1$ , Poisson's ratios  $\nu^1 = \nu^2 = 0.3$ , and thermal expansion coefficients  $\alpha^1 = 1$  (red colour) and  $\alpha^2 = 10$  (blue colour).

### 5.4.1 Metamaterials with Extreme Thermal Expansion

In this example, the unit cell with square symmetry is adopted as the design domain. Three examples are implemented to achieve the extreme effective thermoelastic properties, under the volume fraction constraints  $V^1 = 25\%$  and  $V^2 = 25\%$ . We discuss the following cases:

- (a) Maximization of  $\beta^H$  with horizontal, vertical and diagonal geometric symmetry ( $\beta^H = \beta_{11}^H = \beta_{22}^H$ ;  $\alpha^H = \alpha_{11}^H = \alpha_{22}^H$  in this case).
- (b) Maximization of  $\alpha_{22}^H$  in the vertical direction, under constraints of horizontal and vertical geometrical symmetry, as well as the lower bound of  $C_{2222}^H$ .
- (c) Minimization of  $\alpha_{22}^H$  in the vertical direction, under constraints of horizontal and vertical geometrical symmetry, as well as the lower bound of  $C_{2222}^H$ .

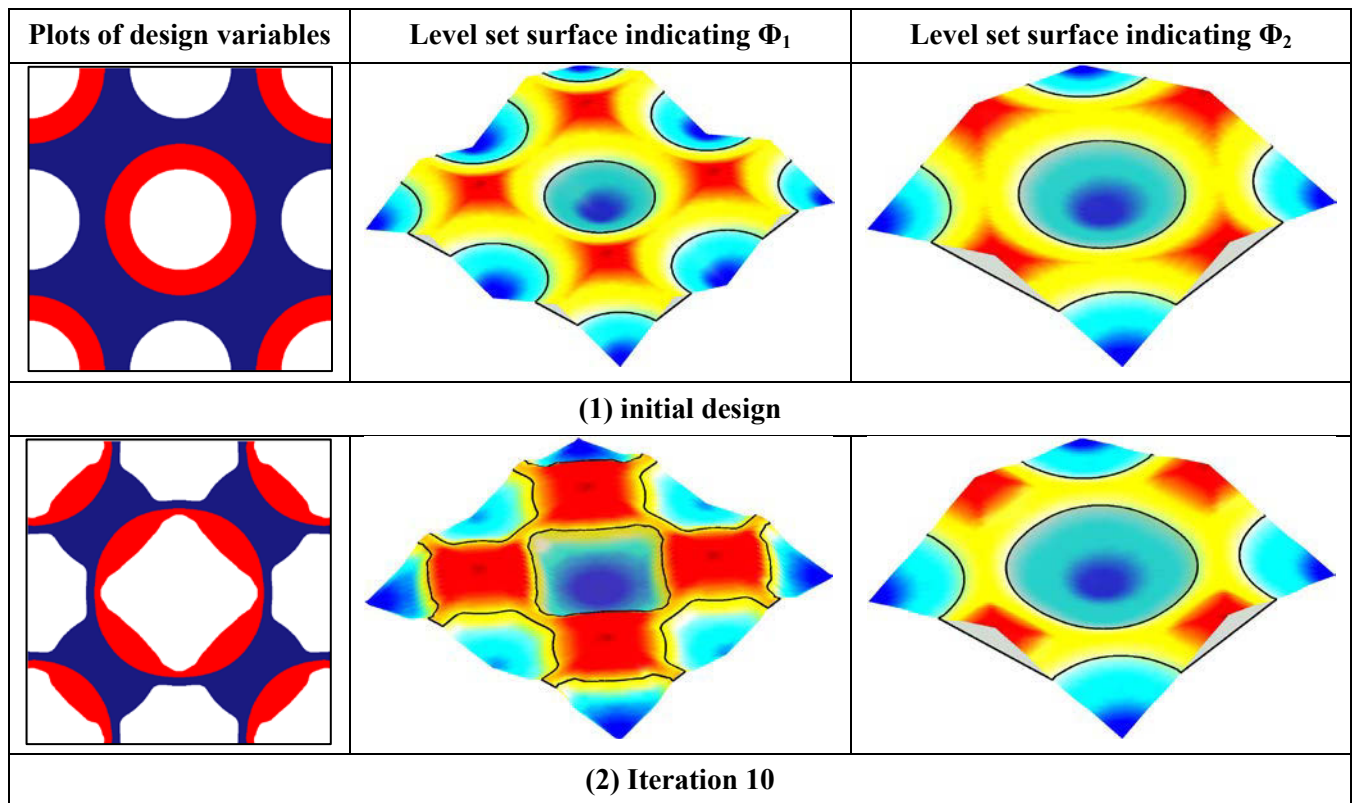
The results of Case (a) given in Figure 5.5 from (1) to (6) as the initial design, four intermediate designs, and the optimized design, respectively. In Figure 5.5, all plots given in the first column represent the distributions of the design variables, in which the red colour indicates the solid material 1, while the blue colour shows the solid material 2. It is noted that here  $\Phi^1$  and  $\Phi^2$  are only two level set functions to implicitly indicate the two types of design variables, rather than each individual material phase.

Figure 5.6 is further used to show the distributions of two solid materials in the optimal design that is given in Figure 5.5(6). The thermal strain and stress coefficients of the optimal design are given in Table 5-1. It can be found that the implicit level set representation (Wang et al. 2003; Allaire et al. 2004) showing unique features, such as a smooth design boundary and distinct material interface, as well as integrated shape optimization and topology optimization as a topological shape procedure. In the process of optimization, the proposed method is able to not only merge existing holes but also create new holes to achieve topological shape evolutions of the unit cell.

The convergence of the objective function and volume fractions over the iterations are given in Figure 5.7 and Figure 5.8, respectively. It can be easily found that the topological evolution of the structure is basically completed within the first 20 iterations, while the objective function is maximized from -8.0 to -2.75 mainly because of the violation of the volume constraint of the initial design. After that, the objective function is then minimized from -2.75 to -3.68, which is to further change the local regions of the topology and evolve the shape of the boundary. From the results, we can find that the optimization is converged

within 100 iterations, with a better computational efficiency, the volume constraints are conservative.

The final topologies for (a), (b) and (c) are shown in Figure 5.9, respectively, while their effective properties are given in Table 5-1. Since the extreme thermal expansion can be obtained at the cost of a very low bulk modulus, the lower limit of the stiffness should be constrained in the optimization. In the case (b) and (c), to achieve a material with directional extreme thermal expansions, the extreme thermal strain coefficients at one direction will lead to extreme stiff at the other direction.



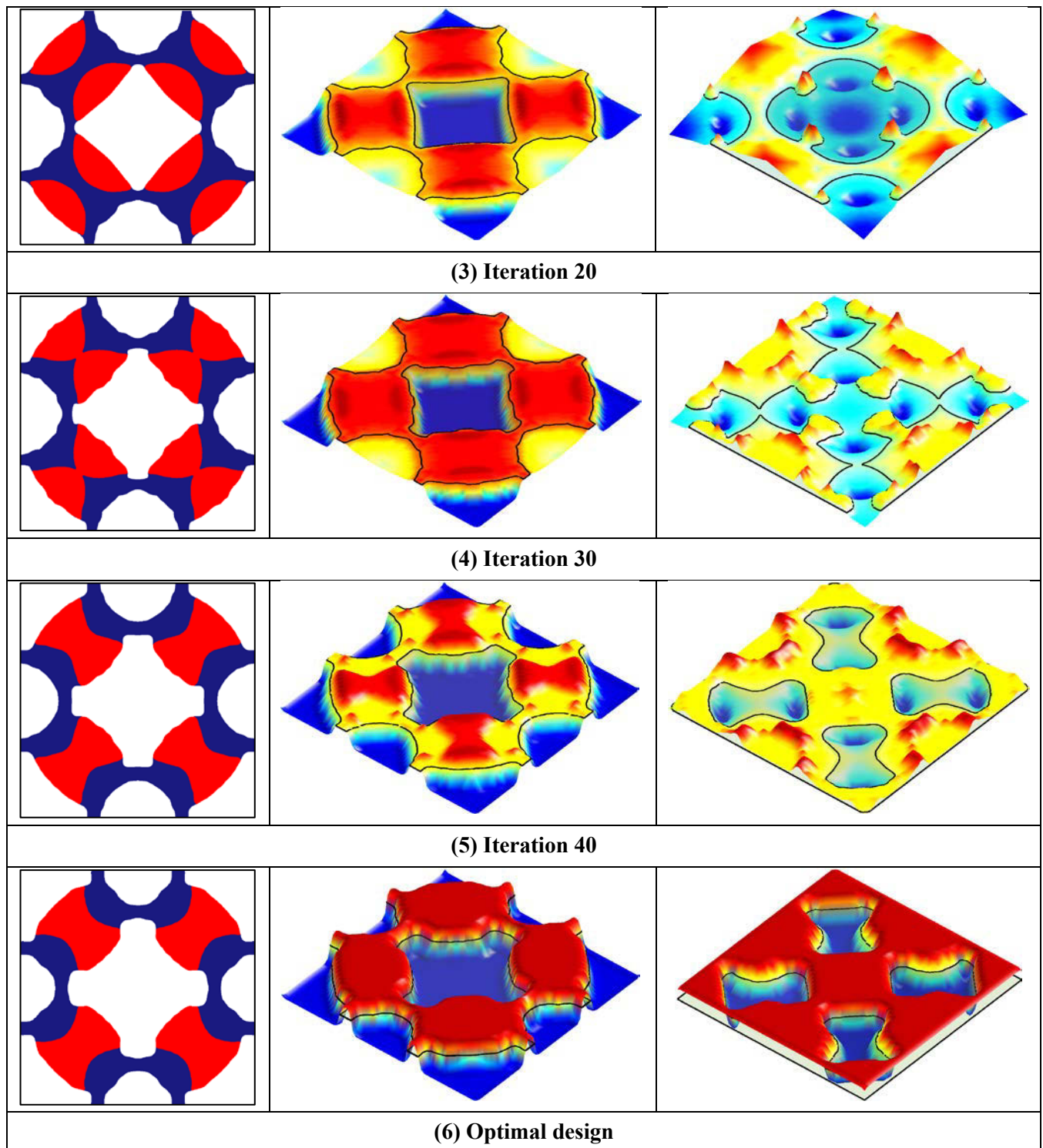
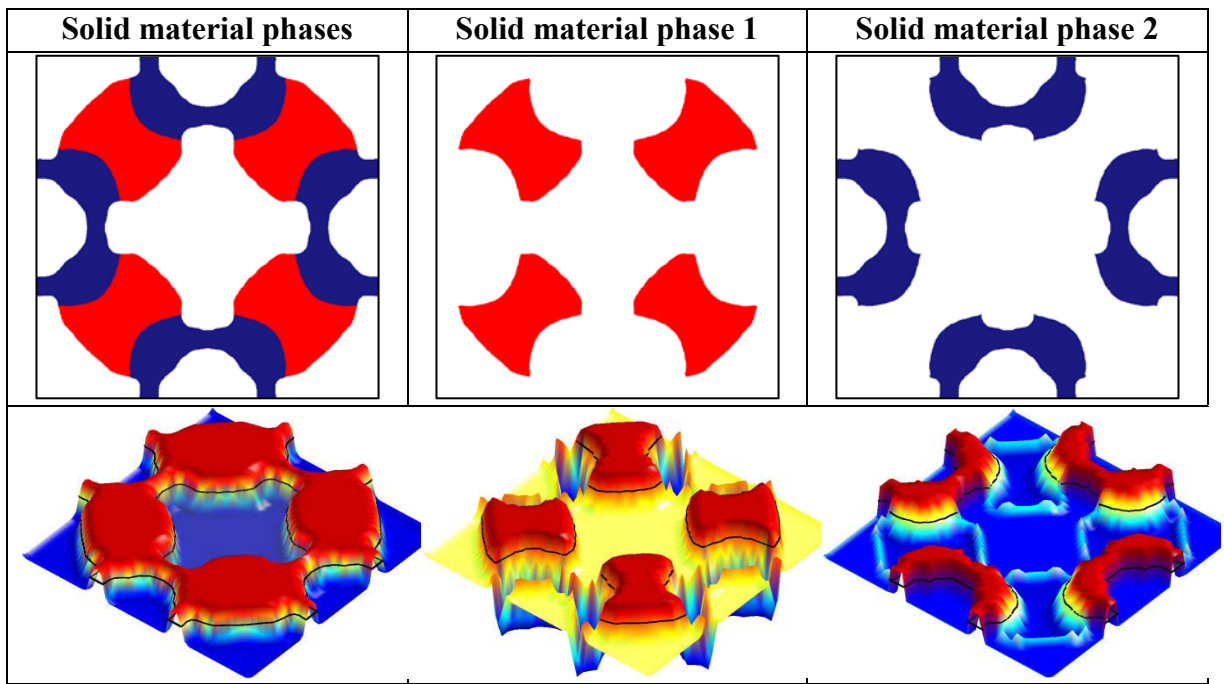
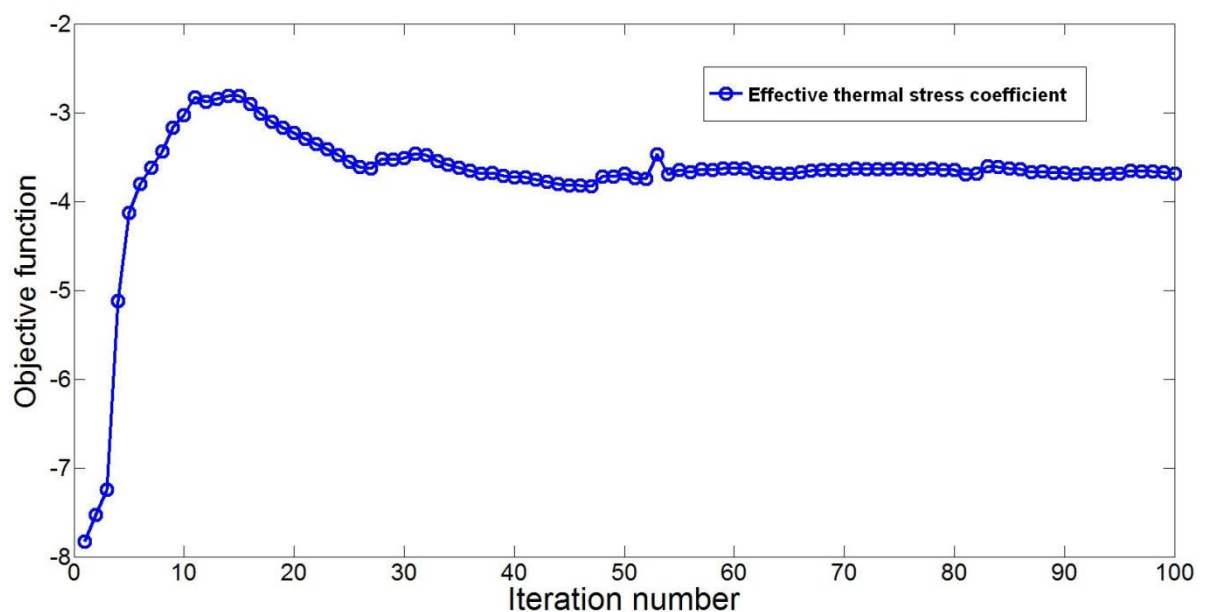


Figure 5.5 Plots of design variables and their level set surfaces ( $\Phi^1$  and  $\Phi^2$ )



**Figure 5.6** Contour plots (first row) and level set surfaces (second row) for solid material phases



**Figure 5.7** Convergence of the objective function

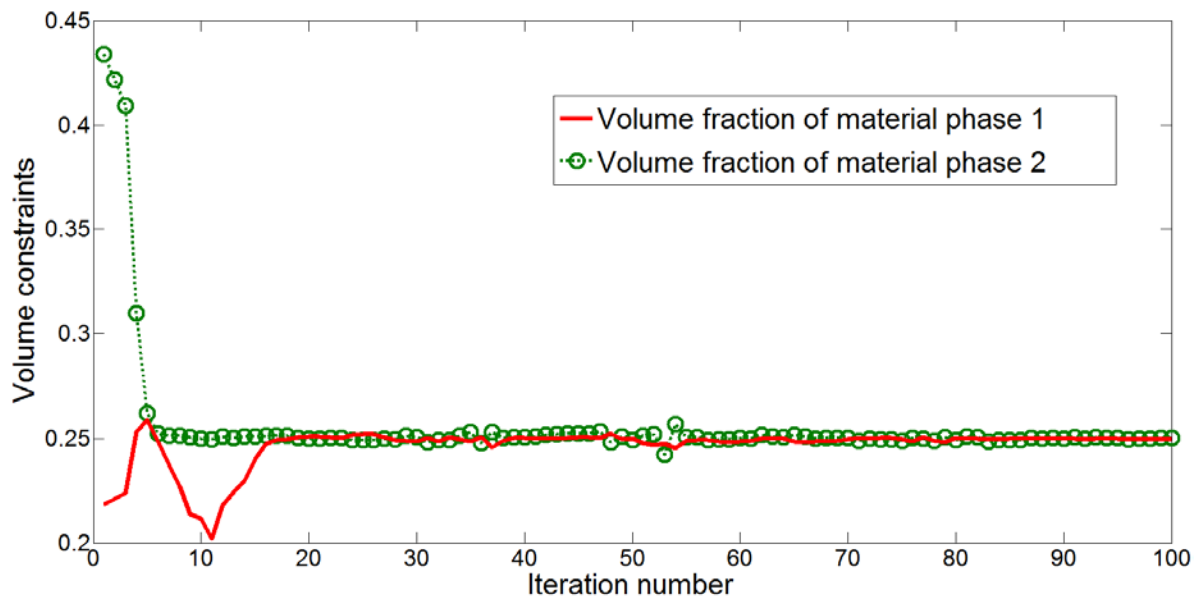
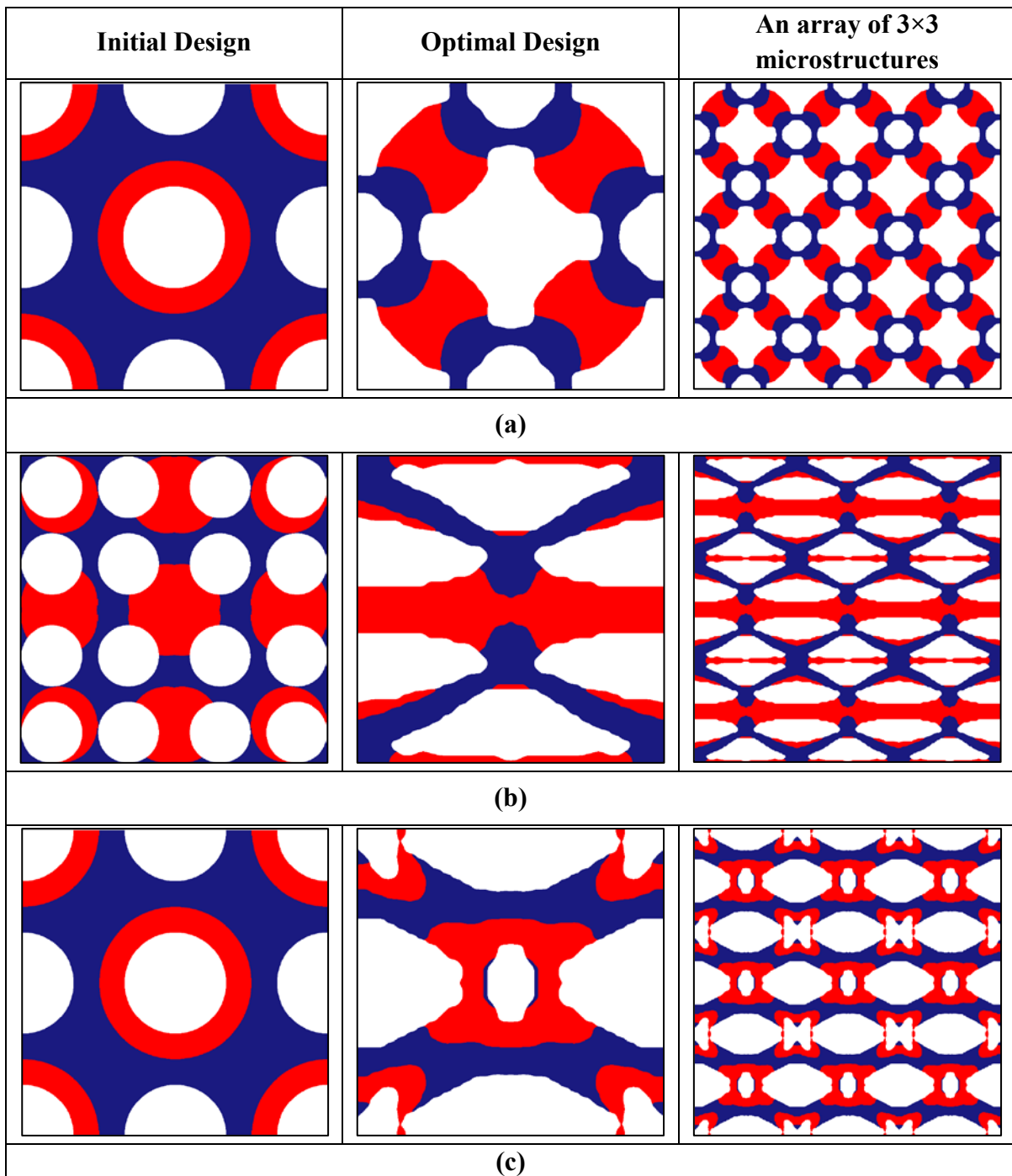


Figure 5.8 Convergence of the volume constraints

Table 5-1 Thermoelastic parameters of optimal microstructures

Case	Objective	Constraint	$\alpha_{11}^H$	$\alpha_{22}^H$	$\beta^H$	$B^H$
(a)	$\text{Max } (\beta^H)$	$B_{low}^H = 0.05$	7.5505	7.5505	1.8420	0.163
Case	Objective	Constraint	$\alpha_{11}^H$	$\alpha_{22}^H$	$C_{1111}^H$	$C_{2222}^H$
(b)	$\text{Max } (\alpha_{22}^H)$	$C_{2222}^H = 0.03$	2.8023	19.6009	0.4043	0.0394
(c)	$\text{Min } (\alpha_{22}^H)$	$C_{2222}^H = 0.05$	8.0927	-3.2901	0.3350	0.0596



**Figure 5.9 Optimal microstructures with extreme effective thermal properties**

((a), (b), and (c) are corresponding to the design case (a), (b) and (c) shown in Table 1)

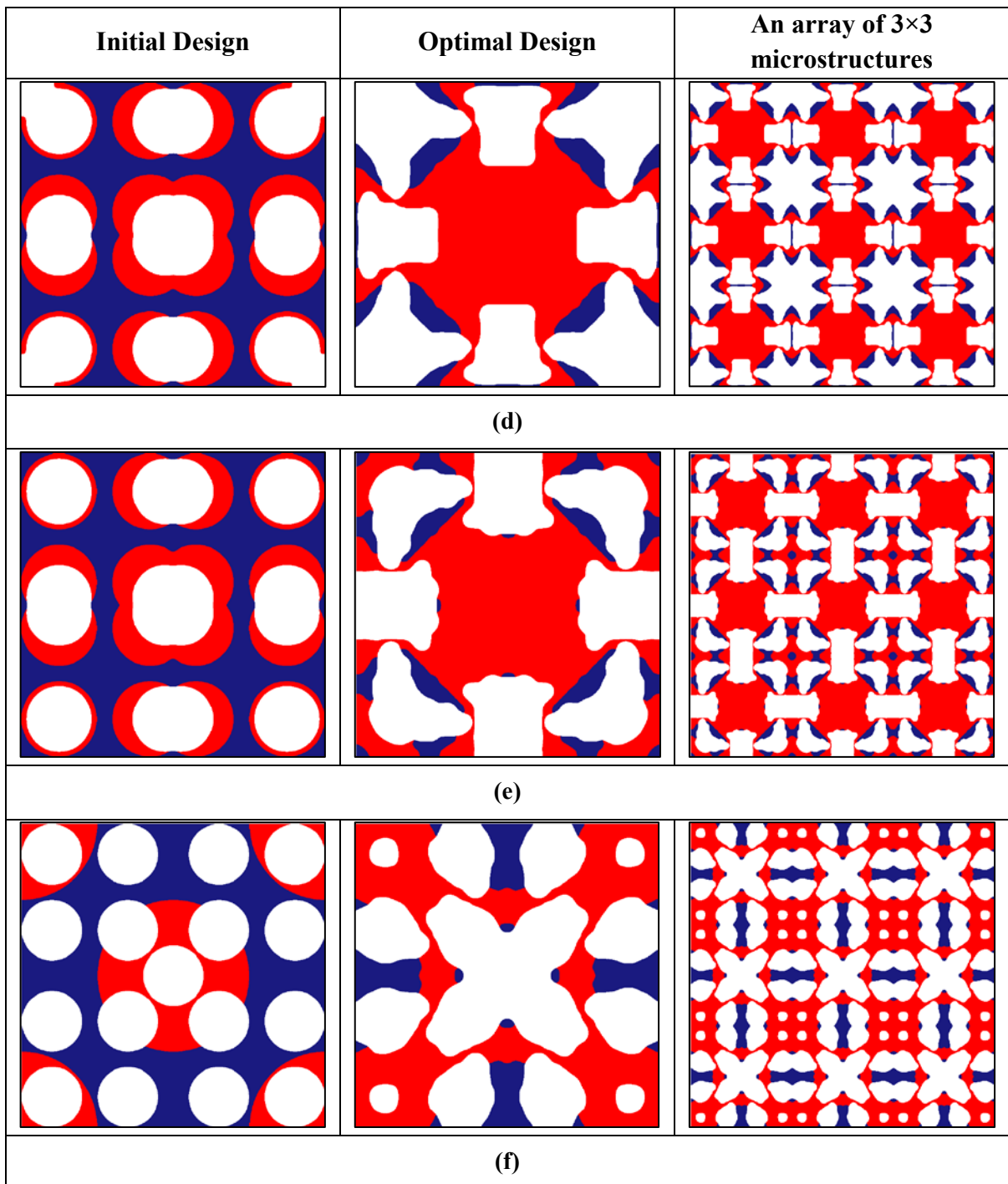
### 5.4.2 Metamaterials with ZTE

In this example, a square unit cell with horizontal, vertical and diagonal symmetry is adopted. The volume fractions for the two solid materials are  $V^1 = 35\%$  and  $V^2 = 10\%$ . There is a lower bound to the effective bulk modulus  $B_{Low}^H = 0.05$ .

The objective function here is to achieve the zero thermoelastic property of the microstructure with the lower limit of the effective bulk modulus. It is well-known that in such inverse material design there will often be multiple local solutions which can satisfy the design with zero thermoelastic property. Three different cases (d), (e) and (f) are used to illustrate such phenomenon, by design the zero thermoelastic materials under different initial guesses. The optimal designs shown in Figure 5.10 demonstrate that how topologically different microstructures can have almost the same values of the thermoelastic property with different effective bulk modulus, under three different initial designs. The different optimized designs also show that the topology optimization problem will easily subject to local minima.

**Table 5-2 Thermoelastic parameters for optimal microstructures**

Case	Objective function	$\alpha^H$	$B^H$
(d)	$\alpha^H = 0$	0.0005000	0.067
(e)	$\alpha^H = 0$	0.0002996	0.0622
(f)	$\alpha^H = 0$	0.0005088	0.0992



**Figure 5.10 Optimal microstructures for zero effective thermal expansion**

((d), (e), and (f) are corresponding to the design case (d), (e) and (f) shown in Table 5-2)

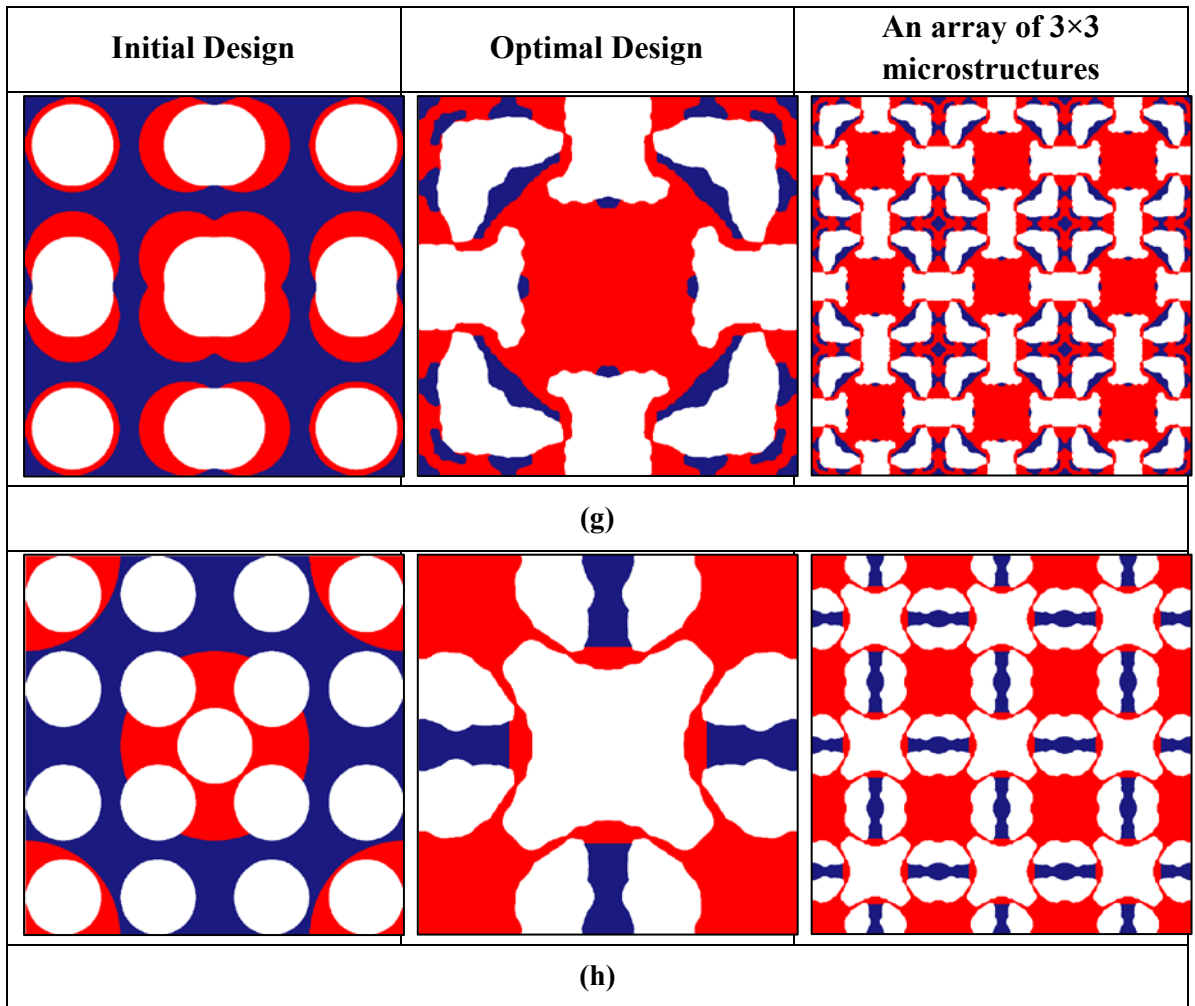
### 5.4.3 Metamaterials with NTE

To obtain the materials with negative effective thermal strain coefficients, the optimization problem is conducted under different initial guesses and volume ratios. The horizontal, vertical and diagonal symmetry are applied to the microstructure. The optimal solutions for the three cases are shown in Figure 5.11, and the corresponding parameters are given in Table 5-3. Beside the common features of the level set methods, it can be seen that these different cases can generate different topological shapes of the unit cell.

The actual mechanisms behind the negative thermal expansion coefficients of the composite materials are very complex. From optimized topologies of the microstructure, we may find that the different material parts of the microstructure inside the design domain may become contact, due to the temperature increase of the microstructure. When a low bulk modulus is allowable, the main mechanism behind the negative thermal expansion phenomenon is the re-entrant cell structure having multi-phase components, which will cause relatively large deformation when heated. The multi-phase interfaces of the structure may bend and make the cell contract, similar to the behaviour of the negative Poisson's ratios (Lakes 1987).

**Table 5-3 Thermoelastic parameters for optimal microstructures**

Case	Objective	Volume Ratio	$\alpha^H$	$B^H$
(g)	$\alpha^H = -0.5$	$V^1 = 40\%, V^2 = 10\%$	-0.501	0.0525
(h)	$\alpha^H = -1.2$	$V^1 = 35\%, V^2 = 10\%$	-0.8031	0.0596



**Figure 5.11 Optimal microstructures for negative effective thermal expansion**

((g), and (h) are corresponding to the design case (g), and (h) shown in Table 5-3)

From the above numerical examples, we can notice that the effective elastic and thermal properties of the microstructure are dependent on both the internal structure (e.g. shapes and topologies) of the unit cell and the way of deformation when loaded. Thus, in order to design a composite material with extreme thermoelastic properties, the microstructure will be prone to generate structures functionally similar to rotating rigid mechanisms (Wang et al. 2014). However, the topological shape optimization is a computational design method mainly for structures, and it is difficult to generate the large rotating deformation like rigid-

link mechanisms. This may be used to explain a phenomenon during the optimization process: the generation of re-entrant type structure that may be necessary for achieving the extreme thermoelastic property. The rotating effect of the design will make the microstructure have hinge-type connections locally inside the design domain. Since the microstructure is required to maintain the lower limit of bulk modulus, from the point of view of continuum structures, it is difficult to use structural shape and topology optimization method to generate microstructures that can exactly reach the extreme bounds of the material properties. However, the topology optimization is a powerful computational design tool, which can systematically create novel microstructures for composites to achieve various desired and extreme properties.

#### **5.4.4 Multifunctional Metamaterial**

In the following numerical examples, we design the metamaterials with NPR and NTE/ZTE simultaneously.

##### *5.4.4.1 Design of Metamaterial with NPR and NTE: Case (1)*

In the first case, to investigate the effect of the two weighting factors,  $\omega_{ij}$  and  $\eta_{ijkl}$ , in the optimization design of the NTE and NPR metamaterials, different sets of initial parameters are used to generate metamaterials with a given value of negative Poisson's ratio -0.5 and at the same time a minimized value of the thermal strain in vertical directions. The initial parameters, objective properties and initial design are given in Table 5-4. Table 5-5 compares the optimal designs and corresponding effective properties of metamaterials with different weighting factors. Based on the optimal results, it is easy to find out that with the weighting factors play an important role in determining the weight of NTE or NPR. When

the weighting factor of the thermal expansion has a higher ratio, the extreme thermal strain in the vertical direction will dominate the design while the Poisson's ratio is close to 0. On the other hand, when given the weighting factor of the elastic tensor a higher ratio, the optimization is more able to achieve a better NPR design close to the objective properties, while the thermal expansion coefficient may be no longer able to remain negative. Hence, in practice, it is more or less a matter of numerical experience to feed appropriate weighting factors to the optimization. Only in this way we can achieve elastic metamaterials with double negative indexes (NTE and NPR) simultaneously.

**Table 5-4 Initial parameters and initial design for Case (1)**

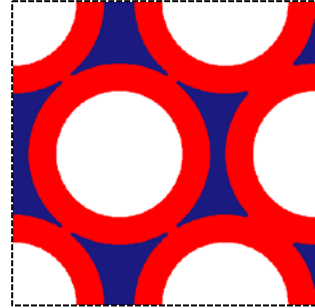
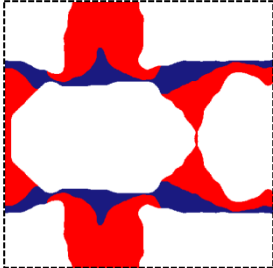
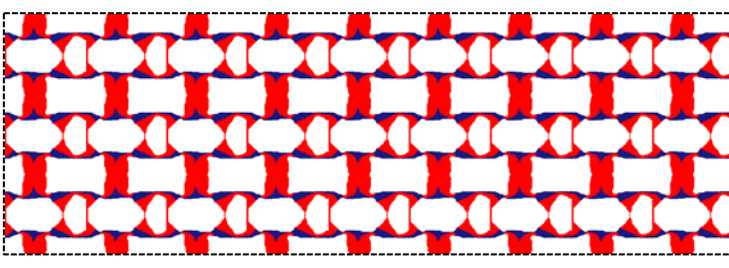
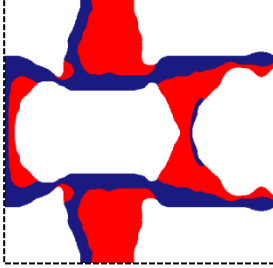
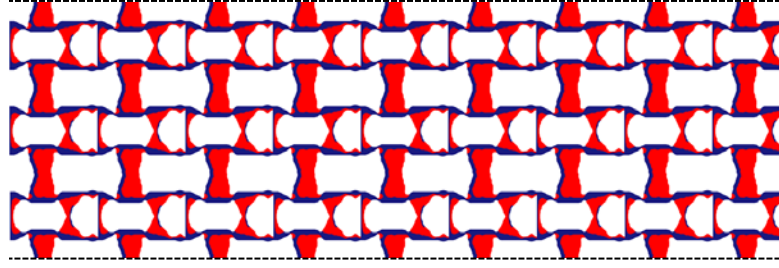
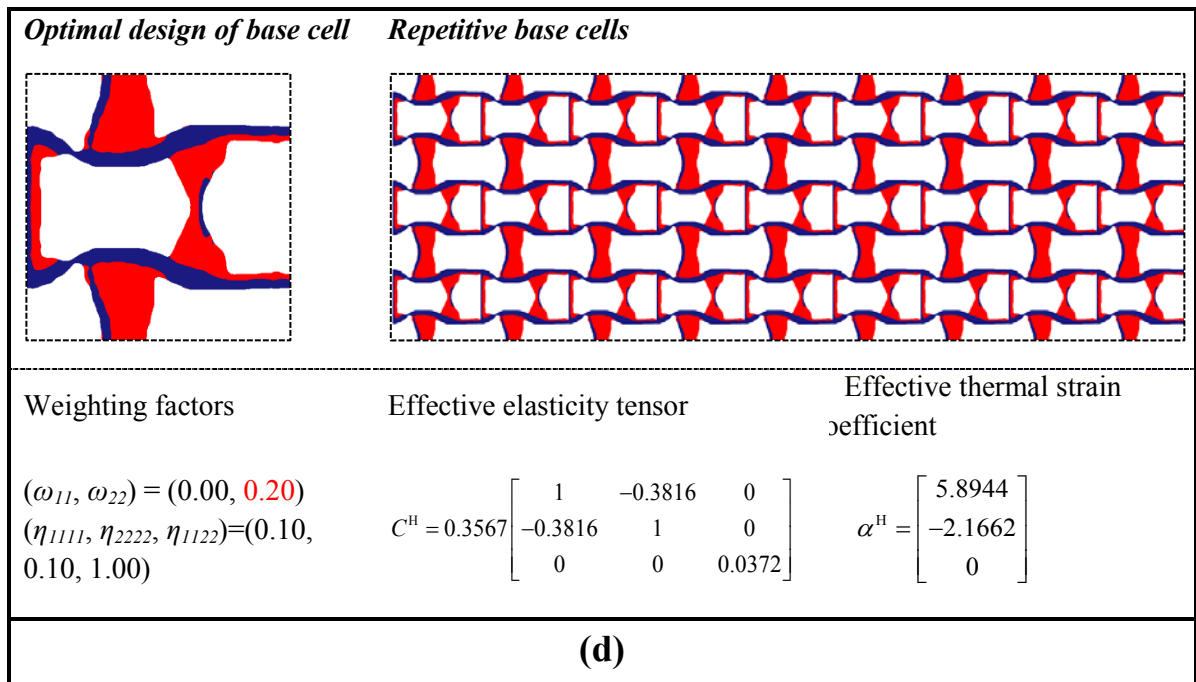
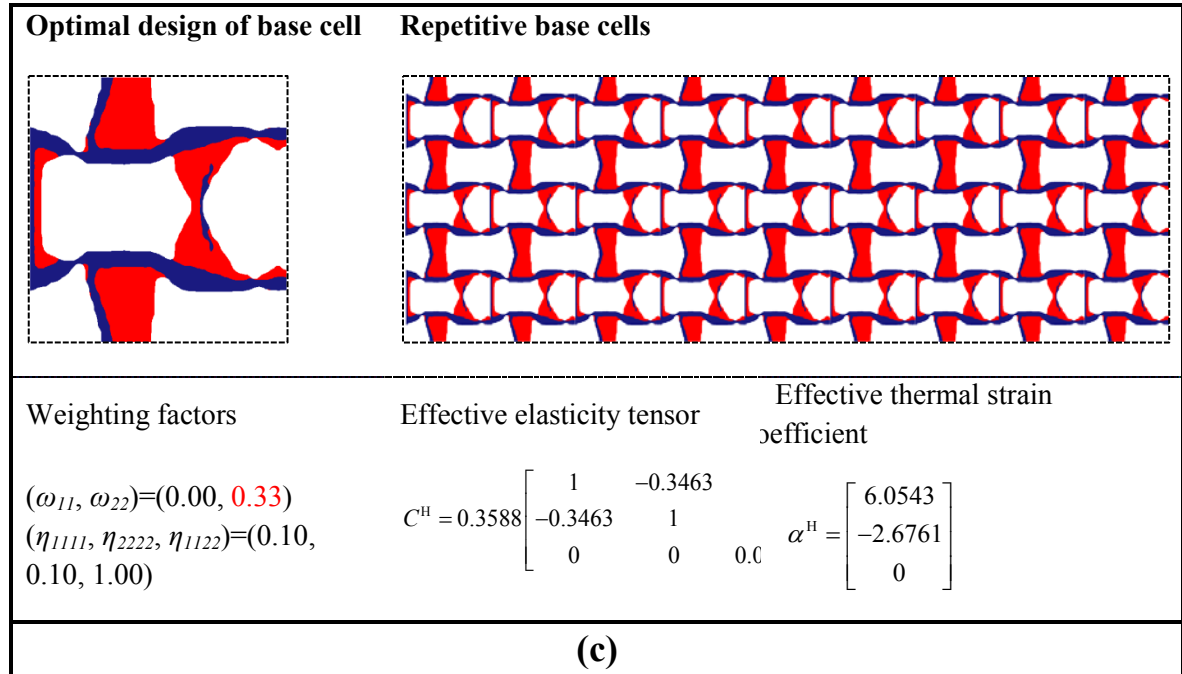
Lower limit (bulk modulus)	Volume fraction	Objective properties	Initial design
0.04	$V^1=0.25$ $V^2=0.1$	$C^{Obj} = 0.4 \begin{bmatrix} 1 & -0.5 & 0 \\ -0.5 & 1 & 0 \\ 0 & 0 & 0 \end{bmatrix}$ Minimize $\alpha_{22}$	

Table 5-5 Initial parameters and corresponding solutions for Case (1)

<i>Optimal design of base cell</i>	<i>Repetitive base cells</i>
	
Weighting factors  $(\omega_{11}, \omega_{22}) = (0.00, 2.00)$ $(\eta_{1111}, \eta_{2222}, \eta_{1122}) = (0.10, 0.10, 1.00)$	Effective elasticity tensor  $C^H = 0.2488 \begin{bmatrix} 1 & -0.1776 & 0 \\ -0.1776 & 1 & 0 \\ 0 & 0 & 0.0241 \end{bmatrix}$
Effective thermal strain coefficient  $\alpha^H = \begin{bmatrix} 6.4682 \\ -7.4820 \\ 0 \end{bmatrix}$	
<b>(a)</b>	

<i>Optimal design of base cell</i>	<i>Repetitive base cells</i>
	
Weighting factors  $(\omega_{11}, \omega_{22}) = (0.00, 0.50)$ $(\eta_{1111}, \eta_{2222}, \eta_{1122}) = (0.10, 0.10, 1.00)$	Effective elasticity tensor  $C^H = 0.3531 \begin{bmatrix} 1 & -0.3092 & 0 \\ -0.3092 & 1 & 0 \\ 0 & 0 & 0.0241 \end{bmatrix}$
Effective thermal strain coefficient  $\alpha^H = \begin{bmatrix} 5.5564 \\ -4.2529 \\ 0 \end{bmatrix}$	
<b>(b)</b>	



Optimal design of base cell	Repetitive base cells	
Weighting factors	Effective elasticity tensor	Effective thermal strain coefficient
$(\omega_{11}, \omega_{22}) = (0.00, 0.15)$ $(\eta_{1111}, \eta_{2222}, \eta_{1122}) = (0.10, 0.10, 1.00)$	$C^H = 0.3924 \begin{bmatrix} 1 & -0.3894 & 0 \\ -0.3894 & 1 & 0 \\ 0 & 0 & 0.0364 \end{bmatrix}$	$\alpha^H = \begin{bmatrix} 6.8767 \\ 0.8572 \\ 0 \end{bmatrix}$
(e)		

#### 5.4.4.2 Design of Metamaterial with NPR and NTE: Case (2)

Case (2) is used to design an orthotropic material to achieve a given negative Poisson's ratio value (-0.5) and a given negative thermal strain tensor in the vertical direction (-0.3). The horizontal and vertical geometric symmetries are included, and the volume fractions are given as 0.3 and 0.1 for two solid phases, respectively.

The initial parameters, such as the weighting factors, objective property values and effective property values achieved after optimization, are given in Table 5-6. The topological shape evolutions and the convergence are all shown in Figure 5.12. The red region denotes the solid phase 1, and the blue region is the solid phase 2, while the white region is the void. The level set surfaces and the corresponding zero level-set contours for the two solid phases are given in Figure 5.13 and 5.14.

From the process of Case (1), it can be found that the integrated shape and topological optimization designs are characterized with a smooth boundary and distinct interface during the optimization (Wang et al. 2003; Allaire et al. 2004). Moreover, in the process of optimization, the proposed method can not only merge existing holes but also create new holes to achieve optimized shape and topology of the base cell. Based on the resulting design, one may notice that the topology of the obtained microstructure is similar to the results given by (Grima et al. 2012). It is known the effective elastic and thermal properties of the microstructure are dependent on both the internal structure of the base cell and the way of deformation to facilitate rotating when loaded. Thus, to design a material with extreme properties, the microstructure will prone to generate rotating rigid mechanisms (Wang et al. 2014).

**Table 5-6 Initial parameters and optimal results for Case (2)**

Case	$(\omega_{11}, \omega_{22})$	$(\eta_{1111}, \eta_{2222}, \eta_{1122})$	Objective properties	Optimal effective properties
(1)	(0.00, 3.00)	(0.03, 0.03, 1.00)	$C^{Obj} = 0.1 \begin{bmatrix} 1 & -0.4 & 0 \\ -0.4 & 1 & 0 \\ 0 & 0 & 0 \end{bmatrix}$ $\alpha_{22}^{Obj} = -0.3$	$C^H = 0.1174 \begin{bmatrix} 1 & -0.4463 & 0 \\ -0.4463 & 0.7759 & 0 \\ 0 & 0 & 0.1303 \end{bmatrix}$ $\alpha^H = \begin{bmatrix} 4.1141 \\ -0.2616 \\ 0 \end{bmatrix}$

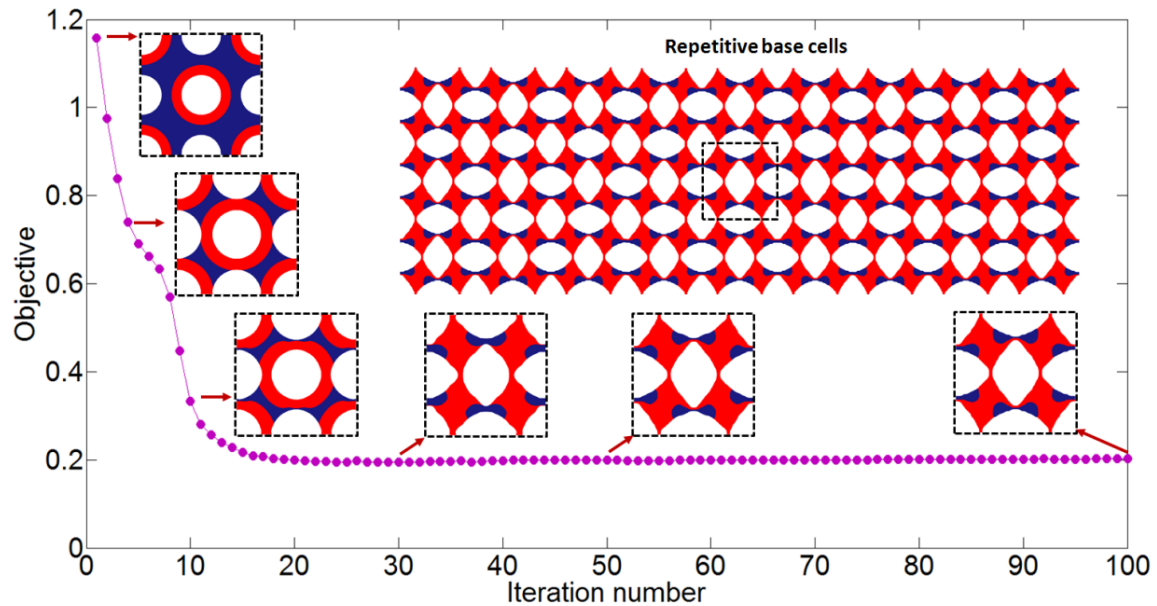


Figure 5.12 Convergent histories of the objective function

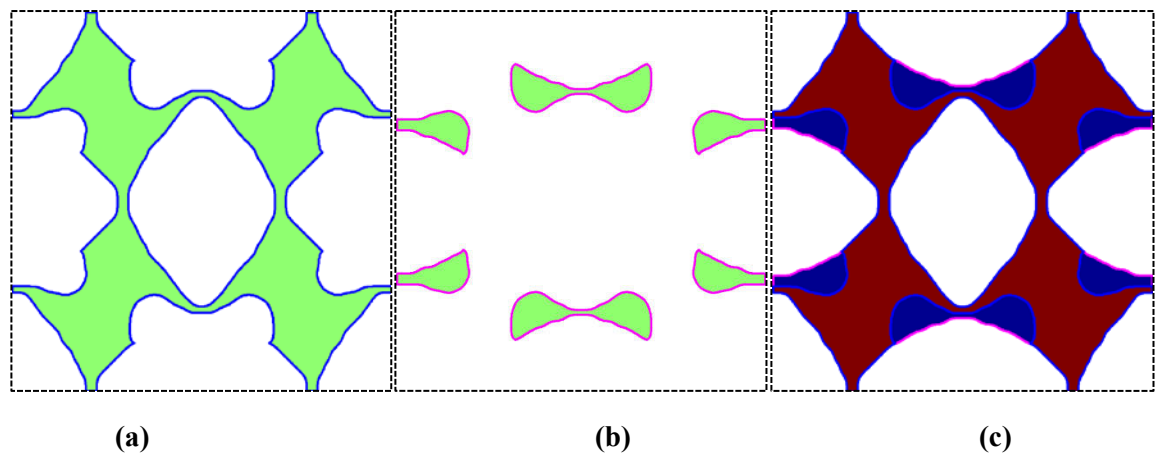
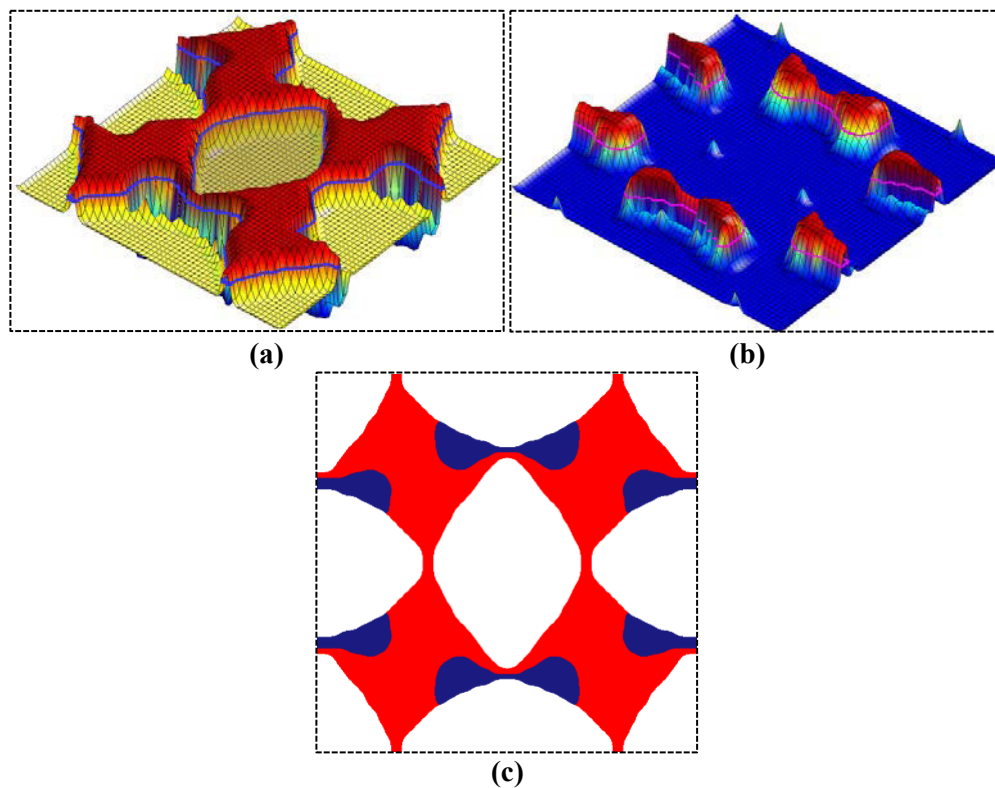


Figure 5.13 (a) Contour of solid 1; (b) Contour of solid 2; (c) Contours of solids



**Figure 5.14 (a) LS surface of solid 1; (b) LS surface of solid 2; (c) Material distribution of two solids**

#### 5.4.4.3 Design of Metamaterial with NPR and NTE: Case (3)

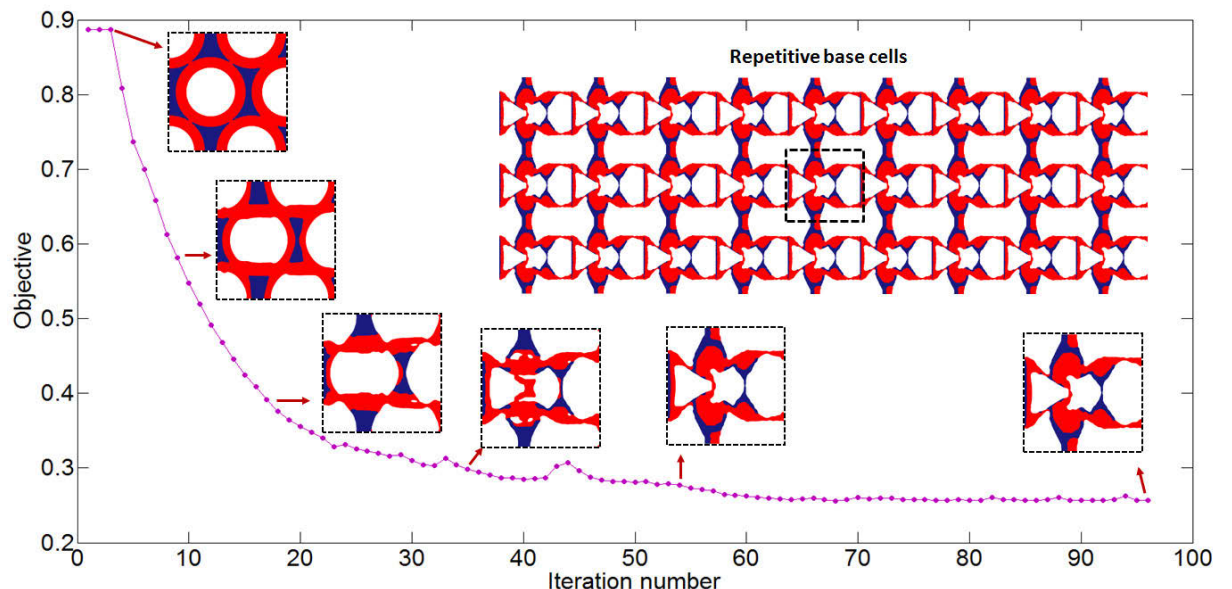
Case (3) is to design metamaterials with a prescribed negative Poisson's ratio -0.5 and at the same time to minimize the thermal strain in horizontal directions to achieve an extreme value. The material volume fractions are 0.25 and 0.1, respectively. In this case, the geometrical symmetries of the unit cell to single-axis symmetry (half symmetry) are considered in the 2D design problem. The parameters and results of the optimization are given in Table 5-7. The convergence and topological designs are shown in Figure 5.15. LS surfaces and the contours of the zero level set for two solid phases are given in Figure 5.16 and 5.17.

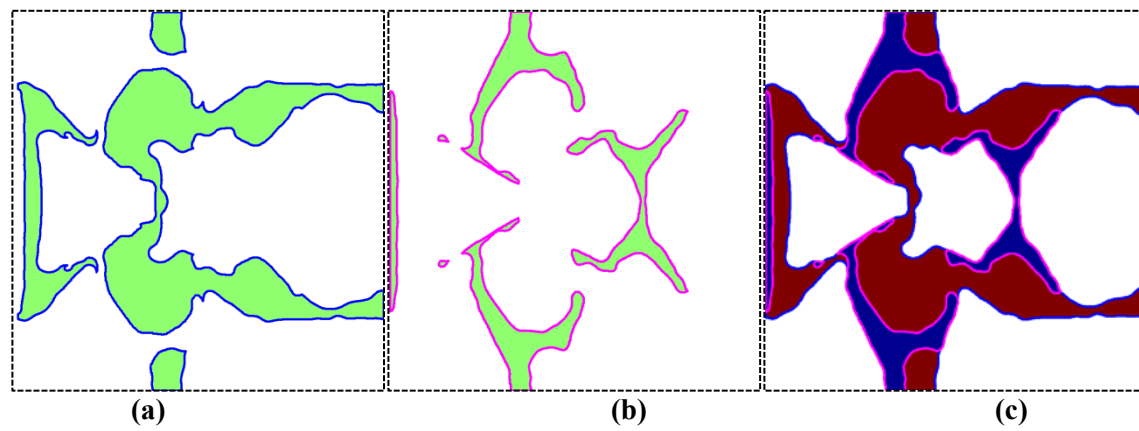
It is said that the extreme thermal expansion can be obtained at the cost of a very low structural stiffness. Thus, to design the metamaterial with extreme thermal expansions in a specific direction, the lower bound of the stiffness should be constrained in the optimization, to make the design physically meaningful. Hence, the lower bound of the bulk modulus is limited to 0.09. According to the final results, it can also be found that to achieve a directional extreme thermal strain will lead to an extreme stiffness at the other direction.

From Case (2) and (3), it can be seen that the generation of re-entrant structures is a key to enable large rotating effect (rigid-body rotations) for a loaded microstructure. However, the topological shape optimization is actually a structural optimization method for continuum structures, which can only make use of structural elastic deformation (strain energy) to mimic rather than create the rigid-body rotations. Hence, it is difficult to allow the microstructure to generate the rotating deformation like conventional rigid-link mechanisms. This may explain the phenomenon that during the optimization process point-to-point hinges or structural disconnections may occur at some local positions of the re-entrant structure. Meanwhile, in the multi-objective optimization problem, two objectives (Poisson's ratio and thermal expansion coefficient) cannot exactly approach the prescribed or the expected values simultaneously. Even so, the proposed optimization method still provided a systematic design method for the microstructure material design with desired elastic and thermoelastic properties.

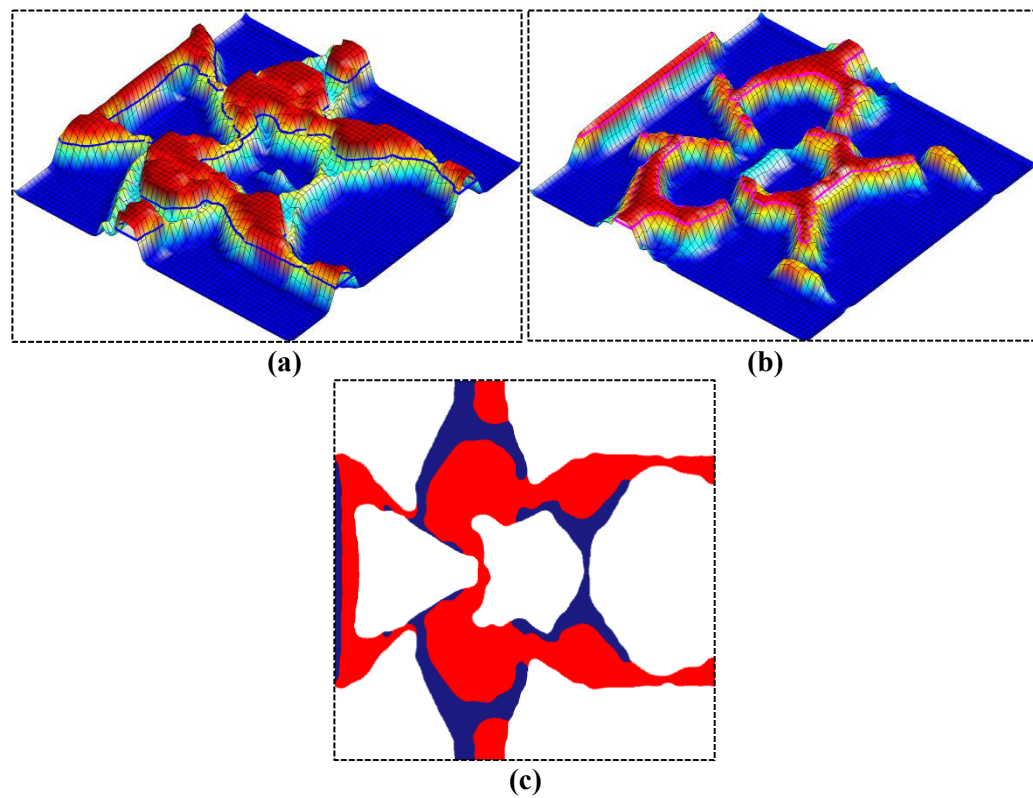
**Table 5-7 Initial parameters and corresponding optimal solutions for Case (3)**

Case	$(\omega_{11}, \omega_{22})$	$(\eta_{1111}, \eta_{2222}, \eta_{1122})$	Objective properties	Optimal effective properties
(3)	(1.80, 0.00)	(0.10, 0.10, 1.00)	$C^{Obj} = 0.08 \begin{bmatrix} 1 & -0.8 & 0 \\ -0.8 & 1 & 0 \\ 0 & 0 & 0 \end{bmatrix}$ <p>Minimize <math>\alpha_{11}</math></p>	$C^H = 0.0732 \begin{bmatrix} 1 & -0.6442 & 0 \\ -0.6442 & 1 & 0 \\ 0 & 0 & 0.1107 \end{bmatrix}$ $\alpha^H = \begin{bmatrix} -3.3560 \\ 3.1220 \\ 0 \end{bmatrix}$

**Figure 5.15 Convergent histories of the objective function**



**Figure 5.16 (a) LS contour of solid 1; (b) LS contour of solid 2;  
(c) LS contours of two solids**



**Figure 5.17 (a) LS surface of solid 1; (b) LS surface of solid 2;  
(c) Material distribution of two solids**

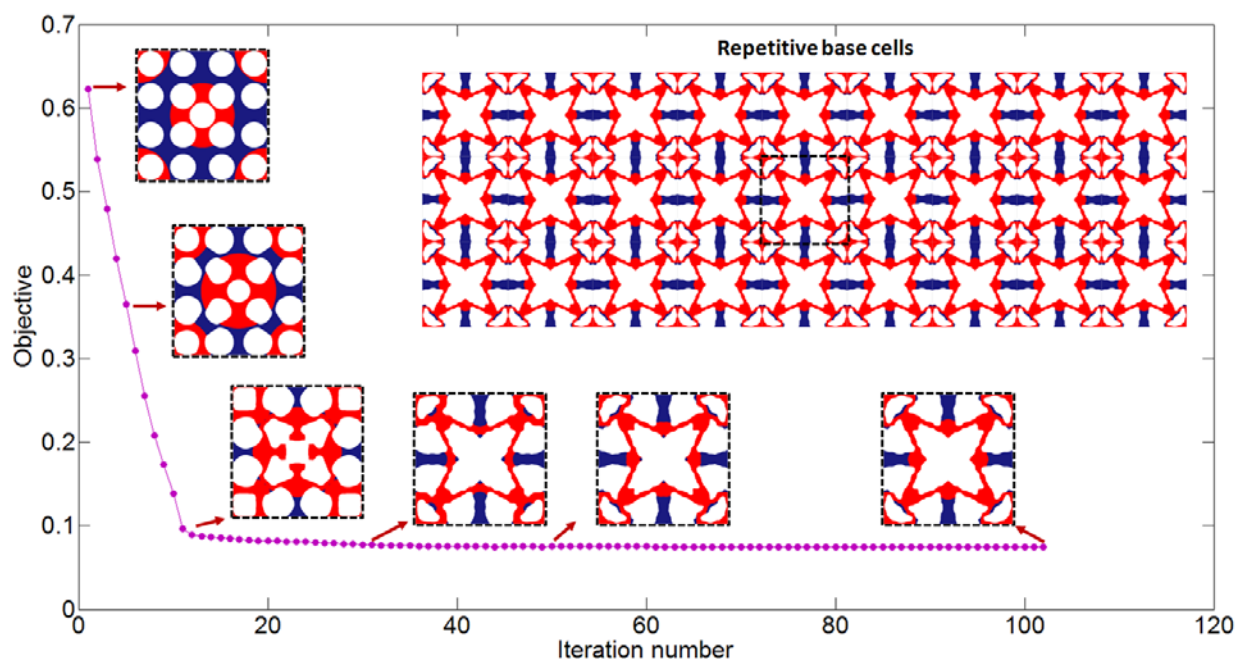
#### *5.4.4.4 Design of Metamaterial with NPR and ZTE: Case (4)*

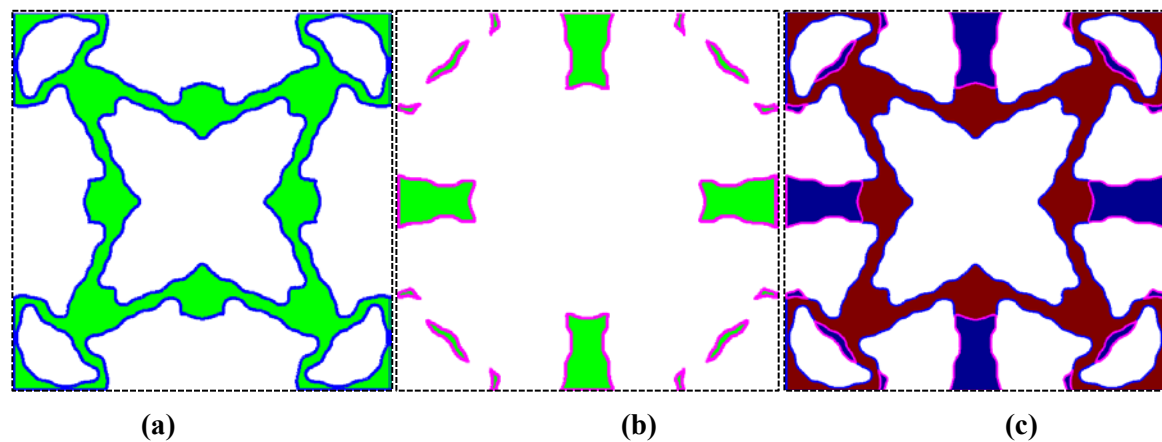
Case (4) is to design the balanced orthotropic (square symmetrical) metamaterial with NPR -0.5 and ZTE. The volume fractions of two solid phases are set to be 0.3 and 0.1, respectively. Other parameters related to the optimization are shown in Table 5-8. The convergence and the topological designs are shown in Figure 5.18. The level set surfaces and the zero level set contours for two solid phases can be seen in Figure 5.19 and 5.20.

This kind of metamaterial with NPR and ZTE can be applied to the engineering applications where controlled thermal expansions are required. For example in the aerospace aviation, deployable antenna is enhanced by the equivalent auxetic (NPR) behaviour used for deep-space missions (Scarpa and Tomlinson 2000). However, spacecraft in deep space missions is operating in an extreme cold environment, and the devices will be supposed to tolerate the harsh environment and operate normally at cryogenic temperatures. In this circumstance, the use of multifunctional metamaterials with NPR and ZTE can significantly reduce thermal stress and improve the resistance of thermal deformation for devices. Other applications, such as blast curtains that open small holes to let the air through but catch flying shards of glass, dental fillings that expand with the tooth or beams that do not change shape at all with temperature, are subjected to a wide range of temperatures. It becomes desirable to apply material with auxetics and zero or low thermal expansion coefficients.

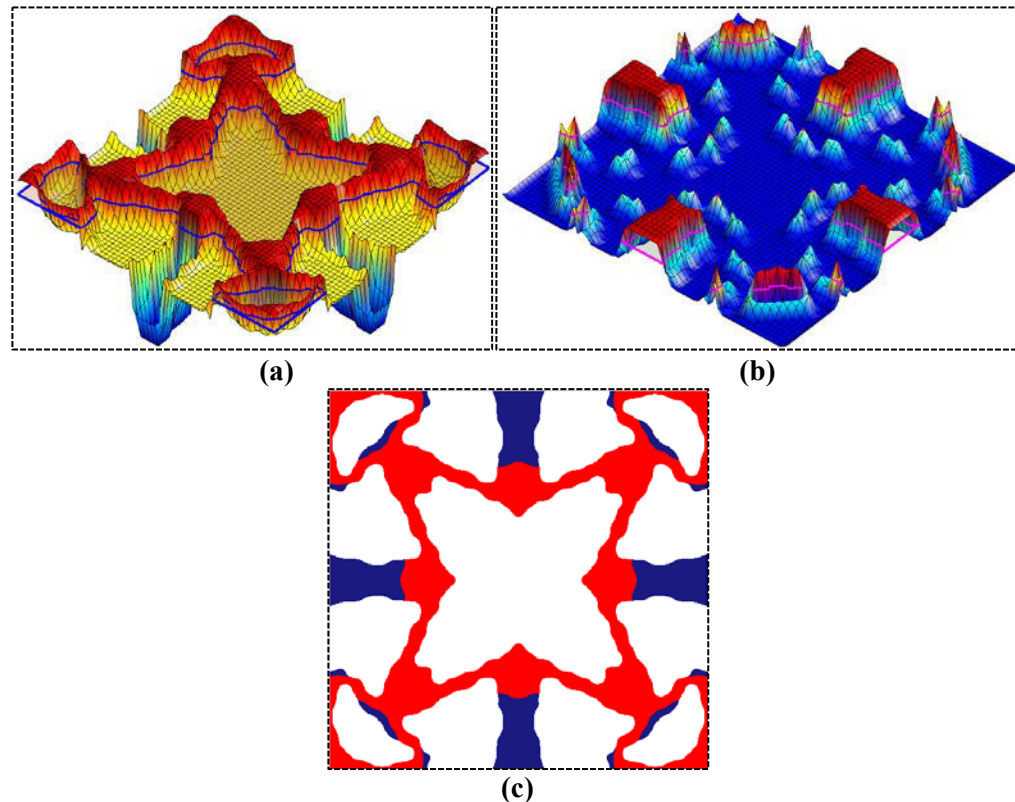
**Table 5-8 Initial parameters and corresponding optimal solutions for Case (4)**

Case	$(\omega_{11}, \omega_{22})$	$(\eta_{1111}, \eta_{2222}, \eta_{1122})$	Objective properties	Optimal effective properties
(2)	(2.00, 2.00)	(0.05, 0.05, 1.00)	$C^{Obj} = 0.04 \begin{bmatrix} 1 & -0.5 & 0 \\ -0.5 & 1 & 0 \\ 0 & 0 & 0 \end{bmatrix}$ $\alpha^{Obj} = \begin{bmatrix} 0 \\ 0 \\ 0 \end{bmatrix}$	$C^H = 0.0616 \begin{bmatrix} 1 & -0.4821 & 0 \\ -0.4821 & 1 & 0 \\ 0 & 0 & 0.06819 \end{bmatrix}$ $\alpha^H = \begin{bmatrix} 0.0821 \\ 0.0821 \\ 0 \end{bmatrix}$

**Figure 5.18 Convergent histories of the objective function**



**Figure 5.19 (a) LS contour of solid 1; (b) LS contour of solid 2; (c) LS contours of two solids**



**Figure 5.20 (a) LS surface of solid 1; (b) LS surface of solid 2; (c) Material distribution of two solids**

### **5.4.5 Summary**

In this section, MPLSM is developed to design the metamaterials with extreme thermal expansion coefficients and multifunctional metamaterials. The capability of creating artificially structured composite metamaterials with specified properties is demonstrated via a series of numerical examples. The extension to three dimensions is straightforward, but computer time will increase dramatically.

# 6 Design of Tissue Engineering Scaffold Architecture

The tissue engineering scaffold is able to provide proper mechanical and mass transport environment to support physiological loading and enhance cell migration and delivery for re-modeling of regenerating tissue. When designing the tissue engineering scaffold, it is required to control the scaffold architecture with multifunctional properties. In this chapter, a systematic topology optimization scheme based on level set method is proposed aiming to design the three dimensional periodic composites with prescribed stiffness, permeability, and porosity. To develop the 3D internal scaffold architecture with desired multifunctional properties, the homogenization method is applied to predict the effective material properties of the composite and the parametric level set method is introduced to find optimized microstructures within the periodical unit cell. To demonstrate the effectiveness and efficiency of applying the PLSM in scaffold design, a range of numerical examples has been conducted to achieve the properties within the cross property bounds between effective bulk modulus and permeability under different porosities.

## 6.1 Homogenization of Elasticity and Permeability

For the design problems in this section, the material is under the assumptions that: material is consist of periodically arranged unit cells; the geometric size of the unit cell is assumed to be much smaller than the bulk material, which justifies scale-decomposition in the homogenization; the effective property of the homogenized microstructure can be predicted by the mechanical behavior of a unit cell. Based on the small parameter perturbation of the

---

displacement, a computational model for the effective properties of the scaffold architecture can be computed by the homogenization method (Hassani and Hinton 1998; Matsui and Terada 2004). The effective elasticity tensor  $\mathbf{C}^H$  relates the macroscopic stress tensor  $\boldsymbol{\sigma}$  to the macroscopic strain tensor  $\boldsymbol{\varepsilon}$  for the porous biomaterial via the linear elasticity law as

$$\boldsymbol{\sigma} = \mathbf{C}^H \boldsymbol{\varepsilon} \quad (6.1)$$

Then, the topological shape optimization will be performed within a unit cell  $Y$ , which is taken as the design domain. The effective stiffness tensor of material can be computed as

$$C_{ijkl}^H = \frac{1}{|Y|} \int_Y (\varepsilon_{pq}^{0(ij)} - \varepsilon_{pq}^{*(ij)}) C_{pqrs} (\varepsilon_{rs}^{0(kl)} - \varepsilon_{rs}^{*(kl)}) dY \quad (6.2)$$

where  $C_{ijkl}^H$  is the effective stiffness tensor,  $\varepsilon^0$  is the unit test strain fields,  $|Y|$  is the volume of the cell,  $Y$  is the area of element  $e$ , and  $\varepsilon^*$  is the strains tensors with the displacement field

$$\varepsilon_{pq}^{*(kl)} = \frac{1}{2} \left( \frac{\partial \chi_p^{kl}}{\partial y_q} + \frac{\partial \chi_q^{kl}}{\partial y_p} \right) \quad (6.3)$$

where  $\chi^{kl}$  is the displacements fields, obtained by solving the following equations:

find  $\chi^{kl} \in U_{period}(Y)$ , such that

$$\int_Y (\varepsilon_{pq}^0 - \varepsilon_{pq}^*(\chi^{ij})) C_{pqrs} \varepsilon_{rs}^*(\nu^{kl}) dY = 0 \quad \forall \nu \in U_{period}(Y) \quad (6.4)$$

where  $\nu$  is virtual displacement field. Since the 3D biomaterial with cubic elastic symmetry is considered in this study, this material has an effective stiffness matrix with three independent components of the form

$$\mathbf{C}^H = \begin{bmatrix} C_{11}^H & C_{12}^H & C_{12}^H & 0 & 0 & 0 \\ C_{12}^H & C_{11}^H & C_{12}^H & 0 & 0 & 0 \\ C_{12}^H & C_{12}^H & C_{11}^H & 0 & 0 & 0 \\ 0 & 0 & 0 & C_{44}^H & 0 & 0 \\ 0 & 0 & 0 & 0 & C_{44}^H & 0 \\ 0 & 0 & 0 & 0 & 0 & C_{44}^H \end{bmatrix} \quad (6.5)$$

The bulk modulus is used to study the resistance of a material to volumetric strain, which is a stiffness measure commonly used in the topology optimization problems. The effective bulk modulus  $B^H$  for the material with cubic elastic symmetry is stated as

$$B^H = \frac{1}{3}C_{11}^H + \frac{2}{3}C_{12}^H \quad (6.6)$$

In macroscopic scale, the permeability of the slowly moving incompressible fluids within porous material can be simulated using the homogenization of Stokes flows through a porous material gives Darcy's law on the macroscopic scale, which states that

$$\mathbf{U} = -\frac{1}{\mu} \mathbf{K}^H \nabla P \quad (6.7)$$

where  $\mathbf{U}$  is the average fluid velocity,  $\nabla P$  is the pressure gradient across the material,  $\mathbf{K}^H$  is the effective fluid permeability tensor and  $\mu$  is the viscosity of the fluid. The numerical approach to the fluid homogenization in this study follows the method described by Guest and Prévost (Guest and Prévost 2006). By applying the Stokes flow and Darcy flow stabilization techniques of Hughes et al. (Hughes et al. 1986), the effective permeability tensor can be computed as

$$\mathbf{K}^H = [K_{ij}^H] = \left[ \frac{1}{|Y|} \int_Y w_{ij} dY \right] = \frac{1}{|Y|} \mathbf{w}^{(i)\top} \mathbf{K}_{ds} \mathbf{w}^{(i)} \quad (6.8)$$

where  $\mathbf{K}^H$  is the effective fluid permeability,  $\mathbf{K}_{ds}$  is Darcy-Stokes viscosity matrix,  $\mathbf{w}^{(i)}$  is the velocity vector solved numerically in the mixed formulation using stabilized finite elements to circumvent the Babuška-Brezzi condition (Guest and Prévost 2006).

The effective permeability tensor, which will take the form:

$$\mathbf{K}^H = \begin{bmatrix} K_{11}^H & 0 & 0 \\ 0 & K_{22}^H & 0 \\ 0 & 0 & K_{33}^H \end{bmatrix} \quad (6.9)$$

For a material with isotropic flow symmetry, it will have  $K_{11}^H = K_{22}^H = K_{33}^H$

The scalar permeability can be computed by

$$k^H = \frac{1}{d} \sum_{i=1}^d K_{ii}^H \quad (6.10)$$

Where  $d$  is the dimensional and equals to 3 in three dimensional problems.

## 6.2 Multi-Objective Optimization Problem

Tissue engineering scaffold is a porous biomaterial designed for mechanical loading and mass transport. To design the composite material with these functions, it requires solving the multi-objective optimization problem.

### 6.2.1 Level Set Material Description Model

At an arbitrary point  $x$ , the elasticity tensor of the material can be stated by

$$\mathbf{C}(x) = \mathbf{C}_{\text{base}} H(\Phi(x)) \quad (6.11)$$

where  $\mathbf{C}_{\text{base}}$  is the elasticity tensor of the material, and  $H(\Phi(x))$  is the Heaviside function of the LSF  $\Phi(x)$  at the point  $x$ .

For the permeability, the material interpolation is conducted when assemble the Darcy-Stokes viscosity matrix  $\mathbf{K}_{\text{ds}}$  as

$$\mathbf{K}_{\text{ds}}(x) = \mathbf{K}_{\text{d}} H(\Phi(x)) + \mathbf{K}_{\text{s}} [1 - H(\Phi(x))] \quad (6.12)$$

where  $\mathbf{K}_{\text{d}}$  is Darcy stiffness tensor and  $\mathbf{K}_{\text{s}}$  is Stokes stiffness tensor. It means that flow through the solid phase is governed by Darcy's law, while the fluid phase is treated as Stokes flow.

Assuming the design domain with volume  $|Y|$ , the porosity of material can be calculated as

$$\mathbf{V} = 1 - \frac{1}{|Y|} \int_Y H(\Phi(x)) dY \quad (6.13)$$

### 6.2.2 Formulation of the Optimization Problem by PLSM

In order to achieve the material properties directly, the optimization problem was defined to minimize the error between the target and the effective bulk modulus and permeability, with constraints on porosity, which is of the form

$$\begin{cases}
 \text{Find } \mathbf{c} \\
 \text{minimize } J = \omega_B (B^H(\mathbf{c}) - B^*)^2 + \omega_k (k^H(\mathbf{c}) - k^*)^2 \\
 \text{subject to } \mathbf{V}(\mathbf{c}) = \mathbf{V}^* \\
 \quad \mathbf{g}(\mathbf{C}^H(\mathbf{c}), \mathbf{K}^H(\mathbf{c})) \leq 0 \\
 \quad \mathbf{h}(\mathbf{c}) = 0
 \end{cases} \quad (6.14)$$

Here  $\mathbf{a}$  is the vector of design variables,  $B^*$  and  $k^*$  correspond to the effective bulk modulus and conductivity of the material microstructure,  $\mathbf{V}^*$  is the required porosity of the porous material, and  $\mathbf{V}(\mathbf{c})$  is the porosity of the material calculated. In practice the porosity constraint is implemented with a tolerance of 1%. The equality constraint  $\mathbf{h}(\mathbf{c}) = 0$  represents the homogenization and associated equilibrium equations. The inequalities  $\mathbf{g}(B^H(\mathbf{c}), k^H(\mathbf{c})) \leq 0$  represent the constraints on the effective constitutive tensors, including symmetry constraints. We will consider cubic symmetry for the elastic properties with isotropic flow symmetry in the study.  $\omega_B$  and  $\omega_k$  are weights which can be chosen to dictate the relative importance of the two objectives in our multi-objective design problem.

The variation of  $C_{ijkl}^H$  with respect to the perturbation of the boundaries for LSF  $\Phi$  can refer to the sensitivity analysis in section 5.3.4.1

Similarly, the sensitivity of  $K_{kl}^H$  with respect to the parameters  $\alpha_i$  is

$$\frac{\partial K_{kl}^H}{\partial c_i} = \frac{1}{|Y|} \int_Y \mathbf{w}^{(i)\top} (\delta(\Phi) \mathbf{K}_d - \delta(\Phi) \mathbf{K}_s) \mathbf{w}^{(j)} \varphi_i(\mathbf{x}) dY \quad (i = 1, 2, \dots, N) \quad (6.15)$$

The sensitivity of the volume constraint (porosity) is

$$\frac{\partial \mathbf{V}}{\partial c_i} = -\frac{1}{|Y|} \int_Y \delta(\Phi) \varphi_i(\mathbf{x}) dY \quad (i = 1, 2, \dots, N) \quad (6.16)$$

### 6.3 Numerical Implementation of the Multi-Objective Topology Optimization Problem

In the numerical implementation, the “artificial” material model will be used for the solid phase and the periodic boundary condition will be applied to the design domain of the unit cell. Geometrical symmetries of the unit cell are considered to achieve cubic elastic symmetric material phase and isotropic flow phase. The standard finite element method (FEM) is employed to discretize the unit cell in order to obtain the displacement field. In this study, the 8-node isoparametric elements will be used to discretise the design domain. The LSF in which the shape and topology are implicitly represented is sampled by using the CS-RBFs at the positions of elemental nodes only for the simplicity, as given in Eq. (14). It should be noted that the CS-RBFs knots are not necessarily at the same positions as the finite element nodes.

When the boundary crosses a 3D element, it is usually hard to accurately calculate strain and stiffness for the elements cut by the moving boundary. To resolve this problem, there have been several methods available, such as, the widely used “ersatz” model (Allaire et al. 2004). In this study, an alternative scheme which is numerically more accurate is applied to evaluate the strain field, based on the computational points ( $3 \times 3 \times 3$  Gauss points) of the element. The solid or void material property for each Gaussian point is evaluated by using the interpolation of CS-RBFs and the materials properties at those elemental nodes located within a compact support domain, and the Gaussian points are used as the computational

points to approximate the strain and stiffness quantities of those 3D finite elements crossed by the moving level-set boundary.

In the numerical implementation, the “artificial” material model will be used for the solid phase and the periodic boundary condition will be applied to the design domain of the unit cell. Geometrical symmetries of the unit cell are considered to achieve cubic elastic symmetric material phase and isotropic flow phase. The standard finite element method (FEM) is employed to discretize the unit cell in order to obtain the displacement field. Here the 8-node isoparametric elements are used with  $3 \times 3 \times 3$  Gauss points as computational points. The equilibrium equations for the homogenization problem are solved using the FEM to calculate the effective material properties. The topology at each iteration is described using a level set function, denoted by  $\Phi$ . A positive value for  $\Phi$  indicates solid phase and a negative value corresponds to void/fluid phase. Meanwhile, the displacement and strain fields are also evaluated based on the points within the influence domain. Thus, the Gauss quadrature can be used to calculate the integrations with high numerical accuracy.

## **6.4 Numerical Examples**

A number of numerical examples are used to demonstrate the effectiveness of the proposed approach in designing the scaffold architecture with the prescribed stiffness and mass transport properties. The artificial material is supposed to have Young’s modulus  $E=1$  and Poisson’s ratio  $\nu=0.3$ . The goal of the design is to achieve target design points with specified effective bulk modulus and permeability within the cross-property upper bounds. For simplicity, the CS-RBF knots are set at the positions of the finite element nodes and the radius of CS-RBF is set to be 2.5 times of the average density point distance in the

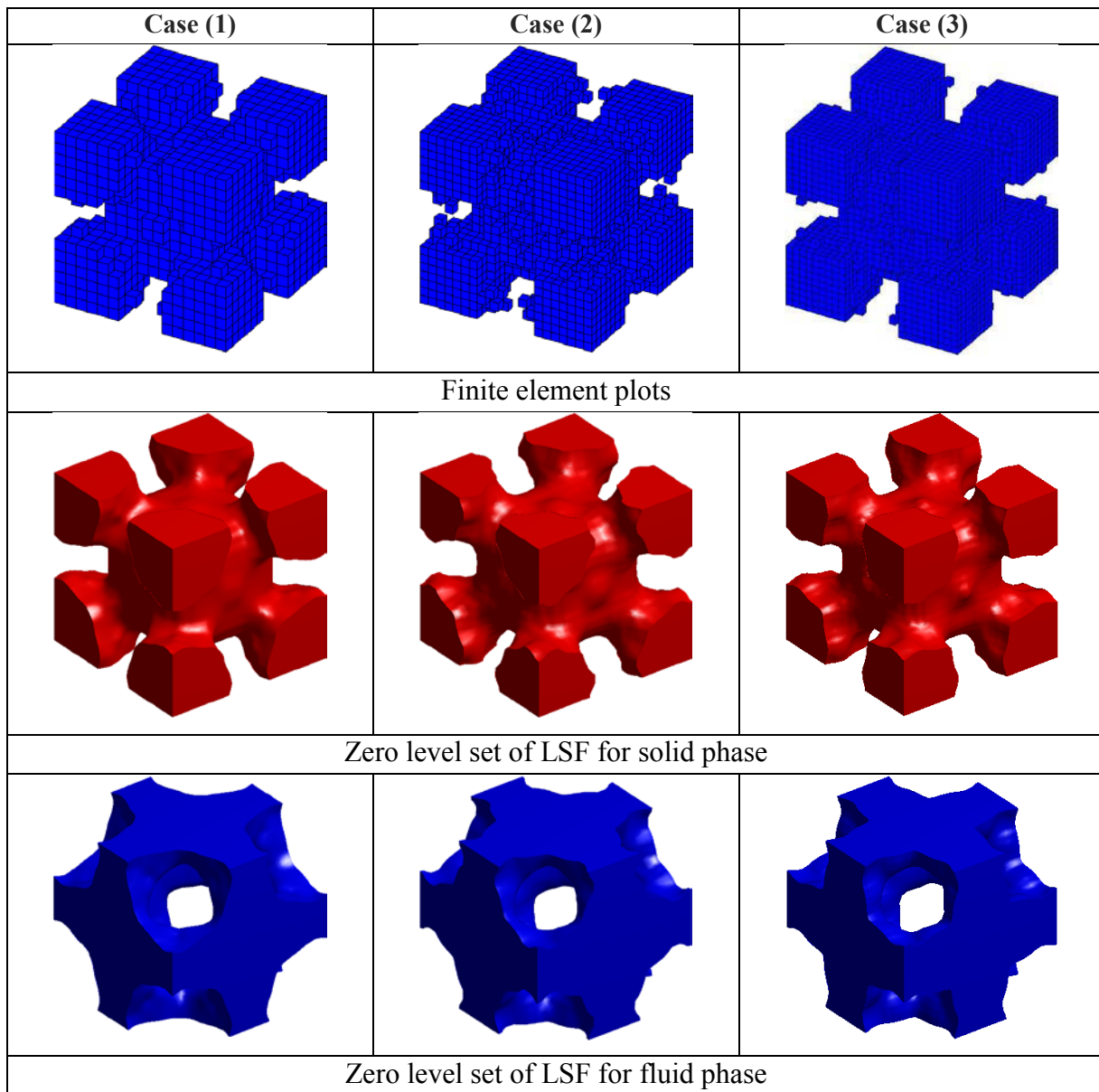
---

numerical examples. Different finite element meshes and different porosities will be used to investigate the effectiveness of the proposed design optimization methodology.

#### **6.4.1 Design Results with Different Mesh Level**

In this section, the microstructure with the porosity 50% and the prescribed bulk modulus 0.22 and permeability 0.0005 is optimized under different meshes, such as  $15 \times 15 \times 15 = 3375$ ,  $20 \times 20 \times 20 = 8000$  and  $25 \times 25 \times 25 = 15625$ . The optimization parameters and the properties of the microstructure are given in Table 6.1, and the final results are shown in Figure 6.1. It is noted that the “Finite Element Plots” are actually elemental stiffness plots. We can firstly obtain the properties over the Gaussian points for any single element, and then it is straightforwardly to plot the element stiffness using the Matlab function. From the finite element plots of the design, it can be found that the optimal topologies are almost the same with different meshes. Furthermore, with the increase of the number of finite elements, the effective properties of the optimized microstructure change slightly, but more iterations and longer computational time are required for the design to converge.

Based on the optimal topology at the zero level set, we can find that the boundary of the material phase is smooth and the material interface is distinct. For most numerical methods a finer mesh may be more suitable for a better description of the boundary condition and a better approximation of the field quantities. As a result, a higher resolution should benefit the topology and shape design, but the computational cost will increase. In this study, the mesh resolution is determined based on our numerical experience, more or less.



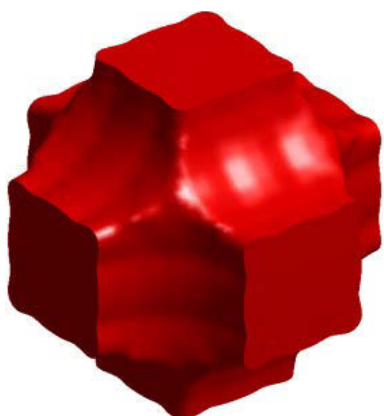
**Figure 6.1 Optimization results for porosity 50% under different mesh level**

**Table 6-1 Optimization parameters and properties of designed microstructures**

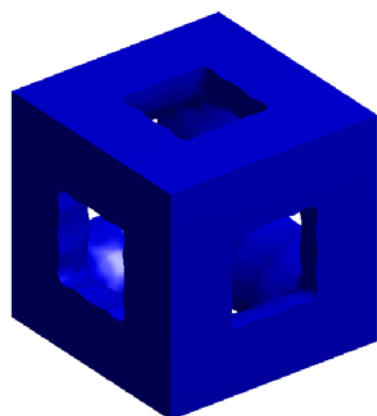
Case	Meshes	Elements	Computational points	Iterations	Achieved porosity	Achieved bulk modulus	Achieved permeability
(1)	$15 \times 15 \times 15$	3,375	91,125	136	50.7545%	0.2167	0.000505
(2)	$20 \times 20 \times 20$	8,000	216,000	199	50.7275%	0.2168	0.000506
(3)	$25 \times 25 \times 25$	15,625	421,875	195	50%	0.2168	0.000505

### **6.4.2 Convergent Histories**

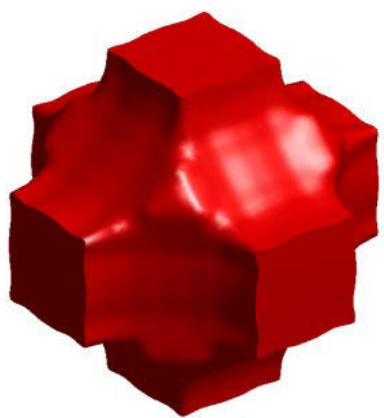
To save the computational time, the mesh for this numerical case is  $15 \times 15 \times 15 = 3375$ . The problem is to design the microstructure under porosity 70% with target effective bulk modulus 0.072 and permeability 0.0028. The evolution of the topology for solid phase and fluid phase during the optimization process are shown in Figure 6.2, and the optimal design arranged in a  $2 \times 2 \times 2$  array is present in Figure 6.3. The parameters of effective permeability tensor and elasticity tensor for the optimal design are given in (6.17). According to the convergent histories shown in Figure 6.4, it can be found that the implicit level set representation (Wang et al. 2003; Allaire et al. 2004) has unique feature which can ensure all the designs including the intermediate designs to have smooth boundary and distinct interface. Furthermore, we can see that the proposed level set approach is able to integrate shape optimization and topology optimization simultaneously as a procedure of topological shape optimization. It is easy to see that the evolution of the topology is completed within the first 40 iterations, and the rest 100 iterations are mainly used to complete the shape variations. Compared with the conventional LSMs, e.g. (Wang et al. 2003; Wang and Wang 2004; Wang et al. 2012), the proposed method has been approved to be more efficient and it can find the optimal design within 150 iterations.



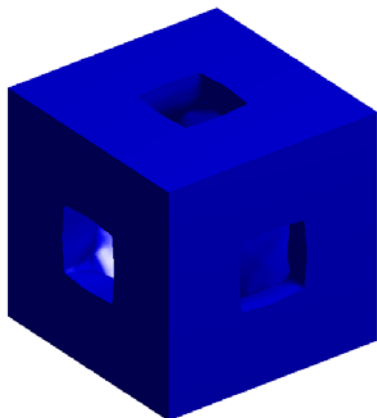
(a1)



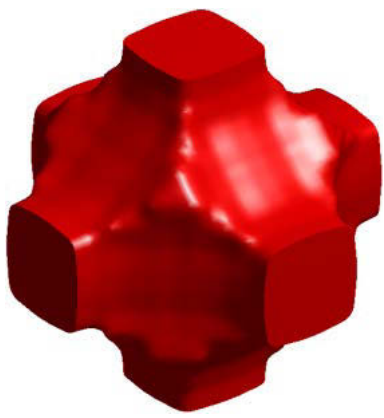
(b1)



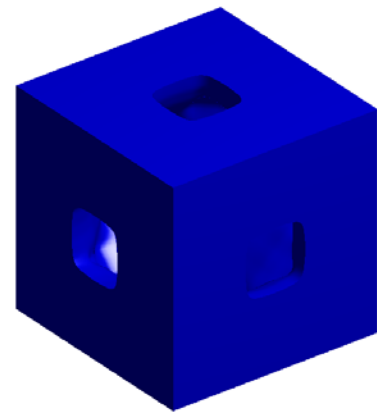
(a2)



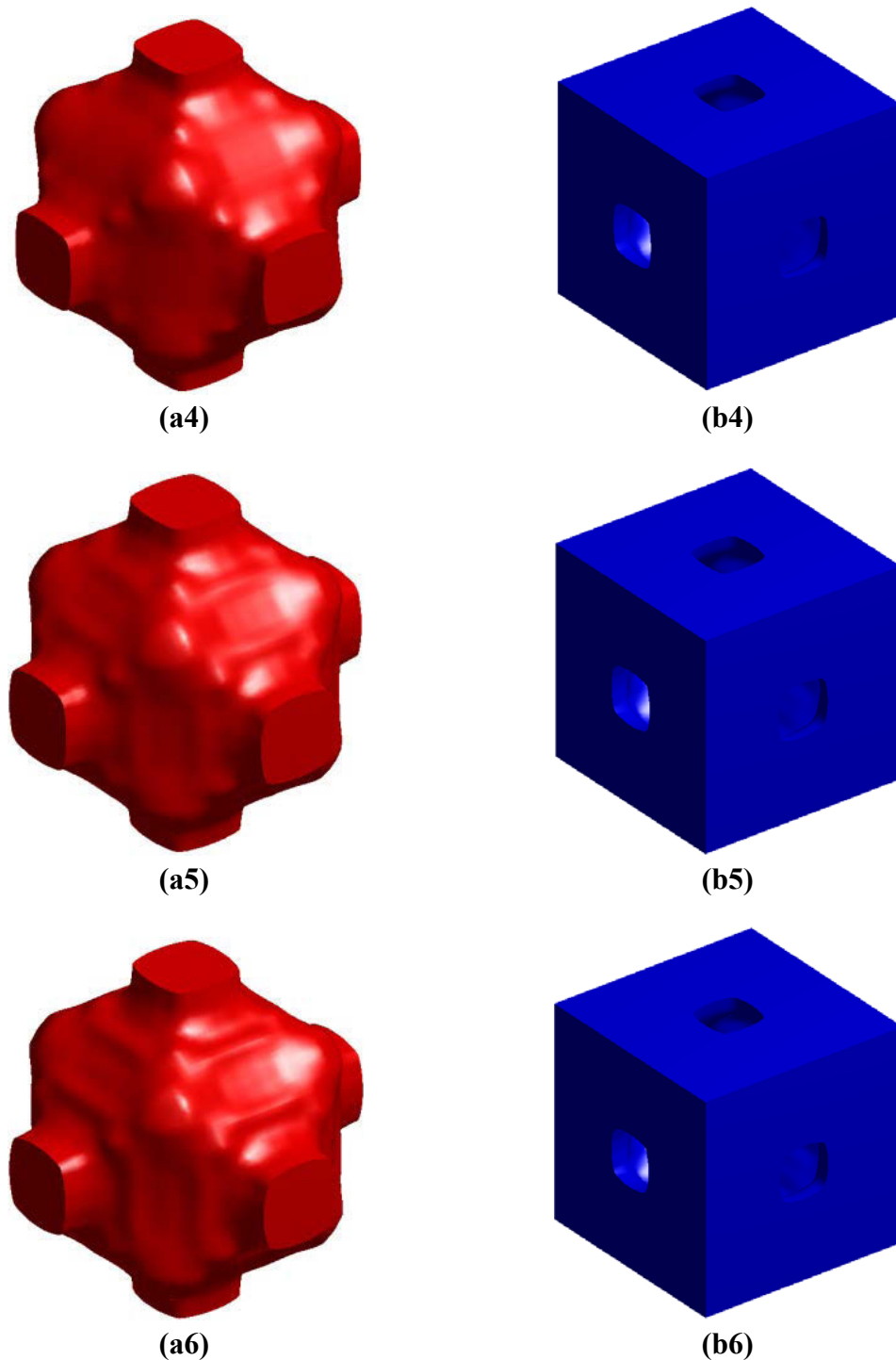
(b2)



(a3)

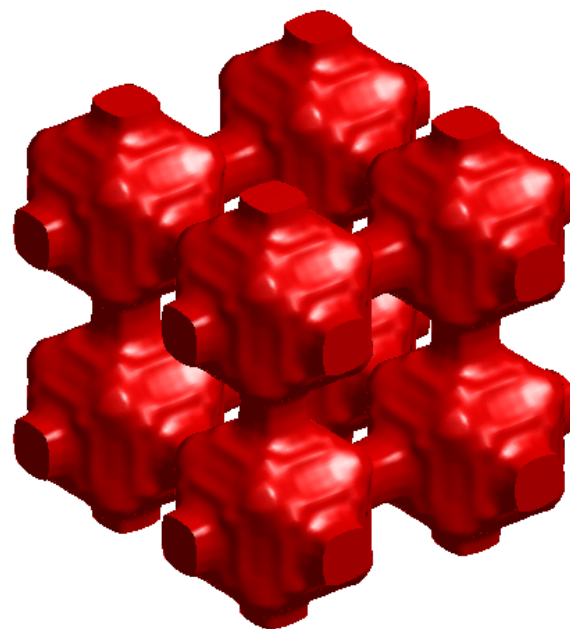


(b3)

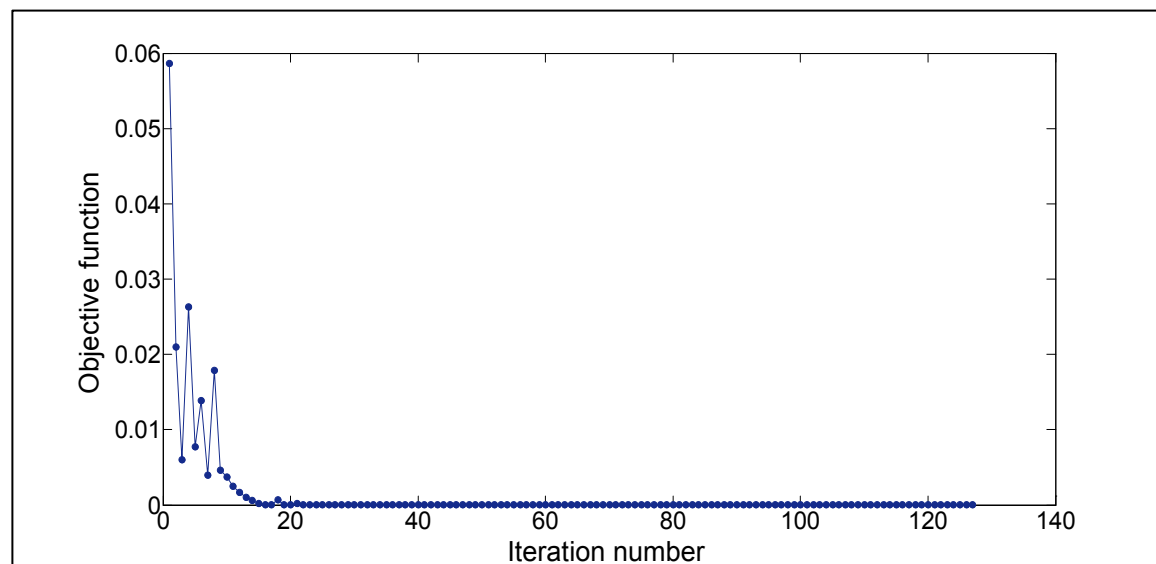


**Figure 6.2 The optimization process of microstructured metamaterial**

(a1-6) solid phase and (b1-6) fluid phase: (1) initial design; (2-5) are the distribution of material at iteration 4, 10, 45, and 90; (6) optimized design.



**Figure 6.3 Repetitive unit cell of the optimal configuration**



**Figure 6.4 Convergent histories of the objective function**

$$\begin{aligned}
 \mathbf{C}^H &= \begin{bmatrix} 0.165 & 0.0208 & 0.0208 & 0 & 0 & 0 \\ 0.0208 & 0.165 & 0.0208 & 0 & 0 & 0 \\ 0.0208 & 0.0208 & 0.165 & 0 & 0 & 0 \\ 0 & 0 & 0 & 0.0321 & 0 & 0 \\ 0 & 0 & 0 & 0 & 0.0321 & 0 \\ 0 & 0 & 0 & 0 & 0 & 0.0321 \end{bmatrix} \\
 \mathbf{K}^H &= \begin{bmatrix} 0.0029 & 0 & 0 \\ 0 & 0.0029 & 0 \\ 0 & 0 & 0.0029 \end{bmatrix}
 \end{aligned} \tag{6.17}$$

### 6.4.3 Optimal Designs with Different Porosities

In this section, we will design microstructures to have a range of effective bulk moduli and permeability values with different porosities. The optimal microstructures with 40%, 50%, and 70% porosities are designed to satisfy the prescribed cross-property parameters. The optimized material microstructures presented in Table 6-2 to 6-4 are similar to the microstructures given in (Guest and Prévost 2006; Chen et al. 2011; Challis et al. 2012). The parameters for different cases are given in Table 6-5. The results show how scaffold architecture affects tissue regeneration, since scaffolds can be fabricated to have different stiffness and permeability values for the same porosity.

It can be found that different initial guesses may result in different optimized microstructures. This phenomenon refers to multiple local solutions due to non-convexity of optimization problem with the homogenized material, even if the MMA that has a strong ability for searching a global optimal solution is employed as the optimizer. It is noted in Guedes et al. (2003) that different initial designs may lead to different microstructural

architecture designs, although the effective properties of the optimization are almost identical. Another reason is that for the whole structure consisting of arrays of periodic unit cells, each unit cell is under periodic boundary condition. Thus the microstructural pattern for repeatedly assembling the same macro structure is not unique, which depends on how to identify or extract the unit cell from the whole periodic material, which is noted in Lin et al. (2004) as well.

We should also note that for the 3D microstructure design, although the final topologies may be similar at the first sight, their detailed geometric features and fine shapes will be different. This indicates that the final properties of the optimized scaffold are not only determined by the topology of the material layout but also by the shape and fine local geometrical details of the internal surface, particularly for the design involving the surface/boundary dependent conditions. As illustrated in Table 6.2-4, different architecture of scaffold microstructures will give rise to different effective stiffness and permeability even under the same porosity. The porosity plays an important role in determining macroscopic properties of the scaffold as well. The range of stiffness can be achieved is constrained by the bounds on effective stiffness derived by Hashin and Shtrikman (1963). Furthermore, it can be seen from the computational results that the arrangement of holes will have a high effect on the effective permeability. It is also noted by Hollister (2005) that for a specified scaffold design the effective permeability will decrease with increase of material, and effective permeability is only determined by the 3D hole arrangement. In addition, based on the equation for calculating the effective permeability, the value of effective permeability is dependent on the fluid velocities in the unit cell.

Table 6-2 Optimal designs of scaffold architecture under the porosity 40%

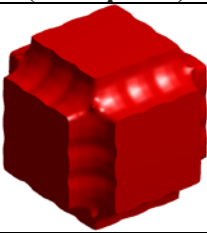
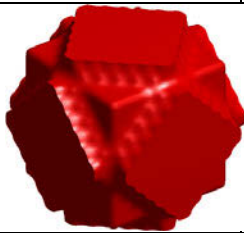
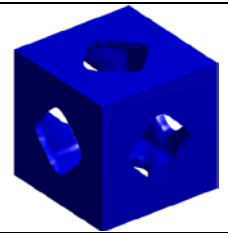
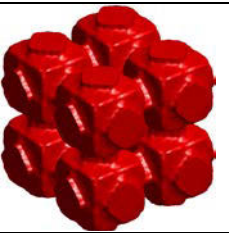
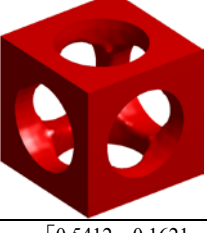
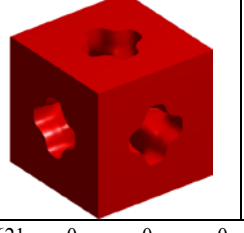
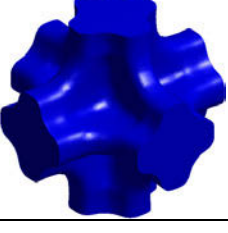
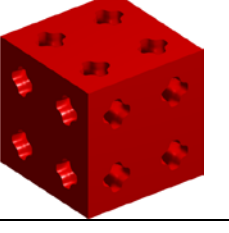
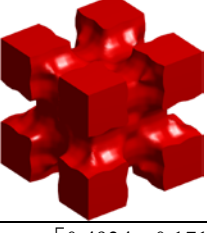
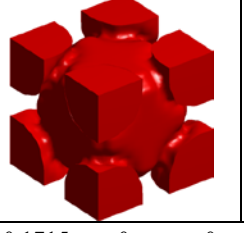
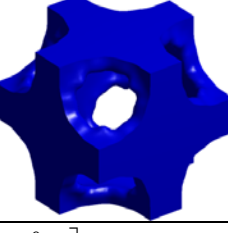
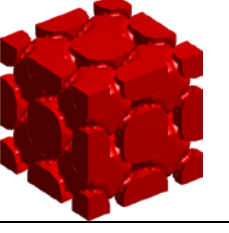
	Initial guess (Solid phase)	Solid phase	Fluid phase	2×2×2 array
Case (a)				
Parameters of material properties	$C^H = \begin{bmatrix} 0.6311 & 0.2099 & 0.2099 & 0 & 0 & 0 \\ 0.2099 & 0.6311 & 0.2099 & 0 & 0 & 0 \\ 0.2099 & 0.2099 & 0.6311 & 0 & 0 & 0 \\ 0 & 0 & 0 & 0.1698 & 0 & 0 \\ 0 & 0 & 0 & 0 & 0.1698 & 0 \\ 0 & 0 & 0 & 0 & 0 & 0.1698 \end{bmatrix} ; K^H = \begin{bmatrix} 0.0035 & 0 & 0 \\ 0 & 0.0035 & 0 \\ 0 & 0 & 0.0035 \end{bmatrix}$			
Initial guess (Solid phase)	Solid phase	Fluid phase	2×2×2 array	
Case (b)				
Parameters of material properties	$C^H = \begin{bmatrix} 0.5412 & 0.1621 & 0.1621 & 0 & 0 & 0 \\ 0.1621 & 0.5412 & 0.1621 & 0 & 0 & 0 \\ 0.1621 & 0.1621 & 0.5412 & 0 & 0 & 0 \\ 0 & 0 & 0 & 0.1513 & 0 & 0 \\ 0 & 0 & 0 & 0 & 0.1513 & 0 \\ 0 & 0 & 0 & 0 & 0 & 0.1513 \end{bmatrix} ; K^H = \begin{bmatrix} 0.3808 \times 10^{-3} & 0 & 0 \\ 0 & 0.3808 \times 10^{-3} & 0 \\ 0 & 0 & 0.3808 \times 10^{-3} \end{bmatrix}$			
Initial guess (Solid phase)	Solid phase	Fluid phase	2×2×2 array	
Case (c)				
Parameters of material properties	$C^H = \begin{bmatrix} 0.4924 & 0.1715 & 0.1715 & 0 & 0 & 0 \\ 0.1715 & 0.4924 & 0.1715 & 0 & 0 & 0 \\ 0.1715 & 0.1715 & 0.4924 & 0 & 0 & 0 \\ 0 & 0 & 0 & 0.1721 & 0 & 0 \\ 0 & 0 & 0 & 0 & 0.1721 & 0 \\ 0 & 0 & 0 & 0 & 0 & 0.1721 \end{bmatrix} ; K^H = \begin{bmatrix} 0.0024 & 0 & 0 \\ 0 & 0.0024 & 0 \\ 0 & 0 & 0.0024 \end{bmatrix}$			

Table 6-3 Optimal designs of scaffold architecture under the porosity 50%

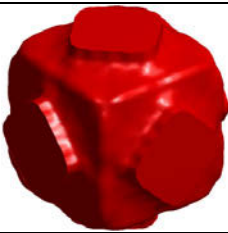
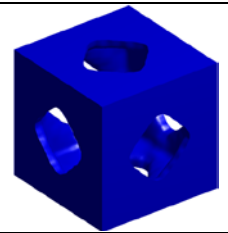
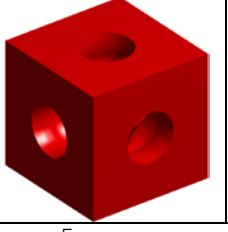
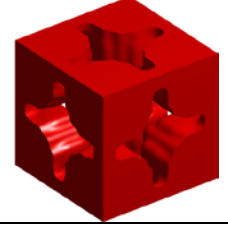
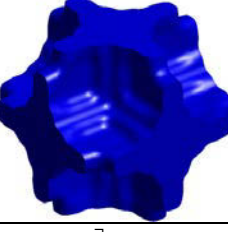
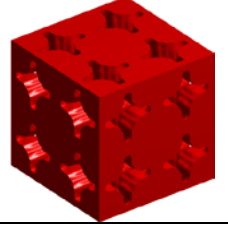
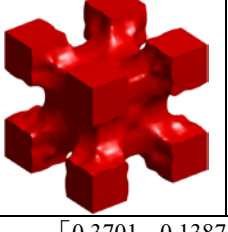
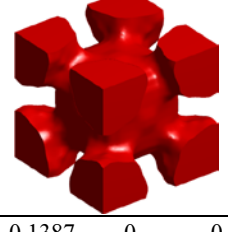
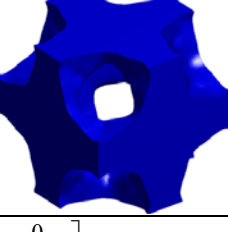
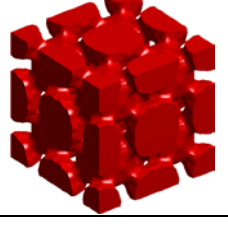
	Initial guess (Solid phase)	Solid phase	Fluid phase	2×2×2 array
	Case (d)			
Parameters of material properties	$C^H = \begin{bmatrix} 0.3645 & 0.0847 & 0.0847 & 0 & 0 & 0 \\ 0.0847 & 0.3645 & 0.0847 & 0 & 0 & 0 \\ 0.0847 & 0.0847 & 0.3645 & 0 & 0 & 0 \\ 0 & 0 & 0 & 0.0936 & 0 & 0 \\ 0 & 0 & 0 & 0 & 0.0936 & 0 \\ 0 & 0 & 0 & 0 & 0 & 0.0936 \end{bmatrix}; K^H = \begin{bmatrix} 0.007 & 0 & 0 \\ 0 & 0.007 & 0 \\ 0 & 0 & 0.007 \end{bmatrix}$			
Case (e)	Initial guess (Solid phase)	Solid phase	Fluid phase	2×2×2 array
Parameters of material properties				
Parameters of material properties	$C^H = \begin{bmatrix} 0.1524 & 0.0164 & 0.0164 & 0 & 0 & 0 \\ 0.0164 & 0.1524 & 0.0164 & 0 & 0 & 0 \\ 0.0164 & 0.0164 & 0.1524 & 0 & 0 & 0 \\ 0 & 0 & 0 & 0.0392 & 0 & 0 \\ 0 & 0 & 0 & 0 & 0.0392 & 0 \\ 0 & 0 & 0 & 0 & 0 & 0.0392 \end{bmatrix}; K^H = \begin{bmatrix} 0.008 & 0 & 0 \\ 0 & 0.008 & 0 \\ 0 & 0 & 0.008 \end{bmatrix}$			
Case (f)	Initial guess (Solid phase)	Solid phase	Fluid phase	2×2×2 array
Parameters of material properties				
Parameters of material properties	$C^H = \begin{bmatrix} 0.3701 & 0.1387 & 0.1387 & 0 & 0 & 0 \\ 0.1387 & 0.3701 & 0.1387 & 0 & 0 & 0 \\ 0.1387 & 0.1387 & 0.3701 & 0 & 0 & 0 \\ 0 & 0 & 0 & 0.1421 & 0 & 0 \\ 0 & 0 & 0 & 0 & 0.1421 & 0 \\ 0 & 0 & 0 & 0 & 0 & 0.1421 \end{bmatrix}; K^H = \begin{bmatrix} 0.0011 & 0 & 0 \\ 0 & 0.0011 & 0 \\ 0 & 0 & 0.0011 \end{bmatrix}$			

Table 6-4 Optimal designs of scaffold architecture under the porosity 70%

Case (g)	Initial guess (Solid phase)	Solid phase	Fluid phase	2×2×2 array
Parameters of material properties	$C^H = \begin{bmatrix} 0.0979 & 0.0416 & 0.0416 & 0 & 0 & 0 \\ 0.0416 & 0.0979 & 0.0416 & 0 & 0 & 0 \\ 0.0416 & 0.0416 & 0.0979 & 0 & 0 & 0 \\ 0 & 0 & 0 & 0.0534 & 0 & 0 \\ 0 & 0 & 0 & 0 & 0.0534 & 0 \\ 0 & 0 & 0 & 0 & 0 & 0.0534 \end{bmatrix}$		$; K^H = \begin{bmatrix} 4.422 \times 10^{-4} & 0 & 0 \\ 0 & 4.422 \times 10^{-4} & 0 \\ 0 & 0 & 4.422 \times 10^{-4} \end{bmatrix}$	
Case (h)	Initial guess (Solid phase)	Solid phase	Fluid phase	2×2×2 array
Parameters of material properties	$C^H = \begin{bmatrix} 0.1650 & 0.0208 & 0.0208 & 0 & 0 & 0 \\ 0.0208 & 0.1650 & 0.0208 & 0 & 0 & 0 \\ 0.0208 & 0.0208 & 0.1650 & 0 & 0 & 0 \\ 0 & 0 & 0 & 0.0321 & 0 & 0 \\ 0 & 0 & 0 & 0 & 0.0321 & 0 \\ 0 & 0 & 0 & 0 & 0 & 0.0321 \end{bmatrix}$		$; K^H = \begin{bmatrix} 0.0029 & 0 & 0 \\ 0 & 0.0029 & 0 \\ 0 & 0 & 0.0029 \end{bmatrix}$	
Case (i)	Initial guess (Solid phase)	Solid phase	Fluid phase	2×2×2 array
Parameters of material properties	$C^H = \begin{bmatrix} 0.1960 & 0.0298 & 0.0298 & 0 & 0 & 0 \\ 0.0298 & 0.1960 & 0.0298 & 0 & 0 & 0 \\ 0.0298 & 0.0298 & 0.1960 & 0 & 0 & 0 \\ 0 & 0 & 0 & 0.0379 & 0 & 0 \\ 0 & 0 & 0 & 0 & 0.0379 & 0 \\ 0 & 0 & 0 & 0 & 0 & 0.0379 \end{bmatrix}$		$; K^H = \begin{bmatrix} 2.269 \times 10^{-4} & 0 & 0 \\ 0 & 2.269 \times 10^{-4} & 0 \\ 0 & 0 & 2.269 \times 10^{-4} \end{bmatrix}$	

**Table 6-5 Initial parameters and corresponding optimal solutions**

<b>Case</b>	$(\omega_B, \omega_k)$	$B^*$	$k^*$	$B^H$	$k^H$
(a)	(1.00, 0.2)	0.2	0.005	0.3369	0.0035
(b)	(1.00, 0.1)	0.28	0.001	0.2849	0.0003808
(c)	(1.00, 0.2)	0.26	0.005	0.2786	0.0024
(d)	(1.00, 0.5)	0.18	0.005	0.18	0.007
(e)	(1.00, 0.5)	0.1	0.01	0.0693	0.008
(f)	(1.00, 0.02)	0.22	0.002	0.2167	0.0011
(g)	(1.00, 0.02)	0.06	0.001	0.0643	0.0004422
(h)	(1.00, 0.02)	0.07	0.005	0.0726	0.0029
(i)	(1.00, 0.02)	0.085	0.0005	0.0879	0.0002669

Since the results have achieved a range of effective bulk modulus, we employed the upper Hashin-Shtrikman bound for the bulk modulus to demonstrate the ability of designing the microstructures by the proposed optimization method. According to Figure 6.5, it can be found that the bulk modulus of the designed material are within the upper Hashin-Shtrikman bound. It is noted by Sigmund (2002) that the requirement of preserving mass transport will restricts the designed microstructures from reaching theoretical upper stiffness bounds. Only considering the optimization of stiffness will lead to closed unit cell architectures which achieve theoretical upper bounds. This can explain why microstructure optimized with a fluid conductance constraint cannot achieve the upper bounds.

In this study, not to achieve maximum effective elastic properties or permeability with a constraint on porosity, the topology optimization approach is used to generate new microstructures with desired properties for scaffold whose properties match those of natural bone tissue. There are many potential applications for topology optimized biomaterial

scaffolds in clinical research. The designed microstructure with a 40% and 50% porosity and high stiffness can be used for fracture fixation and fusion. For spinal cage, it requires a scaffold with sufficient load bearing and limited displacement to ensure bone healing. The microstructures like case (a) and case (f), which almost reach the upper bound of effective stiffness, can be considered in this application. The microstructures with high porosity 70% would be suitable for human trabecular bone such as distal femoral and iliac crest. Scaffold with low stiffness and low permeability are needed for cartilage tissue engineering applications. Such microstructures within the interior of the cross property bounds and away from the upper limits as case g and case i can satisfy the requirements. Considering base material used in this study is artificial, it cannot be compared with the values of material properties for real human tissues. Nevertheless, the optimized microstructures with a range of cross properties can still provide a significant reference on designing the scaffold architectures with controlled material properties.

Furthermore, to illustrate the validity of the numerical results, the obtained property pairs of the microstructures are compared with the properties of bi-optimal porous materials by Challis et al. (2012). The bi-optimal porous material design from by Challis et al. (2012) is obtained by setting equal weighting factors in the objective function ( $\omega_B = \omega_k = 0.5$ ). To clarify the comparison, the computational results from Challis et al. (2012) (the properties of porous material under porosity 10%, 25%, 50%, 75% and 90%) are plotted into a trend line as shown in Fig. 6.6. Taking into account that the different weightings for effective stiffness and permeability set in the objective function and different the target properties, the properties obtained by the proposed optimization method are reasonably around the bi-

optimal cross-property lines. The designed microstructure under the given porosity 50%, case d, shows a close value of cross-property and identical topology with results provided by Challis. It is not surprised to find out the under the same porosity, the topology optimization can achieve a large fluctuation in material properties. The variance of effective stiffness is caused by the different layout of solid material, while effective permeability are influenced by the size and shape of the 3D pores and pore connectivity. To meet the needs of scaffold design, the goal of this study is to achieve a range of cross-properties by distributing a given amount of material with different layouts.

In tissue engineering, the ability to control the architecture of microstructure can provide significant insights to study architectural effect on the biological delivery and tissue regeneration. However, besides the initial studies of designed microstructure, there are many issues remaining to be investigated, for example: How these designed characteristics affect the biological performance? How the material degradation and tissue ingrowth effect on architectural characteristics over the healing time. To address these issues, it requires substantial *in vivo* experimental data. Meanwhile, a number of biophysical stimulus (Kelly and Prendergast 2006; Byrne et al. 2007; Chen and Chan 2007) have developed to provide a insights into design of biodegradable scaffold microstructures. These solutions are conducted based on using scaffolds with designed architecture.

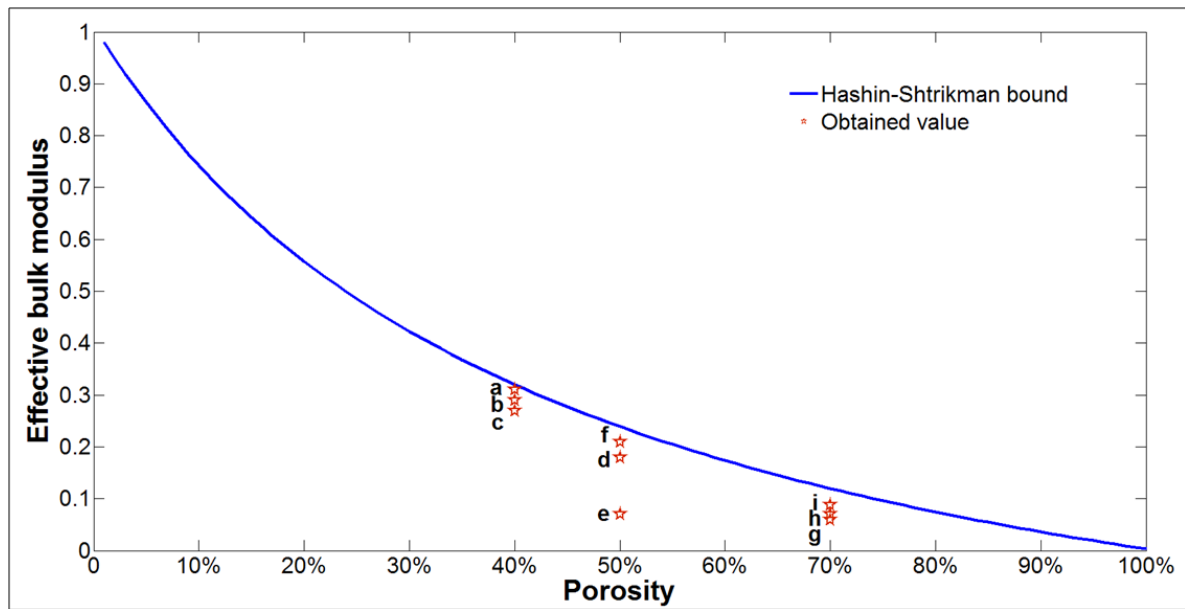


Figure 6.5 Compare the achieved properties of optimal design with the upper Hashin-Shtrikman bound

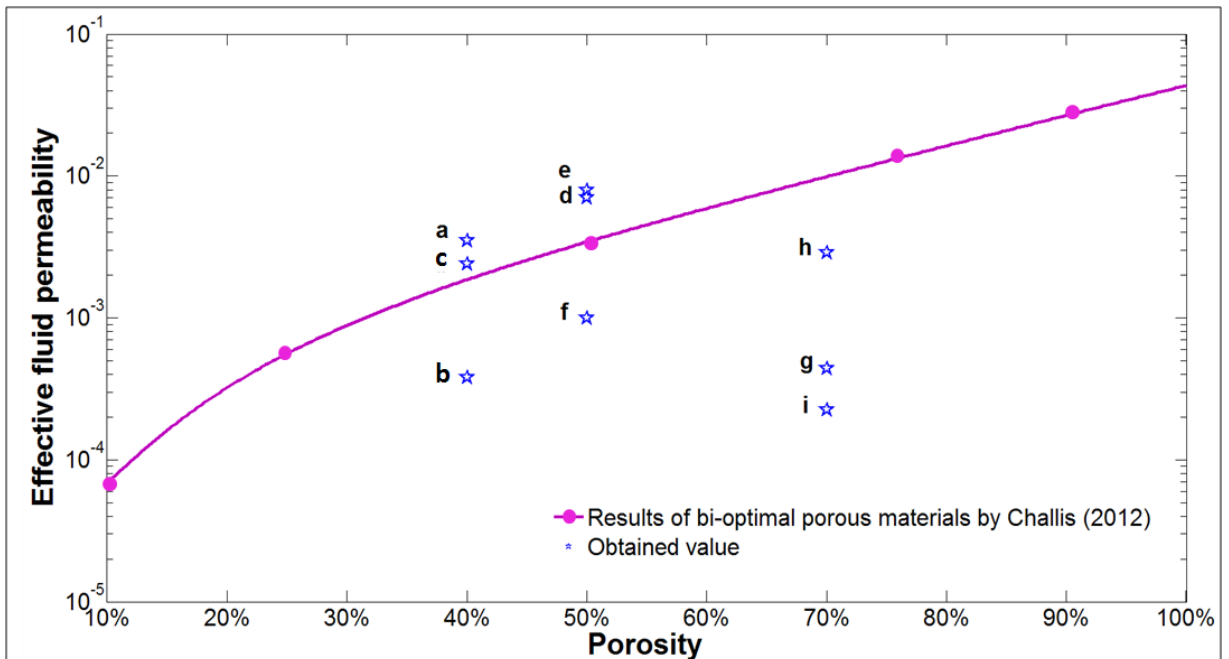


Figure 6.6 Compare the achieved properties of optimal design with the computational results from Challis (2012)

#### **6.4.4 Summary**

The numerical examples imply the capability of the proposed optimization method to distribute the amount of material in different layouts with different effective mechanical and mass transport properties to satisfy the demands in the tissue engineering. Moreover, this technique shows the ability to design scaffold architectures with desired stiffness and permeability, which have significant impact on tissue engineering.

# 7 Conclusions and Future Work

## 7.1 Conclusions

In this thesis, the structural shape and topology optimization problems is studied based on a level set based method.

Firstly, a systematic numerical method for designing the microstructured metamaterial has been proposed, in which the PLSM is incorporated with the numerical homogenization method. In this method, the numerical homogenization method is used to determine the effective properties of the microstructure of the composite, while the PLSM is to implement the inverse design of unit cell for microstructured materials. There is no re-initialization is required, the propagation of the level set surface is driven by dynamically updating the design variables using MMA, which is unconditionally stable and without the limitation of CFL condition. Moreover, this method can freely create new holes inside the material regions of the multi-phase design domain, as a result of the natural extension of the velocity field as well as the removal of the periodically applied global re-initializations. Numerical examples illustrate that the method can maintain the merits of the conventional LSMs, and improve the convergence speed of the optimization process.

Secondly, a topological shape optimization method for multiphase metamaterial design is developed based on the PLSM. This approach is as a matter of fact a general computational design methodology, which is applicable to create any artificially structured composite under periodicity. For a multiphase design problem, in the proposed MPLSM,  $M$  level set

functions are used to describe  $M+1$  material phases including one void phase and  $M$  solid phases. The concept of multi-phase material representation model in SIMP is introduced into the level set methods, thus, each individual phase will be represented through a simple artificial mixture assumption of all level set functions. This method has been successfully applied to design the metamaterial with extreme thermoelastic properties and the multifunctional metamaterial with NPR and NTE/ZTE properties simultaneously.

Lastly, a systematic topology optimization scheme based on PLSM is proposed to design the 3D periodic composites with desired multifunctional properties. The homogenization method is applied to predict the effective material properties including effective stiffness, effective permeability, and porosity. PLSM is introduced to find the optimal periodical microstructure within the 3D internal scaffold architecture. The effectiveness and efficiency of the proposed approach is demonstrated by numerical examples which are able to design the scaffold with a range of multifunctional properties.

## **7.2 Future Work**

In the present study, the optimized designs of micro-structured metamaterials are only obtained in 2D material distribution. In order to conjunct with fabrication via rapid prototyping technique (e.g. Additive Manufacturing, also known as 3D printing) and mechanical characterization, it is necessary to extend the design optimization into 3D structures. Due to the high computational cost of 3D simulation, symmetrical conditions should be applied on the design domain to save the computational time and space. The topologically optimized structures usually have complex geometries, and intrigued shapes and fine features, while

---

the Additive Manufacturing technique is particularly suitable for generating various components with highly complicated shapes and geometries.

In regards to the scaffold design, designing the architecture of the microstructure with controlled material properties is an initial study for the scaffold application in the tissue engineering. The optimization method may also take into account the effect of material degradation and tissue ingrowth on architectural characteristics over the healing time, by integrating a biodegradation model. Hence, how to incorporate time healing effect in the design sensitivity analysis is a challenging topic, to which a well answer is long sought-after.

Last, the combination of the PLSM with the numerical homogenization method has shown its capability in designing mechanical metamaterials of microstructures. Actually, this methodology can be extended to design other problems of materials-by-design, such as the electromagnetic metamaterials (e.g. photonic metamaterials) and the acoustic metamaterials (also named the phononic metamaterials).

# References

- Allaire, G., Jouve, F., et al. (2004). "Structural optimization using sensitivity analysis and a level-set method." Journal of Computational Physics **194**(1): 363-393.
- Allaire, G. and Jouve, F. (2005). "A level-set method for vibration and multiple loads structural optimization." Computer Methods in Applied Mechanics and Engineering **194**(30–33): 3269-3290.
- Andreassen, E. and Andreasen, C. S. (2014). "How to determine composite material properties using numerical homogenization." Computational Materials Science **83**: 488-495.
- Atluri, S. N. and Zhu, T. (1998). "A new Meshless Local Petrov-Galerkin (MLPG) approach in computational mechanics." Computational Mechanics **22**(2): 117-127.
- Atluri, S. N., Han, Z. D., et al. (2004). "A new implementation of the meshless finite volume method, through the MLPG ‘‘mixed’’ approach." CMES: Computer Modeling in Engineering & Sciences **6**(6): 491-514.
- Babuska, I. and Melenk, J. M. (1995). The partition of unity finite element method, DTIC Document.
- Belytschko, T., Lu, Y. Y., et al. (1994). "Element-free Galerkin methods." International Journal for Numerical Methods in Engineering **37**(2): 229-256.
- Belytschko, T., Lu, Y. Y., et al. (1995). "Crack propagation by element-free Galerkin methods." Engineering Fracture Mechanics **51**(2): 295-315.
- Belytschko, T., Xiao, S. P., et al. (2003). "Topology optimization with implicit functions and regularization." International Journal for Numerical Methods in Engineering **57**(8): 1177-1196.
- Bendsøe, M. P. and Kikuchi, N. (1988). "Generating optimal topologies in structural design using a homogenization method." Computer Methods in Applied Mechanics and Engineering **71**(2): 197-224.
- Bendsøe, M. P. and Sigmund, O. (1999). "Material interpolation schemes in topology optimization." Archive of Applied Mechanics **69**(9-10): 635-654.
- Bendsøe, M. P. and Sigmund, O. (2003). Topology optimization: theory, methods and applications, Springer.

- Boschetti, F., Pennati, G., et al. (2004). "Biomechanical properties of human articular cartilage under compressive loads." *Biorheology* **41**(3): 159-166.
- Bourdin, B. (2001). "Filters in topology optimization." *International Journal for Numerical Methods in Engineering* **50**(9): 2143-2158.
- Buhmann, M. D. (2003). *Radial basis functions: theory and implementations*, Cambridge university press Cambridge.
- Burger, M., Hackl, B., et al. (2004). "Incorporating topological derivatives into level set methods." *Journal of Computational Physics* **194**(1): 344-362.
- Byrne, D. P., Lacroix, D., et al. (2007). "Simulation of tissue differentiation in a scaffold as a function of porosity, Young's modulus and dissolution rate: application of mechanobiological models in tissue engineering." *Biomaterials* **28**(36): 5544-5554.
- Challis, V. J., Roberts, A. P., et al. (2008). "Design of three dimensional isotropic microstructures for maximized stiffness and conductivity." *International Journal of Solids and Structures* **45**(14): 4130-4146.
- Challis, V. J., Guest, J. K., et al. (2012). "Computationally generated cross-property bounds for stiffness and fluid permeability using topology optimization." *International Journal of Solids and Structures* **49**(23): 3397-3408.
- Chen, H. and Chan, C. (2007). "Acoustic cloaking in three dimensions using acoustic metamaterials." *Applied Physics Letters* **91**(18): 183518.
- Chen, Y., Zhou, S., et al. (2011). "Microstructure design of biodegradable scaffold and its effect on tissue regeneration." *Biomaterials* **32**(22): 5003-5014.
- Cheng, K. T. and Olhoff, N. (1981). "An investigation concerning optimal design of solid elastic plates." *International Journal of Solids and Structures* **17**(3): 305-323.
- Cioranescu, D. and Paulin, J. S. J. (1979). "Homogenization in open sets with holes." *Journal of Mathematical Analysis and Applications* **71**(2): 590-607.
- de Kruijf, N., Zhou, S., et al. (2007). "Topological design of structures and composite materials with multiobjectives." *International Journal of Solids and Structures* **44**(22): 7092-7109.
- Diaz, A. and Sigmund, O. (1995). "Checkerboard patterns in layout optimization." *Structural and Multidisciplinary Optimization* **10**(1): 40-45.
- Diaz, A. R. and Kikuchi, N. (1992). "Solutions to shape and topology eigenvalue optimization problems using a homogenization method." *International Journal for Numerical Methods in Engineering* **35**(7): 1487-1502.

- Duarte, C. A. and Oden, J. T. (1996). "An h-p adaptive method using clouds." Computer Methods in Applied Mechanics and Engineering **139**(1): 237-262.
- Ecker, K. (2004). Regularity theory for mean curvature flow, Springer.
- Evans, K. E. and Alderson, A. (2000). "Auxetic materials: functional materials and structures from lateral thinking." Advanced Materials **12**(9): 617-628.
- Fleury, C. (1989). "CONLIN: an efficient dual optimizer based on convex approximation concepts." Structural Optimization **1**(2): 81-89.
- Frecker, M. I., Ananthasuresh, G. K., et al. (1997). "Topological synthesis of compliant mechanisms using multi-criteria optimization." Journal of Mechanical Design **119**(2): 238-245.
- Gibiansky, L. V. and Sigmund, O. (2000). "Multiphase composites with extremal bulk modulus." Journal of the Mechanics and Physics of Solids **48**(3): 461-498.
- Gingold, R. A. and Monaghan, J. J. (1977). "Smoothed particle hydrodynamics-theory and application to non-spherical stars." Monthly notices of the royal astronomical society **181**: 375-389.
- Godunov, S. K. (1983). Difference method of numerical computations of discontinuous solutions in hydrodynamic equations, US Army Foreign Science and Technology Center.
- Goulet, R. W., Goldstein, S. A., et al. (1994). "The relationship between the structural and orthogonal compressive properties of trabecular bone." Journal of Biomechanics **27**(4): 375-389.
- Grima, J. N., Chetcuti, E., et al. (2012). "On the auxetic properties of generic rotating rigid triangles." Proceedings of the Royal Society A: Mathematical, Physical and Engineering Science **468**(2139): 810-830.
- Guedes, J. M. and Kikuchi, N. (1990). "Preprocessing and postprocessing for materials based on the homogenization method with adaptive finite element methods." Computer Methods in Applied Mechanics and Engineering **83**(2): 143-198.
- Guedes, J. M., Rodrigues, H. C., et al. (2003). "A material optimization model to approximate energy bounds for cellular materials under multiload conditions." Structural and Multidisciplinary Optimization **25**(5-6): 446-452.
- Guest, J. K., Prévost, J. H., et al. (2004). "Achieving minimum length scale in topology optimization using nodal design variables and projection functions." International Journal for Numerical Methods in Engineering **61**(2): 238-254.

- Guest, J. K. and Prévost, J. H. (2006). "Optimizing multifunctional materials: Design of microstructures for maximized stiffness and fluid permeability." International Journal of Solids and Structures **43**(22): 7028-7047.
- Guest, J. K. and Prévost, J. H. (2007). "Design of maximum permeability material structures." Computer Methods in Applied Mechanics and Engineering **196**(4): 1006-1017.
- Haber, E. (2004). "A multilevel, level-set method for optimizing eigenvalues in shape design problems." Journal of Computational Physics **198**(2): 518-534.
- Hashin, Z. and Shtrikman, S. (1963). "A variational approach to the theory of the elastic behaviour of multiphase materials." Journal of the Mechanics and Physics of Solids **11**(2): 127-140.
- Hassani, B. and Hinton, E. (1998). "A review of homogenization and topology optimization I—homogenization theory for media with periodic structure." Computers & Structures **69**(6): 707-717.
- Hollister, S. J., Madox, R. D., et al. (2002). "Optimal design and fabrication of scaffolds to mimic tissue properties and satisfy biological constraints." Biomaterials **23**(20): 4095-4103.
- Hollister, S. J. (2005). "Porous scaffold design for tissue engineering." Nature materials **4**(7): 518-524.
- Huang, X., Xie, Y. M., et al. (2006). "A new algorithm for bi-directional evolutionary structural optimization." JSME International Journal Series C **49**(4): 1091-1099.
- Huang, X., Xie, Y., et al. (2012). "Evolutionary topology optimization of periodic composites for extremal magnetic permeability and electrical permittivity." Structural and Multidisciplinary Optimization **46**(3): 385-398.
- Hughes, T. J. R., Franca, L. P., et al. (1986). "A new finite element formulation for computational fluid dynamics: V. Circumventing the babuška-brezzi condition: a stable Petrov-Galerkin formulation of the stokes problem accommodating equal-order interpolations." Computer Methods in Applied Mechanics and Engineering **59**(1): 85-99.
- Huisken, G. (1990). "Asymptotic behavior for singularities of the mean curvature flow." J. Differential Geom **31**(1): 285-299.
- Kadic, M., Bückmann, T., et al. (2013). "On anisotropic versions of three-dimensional pentamode metamaterials." New Journal of Physics **15**(2): 023029.
- Kang, H., Lin, C. Y., et al. (2010). "Topology optimization of three dimensional tissue engineering scaffold architectures for prescribed bulk modulus and diffusivity." Structural and Multidisciplinary Optimization **42**(4): 633-644.

- Kang, Z. and Wang, Y. (2011). "Structural topology optimization based on non-local Shepard interpolation of density field." Computer Methods in Applied Mechanics and Engineering **200**(49): 3515-3525.
- Kelly, D. J. and Prendergast, P. J. (2006). "Prediction of the optimal mechanical properties for a scaffold used in osteochondral defect repair." Tissue engineering **12**(9): 2509-2519.
- Kohn, R. V. and Strang, G. (1986). "Optimal design and relaxation of variational problems, I." Communications on Pure and Applied Mathematics **39**(1): 113-137.
- Lakes, R. (1987). "Foam structures with a negative Poisson's ratio." Science **235**(4792): 1038-1040.
- Lakes, R. (1993). "Materials with structural hierarchy." Nature **361**(6412): 511-515.
- Lakes, R. (1996). "Cellular solid structures with unbounded thermal expansion." Journal of materials science letters **15**(6): 475-477.
- Lanza, R., Langer, R., et al. (2011). Principles of tissue engineering, Academic press.
- Lekhnitskii, S. G. (1963). Theory of elasticity of an anisotropic elastic body, Holden-Day.
- Lin, C. Y., Kikuchi, N., et al. (2004). "A novel method for biomaterial scaffold internal architecture design to match bone elastic properties with desired porosity." Journal of Biomechanics **37**(5): 623-636.
- Liu, G. R. and Gu, Y. T. (2001). "A local radial point interpolation method (LRPIM) for free vibration analyses of 2-D solids." Journal of Sound and Vibration **246**(1): 29-46.
- Liu, G. R. and Gu, Y. T. (2005). An introduction to meshfree methods and their programming, Springer.
- Liu, W. K., Jun, S., et al. (1995). "Reproducing kernel particle methods." International Journal for Numerical Methods in Fluids **20**(8 - 9): 1081-1106.
- Luo, Z., Chen, L., et al. (2005). "Compliant mechanism design using multi-objective topology optimization scheme of continuum structures." Structural and Multidisciplinary Optimization **30**(2): 142-154.
- Luo, Z., Tong, L., et al. (2007). "Shape and topology optimization of compliant mechanisms using a parameterization level set method." Journal of Computational Physics **227**(1): 680-705.
- Luo, Z. and Tong, L. (2008). "A level set method for shape and topology optimization of large-displacement compliant mechanisms." International Journal for Numerical Methods in Engineering **76**(6): 862-892.

- Luo, Z., Tong, L., et al. (2009). "Design of piezoelectric actuators using a multiphase level set method of piecewise constants." *Journal of Computational Physics* **228**(7): 2643-2659.
- Luo, Z., Zhang, N., et al. (2012). "A physically meaningful level set method for topology optimization of structures." *CMES - Computer Modeling in Engineering and Sciences* **83**(1): 73-96.
- Luo, Z., Zhang, N., et al. (2013). "Topology optimization of structures using meshless density variable approximants." *International Journal for Numerical Methods in Engineering* **93**(4): 443-464.
- Ma, Z. D., Kikuchi, N., et al. (1995). "Topological optimization technique for free vibration problems." *Journal of applied mechanics* **62**(1): 200-207.
- Makhija, D. and Maute, K. (2013). "Numerical instabilities in level set topology optimization with the extended finite element method." *Structural and Multidisciplinary Optimization*: 1-13.
- Matsui, K. and Terada, K. (2004). "Continuous approximation of material distribution for topology optimization." *International Journal for Numerical Methods in Engineering* **59**(14): 1925-1944.
- Milton, G. W. (1992). "Composite materials with Poisson's ratios close to—1." *Journal of the Mechanics and Physics of Solids* **40**(5): 1105-1137.
- Mlejnek, H. P. (1992). "Some aspects of the genesis of structures." *Structural and Multidisciplinary Optimization* **5**(1): 64-69.
- Nicolaou, Z. G. and Motter, A. E. (2012). "Mechanical metamaterials with negative compressibility transitions." *Nature materials* **11**(7): 608-613.
- Osher, S. and Sethian, J. A. (1988). "Fronts propagating with curvature-dependent speed: algorithms based on Hamilton-Jacobi formulations." *Journal of Computational Physics* **79**(1): 12-49.
- Osher, S., Ronald Fedkiw (2002). *Level Set Methods and Dynamic Implicit Surfaces*. New York, Springer.
- Osher, S. J. and Santosa, F. (2001). "Level set methods for optimization problems involving geometry and constraints: I. Frequencies of a two-density inhomogeneous drum." *Journal of Computational Physics* **171**(1): 272-288.
- Otomori, M., Yamada, T., et al. (2013). "Level Set-Based Topology Optimization for the Design of an Electromagnetic Cloak With Ferrite Material." *Magnetics, IEEE Transactions on* **49**(5): 2081-2084.

- Paulino, G. H. and Le, C. H. (2009). "A modified Q4/Q4 element for topology optimization." *Structural and Multidisciplinary Optimization* **37**(3): 255-264.
- Paulino, G. H., Silva, E. C. N., et al. (2009). "Optimal design of periodic functionally graded composites with prescribed properties." *Structural and Multidisciplinary Optimization* **38**(5): 469-489.
- Peng, D., Merriman, B., et al. (1999). "A PDE-based fast local level set method." *Journal of Computational Physics* **155**(2): 410-438.
- Piat, R., Sinchuk, Y., et al. (2011). "Minimal compliance design for metal-ceramic composites with lamellar microstructures." *Acta Materialia* **59**(12): 4835-4846.
- Rahmatalla, S. F. and Swan, C. C. (2004). "A Q4/Q4 continuum structural topology optimization implementation." *Structural and Multidisciplinary Optimization* **27**(1): 130-135.
- Rozvany, G. I. N., Ong, T. G., et al. (1987). "Least-weight design of perforated elastic plates—I." *International Journal of Solids and Structures* **23**(4): 521-536.
- Rozvany, G. I. N. and Kirsch, U. (1995). "Layout optimization of structures." *Applied Mechanics Reviews* **48**: 41.
- Scarpa, F. and Tomlinson, G. (2000). *Sandwich structures with negative Poisson's ratio for deployable structures*. IUTAM-IASS Symposium on Deployable Structures: Theory and Applications, Springer.
- Schaback, R. and Wendland, H. (1999). "Using compactly supported radial basis functions to solve partial differential equations." *Boundary Element Technology* **13**: 311-324.
- Sethian, J. A. (1999). *Level set methods and fast marching methods: evolving interfaces in computational geometry, fluid mechanics, computer vision, and materials science*, Cambridge university press.
- Sethian, J. A. and Wiegmann, A. (2000). "Structural boundary design via level set and immersed interface methods." *Journal of Computational Physics* **163**(2): 489-528.
- Sigmund, O. (1994). "Materials with prescribed constitutive parameters: an inverse homogenization problem." *International Journal of Solids and Structures* **31**(17): 2313-2329.
- Sigmund, O. and Torquato, S. (1996). "Composites with extremal thermal expansion coefficients." *Applied Physics Letters* **69**(21): 3203-3205.
- Sigmund, O. and Torquato, S. (1997). "Design of materials with extreme thermal expansion using a three-phase topology optimization method." *Journal of the Mechanics and Physics of Solids* **45**(6): 1037-1067.

- Sigmund, O. and Petersson, J. (1998). "Numerical instabilities in topology optimization: a survey on procedures dealing with checkerboards, mesh-dependencies and local minima." *Structural Optimization* **16**(1): 68-75.
- Sigmund, O. (2000). "A new class of extremal composites." *Journal of the Mechanics and Physics of Solids* **48**(2): 397-428.
- Sigmund, O. (2001). "Design of multiphysics actuators using topology optimization—Part I: One-material structures." *Computer Methods in Applied Mechanics and Engineering* **190**(49): 6577-6604.
- Sigmund, O. (2002). On the optimality of bone microstructure. *Symposium on Synthesis in Bio Solid Mechanics*. Neverland, Springer: 221-234.
- Smith, D., Pendry, J., et al. (2004). "Metamaterials and negative refractive index." *Science* **305**(5685): 788-792.
- Sokołowski, J. and Zolesio, J. P. (1992). *Introduction to shape optimization: shape sensitivity analysis*, Springer-Verlag (Berlin and New York).
- Sokolowski, J. and Zochowski, A. (2009). Topological derivative in shape optimization Topological Derivative in Shape Optimization. *Encyclopedia of Optimization*, Springer: 3908-3918.
- Suzuki, K. and Kikuchi, N. (1991). "A homogenization method for shape and topology optimization." *Computer Methods in Applied Mechanics and Engineering* **93**(3): 291-318.
- Svanberg, K. (1987). "The method of moving asymptotes—a new method for structural optimization." *International Journal for Numerical Methods in Engineering* **24**(2): 359-373.
- Svanberg, K. (1998). "Two primal-dual interior-point methods for the MMA subproblems." *Technical Report TRITA-MAT-1998-0S12, Department of Mathematics, Royal Institute of Technology, Sweden, Stockholm*.
- Svanberg, K. (2002). "A class of globally convergent optimization methods based on conservative convex separable approximations." *Siam Journal on Optimization* **12**(2): 555-573.
- van Dijk, N. P., Langelaar, M., et al. (2012). "Explicit level-set-based topology optimization using an exact Heaviside function and consistent sensitivity analysis." *International Journal for Numerical Methods in Engineering* **91**(1): 67-97.
- Veselago, V. G. (1968). "The electrodynamics of substances with simultaneously negative values of  $\epsilon$  and  $\mu$ ." *Physics-Uspekhi* **10**(4): 509-514.

- Wang, M. Y., Wang, X., et al. (2003). "A level set method for structural topology optimization." Computer Methods in Applied Mechanics and Engineering **192**(1): 227-246.
- Wang, M. Y. and Wang, X. (2004). "“Color” level sets: a multi-phase method for structural topology optimization with multiple materials." Computer Methods in Applied Mechanics and Engineering **193**(6): 469-496.
- Wang, M. Y. and Wei, P. (2005). Topology optimization with level set method incorporating topological derivative.
- Wang, S. and Wang, M. Y. (2006). "Radial basis functions and level set method for structural topology optimization." International Journal for Numerical Methods in Engineering **65**(12): 2060-2090.
- Wang, S. Y., Lim, K. M., et al. (2007). "An extended level set method for shape and topology optimization." Journal of Computational Physics **221**(1): 395-421.
- Wang, Y., Luo, Z., et al. (2012). "Topological Optimization of Structures Using a Multilevel Nodal Density-Based Approximant." Computer Modeling in Engineering and Sciences **84**(3): 229-252.
- Wang, Y. Q., Luo, Z., et al. (2014). "Topological shape optimization of microstructural metamaterials using a level set method." Computational Materials Science **87**: 178-186.
- Wendland, H. (1995). "Piecewise polynomial, positive definite and compactly supported radial functions of minimal degree." Advances in computational Mathematics **4**(1): 389-396.
- Wendland, H. (2006). "Computational aspects of radial basis function approximation." Studies in Computational Mathematics **12**: 231-256.
- Xie, Y. M. and Steven, G. P. (1993). "A simple evolutionary procedure for structural optimization." Computers & Structures **49**(5): 885-896.
- Yang, W., Li, Z. M., et al. (2004). "Review on auxetic materials." Journal of Materials Science **39**(10): 3269-3279.
- Zhou, M. and Rozvany, G. I. N. (1991). "The COC algorithm, Part II: topological, geometrical and generalized shape optimization." Computer Methods in Applied Mechanics and Engineering **89**(1): 309-336.
- Zhu, T. and Atluri, S. N. (1998). "A modified collocation method and a penalty formulation for enforcing the essential boundary conditions in the element free Galerkin method." Computational Mechanics **21**(3): 211-222.